

**A grain-scale study of unsaturated flow in
highly swelling granular materials**

Thomas Sweijen

Reading committee:

Prof. dr. S. Luding

Prof. dr. O. Iliev

Prof. dr. ir. J. M. Huyghe

Prof. dr. ir. R. van Genuchten

Dr. M. Schmidt

Copyright © 2017 by Thomas Sweijen

All rights reserved. No part of this material may be copied or reproduced in any way without prior permission of the author.

ISBN: 978-90-6266-488-7

Title: A grain-scale study of unsaturated flow in highly swelling granular materials

NUR code: 934

NUR description: Hydrologie

Number of pages: 209

Cover photo by: Ioannis Zarikos

Printed by: ProefschriftMaken || www.proefschriftmaken.nl

A grain-scale study of unsaturated flow in highly swelling granular materials

Een korrel-schaal-onderzoek van onverzadigde stroming in zwellende en granulaire materialen

(met een samenvatting in het Nederlands)

Proefschrift

ter verkrijging van de graad van doctor aan de Universiteit Utrecht op gezag van de rector magnificus, prof.dr. G.J. van der Zwaan, ingevolge het besluit van het college voor promoties in het openbaar te verdedigen op vrijdag 17 november 2017 des ochtends te 10.30 uur

door

Thomas Sweijen

geboren op 13 maart 1990 te Lage Zwaluwe

Promotor: Prof.dr.ir. S.M. Hassanizadeh

Copromotor: Dr. B. Chareyre

This thesis was accomplished with financial support from the Technology Foundation STW, the technological branch of the Netherlands Organisation of Scientific Research, NWO, and the Dutch ministry of Economic Affairs under contract no. 12538, entitled Interfacial effects in ionized media.

Acknowledgements

*“Every story starts with an idea, but it is the characters
that move that idea forward.”*

Michael Scott

During my PhD experience, I have met many wonderful and remarkable persons who have supported me in successfully finishing my research and to whom I am exceptionally grateful.

First and foremost, I would like to show my gratitude towards my supervisor Majid Hassanizadeh for introducing me to the world of porous media, for our endless discussions, for his excellent ideas and for his thorough comments on my work. Majid encouraged me to work freely and to come up with my own ideas; this requires a lot of trust. For this, I am extremely grateful. I truly enjoy our working relationship, which is very dynamic, interesting, and innovative. Secondly, I would like to thank Bruno Chareyre for introducing me to the world of Yade-DEM, for all his help and for his brilliant ideas to solve various conceptual and technical issues. I am very pleased that Bruno visited Utrecht University when I just started my PhD, this was an excellent jump start for my research.

Next, I would like to thank members of the Environmental Hydrogeology Group at Utrecht University. I truly enjoyed the various discussions and music sessions with Niels Hartog, my former MSc supervisor, as well as Jan van Lopik and Gilian Schout. I also would like to thank visiting PhD student Andrea D’Aniello for his upbeat Italian chat. I am grateful to Ruud Schotting, perhaps not for the large amount of homework’s he often brought to my desk to correct, but for his good advice and for being an excellent teacher during various BSc and MSc courses that I have followed. Of course, I would like to thank members of the Hydrogeology Group that I have met: Willem-Bart Bartels, Amir Raof, Rien van Genuchten, Ioannis Zarikos, Xiaoguang Yin, Luwen Zhuang, Amir Hossein Tavangarrad, Enno de Vries, Nikos Karadimitriou, Ehsan Nikoee, Chaozhong Qin, Sayantan Ganguly, Pierre Le Fur, Mojtaba Mahmoodlu and Shuai Li. I am thankful to Lucas van Oosterhout for setting up the cluster, which speeded up many computations. Moreover, I am grateful to Hamed Aslannejad with whom I shared office and with whom I enjoyed many coffee breaks. Also, I would like

to thank secretaries Annuska and Magreet, who are always happy to help. Finally, I would like to thank Hans van Duijn for his collaboration on a mathematical derivation.

Next, I gratefully acknowledge fellow scientists from P&G who substantially improved the relevance of my work, by providing many comments, discussion, information, and experimental insights. Thank you Szymon Leszczynski, Peter Dziezok, and Mattias Schmidt. Furthermore, I would like to thank the other members of the STW project for their valuable input during the various meetings; thank you Jinqian Ding, Cong Yu, Jacques Huyghe, and Nicolae Tomozeiu. I am also thankful to Stefan Luding for his detailed comments on this thesis.

Finally, I am grateful to my family and friends, who have supported me during the ups and downs of a PhD trajectory. My best wishes to my parents and brother, who, as always, offer the welcoming “Brabantse” company and change of scenery. Also, I would like to thank my Northern Irish friends & family; I enjoy the various trips to NI, which always feel like a relaxing and pleasant holiday. Finally, I would like to thank Amy for her daily support, smiles, and laughter and for being patient with me whilst I was programming, writing, or daydreaming about scientific topics.

Thomas Sweijen

Contents

Chapter 1:	1
Introduction	
1.1 Super absorbent polymers	2
1.2 Swelling of a bed of SAP particles.....	4
1.3 Continuum-scale considerations.....	7
1.4 Grain-scale modelling	13
1.5 Outline of this thesis.....	13

Part I: Dynamics of swelling under saturated conditions

Chapter 2:	16
Grain-scale modelling of swelling granular materials: application to super absorbent polymers	
2.1 Introduction	17
2.2 Discrete Element Method.....	19
2.3 Implementation of swelling particles in DEM	21
2.4 Pore-finite volume method.....	23
2.5 Experimental methods.....	25
2.6 Model setup.....	28
2.7 Verification of the particle model.....	30
2.8 Simulations of a bed of SAP particles.....	33
2.9 Conclusion.....	37
Chapter 3:	38
A model for diffusion of water into a swelling particle with a free boundary: Application to a Super Absorbent Polymer particle	
3.1 Introduction	39
3.2 A numerical model for swelling of a particle	40
3.3 Results	46
3.4 Conclusion.....	51

Part II: Hydraulic parameters of swelling granular materials

Chapter 4:	54
The effects of swelling and porosity change on capillarity: DEM coupled with a pore-unit assembly method	
4.1 Introduction	55
4.2 Numerical model	58
4.3 Numerical simulations	60
4.4 Model testing	64
4.5 SAP particle beds	67
4.6 Conclusion	74
Chapter 5:	76
Capillary pressure-saturation relationships for porous granular materials: pore morphology method vs. pore unit assembly method	
5.1 Introduction	77
5.2 Numerical model	81
5.3 Simulation methods	85
5.4 Results and Discussion	87
5.5. Conclusion	98
Chapter 6:	100
The effect of particle shape on porosity values of swelling granular materials: Discrete element method and the multi-sphere approximation	
6.1 Introduction	101
6.2 Realization of clumps	103
6.3 Numerical methods and experiments	106
6.4 Results and Discussion	109
6.5 Conclusions	117

Part III: Dynamics of swelling under unsaturated conditions

Chapter 7:	120
Dynamic pore-scale modelling of drainage in granular porous media: the pore unit assembly method	
7.1 Introduction	123
7.2 Numerical model	126
7.3 Simulation setup	139
7.4 Results	141
7.5 Conclusions	151
Chapter 8:	152
A grain-scale model for unsaturated flow in deforming packings of swelling particles: a case study on small-scale swelling events	
8.1 Introduction	153
8.2 Numerical methods	153
8.3 Model setup	158
8.4 Results and discussion	162
8.5 Conclusions	168
Chapter 9:	170
Summary and Perspectives	
9.1 Summary	170
9.2 Perspectives	173
Appendices	175
References	195
Samenvatting	206

Chapter 1

Introduction

Swelling is commonly referred to as a spontaneous increase of solid volume, which occurs after a perturbation to restore the equilibrium between a solid and the surrounding fluid. Swelling can be a result of simply changing the fluid that surrounds a solid; for example, replacing air by water. Swelling can also be a result of either a change in chemical composition of the surrounding fluid, such as a change in salinity, or a change in confining pressure that is applied to the solid. An example is the experimental work by Frijns et al. (1997), who have studied the swelling of a sample of intervertebral disc tissue. They inserted the sample into a testing chamber where the sample was in contact with saline water while a confining pressure was applied to the sample. First, the salinity of the water was decreased from its initial value, causing the sample to swell, then an increase in confining pressure was applied, causing the sample to shrink. Their experiments were successfully reproduced using a numerical model by Huyghe and Janssen (1997), which accounted for the interactions of the solid and liquid phase as well as the cations and anions.

Swelling of porous materials poses an intricate and highly coupled problem. It not only causes deformation of the solid phase, but also affects the distribution of the liquid inside the pores, which in turn affects the swelling and deformation of the solid phase. An example is the swelling of a coal bed due to injection and subsequent adsorption of CO₂ inside nanometer pores of coal. Swelling of coal causes an increase in internal stress and a subsequent decrease in permeability (Espinoz et al., 2014; Pan and Conell, 2012 and references therein). The decrease in permeability inhibits the usage of coal beds for further carbon sequestration and/or methane production. Swelling of porous materials also occurs in anthropogenic materials such as swelling of hydrophilic binders inside the coating layer of paper during ink injection (see e.g. Lamminmäki et al., 2012), the swelling of hydrogels in hygienic products (see e.g. Diersch et al., 2010), the swelling of potatoes during frying (Takhar, 2014) and the swelling of rice and couscous during cooking (e.g. Tester and Morrison, 1990; Yeh and Li, 1996). In this thesis, the focus is primarily on the swelling of a particular type of hydrogels, namely Super Absorbent Polymers.

1.1 Super absorbent polymers

Super Absorbent Polymer (SAP) grains are used in a variety of applications, for example: i) to remove water from a pathogen solution to increase the pathogen concentration, which enables detection of the pathogen (Xie et al., 2016); ii) to control shrinkage in cement pastes (e.g. Snoeck et al., 2015); iii) to regulate moisture content in soils (e.g. Woodhouse and Johnson, 1991) and iv) to absorb liquids in hygienic products (e.g. Kabiri et al., 2011).

SAP is made of flexible hydrophilic polymer chains that are crosslinked to form an insoluble polymer network (Buchholz, 1998a). If they were not crosslinked, SAP would dissolve into the liquid rather than absorbing the liquid. At the molecular scale, water molecules will adsorb on the hydrophilic polymers (e.g. Bennethum and Cushman, 1996); this appears as absorption at the particle scale. SAP is often produced in large blocks which are then ground to form particles with an irregular shape (Graham and Wilson, 1998; Omidian et al., 1999); see Figure 1.1a. However, spherical SAP particles can also be produced by an inverse suspension polymerisation; such a particle is shown in Figure 1.1b (Omidian et al., 1999).

Properties of SAP particles can be tailored for a specific application, by varying the composition, shape, and size. In this work, the molecular description of SAP particles is not considered. Instead, we study and characterize individual particles by means of continuum-scale parameters, such as mass, volume, density, particle stiffness and parameters that describe the swelling behaviour of SAP. In what follows, parameters relevant to the description of SAP particles are discussed.

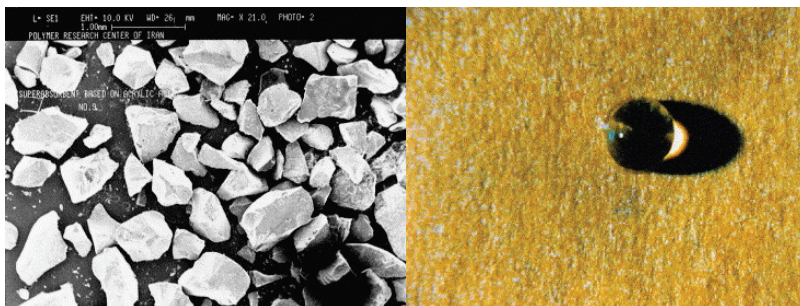


Figure 1.1: Examples of SAP particles, a) ground SAP particles produced from a slab of SAP and b) specially produced spherical SAP particles. Figures are from Omidian et al. (1999).

1.1.1 Continuum-scale parameters to describe individual SAP particles

The maximum amount of liquid that SAP can absorb is commonly referred to as absorption capacity. It depends on: i) the composition of SAP, ii) the composition of absorbed liquid, iii) the applied pressure on SAP particle, and iv) the ambient temperature. The underlying physical process is the restoration of the equilibrium in electrochemical potential between SAP and the absorbent liquid (Huyghe and Janssen, 1997). When there is disequilibrium, a swelling pressure occurs that drives swelling (Buchholz, 1998b). Dry SAP has a relatively high electrochemical potential compared to the free liquid. To equilibrate the electrochemical potential, SAP must absorb liquid and thus reduce its electrochemical potential. Thus, an increase in salinity of the solvent causes a decrease in absorption capacity, because the electrochemical potential of a solvent with increased salinity is larger and thus closer to that of dry SAP. In that case, SAP needs to absorb less liquid to reduce its electrochemical potential to restore equilibrium. An increase in confining pressure causes a decrease of absorption capacity, as the swelling pressure and thus the swelling potential is compensated by the confining pressure (Buchholz, 1998b).

The absorption capacity of SAPs that are commercially produced does indeed vary depending on the situation as described previously. For swelling in distilled water, the absorption capacity is an impressive 1000 gram of water per gram of SAP. For swelling in tap water, the absorption capacity is approximately 220 g/g (see Chapter 2). For applications in hygienic products, the absorption capacity is approximately 30-40 g/g for water with a physiological saline concentration and an applied confining stress of 0.3Psi (see e.g. Chambers et al., 1992).

The swelling rate of SAP is typically described by a first-order kinetic formula where the total amount of absorption increases with time. Most liquid absorption for commercially produced SAP occurs within 5 to 10 min (Esteves, 2011; Omidian et al., 1999). The swelling rate is thought to be controlled by the diffusion of water molecules into SAP, but diffusion may also be related to relaxation of the polymer network (Tanaka and Fillmore, 1979). However, Omidian et al. (1999) found that the swelling rate is dominated by water diffusion. This because the surface area to volume ratio of SAP particles affects the swelling rate; swelling is much faster for small particles than for larger particles. In Chapter 3, we further investigate the swelling of an individual particle by developing an accurate model for water diffusion into spherical particles having a free and moving boundary.

The mechanical parameters of SAP greatly depend on its composition. In general, larger crosslink concentrations yield higher values of shear moduli, because polymer networks become stiffer when connectivity of the polymers are increased by crosslinkers. Also, swelling affects the stiffness of SAP. In the dry state, SAP is

relatively stiff with Young's moduli in the range of MPa, but in a slightly swollen state, the stiffness drops to the range of kPa. The large difference in Young's moduli between dry and swollen state causes great changes in packings of SAP particles. In Chapter 6, we elaborate on the effect of stiffness on the porosity of SAP particle packings.

1.2 Swelling of a bed of SAP particles

In this work, the focus lies on upscaling the behaviour of individual SAP particles to that of a bed of SAP particles. Before evaluating the important concepts of upscaling, from grain scale to continuum scale, we introduce the behaviour of a bed of SAP particles based on experimental investigations.

1.2.1 Free swelling experiment

First, we would like to explain a simple experiment that can be conducted with a small amount of SAP particles and water in a beaker glass. The following thought-experiment is introduced to conceptualize the processes that are present during a swelling event of granular materials.

Consider a glass beaker that contains a layer of SAP particles. A certain volume of water is added to the glass beaker that is less than the total amount of water that the particles can absorb. Directly after the addition of water, SAP particles will start to absorb water, thus they will grow and soften. Subsequently, SAP particles will rearrange themselves by undergoing compression, sliding, twisting and rolling at their contacts with other particles. This will lead to a significant increase of the height of the layer. In the beginning of the swelling process, all SAP particles are immersed in water where, because of swelling, suction occurs. But, water inside the pores will eventually be absorbed and thus the particles are gradually exposed to air, causing the drying out of pores, referred to as drainage. If the water supply to individual SAP particles is not sufficient, the swelling of those SAP particles will slow-down and eventually stop. Once all the water is absorbed by SAP particles, or trapped inside the pores in between the particles, the swelling event ends.

This experiment is referred to as a *free swelling experiment*, because particles are allowed to swell freely (under gravity of course). This experiment can be conducted in many variants to study various effects. For example, a load can be imposed on the SAP

particles to study absorption under load (Buchholz, 1998b). By applying a load, non-linear deformation may occur in addition to swelling; particles may slide and roll less but particles may undergo more compression than in a free swelling experiment, causing the flattening of particles. If a sufficiently large load is applied, the permeability and porosity of the particle bed may become extremely small and thus inhibiting flow of water through the pores of the particle bed (see e.g. Brandt et al., 1987).

To conclude, a variety of processes are mentioned in the free swelling experiment, namely: swelling of particles, softening of particles, water suction inside the bed of SAP particles, and the drying of the pores of the particle bed. The occurrence of these processes gives rise to research questions related to the optimization of SAP particles for commercial purposes, namely: i) how do the porosity, permeability, retention properties, and relative permeability change with time; ii) how are various parameters distributed inside the particle bed? To answer such questions, numerical and experimental tools are required that enable insight in the swelling behaviour of a bed of SAP particles.

1.2.2 Characterization of a bed of swelling SAP particles

Experimental investigation of a bed of SAP particles is difficult, because swelling is fast and the subsequent deformation is large. To characterize the dynamics of a bed of SAP particles, the height of a bed can be measured over time such that continuum-scale dynamics are revealed. Under water-saturated conditions, a free swelling experiment can be conducted where the height of the bed can simply be tracked over time. Under unsaturated conditions, a vertical wicking experiment can be employed, as described by Mirnyy et al. (2012). In that experiment, a layer of initially dry SAP particles was placed in between a plate and an inflatable pillow, which exerted a pressure of 0.3 Psi. The setup was then put vertically and brought into contact with water (see Figure 1.2). In that experiment, water spontaneously imbibed into the layer of particles, causing the particles to swell. The height of the water front and the amount of water uptake were measured such that this experiment could be used for the validation of numerical simulations. For dynamic experiments, processes are reported in terms of liquid uptake, height of the particle bed, and the approximate location of air-water interface. However, these experiments do not yield values for physical quantities such as porosity, permeability, retention properties, relative permeability, and the strength of a particle bed.

To measure physical quantities of a bed of swelling particles, a quasi-static approach is typically employed in which particles are swollen to a certain degree depending on the salinity of water. The underlying concept is to make snap-shots of the

swelling process at various degrees of swelling where various hydraulic and mechanical properties are measured at each swelling degree. This results in relationships for physical properties as function of the degree of swelling. For example, Grosshans et al. (1995) conducted rheology experiments on SAP particles for a variety of swelling degrees such that they could obtain the yield-stress of a particle bed as a function of the degree of swelling. Their results indicated that the yield stress and the Young's modulus of a packing decreases with increasing degree of swelling; see Figure 1.3. Comparable quasi-static experiments have been conducted to measure porosity, permeability, shear moduli, and retention properties (e.g. Diersch et al., 2010; Wang et al., 1998). However, quasi-static measurements do not capture dynamics of swelling and thus the question remains how time would affect the relationships between physical properties and the degree of swelling.

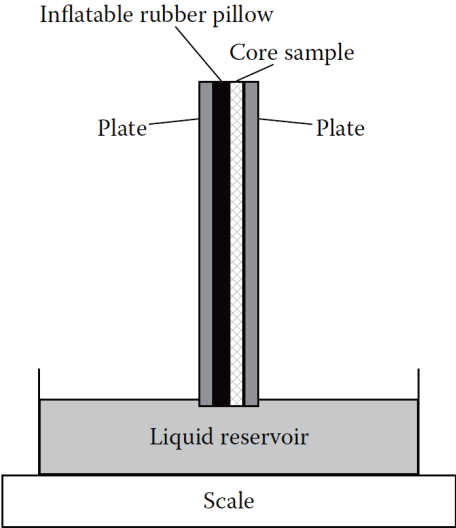


Figure 1.2: Experimental setup for a wicking experiment by Mirnyy et al. (2012). Note that a bed of SAP particles is referred to as core sample.

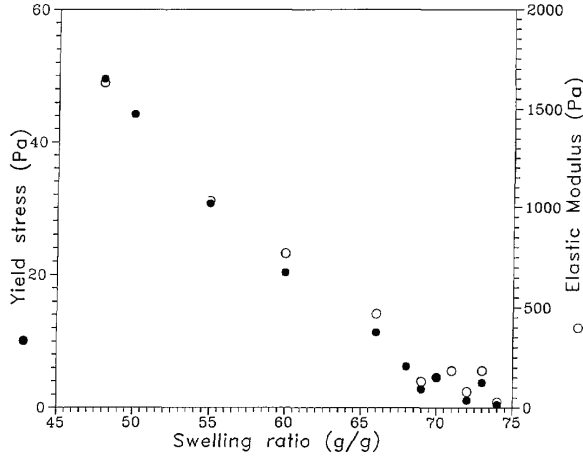


Figure 1.3: Yield stress and elastic modulus as function of the degree of swelling of SAP particles. The Figure was originally reported by Grosshans et al. (1995).

1.3 Continuum-scale considerations

In addition to experimental work, continuum-scale models can be employed to study the swelling behaviour of a bed of SAP particles. Such a model needs to consider swelling, the subsequent deformation of the solid phase, and flow of water. An example of a comprehensive model for swelling of a bed of particles is that by Diersch et al. (2010; 2011). In that model, a Richards-type equation was developed for water flow in an unsaturated porous medium, in which dependencies appear that are tailored for swelling. In what follows, some equations are highlighted that give insight in the swelling process. For a complete overview of all equations, the reader is referred to Diersch et al. (2010). In that work, the following flow equation was obtained for a compressible liquid in a deformable and swelling granular material:

$$\underbrace{\phi \frac{\partial s}{\partial t} + \phi s \beta \frac{\partial p}{\partial t} - \nabla \cdot [k_r K (\nabla p - \rho g)]}_{\text{Flow of compressible fluid}} = - \underbrace{\left[\frac{C_{SAP}^0}{J \rho} + \phi \frac{\partial s}{\partial Q} + s \left(\frac{\partial \phi}{\partial Q} + \frac{\phi}{J} \frac{\partial J}{\partial Q} \right) \right]}_{\text{sink term due to swelling}} \frac{\partial Q}{\partial t} \quad (1.1)$$

where ϕ is the porosity, s is the liquid saturation, ρ is the density of water, g is the gravitational constant, Q is the absorption ratio (mass of swollen SAP divided by mass of dry SAP), β is compressibility of water, p is the water pressure, k_r is the relative permeability of liquid, K is the intrinsic permeability, C_{SAP}^0 is the initial mass of SAP divided by a reference volume, and J is the volumetric dilation. The right-hand side of

equation 1.1 represents a sink term for water because of swelling and subsequent deformation. The change in free water volume per reference is given by: $\frac{\partial \phi s}{\partial t} = \left[\phi \frac{\partial s}{\partial Q} + s \left(\frac{\partial \phi}{\partial Q} + \frac{\phi}{J} \frac{\partial J}{\partial Q} \right) \right] \frac{\partial Q}{\partial t}$ where ϕ is a function of dilation J . The change in water volume due to water uptake by the solid phase is given by: $\frac{c_{SAP}^0}{J\rho} \frac{\partial Q}{\partial t}$. The derivatives $\frac{\partial s}{\partial Q}$, $\frac{\partial Q}{\partial t}$, $\frac{\partial J}{\partial Q}$ and $\frac{\partial \phi}{\partial Q}$ are obtained from empirical relations that were calibrated on quasi-static experiments. Furthermore, the function of $p(s, Q)$ is determined based on experimental investigations. These empirical relations are closure equations for the continuum-scale model and are described in the following section.

1.3.1 Closure equations

To find the closure equations, one must rely on experimental observations of the behaviour of SAP particles. All closure equations and the subsequent parameterization are based on data from experiments, making this approach empirical. Here, we will evaluate the relevant closure equations and their implications as presented in the work of Diersch et al. (2010).

First, the porosity is assumed to have a monotonic dependency on the degree of swelling under constant confining pressure. This is an essential simplification, as it prevents the usage of complex mechanical descriptions, such as swelling dependent deformation laws and measurements of shear moduli of particle beds, at varying degrees of swelling. Figure 1.4 shows a typical data set on porosity vs. the degree of swelling by Mirnyy et al. (2012). Dry SAP particles are highly irregular and stiff, resulting in a large porosity value of ± 0.70 , following Diersch et al. (2011). The SAP particles soften as they absorb water leading to a strong decrease in porosity value. The experimental data in Figure 1.4 is fitted by the following equation (following Diersch et al., 2010):

$$\phi(Q) = \frac{2\phi_{max}}{1 + ((Q - 1)\phi_{scale} + 1)^{\phi_{exp}}} \quad (1.2)$$

where ϕ_{max} is the maximum porosity value, ϕ_{scale} and ϕ_{exp} are fitting parameters and Q is the degree of swelling defined as the mass of swollen SAP over the initial dry mass. The best fit resulted in the following values: $\phi_{max} = 0.9$; $\phi_{scale} = 1$; $\phi_{exp} = 0.65$ (note that these values were not reported in the original work, but extracted here). One disadvantage of prescribing the relation between porosity and the degree of swelling is that the model loses flexibility towards varying confining stresses during simulations; for varying confining stresses, the porosity vs. degrees of swelling relation may be hysteretic and non-monotonic. Therefore, we investigated in Chapter 6 the 3-dimensional surface of porosity as a function of swelling and the state-of-stress for SAP

particles. In that Chapter, the shape of particles is considered and porosity values of simulations are tested to experimental data.

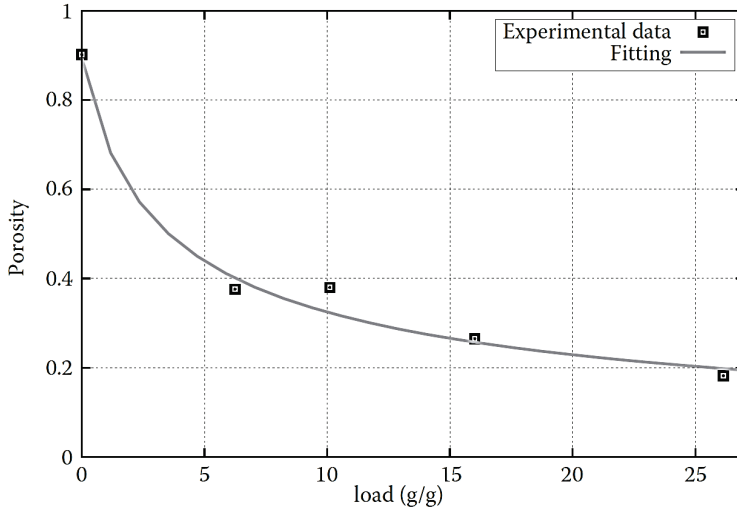


Figure 1.4: Porosity versus the degree of swelling, referred to as load (Mirnyy et al., 2012) which is defined as the ratio of absorbed water over the mass of dry SAP.

Figure 1.5 shows the effect of swelling on the permeability as reported in Grosshans et al (1995). The permeability is affected by two counteracting processes, namely: i) increase of particle radii with swelling, which tends to increase pore sizes and thus the permeability and ii) decrease of porosity with swelling, which tends to decrease the permeability. In Figure 1.5, the increase in particle radii clearly is the dominant process as the permeability strongly increases with the degree of swelling. However, this is dependent on the swelling scenario; if one would apply a relatively large confining pressure, the porosity could become very small and thus the permeability could decrease with increasing degrees of swelling. To have flexibility in this dependency, Diersch et al. (2010) proposed a very general equation:

$$k(Q) = k_{base} [1 + k_{coeff} e^{k_{exp} Q} \sin(2\pi k_{sin} Q + k_{phase})] \quad (1.3)$$

where k_{base} , k_{coeff} , k_{exp} , k_{sin} , and k_{phase} are fitting parameters that can vary for varying confining pressures.

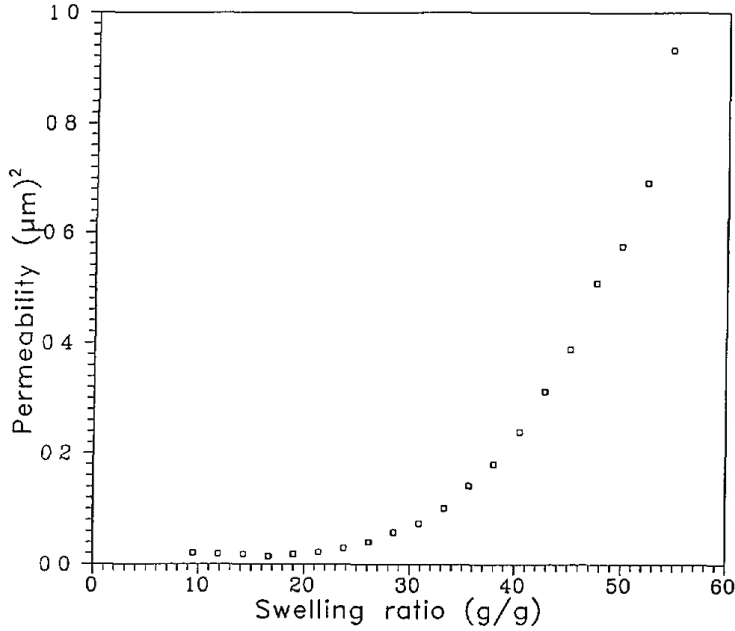


Figure 1.5: Permeability of a bed of SAP particles as function of the degree of swelling (Grosshans et al., 1995).

The capillary pressure-saturation relationship is also dependent on both the confining pressure and the degree of swelling. Diersch et al. (2010) used the Van Genuchten formula (see Appendix A) to describe the capillary pressure-saturation relationship. The Van Genuchten parameter α , which is linearly proportional to the inverse of the entry pressure, is assumed to decrease with the degree of swelling, Q :

$$\alpha(Q) = \begin{cases} \alpha_{max} & Q \leq Q_{thr} \\ \frac{\alpha_{max}}{(1 + \alpha_{scale}(Q - Q_{thr}))^{\alpha_{exp}}} & Q > Q_{thr} \end{cases} \quad (1.4)$$

where α_{max} , α_{scale} , α_{exp} and Q_{thr} are fitting parameters. The value of α_{max} for drainage processes is assumed to be different from the value for wetting. Diersch et al. (2010) assumed Van Genuchten parameter n to be constant. Equation 1.4 does not include a dependency of α on the state-of-stress (or porosity) of the packings. Therefore, the 3-dimensional surface of α , Q , and ϕ is constructed in Chapter 4 in order to study the effect of porosity change on the parameter α .

Equations 1.2 to 1.4 contain a variety of fitting parameters that must be determined experimentally, which is time-consuming. The value of each fitting

parameter carries its own uncertainty and thus one should determine each value carefully to have the parameterization of the numerical model as accurate as possible. An issue with many fitting parameters is that when numerical simulations do not agree with experiments, which parameter or closure equation is responsible for this deviation? Another question is whether such a continuum-scale model is still physical when it has so many fitting parameters, whose physical meaning is difficult to interpret. Moreover, closure equations have been derived assuming a constant confining pressure and a non-hysteretic behaviour, which limits the applicability of the model.

1.3.2 Representative Elementary volume

Despite various concerns raised in section 1.3.1, continuum-scale models have proven to be extremely beneficial to simulate complex processes in porous materials as in the case of swelling of partially-saturated granular materials. However, beds of SAP particles are typically relatively thin and thus continuum-scale models may not be applicable, because the size of the material of interest should exceed the size of one Representative Elementary Volume (REV). An REV corresponds to a minimum domain size over which all micro-scale heterogeneities are averaged out and values of average variables are independent of domain size (see e.g. Bear, 1972). Ideally, the domain of interest is larger than many REV's such that transport phenomena can be considered. This is commonly the case for studies of transport processes in sand columns but even more so for large aquifers or oil reservoirs.

The REV size of a material can be determined by incrementally increasing the averaging domain size while measuring the value of a physical property of interest (e.g. porosity, permeability, capillary pressure-saturation relationships) until the value fluctuates within a sufficiently narrow interval. For example, Karadimitriou et al. (2013) reported the REV of their complex micro models, which are 2-dimensional flow networks made out of PDMS. Based on porosity values, their REV was $5 \times 2.8 \text{ mm}^2$, while their micromodel was $5 \times 30 \text{ mm}^2$. Thus their model comprised of multiple REV's, which enabled studies of transport mechanism; e.g. quasi-static two-phase flow or dynamic two-phase flow (Karadimitriou et al., 2014). Joekar-Niasar and Hassanizadeh (2010) studied dynamic two-phase flow in regular networks of cubic pore bodies. They found an REV of $35 \times 35 \times 35$ pore bodies, based on quasi-static capillary pressure-saturation curves. Culligan et al. (2004) have conducted X-ray tomography experiments on a partially-saturated glass-bead packing to visualize and quantify saturation and air-water interfacial area. Figure 1.6 shows that the porosity converges to a constant value when increasing the domain size. Yuan et al. (2015) have numerically generated capillary pressure-saturation relationships using a grain-scale model for packings of spheres

similar to that by Culligan et al. (2004). They found that the distribution in saturation in the domain yields a much larger REV size than for porosity, which implies that one should find the REV of the quantity of interest.

Complications occur when the domain of interest does not comprise enough pores, or particles, to have an REV. The application of continuum-scale models (e.g. Darcy’s law) for materials smaller than one REV is conceptually doubtful and therefore obtained results are questionable. One solution is to employ a reduced continuum-scale model where processes are simulated in the in-plane directions in terms of properties that are averaged in the through-plane direction (Qin and Hassanizadeh, 2014).

For small domains, an alternative to continuum-scale models is a pore-scale or grain-scale model that can provide detailed distributions of variables of interest. Examples of thin porous media are: layers of fuel cells; fibres in paper; membranes and sheets; and layers of SAP particles in hygienic products.

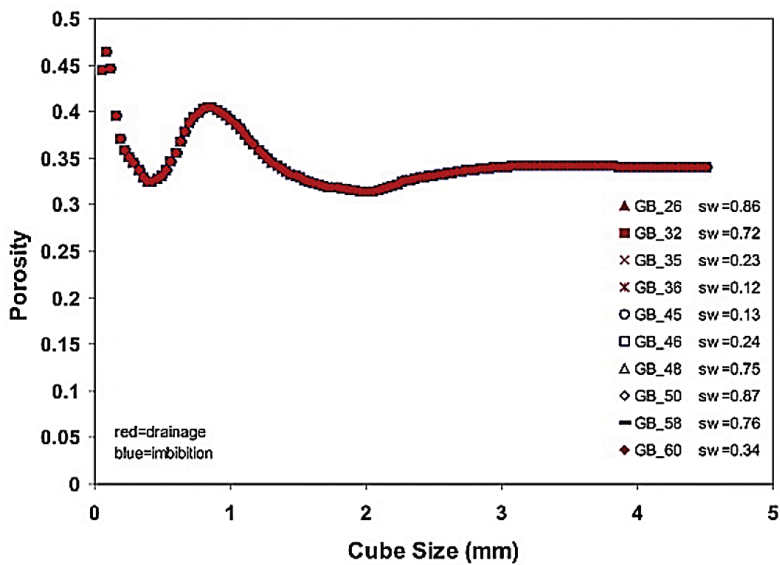


Figure 1.6: Porosity of a sub-sample of a glass-bead packing as a function of the edge size of the cubical subdomain. Figure from Culligan et al. (2004).

1.4 Grain-scale modelling

An alternative to continuum-scale models and experiments is a grain-scale model. A grain-scale model can provide estimates for porosity, permeability and retention properties under various conditions. Usually, the following input parameters are needed as input to grain-scale models: particle size distribution, particle shapes, and particle location from which the latter is determined based on an initial configuration, contact mechanics and loading history.

As mentioned before, swelling of granular materials is a complex process, which requires many fitting parameters to enable continuum-scale simulations. Therefore, a grain-scale model may prove to be a useful addition to both continuum-scale modelling and experimental investigations. A bed of SAP particles and its subsequent swollen state are of the order of millimetre to centimetre scale, which is ideal for grain-scale simulations. That is why we focus on grain-scale modelling of swelling granular materials under partially saturated conditions. Physical processes are simulated at the grain scale and continuum-scale properties are obtained by averaging at the sample scale.

In the following chapters of this thesis, we develop and employ grain-scale models to study the swelling of a bed of SAP particles. We focus on both dynamic and quasi-static aspects of swelling materials, under saturated and unsaturated conditions. The aim is to develop a grain-scale model and to study its versatility in application. Where possible, we provide a proof of principle. While we focus mainly on swelling materials, various concepts are not exclusive to swelling, but can also be applied to other granular materials such as sands and glass beads, and possibly to porous materials in general.

1.5 Outline of this thesis

This thesis contains three main parts: I) dynamics of swelling under saturated conditions, II) hydraulic parameters of swelling granular materials, and III) dynamics of swelling under unsaturated conditions.

In part I, we investigate the dynamics of swelling under saturated conditions. In Chapter 2, we introduce the Discrete Element Method (DEM) and the Pore Finite Volume (PFV) method. Then, we implement swelling in a grain-scale model to simulate a free swelling experiment. Results are compared to experimental data, to test the model. The versatility of the model towards the mechanical description of SAP particles is investigated. In Chapter 3, the swelling of one SAP particle is investigated and a new

physically-based model is derived for water diffusion into a spherical particle having a free and moving boundary.

In part II, we obtain quasi-static relationships for hydraulic parameters as function of the degree of swelling. In Chapter 4, we investigate the effects of swelling and porosity change on the retention properties of packings of spheres which are used as proxies for SAP particle beds. For this, DEM is coupled to the pore-unit assembly method, which is used to construct retention curves following a capillarity algorithm. In Chapter 5, we evaluate this model by constructing retention properties for glass-bead packings and filter sands for which experimental data exists in the literature. In that Chapter, we also evaluate underlying assumptions in constructing retention curves of particle packings. Then, in Chapter 6, we study the effect of particle shape on the relationship of porosity, with the degree of swelling and confining stress. In that Chapter, we compare our results to experimental data of SAP particles.

In part III, we introduce various building blocks of a grain-scale model for swelling of particles under unsaturated conditions. In Chapter 7, we introduce a dynamic model for unsaturated flow in non-deformable packings of spheres using the pore-unit assembly approach. In Chapter 8, dynamic flow is simulated during a small-scale swelling event, which is a step towards coupling of flow with large-scale deformations.

At the end of the thesis, conclusions and perspectives on grain-scale modelling of swelling granular materials is given and an outline for future research is provided.

Part I

Dynamics of swelling under saturated conditions

Grain-scale modelling of swelling granular materials: application to super absorbent polymers

Abstract

Swelling is an important process in many natural materials and industrial products, such as swelling clays, paper, and Super Absorbent Polymer (SAP) particles in hygienic products. SAP particles are capable to absorb large amounts of fluid. Each grain of SAP can absorb water 30 to 1000 times its initial mass, depending on the water composition.

To gain insight in the swelling behaviour of a bed of SAP particles, we have developed a grain-scale model and have tested it by comparing it to experiments. The grain-scale model is based on a combination of the Discrete Element Method (DEM) and the Pore Finite Volume (PFV) method, which we have extended to account for the swelling of individual SAP particles. Using this model, we can simulate the behaviour of individual particles inside a water-saturated bed of swelling SAP particles while considering the hydro-mechanical effects arising from the presence of pore water. The model input includes physical parameters such as particle stiffness and friction angle, which were found in the literature, as well as the particle size distribution and water diffusion coefficients, which were measured experimentally. A swelling rate equation was developed to simulate the swelling of individual particles based on water diffusion into a spherical particle. We performed experiments to measure the rise of the surface of a bed of initially dry SAP particles, which were put inside a glass beaker that contained enough water for the SAP particles to swell and to remain saturated at all times. We used our model to simulate the swelling of that SAP particle bed as a function of time. Simulations show that the numerical model is in reasonable accordance with the experimental data. We have also verified the grain-scale model coupled with PFV with Terzaghi's analytical solution for a small swelling event. Finally, a sensitivity analysis was performed to study the effects of main grain-scale parameters on the larger-scale behaviour of a bed of particles.

2.1 Introduction

Swelling of porous media occurs in many natural and industrial materials *e.g.* clays, foods, biological tissues, papers, and absorbent polymers in hygienic products (Diersch et al., 2010; Romero et al., 2011; Takhar, 2014; Murad and Cushman, 1996). Swelling is a complex process that requires knowledge of the behaviour of both fluid and solid phases and their physical interactions, as well as the chemical interactions inside and around the solid phase (Huyghe and Janssen, 1997; Malakpoor et al., 2007). The process of swelling is defined as the expansion of a (porous) solid because of absorption of a fluid. A distinction can be made between swelling solids *e.g.* cartilages, hydrogels, Super Absorbent Polymers (SAP), and swelling granular media, such as a bed of SAP particles. In this work, we focus on irregularly shaped SAP particles, whose size ranges from 45 to 850 μm and are mostly used as absorbent agent in hygienic products.

During the design of SAP, the initial chemical composition determines its stiffness, absorption rate and absorption capacity (Kabiri et al., 2003; Brandt et al., 1987; Knaebel et al., 1997). SAP consists of long hydrophilic polymer chains (*e.g.* acrylic acid) which expand and bind with water during absorption. To prevent these polymers from dissolving into water, other polymers are used to bind them, which are referred to as cross linkers. A larger cross-linker concentration increases the stiffness of a SAP particle, but at the same time reduces the maximum amount of water that it can absorb (*e.g.* Kneabel et al., 1997). In hygienic products, the stiffness is essential as it increases the strength of a particle bed and thus allows the bed to have better flow properties (Brandt et al., 1987). However, there is an optimum number of cross-linkers that can be added as they decrease the absorption capacity.

Physical properties not only depend on the polymer chemistry of SAP, but also on the production process which affects the shapes and sizes of particles. Particle size affects the swelling rate; the smaller the particle, the larger the surface area to volume ratio, and thus the higher the initial absorption rate (Buchholz, 1998b). In lab-controlled experiments, perfect spherical particles may be generated (Omidian et al., 1999; Esteves, 2011), which are useful for research purposes. However, in many production processes SAP particles are produced by grinding SAP slabs, resulting in angular particles with a wide range of sizes *e.g.* (Brandt et al., 1987; Graham and Wilson, 1998; Wang et al., 1998). Angular particles thus have two main features compared to spherical particles: they have a larger surface area to volume ratio and they are less likely to move in a packing (Graham and Wilson, 1998). Particle shapes also significantly affect the porosity and permeability (Torskaya et al., 2014) as well as the mechanical strength (Cho et al., 2006) of a bed of particles.

Numerous processes occur in a bed of swelling SAP particles. These include: flow of water into the particle bed, absorption of water by the particles, and rearrangement of particles due to swelling and deformation. The swelling of a bed of SAP particles is a highly-coupled process involving both fluid and solid phases. This is often referred to as hydro-mechanical coupling (Terzaghi and Peck, 1968). The hydro-mechanical coupling in a particle bed is usually studied using macro-scale experiments and simulations (*e.g.* Diersch et al., 2011), where permeability and stiffness of a bed are important parameters, see for example Chambers et al. (1992). However, grain-scale effects such as particle-particle friction (Kainth et al., 2007), particle stiffness, and grain shape govern those macro-scale parameters. Experiments that aim to investigate the effect of grain-scale properties on macro-scale parameters are time consuming, difficult, and sometimes not feasible. An alternative is to develop a pore-scale or grain-scale model and to use it alongside experimental investigations.

Perhaps the most suitable method for describing the motion of particles during swelling is the Discrete Element Method (DEM). This method allows for simulations of the movement of individual grains in a granular porous medium (Cundall and Strack, 1979), for example in soils (Belheine et al., 2009; Widuliński et al., 2009), rocks (Wang and Tonon, 2010), and industrial applications such as particle flow in silos (Coetzee and Els, 2009). The grains are considered as discrete elements that can undergo four relative motions at their contact points: sliding, rolling, spinning, and twisting. DEM has been mainly used for qualitative studies, but recent advancements have shown its capability for quantitative simulations within both the elastic and plastic regimes of deformation (Belheine et al., 2009; Plassiard et al., 2009).

Various methods exist to extend DEM and include saturated and/or unsaturated flow. For example, DEM has been coupled to pore network models to simulate 2-dimensional fluid injection into granular materials under saturated conditions (Zhang et al., 2013) and unsaturated conditions (Jain and Juanes, 2009), but also to simulate 3-dimensional drying of granular materials (Kharaghani et al., 2011), where the pore structure was assumed to be fixed while the particles in DEM could move. DEM has also been coupled to Lattice Boltzman (Boutt et al., 2007) and to a finite difference scheme for fluid flow on a fixed grid (Tsuji et al., 1993). In those previous works, simplifications were made to enable simulations of flow in DEM, namely: mono-dispersed packings rather than normally distributed packings, 2-dimensions rather than 3-dimensions, and small deformations rather than large deformations. Recently, the pore finite volume (PFV) method was introduced by Chareyre et al. (2012) and Catalano et al. (2014) into DEM for simulating hydro mechanical coupling under saturated conditions. PFV is an efficient scheme for simulating 3-dimensional flow in the pore-space of packings of spheres (having a particle size distribution) accompanied by large

deformations (e.g. Montellà et al., 2016). Tong et al. (2012) found that the permeability values, which were predicted by the DEM-PFV model for packings of spheres, were in good agreement with experiments.

In those studies, however, absorption of water and swelling of particles were not included. Therefore, the possibility of large swelling of particles has been added to DEM to enable simulations of swelling and the corresponding deformation of a packing of particles. The aim is twofold: i) to investigate whether DEM-PFV is capable to reproduce experiments of a bed of swelling particles, and ii) to study the effect of mechanical parameters on the swelling behaviour of a bed of SAP particles.

In this paper, we first describe the Discrete Element Method (DEM) and the Pore Finite Volume (PFV) model and how we included swelling of individual particles. Then, we discuss our experimental procedures and the model setup. Finally, we use our numerical model to simulate and reproduce experimental data. The model is then used for performing sensitivity analysis on how changes in various particle-scale properties would affect the macro-scale swelling behaviour of a bed of particles.

2.2 Discrete Element Method

In this research, we have extended the open-source software Yade-DEM to include swelling. Yade-DEM is a 3-dimensional discrete element code (Šmilauer et al., 2015). DEM is a particle model that is capable of simulating deformation of granular materials by considering grain-scale interactions. In this research, DEM is employed to simulate the movement of 3-dimensional non-cohesive spheres inside a packing.

DEM simulates the motion of individual particles inside particle packings during deformation. Each particle is defined by its properties such as radius (r_i), Young's modulus (E_i), density (ρ_i), Poisson ratio (ν_i), shear modulus (G_i), and friction coefficient (φ). At a contact between two particles the following processes can occur: normal deformation, shear, and sliding.

The contact mechanics are based on the soft sphere approach. Thus, if particles i and j are pushed towards each other, they may deform locally at their contact. This local deformation is assumed to be linearly elastic and it is measured by the normal displacement δ_{ij}^n [L], defined by:

$$\delta_{ij}^n = \begin{cases} 0 & \text{if } r_i + r_j \leq d_{ij} \\ r_i + r_j - d_{ij} & \text{if } r_i + r_j > d_{ij} \end{cases} \quad (2.1)$$

where d_{ij} [L] is the distance between the centres of particles i and j . An elastic force arises at the contact area of particles i and j , which acts towards reversing the overlap

of particles. The elastic force is calculated using the Hertz-Mindlin theorem (see *e.g.* Johnson, 1987). In this theorem, small deformations are assumed to occur at the contact points between two particles such that $\delta_{ij}^n \ll \min(r_i, r_j)$. Based on the Hertz-Mindlin contact mechanics, the following effective parameters are defined for two particles i and j that are in contact with each other: the effective Young's modulus: $E_{ij} = \left(\frac{1-\nu_i^2}{E_i} + \frac{1-\nu_j^2}{E_j}\right)^{-1}$, the harmonic mean of particle radii: $r_{ij} = \frac{r_i r_j}{r_i + r_j}$, the average shear modulus: $G_{ij} = \frac{G_i + G_j}{2}$, and the averaged Poisson ratio: $\nu_{ij} = \frac{\nu_i + \nu_j}{2}$. Normal displacement causes a normal force at a contact point f_{ij}^n [MLT⁻²], which is given by (Johnson, 1987; Thornton et al., 2011):

$$f_{ij}^n = -k_{ij}^n (\delta_{ij}^n)^{3/2} \quad (2.2)$$

where k_{ij}^n [MT⁻²L^{-1/2}] is the contact stiffness in the normal direction and is given by:

$$k_{ij}^n = \frac{4}{3} E_{ij} \sqrt{r_{ij}} \quad (2.3)$$

In addition to normal displacement, shear may also occur. The elastic force in the tangential direction at a given time step, $(\mathbf{f}_{ij}^t)^{t+\Delta t}$ [MLT⁻²], is history dependent and thus depends on its old value, such that:

$$(\mathbf{f}_{ij}^t)^{t+\Delta t} = (\mathbf{f}_{ij}^t)^t + k_{ij}^t \dot{\mathbf{d}}_{ij}^t \Delta t \quad (2.4)$$

here $\dot{\mathbf{d}}_{ij}^t$ [LT⁻¹] is the relative tangential velocity and is defined as: $\dot{\mathbf{d}}_{ij}^t = (\dot{\mathbf{x}}_i - \dot{\mathbf{x}}_j) + \boldsymbol{\omega}_i \times (\mathbf{x}_c - \mathbf{x}_i) - \boldsymbol{\omega}_j \times (\mathbf{x}_c - \mathbf{x}_j)$. It is a combination of the relative velocity of the two particles ($\dot{\mathbf{x}}_i - \dot{\mathbf{x}}_j$) and their spinning: $\boldsymbol{\omega}_i \times (\mathbf{x}_c - \mathbf{x}_i)$ where $\boldsymbol{\omega}_i$ [degrees T⁻¹] is the angular velocity vector of particle i and \mathbf{x}_c [L] is the position vector of the contact point. The contact stiffness in tangential direction k_{ij}^t [MT²] is given by:

$$k_{ij}^t = \frac{4\sqrt{r_{ij}}G_{ij}}{2 - \nu_{ij}} (\delta_{ij}^n)^{0.5} \quad (2.5)$$

Sliding at the contact can occur if the tangential force surpasses a threshold value, which is determined by a friction coefficient φ (which is the tangent of the particle-scale friction angle):

$$\|\mathbf{f}_{ij}^t\| \leq \varphi f_{ij}^n \quad (2.6)$$

All contact forces, gravitational forces, and forces arising from the presence of pore fluid (see section 2.4.1) contribute to a resultant force vector. The resultant force vector is

recast into an acceleration vector by using Newton's second law. The acceleration is integrated to find the velocity and location of each particle. The reader is referred to Šmilauer et al. (2015) for more details. We use the implementation of the contact model by Modenese et al. (2012).

2.3 Implementation of swelling particles in DEM

To extend DEM to include swelling of particles, we introduce the following two processes due to water absorption: 1) swelling, or growth, of particles and 2) the softening of particles. In the following sections, we describe how those two processes are implemented in the DEM model.

2.3.1 Modelling the swelling of a single particle

First, we define an absorption ratio Q_i^{abs} [-] for each individual particle i , which is based on the mass of absorbed water (M_i^w) and the dry mass of the particle (M_i^s):

$$Q_i^{abs} = \frac{M_i^w + M_i^s}{M_i^s} = \frac{(r_i)^3 \rho_w}{(r_i^0)^3 \rho_s} - \frac{\rho_w}{\rho_s} + 1 \quad (2.7)$$

in which r_i^0 is the initial particle radius, ρ_s is the density of dry SAP and ρ_w is the density of water. Note that the density of the particle itself varies from ρ_s to ρ_w with increasing values of Q_i^{abs} and that we assume that the water density inside the particle is the same as that of water outside the particle. The maximum value of Q_i^{abs} , denoted by Q^{max} , is assumed to be a known constant, following Diersch et al. (2010) and Buchholz (1998b). Q^{max} is usually measured experimentally and it depends on the composition of both the fluid and the solid; see *e.g.* Omidian et al. (1999) and Frijns et al. (1997). The value of Q^{max} for SAP materials is around 30 to 40 g/g for urine (see *e.g.* Wang et al., 1998), about 200 g/g for tap water, and up to 1000 g/g for pure water.

The swelling of a SAP particle is driven by the difference in chemical potential between the SAP particle and the surrounding fluid (Huyghe and Janssen, 1997). We assume that the swelling rate is governed by the diffusion of water molecules into the SAP particle. Based on some simplifications, the absorption of water at the particle scale can be approximated by the following equation, derived in Appendix B:

$$\frac{dQ_i^{abs}}{dt} = K_i \left(\frac{Q^{max} - Q_i^{abs}}{Q_i^{abs}} \right) \quad (2.8a)$$

$$K_i = \frac{3Dr_i}{(r_i^0)^3} \quad (2.8b)$$

in which D is a diffusion coefficient for water molecules in SAP [L^2T^{-1}] and r_i^0 is the initial radius of particle i . For spherical particles, we can recast equations 2.8a and 2.8b into $\frac{dr_i}{dt}$ as function of r_i :

$$\frac{dr_i}{dt} = \frac{D \rho_s}{r_i \rho_w} \left(\frac{Q_i^{max} - Q_i^{abs}(r_i)}{Q_i^{abs}(r_i)} \right) \quad (2.9)$$

At the grain scale, we assume that water undergoes a phase transition across the solid – fluid interface when it gets absorbed, following Diersch et al. (2010). Therefore, the absorption of water is implemented by simply increasing the particle size, thus its radius. We implemented this in the model by defining a growth factor (f) such that the discretized form reads:

$$f_i = \frac{r_i^{t+\Delta t}}{r_i^t} = 1 + \frac{\Delta t}{r_i^t} \frac{dr_i}{dt} \quad (2.10)$$

where we assume that $\frac{dr_i}{dt} = \frac{r_i^{t+\Delta t} - r_i^t}{\Delta t}$, with $r_i^{t+\Delta t}$ being the radius at time $t + \Delta t$ and r_i^t being the radius at time t . Consider particles i and j that are in contact with each other. When the radii of particles i and j increase due to water absorption, the normal displacement, δ_{ij}^n , increases, see equation 2.1. Also, the contact stiffness in normal direction (k_{ij}^n) and tangential direction (k_{ij}^t) would change, see equations 2.3 and 2.5. In the end, the elastic contact force in normal direction f_{ij}^n and subsequently the tangential contact force f_{ij}^t would be affected during swelling of particles i and j , see equations 2.2 and 2.4. Moreover, due to an increase in particle radius, the mass of a particle at time t , M_i^t increases to $M_i^{t+\Delta t}$ at time $t + \Delta t$, following:

$$M_i^{t+\Delta t} = M_i^t \cdot f^3 \quad (2.11)$$

Also, the rotational inertia of a particle \mathbf{I}_i [ML^2] is updated, according to:

$$\mathbf{I}_i^{t+\Delta t} = \mathbf{I}_i^t \cdot f^5 \quad (2.12)$$

Note that in writing equations 2.11 and 2.12 the change in density of a particle is assumed to be negligible, which is a valid assumption because the density of the particle converges from its dry value ($1.6 \text{ g}\cdot\text{cm}^{-3}$) to that of water ($1.0 \text{ g}\cdot\text{cm}^{-3}$) during early stages of water absorption. During which, the particle packing is typically very thin and thus the exact density is not required as gravity and buoyance forces are still insignificant.

2.3.2 Softening of particles

The stiffness of SAP particles depends on the absorption ratio. Water absorption causes a decrease of both Young's and shear moduli (Knaebel et al., 1997). Following Buchholtz (1998a), we describe the shear modulus of a particle G_i [$\text{MT}^{-2}\text{L}^{-1}$] as a function of the absorption ratio (Q_i^{abs}) as follows:

$$G_i = \frac{\beta}{\sqrt[3]{Q_i^{abs}}} \quad (2.13)$$

where β [$\text{MT}^{-2}\text{L}^{-1}$] is constant for all particles and varies for varying polymer content in SAP particles. β is determined using a reference point (Q^{abs}, G). Equation 2.13 only applies to SAP particles that have already absorbed some water and are in a rubbery state. As the transition from dry to rubbery state occurs at a relatively low absorption ratio, we do not consider the transition state in this work. Assuming linear elasticity of the particles, the Young's modulus is related to the shear modulus, by:

$$E_i = 2G_i(1 + \nu_i) \quad (2.14)$$

Equation 2.13 and 2.14 can be implemented into Yade-DEM by simply adjusting the stiffness coefficients k_{ij}^n and k_{ij}^t which are given by equations 2.3 and 2.5, respectively.

2.4 Pore-finite volume method

To simulate hydro-mechanical coupling, Chareyre et al. (2012) have coupled the mechanical framework of DEM with a Pore-Finite Volume (PFV) method, for modelling of fluid movement through particle packings. It also allows for the computation of hydraulic properties of granular materials (Tong et al., 2012). The PFV is briefly described here.

The first step is to apply regular Delaunay triangulation to the assembly of particles, using the solid particle centres as vertices for the tetrahedra. That is, four neighbouring particles form a tetrahedron (see Figure 2.1a). Each tetrahedron contains a pore space, which we refer to as a *pore unit* (see Figure 2.1b). Complementary to tetrahedra are a set of Voronoi diagrams formed by the centres of pore units around a particle. Each pore unit is connected to four adjacent pore units. Consider two adjacent pore units I and J . A flat surface, or facet, separates them. This facet is the narrowest opening between the two pore units, to which we refer as throat IJ (see Figure 2.1c). We assign to throat IJ a resistance to the flow of water. The resistance is calculated via a hydraulic radius, defined as: $R_{IJ}^h = \frac{\Theta_{IJ}}{\nu_{IJ}}$. Here, Θ_{IJ} is the void volume that is associated

with pore throat IJ ; it is the void volume between three particle centres and two adjacent pore unit centres (see Figure 2.1c), and γ_{IJ} is the solid surface area that is present in Θ_{IJ} . The hydraulic conductivity of pore throat IJ , g_{IJ} [TL^5M^{-1}], is defined following Chareyre et al. (2012):

$$g_{IJ} = \alpha \frac{A_{IJ} R_{IJ}^h{}^2}{2\mu} \quad (2.15)$$

where A_{IJ} [L^2] is the cross-sectional area of throat IJ , μ is the dynamic viscosity [$\text{MT}^{-2}\text{L}^{-1}$], and α [-] is a conductivity factor that is equal to unity for spherical particles and smaller for other shapes. In fact, α can be used as a calibration factor to match the calculated permeability to that of experiments. Each pore unit has a fluid pressure p [$\text{MT}^{-2}\text{L}^{-1}$] and each pore throat has a volumetric flow rate q_{IJ} [L^3T^{-1}], which is proportional to the pressure difference:

$$q_{IJ} = g_{IJ} \frac{(p_J - p_I)}{l_{IJ}} \quad (2.16)$$

where l_{IJ} [L] is the distance in between the two pore unit centres.

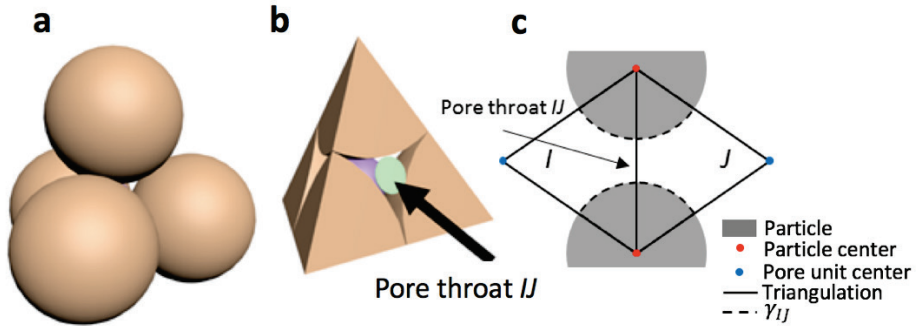


Figure 2.1: Illustration of a pore unit with a) four neighbouring spheres forming a tetrahedron, b) a tetrahedron that encloses one pore unit, and c) a 2-dimensional illustration of one pore throat and its associated volumes, with γ_{IJ} indicating the solid area associated with pore throat IJ .

2.4.1 Inclusion of swelling in PFV method

To implement swelling in the PFV method, we realize that the change of volume of each pore unit is a result of the relative movement of, and water absorption by, the four surrounding particles. We assign a swelling rate to each particle, which results in a rate of water absorption in the surrounding pore units. The change of volume of a pore unit

is balanced by the net flux of water into and out of the pore unit and the rate of absorbed water:

$$\left. \frac{dV_I}{dt} \right|_{relmov} + \left. \frac{dV_I}{dt} \right|_{abs} = \sum_{j=1}^4 q_{IJ} - q_I^{abs} \quad (2.17)$$

where $\left. \frac{dV_I}{dt} \right|_{relmov}$ is the change in pore volume of pore unit I due to relative movement of its surrounding particles (or deformation), q_I^{abs} is the absorption rate that acts in pore unit i , and $\left. \frac{dV_I}{dt} \right|_{abs}$ is the volume change of pore unit I due to swelling of the four surrounding particles. Note that the total absorption rate of one particle is the sum of parts of $\left. \frac{dV_I}{dt} \right|_{abs}$ associated with that particle of all its surrounding pore units. We assume that the density, thus the volume, of water does not change significantly when it gets absorbed, leading to: $\left. \frac{dV_I}{dt} \right|_{abs} = -q_I^{abs}$. Consequently, we only need to solve for pressure using the following equation:

$$\left. \frac{dV_I}{dt} \right|_{relmov} = \sum_{j=1}^4 q_{IJ} \quad (2.18)$$

which is the same as for non-swelling media. The discretized form of equations 2.16 in 2.18 yields a set of linear algebraic equations for pressure. For more information on how to solve for the fluid pressure, the reader is referred to Catalano et al. (2014).

The final step is to compute the forces acting on the particle due to the fluids around it. This includes the effects of buoyancy, viscous forces due to fluid flow, and the difference in fluid pressure surrounding a particle because of flow. For a comprehensive description of the computations of the different forces, the reader is referred to Chareyre et al. (2012).

2.5. Experimental methods

To illustrate the application of our model, we simulated an experiment on the swelling of a bed of SAP particles inside a glass beaker, under fully saturated conditions. For this purpose, we first measured the swelling rate of individual particles and determined the particle size distribution of a batch of dry SAP particles. This information was used as input for our simulations. Finally, we measured and simulated the swelling rate of a bed of SAP particles using our model.

2.5.1 Swelling kinetics of a single particle

To quantify the swelling rate, we used a custom-made imaging system. It consisted of a LED light source emitting at 560 nm, mounted on an objective lens F 3.2/105 mm to get a highly-collimated light beam, a prism (Edmund Optics) with dimensions of 50 mm x 50 mm, a SONY Sonnar F1.8/135 mm objective lens, and a GC-2450 Prosilica camera with a resolution of 5 Mega pixels. This optical setup was able to acquire magnified images of the swelling particle at a frame rate of up to 15 frames per second. The experimental procedure was as follows. First, a single particle was put into a Plexiglas container with dimensions 52x32x7 mm³. Sufficient water was added such that the particle was immersed at all times. At a frequency of 1 frame per second, images were taken at a resolution of 7.8μm per pixel, for a period of 30 minutes. See Figure 2.2 for initial and final state of a particle. The acquired images were processed with image analysis tools to determine the surface area of each particle as a function of time. Then, an equivalent circle was assigned to the surface area. This resulted in obtaining an equivalent particle radius (r_i) as a function of time (see Figure 2.3a). This data was fitted using equation 2.9, where Q^{max} and D were unknown parameters. Q^{max} was determined by measuring the mass of many particles before and after swelling. The experiment was conducted as follows: approximately 2 grams of dry SAP particles were put into a petri dish and subsequently hydrated. After 30 minutes, the mass of the swollen particles was measured. After repeating this experiment, we found $Q^{max} = 216 \text{ g/g} \pm 15\%$. D was determined as a fitting coefficient, for many particles; for each particle, a value of D was fitted to experimental data with $R^2 > 0.86$. The mean value of D was computed and was found to be $4.8 \times 10^{-4} \text{ cm}^2 \cdot \text{min}^{-1}$ and D varied between $7.0 \times 10^{-4} \text{ cm}^2 \cdot \text{min}^{-1}$ and $3.0 \times 10^{-4} \text{ cm}^2 \cdot \text{min}^{-1}$.

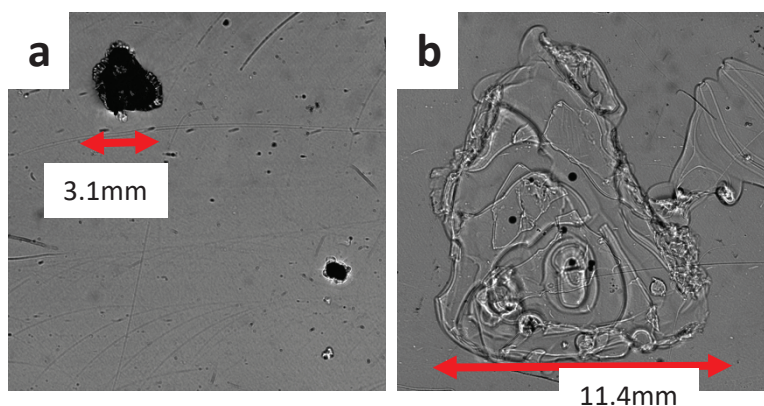


Figure 2.2: Example of an SAP particle a) image of an SAP particle that is slightly swollen b) the same SAP particle in completely swollen state.

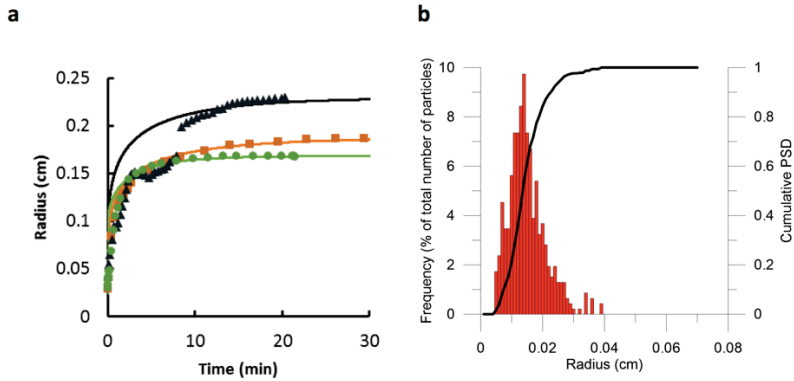


Figure 2.3: a) Swelling kinetics of individual particles under saturated conditions. Each colour represents a different particle with a different initial size ($r_{i,0}$), symbols represent measurements and the dashed lines are the fittings using $D = 4.8 \times 10^{-4} \text{cm}^2 \text{min}^{-1}$ and $Q^{\text{max}} = 216 \text{g/g}$. b) Particle size distribution of dry SAP particles.

2.5.2 Particle size distribution

Using the same imaging setup as described in section 2.5.1, we measured the Particle Size Distribution (PSD) of dry SAP particles. A large number of particles were placed in a dry Plexiglass container such that they did not touch each other. We took images of 500 particles and calculated the equivalent radius of an equivalent circle, which is the same method to that used by Esteves (2011). Figure 2.3b shows the PSD, which is relatively narrow and has a mean radius of $150 \mu\text{m}$ ($\pm 6\%$) and varies between 40 and $310 \mu\text{m}$.

2.5.3 Experiments on a bed of swelling SAP particles

To measure the swelling kinetics of a bed of SAP particles, we placed 100mg of dry SAP particles into a measurement cylinder with a diameter of 2.5cm and a volume of 100ml . This resulted in 0.02gram of SAP particles covering each cm^2 of the bottom of the beaker glass. Then, 60ml of slightly dyed water was poured into the cylinder. The water was dyed to visualize the pore water, because swollen SAP particles are difficult to distinguish from water without a dye. The particles were allowed to swell for 30min . A high-resolution camera was used to capture the swelling process. The images from the camera were carefully interpreted to determine the height of the bed of SAP particles at 30seconds intervals. The height was also measured manually for cross controlling the camera data. The height as function of time was used to test our particle model, as we will describe in the following section. We refer to this experiment as the macro-scale swelling experiment.

2.6 Model setup

To simulate the swelling of a bed of SAP particles, we have chosen the values of input parameters as close as possible to those of SAP particles. In the following subsections, we explain the parameterization and model setup.

2.6.1 Parameterization

Table 2.1 shows values of physical parameters of individual SAP particles. These parameters were the density of dry SAP particles, shear modulus, Poisson ratio, and friction coefficient. The density was set to $1.0 \text{ g}\cdot\text{cm}^{-3}$, which is that of swollen SAP particles, but note that dry SAP has a density of $1.6 \text{ g}\cdot\text{cm}^{-3}$ (Mirnyy et al., 2012). The friction coefficient φ was set to 0.096, which corresponds to the micro-scale friction angle of acrylic acid under dry conditions, namely 5.5° (Lorenz et al., 1997). SAP particles contain complex volume cross-linked and surface cross-linked structures, and thus the friction coefficient varies for different degrees of cross-linking. Due to the complexity of measuring the friction coefficient (Cavarretta et al., 2011), it is often determined through fitting data see *e.g.* Belheine et al. (2009). But, we have chosen to set the value of the friction coefficient to that of acrylic acid. In our sensitivity analysis, we studied the effect of changing the friction coefficient. The Poisson ratio was set to 0.5, which corresponds to an incompressible liquid or solid. The relation between shear modulus and absorption ratio was parameterized by setting β to 22.1 kPa, which was based on experiments on individual SAP particles by Knaebel et al. (1997). In our sensitivity analysis, we also chose β values of 15.5 kPa and 31.1 kPa.

Table 2.1: parameters for SAP particles

Parameter	Value	Sensitivity analysis	Reference
Density (dry)	1.6 g cm^{-3}	-	Mirnyy et al. (2010)
Density (swollen)	1.0 g cm^{-3}	-	
Poisson ratio, ν	0.5	-	Wilson et al. (2006)
Shear modulus			
G	7.1 kPa	5 kPa – 10 kPa (@30g/g)	Knaebel et al. (1996)
β	22.1 kPa	15.5kPa–1.1kPa	
Friction coefficient	0.096	0.017 – 0.84	Lorenz et al. (1997)

2.6.2 Modelling the experiments

A model scenario was setup to closely mimic our macro-scale swelling experiment. We considered a modelling domain of $2 \times 2 \times 20 \text{ cm}^3$ to simulate the beaker glass. A cloud of particles was generated having the particle size distribution of SAP particles, which was measured as explained in section 2.5.2. We used 0.02 gram of SAP particles for each cm^2 of bottom of the modelling domain, which was the same particle concentration that was used in our macro-scale swelling experiments. Consequently, 2720 particles were used for simulations. We performed simulations for varying number of particles in the $2 \times 2 \times 20 \text{ cm}^3$ modelling domain, to determine whether 2720 particles would be more than the minimum number of particles that are required for the results to be representative and independent of size. We found 2000 particles or more would be sufficient.

After the particle cloud was generated, we simulated the deposition of particles due to gravity. This resulted in a one-layer array of particles at the bottom of the modelling domain, as it was the case in experiments. The same particle array was used as the initial configuration for all simulations.

The boundary conditions were set to mimic a stress-free swelling experiment inside a beaker glass. The bottom and sidewalls were assumed to be rigid and subjected to no-flow boundary conditions. The upper boundary of the bed of particles, however, was allowed to move freely. The water pressure of pores along the upper boundary was set equal to zero. During the simulation, the location of the top boundary was tracked and compared to the height of the SAP particle bed in our macro-scale swelling experiments.

The time step was allowed to vary between 10^{-7} and 10^{-5} seconds. It was determined as follows (see Šmilauer et al. (2015) for details). For each contact point of two particles, a characteristic time step was determined based on its eigen frequency. A list of characteristic time steps was compiled and the minimum value was determined. To ensure numerical stability, the minimum value was divided by safety factor of 10 as the new time step. However, to speed up the calculations, the change of radii of particles due to water absorption was applied only once in every 500 time steps. We varied the frequency of this update and we found no effect on the swelling behaviour. Also, the pore pressure field was updated only every 500 time steps. Simulations were carried out until equilibrium was achieved in the packing, which occurred after 10 minutes. This was equivalent to a runtime of one-week, using a single core of a 3.2 GHz processor.

2.7 Verification of the particle model

Here, we present the results of the simulation of a bed of swelling SAP particles. First, we verify the implementation of hydro-mechanical coupling during a small swelling event. Secondly, we verify the mass conservation of water in the model during swelling of a bed of SAP particles.

2.7.1 Verification of the hydro-mechanical coupling during swelling

We have used Terzaghi's analytical solution (Terzaghi and Peck, 1968) for consolidation of a porous medium to verify the pore water pressure evolution during a swelling event. Consolidation is the process where the porosity of a porous medium is decreased due to an increase in confining stress. This is, however, possible only if the pore fluid flows out of the porous medium, which is a time dependent process. Similarly, a decrease in confining stress can cause a subsequent expansion, or swelling, of the porous medium (Terzaghi and Peck, 1968). Consider a sample of SAP particles that has an absorption ratio of 10 g/g. The relaxation of excess pore water pressure after a perturbation is given by the following equations, see Catalano et al. (2014) for more detail:

$$\frac{P_w(Z, T_v)}{P_{w,0}} = \sum_{m=0}^{\infty} \frac{4}{\pi(2m+1)} \cdot \sin\left(\frac{\pi}{2}(2m+1)Z\right) \cdot e^{-\left(\frac{\pi}{2}(2m+1)\right)^2 T_v} \quad (2.19a)$$

$$T_v = \frac{t}{H^2} \frac{K_h \bar{E}}{\rho_w g} \quad (2.19b)$$

$$Z = \frac{z}{H} \quad (2.19c)$$

where P_w and P_w^0 [$\text{MT}^{-2}\text{L}^{-1}$] are the excess pore water pressure and the initial pore water pressure, respectively, T_v is dimensionless time, H [L] is half of the thickness of the sample, Z [-] is the normalized thickness, \bar{E} [$\text{MT}^{-2}\text{L}^{-1}$] is the tangent modulus of the sample, g [LT^{-2}] is the gravitational constant and K_h [LT^{-1}] is the hydraulic conductivity of the sample.

To test our model, we have compared it to the analytical solution. We have simulated a sample of swollen SAP particles by generating 5000 particles in a modelling domain of $0.15 \times 0.15 \times 0.15 \text{ m}^3$. We used the particle size distribution that we previously measured, but it was scaled to a swelling ratio of 10 g/g. To confine the sample, a confining pressure of 250 Pa was applied on all six boundaries. This confining pressure corresponds to roughly the average pressure over time for a SAP particle that is located in the centre of a bed of particles that swells from the height of one single layer to the

height of a fully swollen bed of SAP particles, namely 7.56 cm (see section 2.8.1). The particle packing was immersed in water, with the top boundary being a water reservoir at a constant pressure of zero, while the other boundaries were subjected to no-flow conditions. After the packing was generated, virtual consolidation and permeability tests were used to determine the Young's modulus (1.3kPa) and the permeability ($7.2 \times 10^{-10} \text{ m}^2$) of the material. Next, a swelling step was applied by increasing all particle radii with a factor, $f = 1.0001$, which was a typical value during simulations of a bed of SAP particles. After the particle radii were increased, the DEM model was run until the particles were in equilibrium.

In Figure 2.4, the pore pressure profiles are plotted for our simulations and those by equation 2.19. It is clear that the analytical solution and simulations coincide well. Therefore, we concluded that water pressure is modelled correctly during swelling.

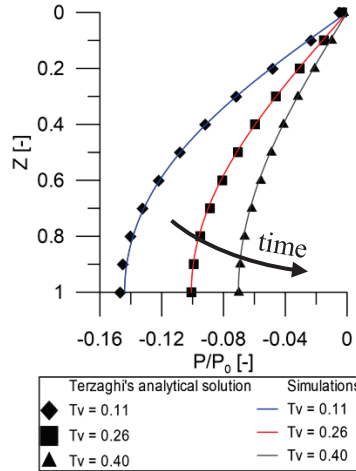


Figure 2.4: Terzaghi's solution for consolidation (symbols) and one-step swelling results by Yade-DEM (solid line). Different colours represent different times. Results are for a swelling factor 1.0001, absorption ratio of 10g/g and a confining stress of 250Pa.

2.7.2 Verification of mass balance during swelling

Here, we verify the mass balance of water in the model, by comparing the water volume in the model by the time integral of the water flux across the model boundary. In addition, we use a macro-scale mass balance equation for swelling granular materials by Diersch et al. (2010) to verify our results,

$$\bar{q} = 4H^0 J_v \left[\frac{\rho_s(1-\phi^0)}{\rho_w J_v} + \frac{\partial \phi}{\partial \bar{q}} + \frac{\phi}{J_v} \frac{\partial J_v}{\partial \bar{q}} \right] \frac{\partial \bar{q}}{\partial t} \quad (2.20)$$

where \bar{q} [LT^{-1}] is the water flux into the modelling domain, ϕ [-] is the porosity, ϕ^0 is

the initial porosity, H^0 [L] is the initial thickness of the bed of particles, J_v [-] is the dilatation of the modelling domain such that $J_v = \frac{\bar{V}}{\bar{V}^0}$, \bar{V} and \bar{V}^0 [L³] are the volume of the modelling domain and its initial volume, respectively. \bar{Q} [-] is the macro-scale absorption ratio, which is given by:

$$\bar{Q} = \frac{(\bar{V}_s - \bar{V}_s^0) \rho_w}{\bar{V}_s^0 \rho_s} \quad (2.21)$$

where \bar{V}_s and \bar{V}_s^0 [L³] are the total solid volume and its initial value, respectively. We have plotted the volume increase of the modelling domain with respect to its initial volume ($\bar{V} - \bar{V}^0$). We have plotted in Figure 2.5 three curves of $\bar{V} - \bar{V}^0$ based on: 1) the volume of the modelling domain as found in DEM indicated by the solid line, 2) integration of the water flux through the top boundary over time as found in PFV indicated by the dashed line, and 3) integration of the flux in equation 2.20 over time indicated by the dots. In Figure 2.5 results obtained with equation 2.20 corresponds very well to the volume increase of the modelling domain, which indicates that the relation between ϕ , J_v , and \bar{Q} is modelled correctly in our model. However, the volume of water that enters via the top boundary is 2.1% lower than the actual volume increase of the modelling domain, which is probably because $\left. \frac{dV_l}{dt} \right|_{remov}$ is approximated by the change of volume of a tetrahedron rather than the void volume of a pore unit, such that the computational effort is reduced.

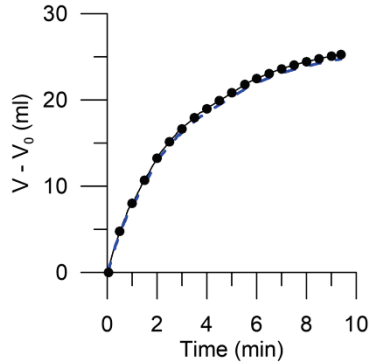


Figure 2.5: Volume increase of the simulation domain due to the swelling of SAP particles. The solid line represents the volume increase as found in the model whereas the symbols shows the solution of equation 2.20, following Diersch et al. (2010) and the dashed line represents the integration of the water flux as found in the PFV model.

2.8 Simulations of a bed of SAP particles

Here, we test the model by simulating the macro-scale swelling experiment and by comparing it with experimental data. Finally, a sensitivity analysis is done on micro-mechanical parameters.

2.8.1 Simulation of macro-scale swelling experiments

Figure 2.6 shows the height of the SAP particle bed as a function of time for experiments and simulations with our model. Three main features are important in this Figure. The final height of the SAP particle bed that was simulated by our model (7.56cm) was fairly close to the measured value (7.13cm). The initial swelling rate in experiments and our model agree well. But, when the bed reached 2 cm, the swelling rate starts to decrease in experiments causing the simulated swelling rate to overestimate the height of the particle bed. The decrease of the swelling rate in experiments can be related to i) limited water availability inside the SAP particle bed due to clogging inside the bed, which is not accounted for in simulations, ii) the SAP particles swell heterogeneously during swelling whereas we assume particles to remain spherical, or iii) the local confining pressure acting on the SAP particles reduces the swelling rate. In this research, however, it is not possible to identify which process is causing the deviation in swelling rate.

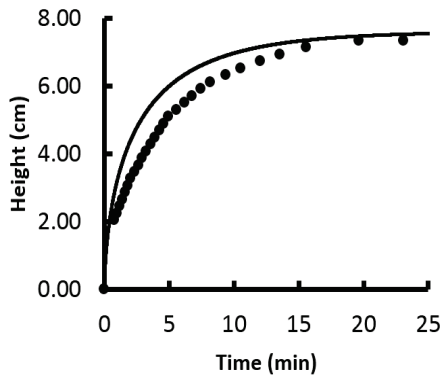


Figure 2.6: Results on the evolution of the height of a bed of SAP particles during swelling. Experimental data are shown by symbols while the solid lines represent simulation results.

2.8.2 Effect of the diffusion coefficient

The diffusion coefficient, D , may vary for varying SAP types, to study its effect on the swelling behaviour of a bed of particles, we have changed D to 1.0×10^{-4} and $1.0 \times 10^{-3} \text{ cm}^2 \text{ min}^{-1}$. Results are shown in Figure 2.7. It is clear from Figure 2.7a that reducing D slows down the swelling of the bed of particles. To study whether the arrangement of particles was affected by a change in diffusion coefficient, other than the change in swelling kinetics, we plotted in Figure 2.7b the height vs. normalized time (t^*) as: $t^* = \frac{tD}{H_0^2}$, where H_0 is the initial thickness of the particle bed. The three simulations with varying diffusion coefficient show identical evolution of height with t^* . This indicates that the particle rearrangement during swelling is not affected too much by changing the diffusion coefficient within the tested range, and the time scales linearly with the inverse of D .

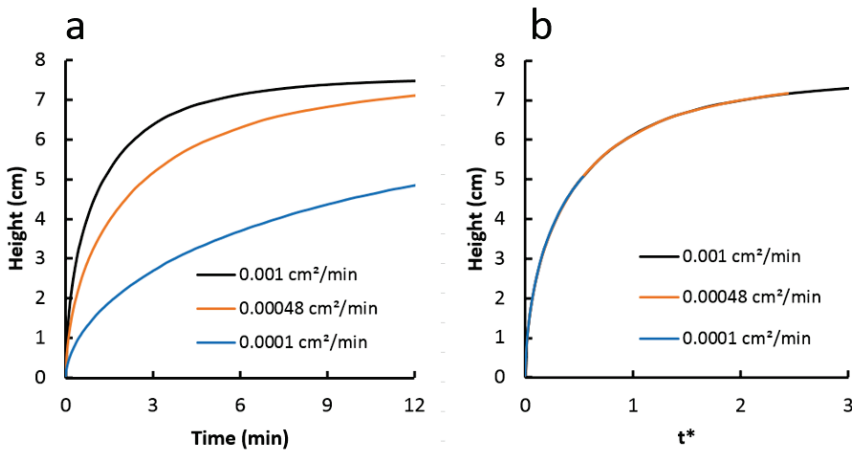


Figure 2.7: The effect of the diffusion coefficient (D) on the swelling behaviour of a bed of SAP particles, a) height vs. time, and b) height vs. normalized time $t^* = \frac{tD}{H_0^2}$, where H_0 is the initial height of the particle bed.

2.8.3 Effect of mechanical parameters

Here, we discuss the effect of the friction coefficient (φ) and the reference shear modulus (β) on the swelling behaviour of a bed of swelling SAP particles. The friction coefficient is a lumped parameter, which includes the friction intrinsic to the particle material and the surface roughness (Cavarretta et al., 2011). Both may vary for different batches of SAP particles either due to their chemical composition or due to the manufacturing process. They may also vary because of surface treatments, see for example Kainth et al. (2007). We performed a series of simulations with friction

coefficients ranging from 0.017 to 0.84, corresponding to micro-scale friction angles 1° to 40° . The simulation results showed that a larger friction coefficient yields a larger height of the particle bed after swelling, as seen in Figure 2.8a. In other words, after swelling with a larger friction coefficient, a larger porosity is achieved, which is evident from Figure 2.8b. A larger porosity is a result of particles that cannot move and rearrange themselves easily inside a particle bed at a larger friction coefficient, in contrast to a smaller friction coefficient.

The stiffness of SAP particles, parameterized by β , may vary with their polymer chemistry (Brandt et al., 1987; Knaebel et al., 1997). An increase in particle stiffness of SAP particles, due to a change in their chemistry, decreases Q^{max} and may also alter the swelling behaviour of a bed of SAP particles. Here, we assume that Q^{max} remains constant but β changes. Results in Figure 2.9 show that a lower β value results in more compaction of the bed under its own weight, and thus a lower height after swelling. However, the effect of β was relatively small, as the final height varies between 7.45 cm (for $\beta = 15.5$ kPa) and 7.64 cm (for $\beta = 31.1$ kPa), compared to 7.56 cm as found for the reference case; $\beta = 22.1$ kPa.

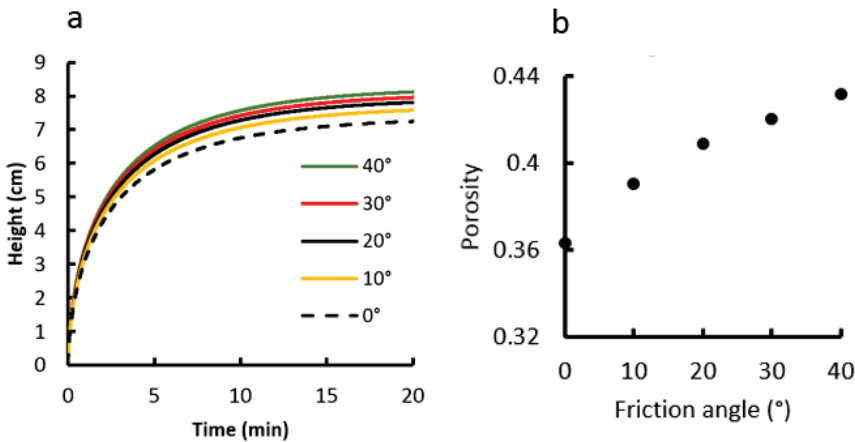


Figure 2.8: Swelling of a bed of particles for different particle friction coefficients, from 0.017 to 0.84. a) height vs time b) the porosity after swelling vs. the friction coefficient.

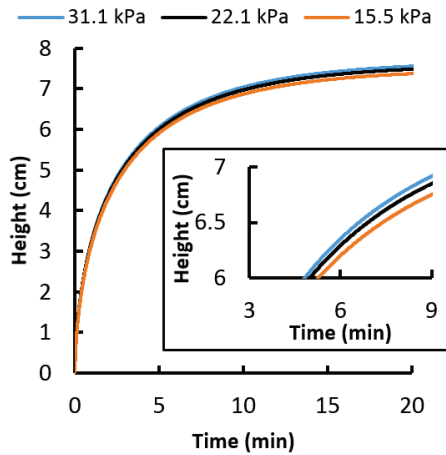


Figure 2.9: The effect of reference shear modulus (G_f ; values shown in kPa) in terms of β on the swelling of a bed of particles in terms of height vs time. The insert shows the enlargement of change of height at later times.

2.8.4 Flow of water during swelling

A major issue with swelling granular materials is that blockage of pores may slow down the swelling rate of a bed of particles. In principle, there are two competing processes, namely: i) swelling of particles and ii) dissipation of excess water pressure that arises due to the changes in pore spaces. In Figure 2.10a, we show typical profiles of water pressure inside a bed of swelling particles at different times. In that Figure, the height is normalized with respect to the thickness of particle bed at any given time. As water gets absorbed by particles, the pressure is negative in the particle bed with the lowest value being at the bottom. This pressure gradient also corresponds to the fact that water enters the bed of particles from above and moves down the particle bed to replenish water absorbed by particles. At the end of the absorption process, water pressure distribution becomes hydrostatic. In fact, at time $t = 0$, the water pressure distribution is hydrostatic. But negative values rapidly develop as water gets absorbed. This is shown in Figure 2.10b, where the water pressure averaged over the whole particle bed is plotted as function of time. A minimum value is reached within a short time (around $t = 0.4$ min for $\alpha = 1$) and then it increases slowly. Another simulation was conducted for a particle bed having a lower permeability value, using $\alpha = 0.01$. We found that both curves for height evolving over time for $\alpha = 0.01$ and $\alpha = 1$ were similar. But, simulations with $\alpha = 0.01$ did show lower values of pressure because the lower permeability (see Figure 2.10b).

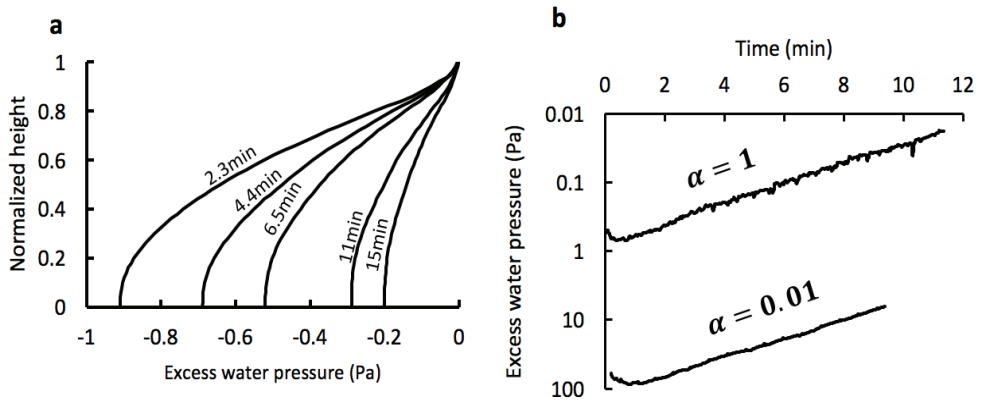


Figure 2.10: a) Normalized depth vs. water pressure profiles at different times for $\alpha = 1$. b) The evolution of excess water pressure that is averaged over the whole particle bed for $\alpha = 1$ and $\alpha = 0.01$.

2.9 Conclusion

In this research, a particle model has been developed to simulate the swelling of granular materials. For this purpose, an existing Discrete Element Method (DEM), coupled with a Pore Finite Volume (PFV) method, was extended to include the swelling of individual particles. The model was physically based and its input parameters were derived from literature and in-house experiments. To describe the swelling rate of individual particles, an analytical equation was derived that describes the swelling rate driven by diffusion of water into SAP particles. We have performed experiments and simulations of a bed of swelling SAP particles inside a glass beaker. We find that our model results agree relatively well with experimental data, except for the swelling rate after 2 minutes, which was slightly faster in simulations. Sensitivity analyses were done on the friction coefficient, shear modulus, and diffusion coefficient. Model results indicate that decreasing the friction coefficient or particle stiffness lowers the porosity, and that changing the diffusion coefficient only affects the time it takes to obtain equilibrium but not the particle rearrangement. Moreover, the model indicates that during swelling, fluid has to be distributed through the particle bed. This is associated with an increase of water suction inside the particle bed. The magnitude of the suction pressure is related to the permeability of the sample. The numerical model is a useful model to study the effect of various parameters on the complex behaviour of swelling SAP particles.

A model for diffusion of water into a swelling particle with a free boundary: Application to a Super Absorbent Polymer particle

Abstract

In this work, a model is developed for describing the swelling of an individual particle, made of Super Absorbent Polymers (SAP). Governing equations for the water uptake at the particle surface, diffusion of water into the particle and the subsequent swelling are developed for an irregularly shaped particle. The modelling domain is assumed to have a free and moving boundary, thus a moving particle surface, to account for the increase in particle size. In addition, the entrance of water through the particle surface is modelled as a first-order kinetic process. The proposed model is then simplified for a spherical particle, made dimensionless, projected onto a fixed grid, and solved using an explicit numerical scheme. A dimensionless number is defined as the ratio of kinetics of water uptake at the particle surface to the water diffusivity. Using this dimensionless number, three regimes of swelling kinetics can be identified: i) diffusion is dominated, ii) water uptake is limiting, or iii) both processes are acting. Numerical results indicate that experimental data from literature can be reproduced when assuming water uptake kinetics at the particle surface to be very fast; i.e. instantaneous, thus diffusion being the controlling mechanism. Of course, for SAP particles having a different composition, the particle surface may slow down the swelling kinetics. Our model is compared to three other models found in the literature. They all give a similar result but with different diffusive coefficients.

3.1 Introduction

Super absorbent polymers (SAPs) are used in a variety of applications, for example: i) to absorb fluids in hygienic products (Buchholz and Graham, 1998); ii) to control shrinkage in cement pastes (e.g. Snoeck et al., 2015); iii) to regulate moisture content in soils (e.g. Woodhouse and Johnson, 1991); iii) to remove water from a pathogen suspension in order to increase the pathogen concentration to a detection limit (Xie et al., 2016). SAPs are hydrophilic polymers that are lightly cross-linked and some SAPs have been reported to absorb demineralized water up to 1000 times their initial weight and saline water up to 30 times (Zhohuriaan-Mehr and Kabiri, 2008). When SAP particles form a bed, not only the particle properties but also the properties of the bed become important for the performance of the SAP particles and their corresponding swelling behaviour.

To investigate the behaviour of a bed of swelling SAP particles, a macro-scale model can be employed; see for example Diersch et al. (2010). Macro-scale models require relations to describe the dynamics of swelling. They are typically parameterized using experiments and thus are not always physically based. Another method is to employ a grain-scale model, such as the Discrete Element Method, DEM (Sweijen et al., 2017b). DEM is a particle model that can describe the movement of individual particles inside a packing of spheres during deformation and/or swelling. For DEM simulations of swelling SAP particles, an expression is needed to describe the swelling rate of individual particles as a function of the particle size, which evolves with time. There exist empirically-based expressions that are obtained from fitting experimental data of swelling particles (see e.g. Omidian et al., 1998; Esteves, 2011; Kabiri et al., 2003). For DEM simulations, a simple expression is preferable as it reduces the numerical computations. But, one would be interested to know whether such an expression can be linked to a physically-based relation for the degree of swelling evolving over time. For this purpose, a rigorous fully-coupled model of fluid diffusion into a swelling particle (including its deformation) is needed (see e.g. Huyghe and Janssen, 1997).

Water transport in a swelling grain has previously been studied by Radu et al. (2001), who studied drug release from a one-dimensional swelling polymer. They modelled non-linear diffusion (Fujita-type diffusion) inside a particle having a free boundary at the surface of the particle as well as an internal boundary inside the polymer, which mimics the transition from dry polymer to hydrated polymer. The problem of transport in a domain that has a free boundary is a well-studied problem, where the free boundary is often referred to as a Stefan type boundary condition. Examples are the work by Van Noorden and Pop (2007), who have developed a model of cations and ions

diffusion in a domain that has a free boundary, to study dissolution and precipitation of crystal. Van De Fliert and Van Der Hout (2000) developed a mathematical model for drying of paints, where pigments and resins are conserved but solvents can evaporate over a moving boundary, thus making it a diffusive and evaporation problem. Weiqing (1990) studied solidification due to superheating (or cooling) in which thermal diffusivity is coupled to a free boundary.

While a variety of complex models exist to describe the swelling of one particle, relatively simple empirical equations remain convenient for fitting experimental data. To test these empirical equations, we compare existing (semi-) empirical equations to a newly developed physically-based model, which accounts for linear diffusion of water into a swelling particle, with a free boundary. In addition, water uptake at the particle's surface is assumed to be a kinetic process in itself, which in combination with water diffusion governs the swelling rate of a particle. First, a set of equations for an arbitrary shaped particle is derived, assuming a constant polymer volume (i.e. no mixing occurs). Then, the equations are simplified for the swelling of a spherical particle and are solved numerically. Model results are compared to (semi-) empirically equations and experimental data on swelling of spherical particles from Esteves (2011). Finally, the effect of coating of particles is evaluated in terms of kinetics in water uptake along the particle's surface.

3.2 A numerical model for swelling of a particle

Here, a set of equations is derived to describe diffusion of water into a swelling particle that is submerged into sufficient water. We assume that the polymer and water are both incompressible and that the polymer volume does not change due to dissolution. We start by describing the swelling of an arbitrary shaped particle. Then, a parameter is introduced to capture the uptake rate of water along the particle surface. Finally, equations are applied to a spherical particle.

3.2.1 Swelling of an irregularly shaped particle

Consider a particle that has an arbitrary initial shape filling a domain indicated by $\Omega(0)$. At time $t > 0$, the domain is given by $\Omega(t)$. At each point $\bar{x} \in \Omega(t)$, the local volume fraction of water is denoted by $\theta(\bar{x}, t)$. A constrain is applied to $\theta(\bar{x}, t)$ using $\theta_0 \leq \theta(\bar{x}, t) \leq \theta_{max}$, where θ_{max} and θ_0 are the maximum and initial value of θ , respectively, which are both constant over time and space. Per definition, θ_{max} is smaller than unity, because unity would indicate that there is no solid present. The boundary of the domain is denoted by $\partial\Omega(t)$ at which $\theta = \theta_b$, thus θ_b is the value of θ

at the boundary. The boundary has an outward normal \bar{n} and a velocity \bar{v} . Diffusion into a particle is described by the following set of equations:

$$\left. \begin{aligned} \frac{\partial \theta}{\partial t} + \text{div } \bar{q} &= 0 \\ \bar{q} &= -D \nabla \theta \end{aligned} \right\} \text{ for } \bar{x} \in \Omega \text{ and } t > 0 \quad (3.1a)$$

$$\theta|_{\partial\Omega(t)} = \theta_b \text{ for } t > 0 \quad (3.1b)$$

$$\theta|_{t=0} = \theta_0 \quad (3.1c)$$

where \bar{q} denotes the water flux and D is a diffusion coefficient which we assume to be a material constant and thus to be independent of time and location. Note that in this work, diffusion is assumed to be linear for sake of simplification (i.e. D is a constant), but water diffusion into a dry particle can be non-linear diffusion such that D would be a function of θ .

For a swelling particle, an equation for the moving boundary $\partial\Omega(t)$ is required that considers water that enters the growing particle via its boundary. Let us consider a small surface element of $\partial\Omega(t)$, with an area A , that moves in space from time t to time $t + \Delta t$. The particle grows into water, within which $\theta = 1$. This results in an excess volume of water (V_{excess}) inside the particle, near the boundary, that has to diffuse into the particle. This volume is given by

$$V_{excess} = (1 - \theta_b)(\bar{v} \cdot \bar{n})A\Delta t \quad (3.2)$$

This volume of water diffuses into the particle, for which we can write:

$$V_{excess} = -D[-\bar{n} \cdot \nabla \theta|_{\partial\Omega(t)}]A\Delta t = D(\nabla \theta \cdot \bar{n})A\Delta t \quad (3.3)$$

Combining equations 3.2 and 3.3 yields the volume balance:

$$D(\nabla \theta|_{\partial\Omega(t)} \cdot \bar{n}) = (1 - \theta_b)(\bar{v} \cdot \bar{n}) \quad (3.4)$$

which relates the water flux at the boundary to the speed of the boundary. Equation 3.4 ensures volume conservation across a moving boundary. It has been employed by Fasano and Mikelic (2002) to account for the effect of water absorption by a spherical particle on unsaturated flow of water surrounding that particle. Equations 3.1 and 3.4 yield a complete set of equations that can be solved for water diffusion in an arbitrary domain and its subsequent swelling. It is a classical one-phase free boundary problem for which numerous literature is available, see for example Crank (1984).

3.2.2 Rate of water uptake at the particle surface

The uptake of water molecules at the surface can be a kinetic process in itself. If the uptake is very fast or instantaneous, the value of θ_b is given by a constant value of θ_{max} which corresponds to the maximum absorption capacity of a hydrogel. If the uptake evolves in time, θ_b depends on time. Assuming that this behaves as first-order kinetics, one has:

$$\frac{\partial \theta_b}{\partial t} = k(\theta_{max} - \theta_b). \quad (3.5)$$

in which k [T^{-1}] is a kinetic constant. Similar forms of equation 3.5 have been employed to describe the swelling of hydrogels (see e.g. Buchholz, 1998a), but we employ it here as a kinetic law for water uptake at the particle's surface. Integration of equation 3.5 yields:

$$\theta_b = \theta_{max} - (\theta_{max} - \theta_0)e^{-kt}. \quad (3.6)$$

Equation 3.6 is valid provided that the initial and boundary conditions are compatible such that $\theta_0 = \theta_b$ at $\partial\Omega$ for $t = 0$.

3.2.3 Swelling of a spherical particle

Equations 3.1 and 3.4 can be simplified to describe the swelling of a sphere with initial radius $R_0 > 0$. Let $R = R(t)$ being the radius at time $t > 0$. Assuming radial symmetry, equation 3.1a is rewritten in terms of radial coordinates:

$$\frac{\partial \theta(r, t)}{\partial t} = \frac{D}{r^2} \frac{\partial}{\partial r} \left(r^2 \frac{\partial \theta(r, t)}{\partial r} \right) \quad \text{for } 0 < r < R(t) \text{ and } t > 0 \quad (3.7)$$

Equation 3.4 can be rewritten for radial coordinates by realizing that $(\vec{\nu} \cdot \vec{n}) = \frac{dR}{dt}$ and $\nabla \theta|_{\partial\Omega(t)} \cdot \vec{n} = \frac{\partial \theta}{\partial r}|_R$, so that we obtain:

$$D \frac{\partial \theta}{\partial r}|_R = (1 - \theta_b) \frac{dR}{dt} \quad (3.8)$$

Equation 3.8 complies with a volume balance of a swelling spherical particle, on which we elaborate in Appendix C. We introduce a diffusive reference time $t_r = \frac{R_0^2}{D}$. Then, equations 3.6 – 3.8 are made dimensionless using the following parameters:

$$T = \frac{t}{t_r} \quad (3.9a)$$

$$r^* = \frac{r}{R_0} \quad (3.9b)$$

$$R^*(T) = \frac{R(t)}{R_0} \quad (3.9c)$$

This leads to the set of equations:

$$\frac{\partial \theta}{\partial T} = \frac{1}{r^{*2}} \frac{\partial}{\partial r^*} \left(r^{*2} \frac{\partial \theta}{\partial r^*} \right) \quad \text{for } 0 < r^* < R^*(T) \text{ and } T > 0 \quad (3.10a)$$

$$\left. \frac{\partial \theta}{\partial r^*} \right|_{R^*} = (1 - \theta(R^*, T)) \frac{dR^*}{dT} \quad \text{for } T > 0 \quad (3.10b)$$

$$\theta|_{r^*=R^*(t)} = \theta_{max} - (\theta_{max} - \theta_0)e^{-KT} \quad (3.10d)$$

where:

$$K = \frac{R_0^2 k}{D} \quad (3.10e)$$

Note that K is the only dimensionless group in this problem. It represents the ratio of characteristic time scales of diffusion ($\frac{R_0^2}{D}$) over that of water uptake ($\frac{1}{k}$).

3.2.4 Spatial transformation

Equations 3.10 form a moving boundary problem as R^* changes with time. To simplify the numerical implementation of equations 3.10, we transform them to an equivalent problem on a fixed domain, by defining a new spatial variable (Caldwell and Kwan, 2004; Kutluay et al., 1997)

$$X = \frac{r^*}{R^*(T)} = \frac{r}{R(t)} \quad \text{where } 0 \leq X \leq 1. \quad (3.11)$$

By writing $\varphi(X, T) = \varphi\left(\frac{r^*}{R^*(T)}, T\right) \equiv \theta(r^*, T)$, we can use the chain rule of differentiation to obtain the following relationships:

$$\frac{\partial \theta}{\partial r^*} = \frac{\partial \varphi}{\partial r^*} = \frac{1}{R^*(T)} \frac{\partial \varphi}{\partial X} \quad (3.12)$$

$$\frac{\partial \theta}{\partial T} = \frac{\partial \varphi}{\partial T} + \frac{\partial \varphi}{\partial X} \frac{\partial X}{\partial T} = \frac{\partial \varphi}{\partial T} - \frac{r^*}{[R^*(T)]^2} \frac{dR^*(T)}{dT} \frac{\partial \varphi}{\partial X}. \quad (3.13)$$

Using expressions 3.12 and 3.13 in equation 3.10a gives:

$$\frac{\partial \varphi}{\partial T} - \frac{r^*}{[R^*(T)]^2} \frac{dR^*(T)}{dT} \frac{\partial \varphi}{\partial X} = \frac{1}{X^2 [R^*(T)]^2} \frac{1}{R^*(T)} \frac{\partial}{\partial X} \left(X^2 [R^*(T)]^2 \frac{1}{R^*(T)} \frac{\partial \varphi}{\partial X} \right). \quad (3.14)$$

Multiplying this equation by $[R^*(T)]^2$ and using equation 3.11 results in

$$[R^*(T)]^2 \frac{\partial \varphi}{\partial T} = \frac{1}{X^2} \frac{\partial}{\partial X} \left(X^2 \frac{\partial \varphi}{\partial X} \right) + XR^*(T) \frac{dR^*(T)}{dT} \frac{\partial \varphi}{\partial X}. \quad (3.15)$$

Finally, we introduce variable $Z(T) = \frac{1}{2} [R^*(T)]^2$ in equations 3.15 and 3.10b. This results in the following transformed set of equations:

$$2Z(T) \frac{\partial \varphi}{\partial T} = \frac{1}{X^2} \frac{\partial}{\partial X} \left(X^2 \frac{\partial \varphi}{\partial X} \right) + X \frac{dZ(T)}{dT} \frac{\partial \varphi}{\partial X} \quad \text{for } 0 < X < 1 \text{ and } T > 0 \quad (3.16a)$$

$$\frac{dZ(T)}{dT} = \frac{1}{1 - \varphi|_{X=1}} \frac{\partial \varphi}{\partial X} \Big|_{X=1} \quad \text{for } T > 0 \quad (3.16b)$$

$$\varphi|_{X=1} = \theta_{max} - (\theta_{max} - \theta_0) e^{-KT} \quad (3.16c)$$

$$\varphi(X, 0) = \theta_0 \quad \text{for } 0 < X < 1. \quad (3.16d)$$

Because of the coordinate transformation in equations 3.12 and 3.13, the conservative form of equations 3.10 transformed into a non-conservative form in equations 3.16. To maintain mass conservation, Van De Fliert and Van Der Hout (2000) as well as Van Noorden and Pop (2007) employed a mass-based transformation that resulted in a conservative but complex formulation. The coordinate transformation in equations 12 and 13 could in principle lead to a loss of mass in the computations. However, keeping the discretization sufficiently small, the effect is limited.

3.2.5 Discretization

To solve equations 3.16, we use the forward Euler scheme, following the work on one-dimensional Stefan's type problems by Kutluay et al. (1997) and the work on swelling particles by Bouklas and Huang (2012). We discretise the spatial domain of $X = [0,1]$ into N segments of size ΔX and we introduce time step ΔT . Let φ_i^k denote the approximation of $\varphi(i\Delta X, k\Delta T)$ where $i = 0, 1, 2 \dots N$ and $k = 0, 1, 2 \dots$. Note that $i = 0$ represents the centre of a sphere and $i = N$ represents the boundary of a sphere. Equation 3.16a is solved using a forward Euler scheme, where the diffusion is evaluated by a mid-point scheme:

$$2(Z^k) \frac{\varphi_i^{k+1} - \varphi_i^k}{\Delta T} = \frac{1}{(X_i^2) \Delta X} \left[J_{i+\frac{1}{2}}^k - J_{i-\frac{1}{2}}^k \right] + X_i \frac{dZ}{dT} \Big|_i^k \frac{\partial \varphi}{\partial X} \Big|_i^k \quad (3.17)$$

We introduce the following approximations:

$$J_{i+\frac{1}{2}}^k = \left(X_{i+\frac{1}{2}}\right)^2 \left(\frac{\varphi_{i+1}^k - \varphi_i^k}{\Delta X}\right) \quad (3.18a)$$

$$J_{i-\frac{1}{2}}^k = \left(X_{i-\frac{1}{2}}\right)^2 \left(\frac{\varphi_i^k - \varphi_{i-1}^k}{\Delta X}\right) \quad (3.18b)$$

$$\left.\frac{\partial \varphi}{\partial X}\right|_i^k = \frac{\varphi_{i+1}^k - \varphi_{i-1}^k}{2\Delta X} \quad (3.18c)$$

$$\left.\frac{dZ}{dT}\right|^k = \frac{1}{1 - \varphi_{i=n}^T} \frac{\varphi_{i=n}^k - \varphi_{i=n-1}^k}{\Delta X} \quad (3.18c)$$

$$Z^{k+1} = Z^k + \left.\frac{dZ}{dT}\right|^k \Delta T \quad (3.18d)$$

$$\varphi_{i=n}^{k+1} = \theta_{max} - (\theta_{max} - \theta_0)e^{-K(T^k + \Delta T)} \quad (3.18e)$$

Following the forward Euler scheme, φ_i^{k+1} can be solved explicitly by:

$$\varphi_i^{k+1} = \varphi_i^k + \left(\frac{\Delta T}{2Z^k X_i^2 \Delta X}\right) \left[J_{i+\frac{1}{2}}^k - J_{i-\frac{1}{2}}^k\right] + \left(\frac{\Delta T X_i}{2Z^k}\right) \left.\frac{dZ}{dT}\right|^k \left.\frac{\partial \varphi}{\partial X}\right|_i^k \quad (3.19)$$

A zero-flux boundary condition at the centre of the sphere is imposed by considering equation 3.18a at $i = 1$ differently, namely: $J_{i-\frac{1}{2}}^k = 0$, and $\left.\frac{\partial \varphi}{\partial x}\right|_i^k = \frac{\varphi_{i+1}^k - \varphi_i^k}{\Delta x}$.

The minimum time step for this set of equations is given by the minimum time step for a forward Euler scheme for linear diffusion, which must satisfy $\Delta T < \frac{1}{2}(\Delta X)^2$ (note that ΔT and ΔX are dimensionless). Although, the main process is that of linear diffusion, the expansion of the particle resulted in an additional convective term (see equation 16a). This may cause the time-step to be smaller than that of linear diffusion. We applied a safety factor of 0.01 on the minimum time step to ensure that the computed water distribution had non-oscillatory behaviour. After a mesh-independency check, we set N at 300. The mass convergence of the numerical simulation was determined by computing the solid volume after swelling (i.e. after large times), for which we know the exact solution in dimensionless term, namely: $\frac{4}{3}\pi$. The mass loss was always less than 0.005 of the initial volume.

We simulate experiments by Esteves (2011), who has studied the swelling of spherical SAP particles. In that study, θ_0 was zero and the maximum value of $\frac{R}{R_0}$ at equilibrium was 2.79, which yields $\theta_{max} = 0.95$. These values were used for numerical computation.

3.3 Results

In this work, two distinctive kinetic processes are identified, namely: diffusion of water into a spherical particle and the water uptake at the particle surface (i.e. boundary of the modelling domain) of that particle. Those two processes yield three types of swelling kinetics, with the value of K as indicator. The first type is where water uptake at the particle surface is instantaneous ($K \rightarrow \infty$) and thus diffusion controls the swelling kinetics. The second type is where diffusion of water is faster than the uptake of water at the particle surface (i.e. $K \ll 1$). Finally, the third type is where the value $K = O(1)$. Then, both diffusion and water uptake balance and both affect the swelling kinetics. In what follows, we will evaluate all three regimes, compare our results to experiments and discuss the usefulness of the parameter K for practical applications.

3.3.1 Instantaneous water uptake at the surface

In this section, we assume that the SAP material at the surface instantaneously absorbs water to the maximum capacity θ_{max} such that diffusion controls the swelling kinetics. Thus, in the numerical scheme, equation 3.18e reduces to $\varphi_{i=n}^{k+1} = \theta_{max}$. Figure 1a shows the distributions of φ within the particle at different times. These are indeed diffusive profiles of water migrating into a sphere. Figure 3.1b shows the same diffusive profiles, but now in terms of dimensionless radius r^* , which shows the increase in particle radii and the subsequent shift in diffusive profiles.

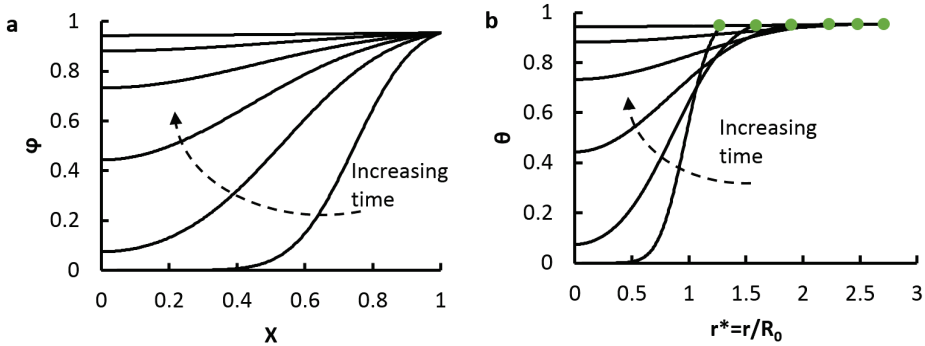


Figure 3.1: Profiles of volume fraction of water for instantaneous water uptake at the particle surface, using $\varphi|_{x=1} = \theta_{max}$, for a) $\varphi(X, T)$ and b) $\theta(r^*, T)$ with the green symbols representing the boundary of the sphere. Note that the maximum values of both φ and θ are $\theta_{max} < 1$.

In Figure 3.2, the swelling of a spherical particle is plotted as the radius versus time, using three models found in the literature and our model for instantaneous water uptake at the particle surface. Expressions for radius and absorption ratios as function of time are given in Table 3.1. Obviously, the results are strongly affected by the value of diffusion coefficient. If we use the same diffusivity, the model by Sweijen et al. (2017b) gives a similar initial swelling rate as the model presented here (see Figure 3.2a). But, the swelling rates starts to deviate when $\frac{R}{R_0}$ is larger than two, after which the model presented in this paper yields a larger swelling rate. The initial swelling rates of the models by Buchholz (1998) and Omidian et al. (1998) are significantly lower than in our case. Alternatively, we used different values for the diffusion coefficient in different models to have them approach our result as closely as possible. This required reducing the value of diffusion coefficient by multiplying it with a factor D_{scale} . Results are shown in Figure 3.2b and values of D_{scale} are given in Table 3.1.

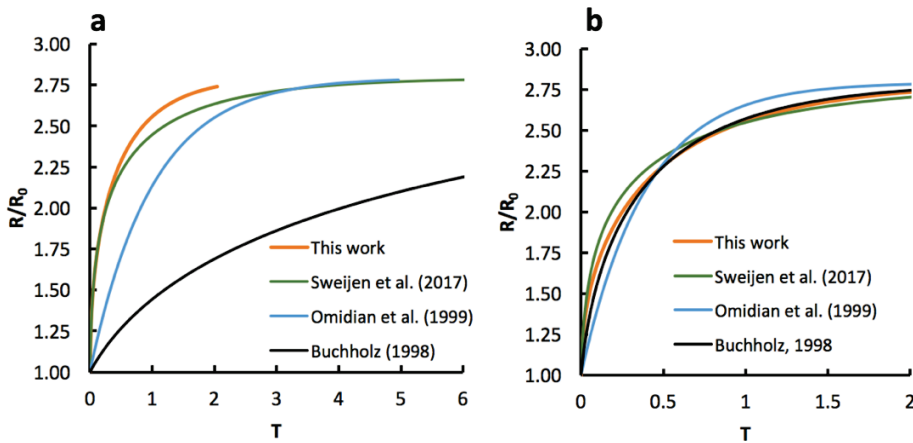


Figure 3.2: Particle radius as function of normalized time T for four different models: a) assuming a constant value of D for all equations and b) all equations were fitted to the curve obtained in this work by multiplying the diffusion coefficient with D_{scale} reported in Table 3.1.

Table 3.1: Equations found in the literature describing the swelling of one SAP particle.

Equation	D_{scale}	Reference
$\frac{R}{R_0} = \left(\frac{R_m}{R_0} - 1\right)(1 - e^{-kt}) + 1$	0.39	Omidian et al. (1998)
$\frac{dQ}{dt} = \frac{\pi^2 D}{R_0^2}(Q^{max} - Q)$	0.069	Buchholz (1998a)
$\frac{dQ}{dt} = \frac{3Dr_i}{(r_i^0)^3}\left(\frac{Q^{max} - Q}{Q}\right)$	0.70	Sweijen et al. (2017b)

Note that: $Q = \frac{M_w + M_s}{M_s}$ with M_w being the mass of absorbed water and M_s the mass of dry SAP. Assuming a spherical particle and incompressibility of water, equations by Buchholz (1998) and Sweijen et al. (2017b) can be rewritten in terms of $\frac{dR}{dt}$ which would yield $R(t)$ by numerical integration. The equation by Omidian et al. (1998) contains a kinetic constant k that is assumed to be equal to $\frac{D}{R_0^2}$. The values of diffusion coefficients were reduced by a factor of D_{scale} to obtain plots in Figure 3.2b.

3.3.2 Kinetic water uptake at the surface

When the diffusion of water is assumed to be much faster than the uptake of water at the particle surface (i.e. $K \ll 1$), θ will be almost constant over r^* . Thus, $\theta(r^*, T)$ will approach $\theta(T)$ when K approaches zero, where the value of $\theta(T)$ is given by expression 3.10d. Therefore, the swelling rate of a particle is then solely dependent on the water uptake rate at the surface of the particle, i.e. water that enters the particle is instantaneously redistributed by diffusion. To derive an equation for $R^*(T)$, consider the following volume balance:

$$V(T) = V_0 + V_w(T) \quad (3.20)$$

where $V(T)$ is the total volume of a spherical particle, V_0 is the initial volume and $V_w(T)$ is the volume of absorbed water. Hence:

$$\frac{4}{3}\pi(R^*)^3 = \frac{4}{3}\pi + \int_0^{R^*} \theta(T)4\pi r^2 dr \quad (3.21)$$

which yields:

$$(R^*)^3 = 1 + \theta(T) \times (R^*)^3. \quad (3.22)$$

Finally, we obtain:

$$R^*(T) = \sqrt[3]{\frac{1}{1 - \theta(T)}} \quad (3.23)$$

in which $\varphi(T)$ is given by equation 3.16c. Formula 3.23 is plotted in Figure 3.3 for $K = 0.5$.

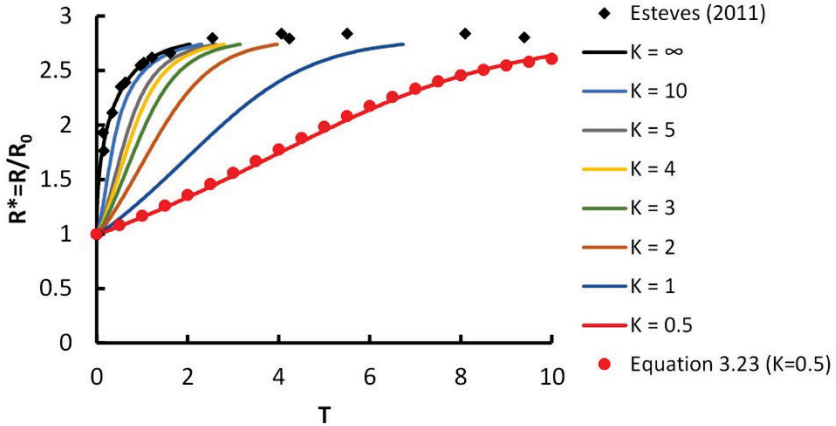


Figure 3.3: Swelling of a sphere expressed as $R^*(T)$, the value of K is increased from 0.5 to infinity. Black symbols indicate experimental data by Esteves (2011), using $D = 6.0 \times 10^{-5} \text{ cm}^2 \text{ min}^{-1}$ and red symbols indicate the solution of equation 3.23 using $K = 0.5$.

3.3.3 Intermediate regime of water uptake and diffusion

Next, we consider situations where $K = O(1)$; i.e. both diffusion and water uptake at the surface balance and both affect the swelling kinetics. We have solved the full set of equations in 3.16 to simulate the swelling of a sphere for K values ranging from 0.5 to 100. Results are shown in Figure 3.3. For large values of K (i.e. >10) the solution will converge to the case of instantaneous water uptake along the particle surface (see section 3.1) and thus diffusion becomes the rate controlling process. This fact is supported by the diffusive profiles of φ in Figure 3.4a,b. In contrast, for smaller values of K (i.e. $K \leq 1$), the solution will converge to that of equation 3.23, where the profiles of φ are relatively flat compared to larger K values, because diffusion is much faster than water uptake along the particle surface (see Figure 3.4c,d).

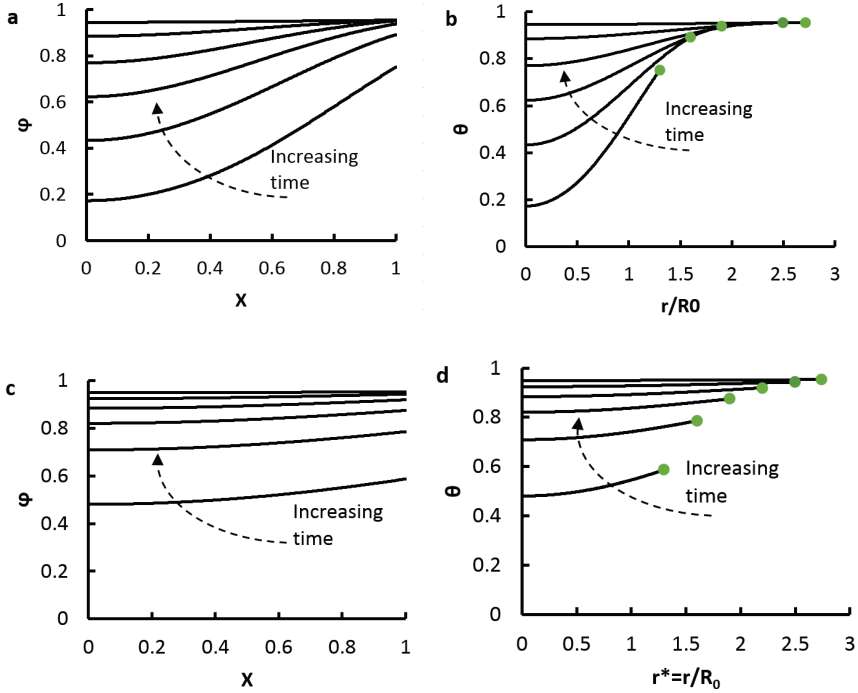


Figure 3.4: Water content profiles for a,b) $K = 10$ and c,d) $K = 1$. Green symbols indicate the boundary of the particle. Note that the maximum values of both ϕ and θ is θ_{max} , which is always smaller than unity.

3.3.4 Comparison with experiments

To test our model and the importance of K , we have plotted experimental data by Esteves (2011) who measured the radius of roughly spherical SAP particles as a function of time. Hence, these experimental results should compare to our model of spherical particles. In Figure 3.3, experimental data are plotted as a function of dimensionless time and fitted to our simulations for instantaneous water uptake at the particle surface ($K = \infty$). In order to convert real time of experiments to dimensionless time, a diffusion coefficient is required following equation 3.9a. This diffusion coefficient is thus a fitting parameter that has been set to $D = 6.0 \times 10^{-5} \text{ cm}^2 \text{ min}^{-1}$. Our results for finite values of K did not yield a good match to experimental data, whereas $K = \infty$ did result into a good match. This can be explained by the fact that SAP particles in the work of Esteves (2011) did not have a coating layer and therefore we do expect instantaneous water uptake at the surface of the particle.

3.3.5 Implications and application of the value of K

In practice, the kinetics of water uptake at the particle surface can be beneficial for the commercial design of SAP particles or other swelling products. The kinetics can be changed by applying a coating or a membrane to the surface of the particle. Such a treatment basically affects the value of the parameter K. For example, slowing-down of the initial swelling rate can be beneficial for a bed of SAP particles. If the initial swelling rate is too large, the pores between SAP particles may clog before all water has infiltrated into the particle bed, leaving parts of the particle bed dry, which of course is inefficient. Slowing-down of the initial swelling rate by applying a coating layer, may allow water to redistribute completely inside a particle bed before the swelling becomes significant.

3.4. Conclusion

In this research, a model is presented to describe diffusion of water into a swelling particle, where the particle surface can move. The model is simplified for a spherical particle and solved using an explicit forward Euler scheme. Modelling results yielded similar plots of radius over time compared to other models in the literature, albeit that they all result in distinctively different diffusion coefficients. A kinetic term was included for reduced water uptake at the surface of a swelling particle, to study its effect on the swelling rate of that particle. Three regimes were identified based on the controlling mechanism of swelling, namely: 1) diffusion controlled, 2) water-uptake controlled and 3) both diffusion and water-uptake controlled. By slowing down the water uptake at the surface of a particle, using for example a coating layer, the initial swelling rate can be reduced.

Part II

Hydraulic parameters of swelling granular materials

Chapter 4

The effects of swelling and porosity change on capillarity: DEM coupled with a pore-unit assembly method

Abstract

In this Chapter, a grain-scale modelling technique has been developed to generate the capillary pressure-saturation curves for swelling granular materials. This model employs only basic granular properties such as particles size distribution, porosity, and the amount of absorbed water for swelling materials. Using this model, both drainage and imbibition curves are directly obtained by pore-scale simulations of fluid invasion. This allows us to produce capillary pressure-saturation curves for a large number of different packings of granular materials with varying porosity and/or amount of absorbed water. The algorithm is based on combining the Discrete Element Method (DEM) for generating different particle packings with a pore-unit assembly approach. The pore space is extracted using a regular triangulation, with the centres of four neighbouring particles forming a tetrahedron. The pore space within each tetrahedron is referred to as a pore unit. Thus, the pore space of a particle packing is represented by an assembly of pore units for which we construct drainage and imbibition capillary pressure-saturation curves. A case study on Hostun sand is conducted to test the model against experimental data from literature and to investigate the required minimum number of particles to have a Representative Elementary Volume. Then, the capillary pressure-saturation curves are constructed for Super Absorbent Polymer (SAP) particles, for different combinations of porosities and amounts of absorbed water. Each combination yields a different configuration of pore units, and thus distinctly different capillary pressure-saturation curves. All these curves are shown to collapse into one curve for drainage and one curve for imbibition when we normalize capillary pressure and saturation values. We have developed formulas for the Van Genuchten parameters as a function of porosity and the amount of absorbed water.

Published as: Sweijen, T., Nikoee, E., Hassanizadeh S. M. and Chareyre, B. (2016). The Effects of Swelling and Porosity Change on Capillarity: DEM Coupled with a Pore-Unit Assembly Method. *Transport in Porous Media*, 113(1), 207-226

4.1 Introduction

Swelling and deformation of granular porous media under variably saturated conditions is a common phenomenon in geotechnical problems, product engineering, and biological tissues. Examples are swelling clays (Murad and Cushman 1996; Bennethum and Cushman 1996; Romero et al. 2011), foods (Takhar 2014), paper and tissues (Sun et al. 2014; Qin et al. 2014), biopolymers (Singh et al. 2003; Malakpoor et al. 2007) and absorbent polymers in hygienic products (Diersch et al. 2010). Numerical models have been employed to study the swelling and the subsequent deformation of granular materials. An example is a model for the swelling of hydrogels that is based on the exploitation of the entropy inequality by Huyghe et al. (1997), which was validated against experiments by Frijns et al. (1997). Also, a numerical model was developed by Diersch et al. (2010) for the simulation of partially-saturated swelling granular materials, such as Super Absorbent Polymer (SAP) particles used in hygienic products. That model employs empirical equations to account for the effect of swelling and the subsequent deformation on hydraulic parameters such as capillary pressure-saturation curve, permeability, and porosity.

It is well known that the presence of pore water inside a porous medium affects the behaviour of the porous medium during deformation and that the deformation affects hydraulic properties of a porous medium. For instance, the presence of liquid bridges between grains increases the cohesion in a granular material and therefore stiffens the material (Lu et al. 2007; Scholtès et al. 2009). Moreover, any change in the structure of the porous medium causes a change in its permeability; e.g. lowering the porosity lowers the permeability (Bear 1972). The interaction between pore fluids and solid grains and its subsequent effect on the mechanical behaviour of the medium is referred to as hydro-mechanical coupling (Tarantino and Tombolato 2005; Simms and Yanful 2005; Nikoee et al. 2013; Choo et al. 2015). A key ingredient of the hydro-mechanical coupling of partially-saturated porous media is the capillary pressure-saturation relationship.

Commonly, the capillary pressure-saturation relationship is obtained from direct measurements of capillary pressure and saturation on samples of a material. That relationship strongly depends on the state-of-stress of the sample, among other factors. For example, experiments on soil samples reveal that the air entry pressure increases when the porosity is reduced (Gallipoli et al. 2003; Lins and Schanz 2005; Nuth and Laloui 2008; Tarantino 2009; Mašin 2010; Salager et al. 2010; Rostami et al. 2013; Oh and Lu 2014). In order to study the hydro-mechanical coupling, Salager et al. (2010) performed a large number of drying experiments on clayey silty sand. They showed that there is a relationship among capillary pressure, saturation, and porosity, forming a 3-dimensional surface. For swelling absorbing media, the capillary pressure-saturation

relationship not only depends on the porosity, but also on the amount of absorbed water (Diersch et al. 2010).

Ideally, for the modelling of hydro-mechanical coupling, one needs to determine the capillary pressure –saturation relationships for many different packings of a given material under a large number of different stress conditions. This means that many complicated and time-consuming measurements are needed for a complete characterisation of a swelling and deformable porous medium. An alternative method is to use a pore-scale model, in combination with limited experimental work, to construct capillary pressure-saturation curves, under a very wide range of conditions. Using pore-scale models, the effect of pore-scale processes on the larger-scale behaviour can be investigated. A commonly used pore-scale model is the pore-network model, where pore bodies are connected by pore throats in a three-dimensional network. For example, Øren et al. (1998) have used a pore-network model to construct the capillary pressure-saturation curve, permeability, and the relative permeability for Bentheimer sandstone, based on a geometry obtained from 3-dimensional visualization. Joekar-Niasar et al. (2010) have studied the effect of different pore throat shapes on the capillary pressure-saturation curve for glass-bead packings, using a pore-network model. Raof and Hassanizadeh (2012) successfully simulated capillary pressure-saturation and relative permeability curves for both a carbonate rock sample and Fontainebleau sandstone. They included the effect of corner flow in their model. However, pore-network models do not take grain-to-grain interactions into account and do not model grain movements. Therefore, pore-network models alone are not enough for modelling deformation of granular materials.

For pore-scale simulations of a deforming bed of particles, the Discrete Element Method (DEM) is a good alternative. DEM efficiently describes the movement of solid grains inside particle packings during deformation. DEM was introduced by Cundall and Strack (1979). Since then, it has been used for geotechnical simulations of deforming soils (e.g. Widuliński et al. 2009; Belheine et al. 2009; Shmulevich and Rubinstein 2007; Wang and Tonon 2010; Plassiard et al. 2009) and particle flow in silos (e.g. Coetzee and Els 2009; Xu et al. 2011; Sykut et al. 2008).

Much research has been conducted on the inclusion of hydro-mechanical coupling in DEM. Chareyre et al. (2012) have implemented the hydro-mechanical coupling for saturated conditions. A two-way coupling was presented in Catalano et al. (2014), where fluid exerted forces on the solid grains and the movement of grains influenced the flow of fluid inside the packing. For unsaturated granular materials, Scholtès et al. (2009) have implemented the effect of pendular bridges. However, the pendular bridges were assigned a priori to particles contact area rather than obtained as a consequence of flow of water. Jain and Juanes (2009) developed a two-phase flow

algorithm coupled with a DEM model, to study gas migration in sediments. The effects of entry pressure and fracturing of bonds during the process of drainage were considered. Behseresht et al. (2008) coupled the level set method and the DEM model, to simulate the gas-brine interface through a sediment bed. In this way, the mechanistic behaviour of the grains during drainage could be studied. Mousavi and Bryant (2012) have studied the effect of cementation on the capillary pressure-saturation curve. They first constructed a random packing of spheres in which the radii of the spheres were increased to simulate cementation, then the capillary pressure-saturation curve was constructed by applying a Delauney tessellation, following Behseresht et al. (2008). Gladkikh and Bryant (2005) developed a quasi-static imbibition model that they have applied on a Finney packing (Finney, 1970), which is a packing of equally sized spheres of which the coordinates have been measured. Kharaghani et al. (2011) coupled a capillary tube network model with DEM and simulated time-dependent drying of an initially saturated porous material. By coupling it to DEM, inter-granular forces were updated using DEM, depending on the location of the air-water interface. Holtzman and Juanes (2010) have studied two-phase flow patterns in a deformable solid for varying capillary numbers, using a 2-dimensional spring dash-pot model. Hydro-mechanical coupling was achieved by accounting for fluid pressure, which exerts force on a particle, and the contact forces between particles. All afore-mentioned methods have their merits and disadvantages, but it is clear that insight in hydro-mechanical coupling can be obtained using DEM. However, the effects of porosity and swelling of particles on capillary pressure-saturation curves have not yet been studied using the hydro-mechanical coupling in DEM.

The aim of this research is to study the effects of porosity change and swelling on the capillary pressure-saturation curve, using a pore-scale model. For this purpose, a model has been setup where we have combined a pore-unit assembly method with DEM, to account for hydro-mechanical coupling. Using this model, we can construct capillary pressure-saturation curves for drainage and imbibition, under a variety of conditions, as described below.

The study material is Super Absorbent Polymer (SAP) particles, which are used in liquid-absorbent hygienic products. SAP particles are capable of absorbing water up to 200 times their initial weight and brine up to 30 times their initial weight (Brandt et al. 1987; Diersch et al. 2010). The hydraulic properties of a bed of SAP particles depend on the induced porosity and/or the amount of absorbed water.

We must point out that we implement a one-way coupling, where the packing does not change during drainage and imbibition. Thus, we assume that drainage and imbibition occurs much faster than the absorption of water by the SAP particles and that neither drainage nor imbibition rearrange SAP particles. Therefore, we can compute the

quasi-static capillary pressure-saturation curve for imbibition in “frozen” packings of spherical particles.

The content is ordered as follows. First, we describe DEM and the pore-unit assembly method. Next, we explain the numerical simulations. Finally, we analyse and discuss the results based on the constructed capillary pressure-saturation curves.

4.2 Numerical model

In this research, the open-source software Yade-DEM is used to generate different particle packings using Hertz-Mindlin contact mechanics as introduced in Chapter 2. In what follows, the pore-unit assembly methodology is explained along with a numerical code to obtain capillary pressure-saturation curves.

4.2.1 Extraction of the pore-unit assembly

The pore space of a granular medium can be subdivided into pore bodies and pore throats. Pore bodies contain most of the void volume; whilst pore throats are the relatively narrow transects that connect pore bodies to each other. In case of a packing of spherical particles, the pore space is often extracted using a classic triangulation (Gladkikh and Bryant 2005; Mason and Mellor 1995) or a regular triangulation (Chareyre et al. 2012; Yuan et al. 2015; Catalano et al. 2014). A regular Delaunay triangulation is capable of subdividing the pore space of packings with variable particle sizes, in contrast to classic triangulation which can only handle constant particle sizes. Here, a regular triangulation is employed to subdivide the pore space into tetrahedra, each formed by four neighbouring particles. Vertices of a tetrahedron are located at the centres of those particles. The pore space enclosed within a tetrahedron is called a one pore unit. Thus, the network of tetrahedra forms a pore-unit assembly.

The geometry of each individual tetrahedron enclosing one pore unit (see Figure 4.1) can be described as follows. 1) Each vertex of the tetrahedron is at the centre of a particle. 2) In each corner of a tetrahedron a part of a particle is located. 3) One tetrahedron is connected to 4 neighbouring tetrahedra. 4) The facet of a tetrahedron is shared by two touching tetrahedra, and is considered as a pore throat.

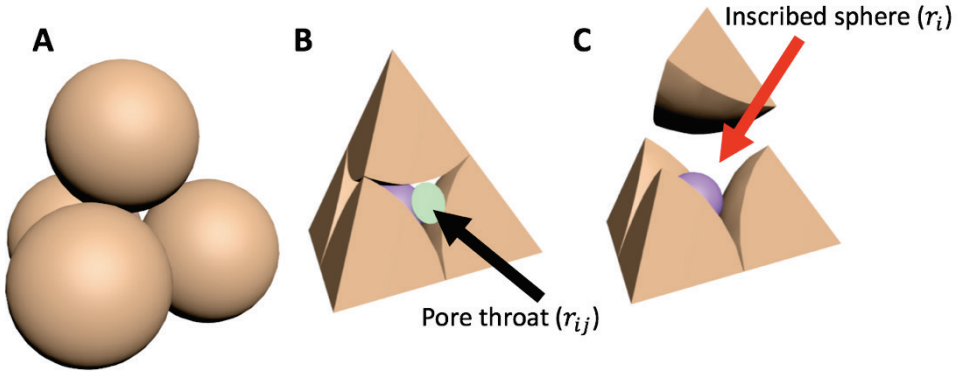


Figure 4.1: Illustration of a pore unit: a) a pore unit that is enclosed by four particles; b) a tetrahedron that encloses one pore unit, where the green circle shows the inscribed circle of a pore throat; c) an inscribed sphere in a pore unit; note that the upper grain has been moved away to expose the inscribed sphere.

4.2.2 Invasion criteria

The pore-unit assembly is used to construct the capillary pressure-saturation curves. To do so, two geometrical properties of a pore unit are essential. These are the radius of the inscribed circle of a pore throat (r_{ij}) and the radius of the inscribed sphere of a pore unit (r_i), which are shown in Figure 4.1. Both properties are used to determine the invasion criteria for drainage and imbibition. For drainage, a single invasion criterion is considered, namely the entry pressure associated with pore throats. For imbibition, two criteria are considered, namely the entry pressure of a throat, and the largest stable curvature inside a pore unit.

To determine the entry pressure of a pore throat, consider two connected pore units (i and j) that have a shared pore throat with an inscribed circle radius r_{ij} , which is the smallest circle that is tangent to the three enclosing particles (see e.g. Ogarko et al., 2014). If pore unit i is saturated with air and pore unit j is saturated with water, then an air-water interface is located at pore throat ij . The air-water interface will have a complex shape, resembling both a spherical cap and a liquid bridge. Here, it is assumed that the air-water interface has the shape of a spherical cap, following Gladkikh and Bryant (2005) and Torskaya et al. (2014). Therefore, the entry pressure of a throat, P_e^{ij} , is given as:

$$P_e^{ij} = \frac{2\gamma}{r_{ij}} \quad (4.1)$$

where γ is the interfacial surface tension between water and air (0.072 Nm^{-1}). For air to invade pore unit j , the pressure difference between the air and water reservoir ($P^i - P^j$) should be larger than the entry pressure ($P^i - P^j > P_e^{ij}$). This is the criterion used during drainage. We assume that once the pore throat ij is invaded, the pore unit j will be instantaneously filled by the air phase. New air-water interfaces will be formed at pore throats between pore unit j and its neighbouring pore units. Criterion $P^i - P^j > P_e^{ij}$ will be checked again.

For imbibition, consider pore units j and i filled by water and air, respectively. For water to invade the air-saturated pore unit i via pore throat ij . The pressure difference $P^i - P^j$ should be lower than the entry pressure, P_e^{ij} . But, pore unit i will not be fully invaded by water. Stable air-water interfaces can form within the pore unit. For full invasion of the pore unit to occur, the pressure difference should drop below a threshold value. This threshold value is equal to $\frac{2\gamma}{r_i}$, where r_i is the largest radius of curvature of a stable air-water interface that can exist inside a pore unit, which is that of the inscribed sphere of pore unit i . The radius of the inscribed sphere (r_i) is found using a Cayley-Menger determinant, which is a method for finding the radius of an inscribed sphere for four neighbouring spheres (whether touching or non-touching). For more information, the reader is referred to Mackay (1973) and Michelucci (2004).

A complication occurs when a cluster of particles is not closely packed and, as a result, those particles form a large pore wherein more than one inscribed sphere can be fitted. In this situation, triangulation may subdivide a large pore into two or more tetrahedra, even though it should be considered as one single pore. Then it is possible that these pore units are separated by a ‘‘pore throat’’ whose radius r_{ij} is larger than the radii of the inscribed spheres. This is merely an artefact of triangulation. The presence of larger pores does not affect the simulations of drainage, since the smallest pores determine the location of the air-water interface. For imbibition, we allow r_{ij} to be larger than r_i since the largest hemisphere that we can fit in a pore should determine the threshold pressure for imbibition.

4.3 Numerical simulations

The general outline of the numerical simulations is shown in a flow chart in Figure 4.2. First, for a certain amount of absorbed water and porosity, we generate a particle packing using Yade-DEM. For this particle packing, the pore geometry is extracted using the pore-unit assembly method. Finally, the capillary pressure-saturation curve is constructed. The procedure is explained in detail in the following sections.

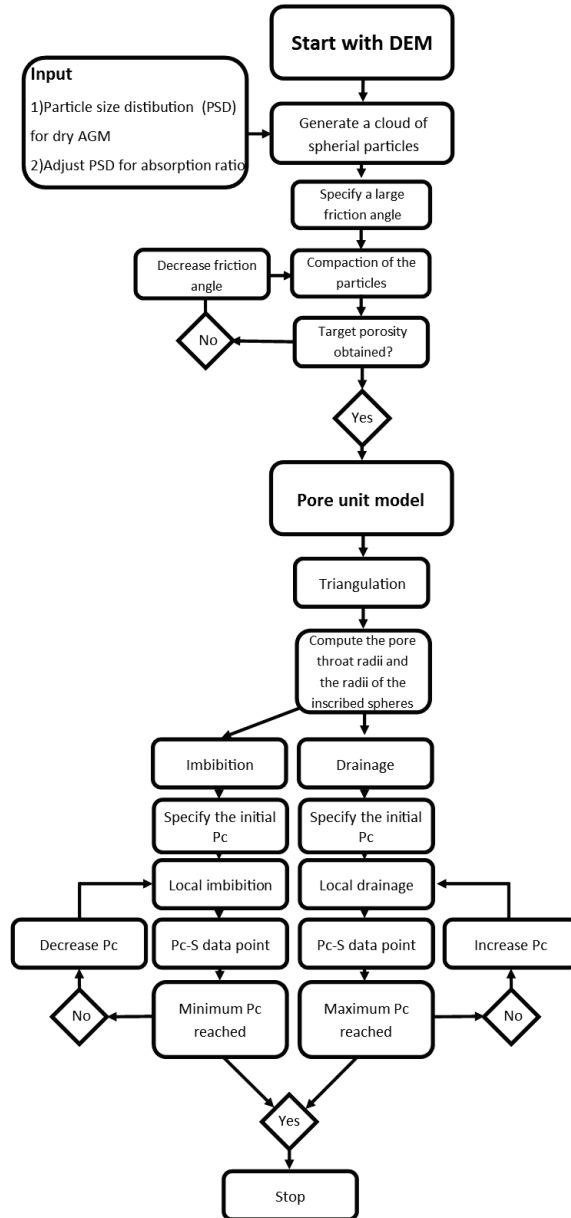


Figure 4.2: Flow chart for the calculation of capillary pressure-saturation curves.

4.3.1 The particle size distribution and water absorption ratio

In our simulations, we start with a given particle size distribution that corresponds to that of dry SAP particles. This is then adjusted to account for the target value of the amount of absorbed water. The amount of absorbed water is quantified using the absorption ratio (Q), as defined by Buchholz et al. (1998):

$$Q = \frac{M_w + M_s}{M_s} \quad (4.2)$$

where M_s is the mass of dry SAP and M_w the mass of absorbed water. As the particles are assumed to be spherical, we may recast equation (6) into:

$$Q = \frac{M_w + M_s}{M_s} = \frac{\rho_w \left[(R_i)^3 - (R_i^0)^3 \right] + \rho_s (R_i^0)^3}{\rho_s (R_i^0)^3} \quad (4.3)$$

where R_i^0 and R_i are the radii of particle i before and after swelling, respectively. ρ_w is the density of water, which is set to 1 g cm^{-3} and ρ_s is the density of dry SAP, which is set to 1.6 g cm^{-3} , following the reported value by Mirnyy et al. (2012). Equation 4.3 is inverted to obtain:

$$R_i = R_i^0 \left(1 + \frac{\rho_s}{\rho_w} (Q - 1) \right)^{\frac{1}{3}} \quad (4.4)$$

Thus, an initial particle size distribution with radii R_i^0 can now be adjusted for the amount of absorbed water. The particle packing is then created with this size distribution.

4.3.2 Generating particle packings

The particle packings were generated for a predefined particle size distribution corresponding to a given absorption ratio, and for a target porosity. The dry SAP particle radii were assumed to have a mean value of $150 \mu\text{m}$ and a normal distribution with a standard deviation of $30 \mu\text{m}$. First, a cloud of particles was generated within a cubic domain with dimensions $0.15\text{m} \times 0.15\text{m} \times 0.15\text{m}$, using the particle size distribution with radii scaled for the absorption ratio according to equation 4.4. The Poisson ratio of the particles was set to 0.5. This is because swollen SAP particles contain predominantly water and if we assume that water has no time to diffusive out the SAP particle, the particles can be considered incompressible. The Young's modulus of the particles was set to 100kPa . This value corresponds to slightly swollen hydrogels (Anseth et al., 1996). Of course, the exact value of Young's modulus is not required as a target porosity is achieved. Next, the cloud of particles was compacted by applying a confining pressure,

which was different for different target porosities (50Pa for a target porosity of 0.45 and 2.500Pa for a target porosity of 0.10). For this step in the simulations, we started with an artificially large friction angle of 50°. This was done to obtain a relatively loose packing with a larger porosity than the target porosity. Then, to reduce the porosity, the contact friction was reduced progressively such that the particles would slide into a more stable configuration, until the porosity matched the target porosity. This method is based on that of Chareyre et al. (2002). The final particle packing was at equilibrium under the applied confining pressure.

4.3.3 Modelling the capillary pressure-saturation curve

To obtain the capillary pressure-saturation curve, the boundary conditions in the pore-unit model were chosen to mimic a column experiment. The top boundary of the modelling domain in Yade-DEM was assumed to be a non-wetting phase reservoir (e.g. air) at a pressure P_{nw} ; the bottom boundary was considered to be a wetting phase reservoir (e.g. water) at a pressure P_w . The side walls were considered impermeable. For quasi-static simulations, where the viscous effect of water flow is not of importance, the capillary pressure (P_c) is equal to the pressure difference between the two reservoirs:

$$P_c = P_{nw} - P_w \quad (4.5)$$

For drainage simulations, we started with a very low capillary pressure, which was then increased incrementally in order to allow air to infiltrate increasingly smaller pores. For imbibition simulations, we started with a very large capillary pressure, which was then decreased incrementally such that water could invade increasingly larger pores.

In the pore-unit model, the simulation procedure was as follows: 1) a capillary pressure was specified. 2) For drainage, the pore throats of all water saturated pore units were checked to determine whether they could be invaded by air. For imbibition, the pore throats of all air saturated pore units were checked whether water could invade. 3) Drainage of a water-saturated pore unit by air (or vice versa during imbibition) was allowed only when both phases were connected to their corresponding reservoirs. 4) Capillary pressure was increased during drainage and decreased during imbibition. 5) An algorithm was implemented to keep track of disconnected blobs of air and water, to ensure that no displacement of disconnected blobs could occur. These disconnected blobs would form the residual air or water saturation at the end of either imbibition or drainage, respectively. Finally, all simulated capillary pressure-saturation curves were fitted with the Van Genuchten function (Genuchten, 1980), see Appendix A.

4.4 Model testing

In this section, we test our pore unit model by constructing capillary pressure-saturation curves for Hostun sand, for which the measured drainage and imbibition curves were found in the literature. Hostun sand was chosen instead of SAP particles, because only few data are available on the capillary pressure-saturation curves for SAP particle beds. We generated a packing of Hostun sand, based on the particle size distribution and a porosity of 0.39 as reported by Lins and Schanz (2005).

First, the simulations for Hostun sand were used to determine the minimum number of particles that is required for the capillary pressure-saturation curve to be independent of the number of particles. This follows the concept of Representative Elementary Volume (REV), which implies that the effects of small-scale heterogeneities are averaged out. The calculations were conducted for packings with different numbers of particles, varying from 1000 to 5000. Results showed that different primary drainage curves were obtained for different numbers of particles; see Figure 4.3. But, the curves converged for packings of 4000 particles and more. The main imbibition curves were less sensitive to the number of particles of the packing. Packings of 4000 particles have approximately 19.000 pore units and 38.000 pore throats; not including the boundary pore units.

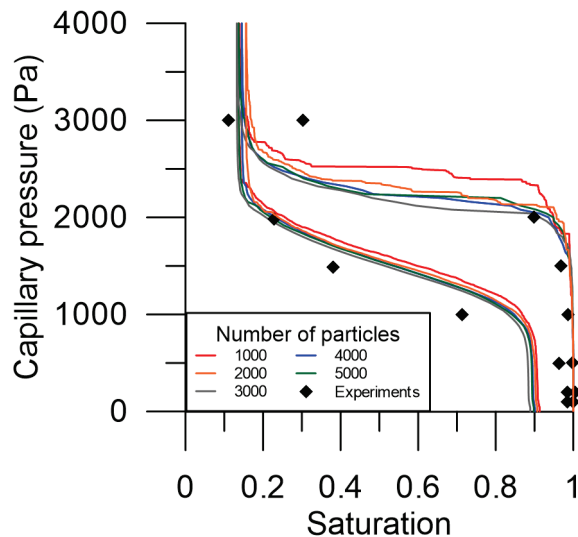


Figure 4.3: The capillary pressure-saturation curves for Hostun sand with a porosity value of 0.39, for packings of different number of particles (solid lines of different colours). Symbols show experimental data by Lins and Schanz (2005) for Hostun sand.

Another aspect related to the concept of REV is the variation in simulated curves for different realizations of the same packing. To illustrate this variation, different packings with the same number of particles were generated for different random distributions in the particle location. This was done for two cases: 1000 and 4000 particles. For each case, six capillary pressure-saturation curves were constructed. Figure 4.4a shows that the primary drainage curves obtained for different realizations of a packing of 1000 particles were substantially different from each other. However, for 4000 particles, there was much less variation as shown in Figure 4.4b. For both 1000 and 4000 particles, the main imbibition curve varied very little for different realizations. Based on these results, we decided that the REV size should be around 4000 particles. All simulations hereafter were carried out for an assembly of 4000 particles.

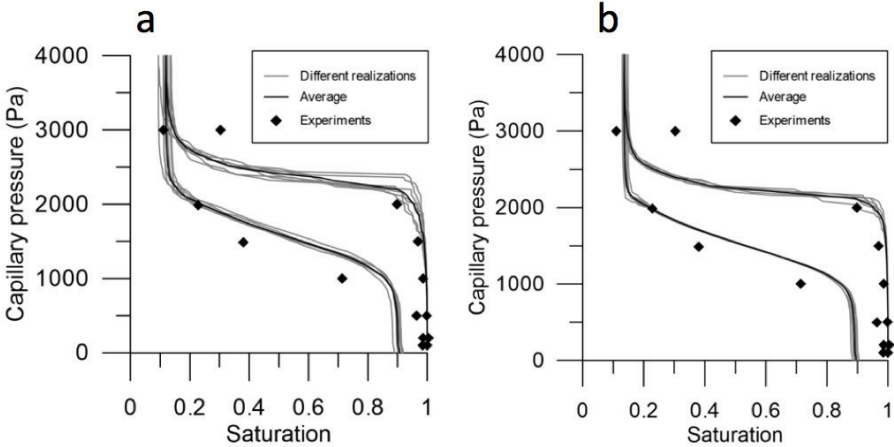


Figure 4.4: The capillary pressure-saturation curves (thin lines) for Hostun sand with a porosity of 0.39, for different realizations of the packing: a) 1000 particles, b) 4000 particles. The average curve is shown by the thick line. Experimental data by Lins and Schanz (2005).

Then, we simulated capillary pressure-saturation curves for Hostun sand and compared them to experimental data by Lins and Schanz (2005), as shown in Figure 4.4b. Lins and Schanz (2005) measured the capillary pressure-saturation curve for capillary pressures up to 80kPa. But, for capillary pressures higher than 4kPa water was found to be almost in a residual state. Water saturation decreased only when the capillary pressure was increased substantially; this process was not included in our model. Therefore, the experimental data by Lins and Schanz (2005) are shown here for capillary pressures up to 4kPa. Figure 4.4b shows that our simulations of Hostun sand are in

reasonable agreement with the measured curve. We have fitted the experimental data and the simulated curves with the Van Genuchten function, values of α and n are shown in Table 4.1. Results show that the values of n for drainage (n_{dr}) and imbibition (n_{imb}) are larger for the simulated curves than for experimental data, because the simulated curves are less steep than the experimental data. The value of α for drainage (α_{dr}) is overestimated by the simulated curves compared to experimental data, whereas the value of α for imbibition (α_{imb}) is underestimated.

The residual water saturation in our simulations was 0.14, which was close to the experimentally measured value of 0.11. Due to the angular shape of sand grains, corner flow of water at low saturation allows for additional drainage in experiments, therefore an even lower saturation can be reached. Moreover, the maximum water saturation after imbibition was 0.90, which is lower than the experimental value, namely 0.98. This may also be related to the fact that particles are modelled as spheres in DEM, whereas sand is typically less round and more angular. The maximum water saturation is lower in packings of spherical grains. For example, the maximum water saturation in experiments with glass bead packings has been found to be 0.92 (Culligan et al. 2004), or 0.74 to 0.92 (Dullien et al. 1988).

Table 4.1: Van Genuchten parameters for drainage and imbibition capillary pressure-saturation curves for experimental data by Lins and Schanz (2005) and simulated curves for 4000 particles.

	<i>Experimental data</i>	<i>Simulated curves</i>
α_{imb} (1/Pa)	8.76×10^{-4}	6.8×10^{-4}
n_{imb}	3.8	6.6
α_{dr} (1/Pa)	3.95×10^{-4}	4.5×10^{-4}
n_{dr}	7.9	21

4.5 SAP particle beds

Capillary pressure-saturation curves for main drainage and primary imbibition were simulated for a typical range of absorption ratios: from 5 to 40 g/g (see for example Brandt et al., 1987) and porosity values: from 0.10 to 0.43 (see for example Mirnyy et al., 2012). In this section, we report the dependency of the capillary pressure-saturation curve on porosity and absorption ratio. For sake of completeness, the dependency of permeability on porosity and absorption ratio is evaluated in Appendix D.

4.5.1 Effects of porosity and absorption ratio

Diersch et al. (2010) have developed a macro-scale numerical model for swelling granular materials under partially saturated conditions. In that model, the Van Genuchten parameter α was considered to be dependent on the absorption ratio (Q) and the porosity (ϕ), based on experimental evidence. But, the Van Genuchten parameter n was assumed to be constant. In their model, the load that was applied (P) to confine the sample was assumed to be constant. Therefore, the porosity was only considered to change with changing absorption ratio. Thus, it was assumed that both α and ϕ uniquely vary with Q . Both dependencies were experimentally determined and used as input for the macro-scale simulations. However, for a varying confining load, porosity can change independently of Q . Thus, α should be dependent on porosity and absorption ratio. To study the effects of both ϕ and Q on α separately, we kept one variable constant while varying the other. By keeping Q constant while varying ϕ , the effect of consolidation on α was studied. On the other hand, we increased Q while releasing net-stress to keep ϕ constant.

First, capillary pressure-saturation curves were obtained for different absorption ratios, at a variety of constant porosity values. Examples of typical curves are shown in Figure 4.5. These curves were fitted with the Van Genuchten formula ($R^2 > 0.98$) such that the values of α_{dr} , n_{dr} , α_{imb} and n_{imb} could be determined. In general, increasing the absorption ratio at a fixed porosity causes the volume of the sample to increase (due to larger grain sizes). Packings with larger grains, at a constant porosity, will have a lower entry pressure (and thus a higher value of α_{dr} and α_{imb}), because the pore sizes become larger. Indeed, our results showed that both α_{dr} and α_{imb} increase with an increasing Q , as shown in Figure 4.6a.

Next, capillary pressure saturation curves were obtained for packings with different porosities, at a number of constant absorption ratios. Results show that both α_{dr} and α_{imb} decrease (i.e. we will have a larger entry pressure) with decreasing porosity as seen in Figure 4.6b. An increase in entry pressure, due to a decrease in porosity is in agreement with experimental observations that are reported in the literature

(Vanapalli et al. 1996; Lins and Schanz 2005). For example, Lins and Schanz (2005) have shown that the entry pressure for imbibition increases from 0.3kPa for loosely packed Hostun sand with a porosity of 0.47 to 0.7kPa for densely packed Hostun sand with a porosity of 0.39. This corresponds to a change in α from approximately 0.0033 Pa⁻¹ to approximately 0.0014 Pa⁻¹. Oh and Lu (2014) studied the retention properties of weathered granite. They found an increase in entry pressure, for main imbibition, from 1130 Pa to 2110 Pa for a change in porosity from 0.37 to 0.32. This corresponds to a change in α from approximately 0.0009 Pa⁻¹ to approximately 0.0005 Pa⁻¹. However, they noted that the main imbibition curves were less affected by a change in porosity than the drainage curves.

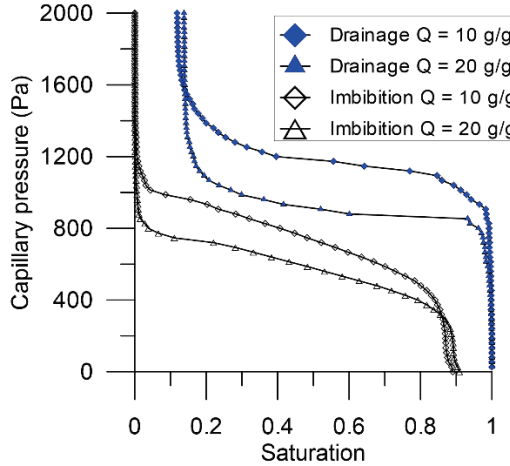


Figure 4.5: Drainage and imbibition capillary pressure-saturation curves for different values of absorption ratio at a constant porosity of 0.30.

The results in Figure 4.6a and 4.6b were fitted by the following formula ($R^2 > 0.98$):

$$\begin{aligned} \alpha_{dr} &= e^{3.50\phi - 8.9} \times Q^{\frac{1}{3}} \\ \alpha_{imb} &= e^{2.14\phi - 8.0} \times Q^{\frac{1}{3}} \end{aligned} \quad (4.6)$$

Note that equation 4.6 is valid for porosity values varying between 0.10 and 0.43. Diersch et al. (2011) assumed the value of α_{dr} to be $\frac{1}{2}\alpha_{imb}$. That ratio falls within the range of values suggested by equation 4.6. There we find that α_{dr} varies from $0.40\alpha_{imb}$ for (for $\phi = 0.10$) to $0.72\alpha_{imb}$ (for $\phi = 0.43$).

Moreover, we found that the Van Genuchten parameter n has a weak dependency on the porosity value and has no dependency on the absorption ratio, see

Figure 4.7. The value of n during imbibition (n_{imb}) was fitted with a second order polynomial equation ($R^2 = 0.82$):

$$n_{imb} = -25.5\phi^2 + 16.1\phi + 5.0 \quad (4.7)$$

Whereas for drainage, the values of n were much more scattered and as a consequence the quality of the fitting was less ($R^2 = 0.32$). Due to the large values of n_{dr} , namely $n_{dr} > 0.12$, small difference in n_{dr} do not affect the capillary pressure-saturation curve significantly. Therefore, the capillary pressure-saturation curves can be relatively close to each other, but can have large variation in n_{dr} . Thus, all curves have a similar flat curve, which is further elaborated on in section 4.5.4. The fitting equation is given by:

$$n_{dr} = -157\phi^2 + 83.3\phi + 7.3 \quad (4.8)$$

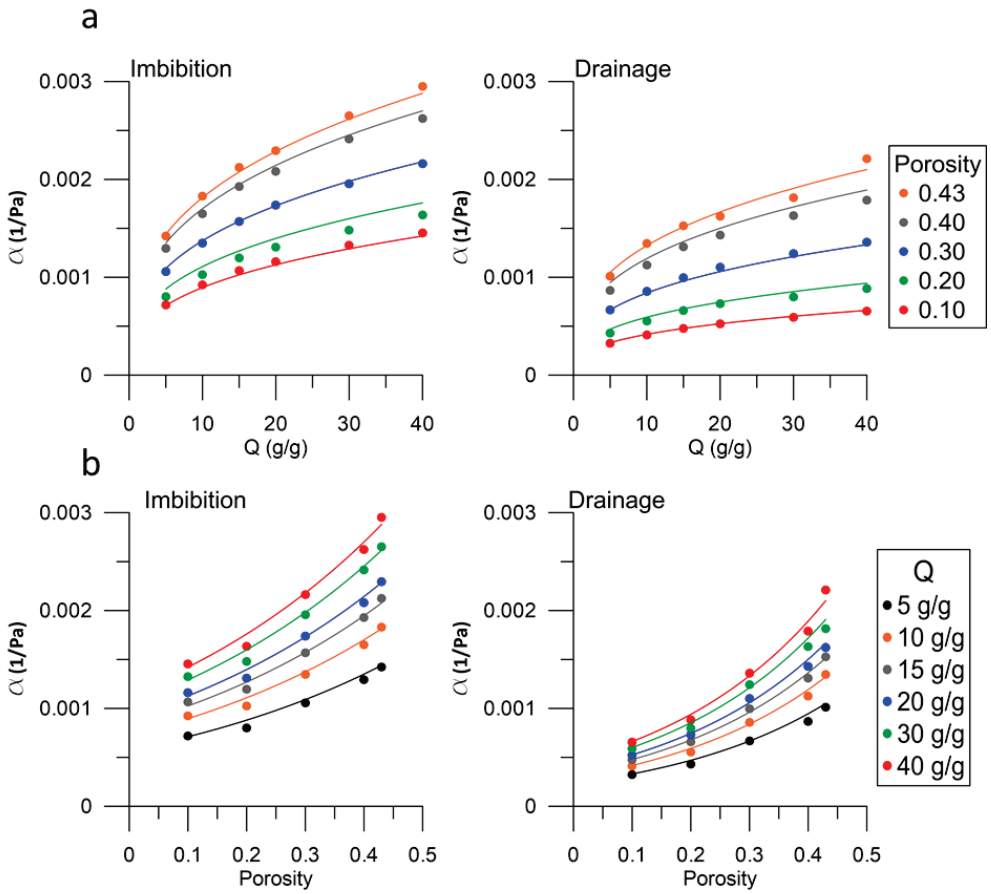


Figure 4.6: Van Genuchten parameter α for imbibition and drainage as a function of a) the absorption ratio and b) the porosity. Symbols represent values of α of simulated capillary pressure-saturation curves, while coloured lines represent fitting curves that are given in equation 4.6.

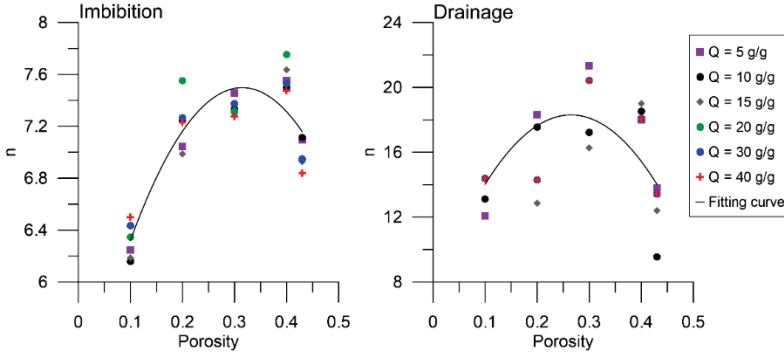


Figure 4.7: The Van Genuchten parameter n as a function of porosity for imbibition and drainage. Symbols represent data points from simulated capillary pressure-saturation curves, while solid lines represent fitting curves that are given by equation 4.7 and 4.8 for imbibition and drainage, respectively.

4.5.2 Maximum water saturation

Another aspect of the capillary pressure-saturation curve is the amount of trapped air after primary imbibition. In our model, residual air is present as disconnected air-saturated pore units. A trapped air ganglion is formed when the movement of water disconnects a cluster of air-saturated pore units from the air reservoir. The residual air saturation formed at the end of an imbibition process (S_r^{air}) corresponds to the maximum water saturation (S_{max}):

$$S_r^{air} = 1 - S_{max} \quad (4.9)$$

The residual air saturation depends on the pore structure of the porous medium. Figure 4.8 shows that the maximum water saturation (or the residual air saturation) depends on the porosity of the packing but not much on the absorption ratio. The absorption ratio causes swelling of all particles and thus does not change the network of pore units other than a translation of the size distribution. Therefore, the maximum water saturation is almost insensitive to the absorption ratio.

However, the maximum water saturation does depend on the porosity; the higher the porosity the lower the maximum water saturation. This phenomenon can be explained by the micro-scale heterogeneity of the pore structure. At higher porosity values, more clusters exist that contain relatively larger pore units. Water will flow via the smaller surrounding pore units rather than the high porosity clusters, leading to the trapping of residual air phase in the high porosity clusters. The maximum saturation was fitted as function of porosity ($R^2 = 0.78$), but S_{max} was not dependent on Q , such that S_{max} is described by:

$$S_{max} = -\phi^2 + 0.31\phi + 0.92 \quad (4.10)$$

Equation 4.10 is valid for porosity values between 0.10 and 0.43.

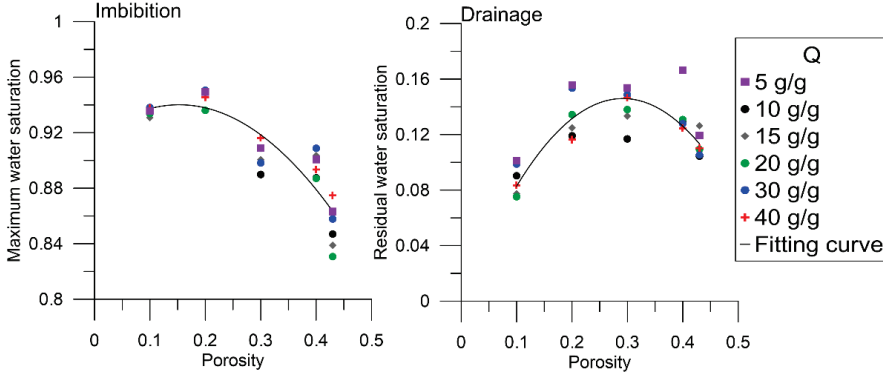


Figure 4.8: Maximum water saturation during imbibition (S_{max}) and residual water saturation during drainage (S_r^w) as a function of porosity. Symbols represent data points from simulated capillary pressure-saturation curves, while solid lines represent fitting curves that are given by equation 4.10 and 4.11.

4.5.3 Residual water saturation

Another feature of the capillary pressure-saturation curve for main drainage is the residual water saturation (S_r^w). Figure 4.8 shows a weak dependency of residual water saturation on the porosity. We have fitted the S_r^w on porosity using a second-order polynomial equation ($R^2 = 0.67$) for porosity values varying from 0.10 to 0.43:

$$S_r^w = -1.7\phi^2 + \phi \quad (4.11)$$

Imbibition

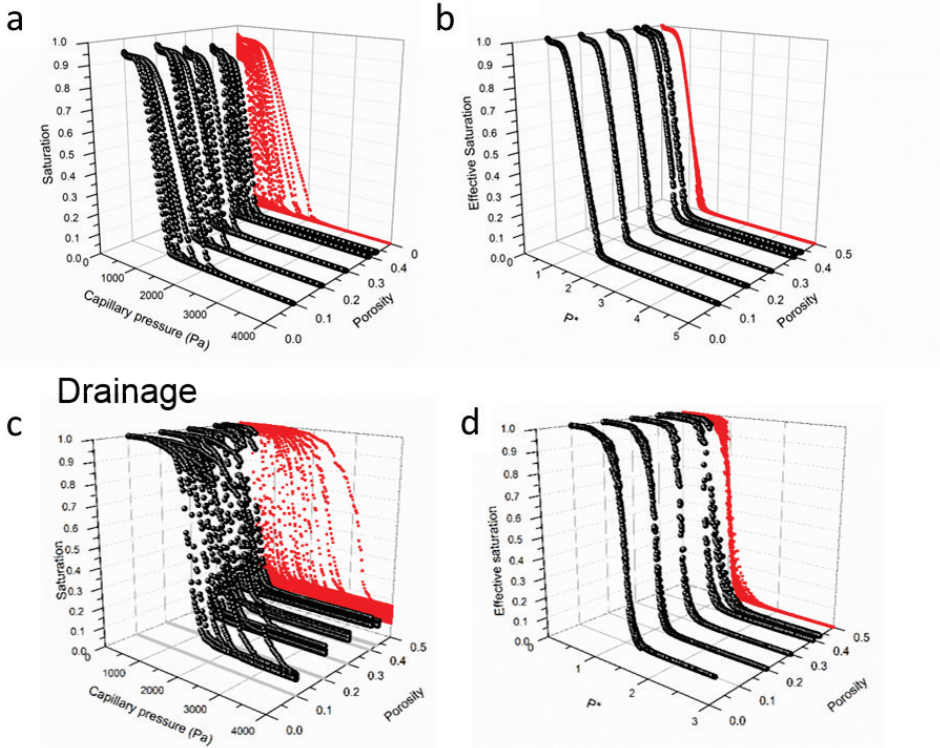


Figure 4.9: $P_c - S - \phi$ plots for SAP particles at different absorption ratios. For each porosity value, there are five different P_c - S curves corresponding to different values of absorption ratios. Red curves show the projections of P_c - S curves on the P_c - S plane; a) all imbibition capillary pressure-saturation curves of SAP particles; b) Plot of the normalized capillary pressure ($P^* = P_c \alpha$) vs. effective saturation (S_{eff}) for imbibition; c) all drainage capillary pressure-saturation curves of SAP particles; d) Plot of the normalized capillary pressure ($P^* = P_c \alpha$) vs. effective saturation (S_{eff}) for drainage.

4.5.4 Normalizing capillary pressure-saturation data points

We have plotted the capillary pressure-saturation curves for drainage and imbibition, for different porosities and absorption ratios, with the following axes: capillary pressure, saturation, and porosity (see Figure 4.9). The 2-dimensional projection of the resulting 3-dimensional surface on the capillary pressure-saturation plane, shows the spreading in the capillary pressure-saturation curves for both drainage and imbibition. We used the Van Genuchten parameter α for each capillary pressure-saturation curve to normalize the capillary pressure by defining:

$$P^* = P_c \alpha \quad (4.12)$$

We also replaced saturation values for each curve with the effective saturation. The plots of P^* versus effective saturation are shown in Figure 4.9b and 4.9d. As can be seen, the curves for drainage have almost collapsed into one single curve for drainage and the curves for imbibition have almost collapsed into one single curve for imbibition, showing that $P^*(S_{eff})$ is independent of the porosity value and the absorption ratio. The value of n_{imb} for the $P^*(S_{eff})$ relationship for imbibition was 7.03, which is close to the average value of n_{imb} for all individual drainage curves, namely 7.24. Moreover, the value of n_{dr} for the $P^*(S_{eff})$ relationship for drainage was 15.8, which is close to the average value of n_{dr} for all individual drainage curves, namely 16.3. The fact that normalizing the capillary pressure-saturation curves for drainage and imbibition yields one curve for drainage and one curve for imbibition implies that the variation in n can be neglected and thus n can be considered as a constant for the range of porosity values [0.10 – 0.43] and absorption values [5 – 40 g/g] that we considered in this study.

4.6 Conclusion

In this study, a pore-scale model was developed to construct capillary pressure-saturation curves for swelling granular materials. The material of interest consists of particles of Super Absorbent Polymers (SAP). This model is based on combining the Discrete Element Method (DEM) and the pore-unit assembly method. It is capable of producing capillary pressure-saturation curves for different particle packings, based on simple physical parameters: particle size distribution, porosity, and in case of swelling granular materials, the amount of absorbed water. In order to test the model, capillary pressure-saturation curves were constructed for Hostun sand. They were found to be in relatively good agreement with experimental data from the literature. Then, a large number of capillary pressure-saturation curves for primary imbibition and drainage were constructed for different porosities and different amounts of absorbed water. The simulated data were used to develop a relationship for the Van Genuchten parameter α and n dependent on the amount of absorbed water and porosity. When we normalized the capillary pressure by $1/\alpha$ (proportional to the entry pressure) and plotted it against the effective saturation, we found that all drainage curves collapsed into one single drainage curve and all imbibition curves collapsed into one single imbibition curve, proving that both normalized curves are independent of porosity and absorption ratio. This implies that we can capture the effects of porosity and absorption ratio in the Van Genuchten parameter α , maximum water saturation (during imbibition) and residual water saturation (during drainage) while keeping n constant.

Capillary pressure-saturation relationships for porous granular materials: pore morphology method vs. pore unit assembly method

Abstract

In studies of two-phase flow in complex porous media it is often desirable to have an estimation of the capillary pressure-saturation curve *prior* to measurements. Therefore, we compare in this research the capability of three pore-scale approaches in reproducing experimentally measured capillary pressure-saturation curves. To do so, we have generated 12 packings of spheres that are representative of four different glass-bead packings and eight different sand packings, for which we have found experimental data on the capillary pressure-saturation curve in the literature. In generating the packings, we matched the particle size distributions and porosity values of the granular materials. We have used three different pore-scale approaches for generating the capillary pressure-saturation curves of each packing: i) The Pore Unit Assembly (PUA) method in combination with the Mayer and Stowe-Princen (MS-P) approximation for estimating the entry pressures of pore throats, ii) the PUA method in combination with the hemisphere approximation, and iii) the Pore Morphology Method (PMM) in combination with the hemisphere approximation. The three approaches were also used to produce capillary pressure-saturation curves for the coating layer of paper, which is a granular material in itself and used in inkjet printing. Curves for such layers are extremely difficult to determine experimentally, due to their very small thickness and the presence of extremely small pores (less than one micrometer in size). Results indicate that the PMM and PUA-hemisphere method give similar capillary pressure-saturation curves, because both methods rely on a hemisphere to represent the air-water interface. The ability of the hemisphere approximation and the MS-P approximation to reproduce correct capillary pressure seems to depend on the type of particle size distribution, with the hemisphere approximation working well for narrowly distributed granular materials.

Published as: Sweijen, T., Aslannejad H., Hassanizadeh S. M. (2017). Capillary pressure-saturation relationships for porous granular materials: pore morphology method vs. pore unit assembly method. *Advances in Water Resources* 107(2017), 22-31

5.1 Introduction

The relationship between capillary pressure and saturation plays an important role in many applications of porous materials, such as inkjet printing (Rosenholm, 2015), water flow in hygienic products (Diersch et al., 2010), water distribution in fuel cells (Qin, 2015), oil and gas reservoir engineering, and unsaturated soils (Lins and Schanz, 2005). This relationship depends on both the geometry and dimensions of the pore space (Likos and Jaafar, 2013; Mousavi and Bryant, 2012; Øren and Bakke, 2003; Torskaya et al., 2014).

Usually, it is possible to represent the pore space of a granular material by a network of pore bodies and pore throats. The pore bodies account for most of the void volume, while the pore throats, which connect neighbouring pore bodies, act as narrow pathways that account for the resistance to flow. The network of pore bodies and pore throats is typically complex and highly irregular. This network can be constructed by, for example, one of the following methods: 1) it can be randomly generated based on the pore throat size distribution, pore body size distribution, the distribution in number of pore throats per pore body (i.e. coordination number), and either the porosity value or permeability value of the granular material (Lindquist et al., 2000; Raof and Hassanizadeh, 2010), 2) it can be extracted from the pore geometry inside an artificially generated pack of spheres (Gladkikh and Bryant, 2005; Yuan et al., 2015) or 3) it can be extracted from a 3-dimensional reconstruction of the porous material, based on advanced imaging methods such as X-ray tomography and micro-CT (Joekar-Niasar et al., 2010; Lindquist et al., 1996).

Several advanced direct imaging techniques are available, which can be classified as destructive and non-destructive methods. An example of a destructive method is focused ion beam-scanning electron microscopy (FIB-SEM), where SEM is used for imaging the surface and a focused ion beam is used to remove a thin layer of the material and expose the underlying surface for SEM imaging. Using image analysis techniques, a 3-dimensional high-resolution reconstruction of the pore space can be obtained in binary mode. The resolution of this method is in the order of nanometer. However, the acquisition of FIB-SEM images is time consuming (between 4 and 12 hours depending on sample size and slicing thickness) and the analysed volume is typically very small (Aslannejad et al., 2017; Bultreys et al., 2016). An example of a non-destructive method is X-ray computed tomography that provides 3-dimensional structural information, with a resolution in the range of micrometer to millimeter scale. It can visualize not only the pore space but also fluid distributions inside the porous material (e.g. Culligan et al., 2004). However, direct measurements of the pore geometry

are not trivial and it remains time consuming, especially for visualization of numerous samples. As an alternative, for the purpose of studying various factors that affect hydraulic properties of granular materials, one may use numerically-generated packings of spheres.

One way to generate a packing is to place spheres randomly in a stable configuration by trial and error until a desired porosity is obtained. Bakke and Øren (1997) generated packings of randomly located spheres, before compaction was applied by scaling all particle locations in the vertical direction. The pore geometry was extracted using image analysis techniques on the packing of spheres. Based on the resulting pore geometry, a pore network was constructed that was used to obtain capillary pressure-saturation curves and the relative permeability curves. Mousavi and Bryant (2012) generated a random packing of ductile spheres in which cementation was modelled by increasing the radii of the spheres while accounting for a net transport of solid-phase, due to pressure-dissolution, from finer grains to coarser grains. Once a packing was produced, triangulation was applied to extract the pore geometry and subsequently to construct the capillary pressure-saturation curve. They studied the effect of cementation on the capillary pressure-saturation relationship.

Alternatively, one may start with a collection of sparsely placed spheres and use the Discrete Element Method (DEM) to determine their stable configuration. DEM is based on determining the force interactions between different spherical particles during their displacement and compaction. DEM has been used to simulate geo mechanical processes, such as triaxial tests (Belheine et al., 2009; Widuliński et al., 2009), soil tillage (Shmulevich, 2010), as well as industrial processes such as particle flows in silos (Langston et al., 1995). DEM has been used to construct particle packings with a predefined particle size distribution and porosity (Tong et al., 2012; Yuan et al., 2015). One disadvantage of DEM is that the shape of individual particles is simplified to a sphere, which may not be appropriate for irregularly shaped particles. Nevertheless, packings of spheres have proved to be valuable for the study of processes in granular materials.

The pore space in spherical particle packings is often extracted using Delaunay tessellation, also known as triangulation, where centres of four neighbouring particles are connected to form a tetrahedron. This tetrahedron is then assumed to enclose one pore unit such that an assembly of pore units represents the whole pore space (Mason and Mellor, 1995). We refer to this method as the Pore Unit Assembly (PUA) method. Gladkikh and Bryant (2005) have used triangulation to extract the pore space of a Finney packing, which is a packing of equally-sized spheres whose locations have been

measured (Finney, 1970), to obtain the capillary pressure-saturation curve for imbibition. Yuan et al. (2016) generated packings of spheres, using DEM, which represented the glass-bead packing used in experiments of Culligan et al. (2004). Then, they used PUA to construct the drainage capillary pressure-saturation curve for that packing. They found good agreement with experimental data of Culligan et al. The concept of PUA can be generalized such that it can be applied to other porous materials types.

Another method to compute the capillary pressure-saturation curve from both direct pore geometry measurements and packings of spheres is the Pore Morphology Method (PMM). In PMM, the air-water interface is represented by a hemisphere where the radius of that sphere is related to the capillary pressure, using Young's Laplace equation. PMM divides the pore structure into voxels. Then, for a certain capillary pressure, PMM identifies where an air-water interface would fit in the pore space while maintaining the connectivity of the air phase to its reservoir. At each capillary pressure, the distribution of water and air phase is known, such that the capillary pressure-saturation curve can be calculated (Hilpert and Miller, 2001). Vogel et al. (2005) have compared the capillary pressure-saturation relationship of PMM with those obtained from a pore-network model and Lattice Boltzmann simulations, where they solved for two-phase Navier-Stokes on the actual pore geometry. The pore network contained a 3-dimensional network of capillary tubes with the same statistical information on pore throat size distribution and coordination number as used in PMM computations. In that research, a 3-dimensional reconstruction was made of a sintered glass sample using X-ray tomography results. The pore space was then used to compute the capillary pressure-saturation curve using the three different models. Results showed that Lattice Boltzmann gives lower values of capillary pressures compared to that of the PMM and the pore network model. The capillary pressure-saturation curves for PMM and the pore network model were approximately the same, because the pore network model inherited the pore structure that was extracted in the pore morphology method. However, the question remains on how well both models can predict the capillary pressure-saturation curve of granular materials if the pore network is not directly based on the statistical information from PMM, but rather on the discretization of the pore space into pore throats and bodies.

An essential factor in determining the capillary pressure-saturation curve is the shape and curvature of the air-water interface (Prodanović and Bryant, 2006; Vidales et al., 1998). Air-water interfaces in granular materials can have complex shapes, whose curvatures are difficult to determine. In pore-scale models, the curvature, at which air

can invade a water-saturated pore throat, can be estimated by either the Mayer and Stowe-Princen (MS-P) approximation or by the so-called hemisphere approximation. The MS-P approximation assumes that the main terminal meniscus (MTM) has just passed through a pore throat opening (so, it is inside the pore throat) and corners in the invaded part of the pore throat are still filled by water. Then, the capillary pressure of the MTM can be assumed equal to that of the arc menisci (AM) which are present in the corners. The radius of the curvature of AM in the cross-section of a pore throat can be determined by a force balance. The second curvature, along the pore throat, is assumed to be flat. This assumption is valid only if the pore throat is elongated. Nevertheless, Prodanović and Bryant (2006) have used the level-set method to study the shape of an air-water interface in pore throats formed between spherical particles. They showed that the 3-dimensional curvature of air-water interface in a throat can be obtained by the MS-P approximation. The hemisphere approximation assumes that the air-water interface has a spherical shape, and thus assumes a contact angle of zero. In PMM, the air-water interface is represented by a hemisphere (Hilpert and Miller, 2001) while in PUA method and pore-network models both the hemisphere and the MS-P approximations have been used.

To investigate the ability of PUA and PMM to estimate capillary pressure-saturation curves of granular materials, we studied 12 granular materials for which experimental data are reported in the literature. In addition, we studied the coating layer of paper which has a mean pore size of 180 nm (Aslannejad et al, 2017). We generated for each granular material a spherical particle packing by matching the particle size distribution and the porosity value of the granular material of interest, using DEM. This packing was then imported into both PMM and PUA to construct capillary pressure-saturation curves for drainage using three different methods: (i) using PUA where entry pressures are given by the Mayer and Stowe-Princen method, (ii) using PUA where entry pressures are given by the hemisphere approximation, and (iii) using PMM in combination with the hemisphere approximation.

The aims of this research were as follows: a) determine how capillary pressure-saturation curves from PUA and PMM compare to those from experiments and how this is affected by the choice of approximation for the entry pressure, using either the MS-P approximation or hemisphere approximation; b) determine how the shape of the air-water interface is affected by the particle size distribution. To do this, three comparisons were made, namely: i) we compared capillary pressure-saturation curves constructed by PMM to those of PUA, both of them using the hemisphere approximation; ii) we compared the hemisphere approximation with the MS-P approximation, both used in

PUA, to understand what their main differences are, and iii) we compared capillary pressure-saturation curves obtained with PUA, using both MS-P and the hemisphere approximations, to existing experimental data to determine their ability of reproducing experimental results.

5.2 Numerical model

To construct a packing of spheres with a predefined porosity value and particle size distribution, we use open source software Yade-DEM (Šmilauer et al., 2016), which is a 3-dimensional particle model based on the Discrete Element Method (DEM). In this work, we employ the same approach as in Chapter 4 to construct packings of spheres.

5.2.1 Pore unit assembly method

The pore unit assembly method (PUA) that we use in this Chapter is a module in Yade-DEM (Chareyre et al., 2012; Yuan et al., 2016). PUA relies on a regular triangulation to subdivide the pore space of packings of spheres into pore units, see Figure 5.1a. In a triangulation, the centres of four neighbouring particles form the vertices of a tetrahedron, see Figure 5.1b. The void space that is present within a tetrahedron is referred to as a *pore unit*. Each tetrahedron is connected to four other tetrahedra. The facet that is shared between two pore units of adjacent tetrahedra represents the narrowest opening between two tetrahedra, which we refer to as a *pore throat*. A pore throat has zero length but has a cross-sectional area.

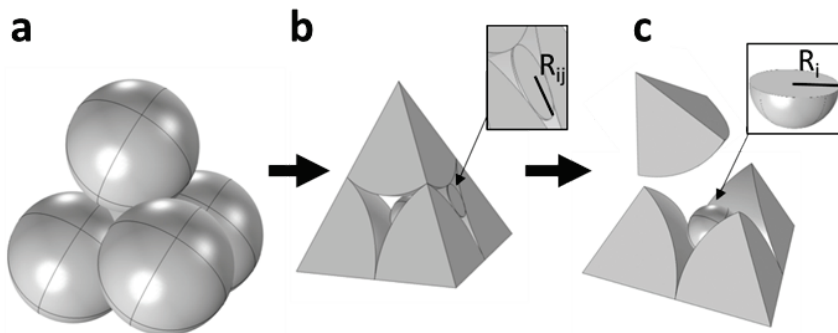


Figure 5.1: Illustration of a pore unit: a) four spheres enclose one pore unit, b) a tetrahedron that is a result of regular triangulation, with pore throat radius R_{ij} and c) illustration of the inscribed sphere of a pore unit with a radius R_i .

To construct capillary pressure-saturation curves for drainage in PUA, it is essential to know the entry pressure that is required for air to invade a water-saturated pore unit via one of its four pore throats. Consider an air-saturated pore unit i at an air pressure P_i and a water saturated pore unit j at a water pressure P_j . For air to invade pore unit j , the pressure difference between pore units i and j ($P_i - P_j$) should be larger than the entry pressure of pore throat ij , namely P_{ij}^e . To compute the entry pressure of pore throat ij , two different methods can be used. Both methods are based on the Young-Laplace equation, which relates the entry pressure to the curvature of the air-water interface:

$$P_{ij}^e = \gamma_{aw} \left(\frac{1}{r'} + \frac{1}{r''} \right) \quad (5.1)$$

where r' and r'' are two principal radii of curvature of the air water interface and γ_{aw} is the air-water interfacial tension.

The first method is known as the Mayer and Stowe-Princen method (Mayer and Stowe, 1965; Princen, 1969). We refer to this method as *PUA-MS-P*. To explain this method, consider an elongated pore throat ij , between air-saturated pore unit i and water saturated pore unit j (see Figure 5.2a). Let's assume that air has just invaded pore throat ij . The entry pressure can be computed from the balance of forces acting on the air-water interface in the cross-section of pore throat ij , by assuming that the capillary pressure just after invasion is the same as the entry pressure of that pore throat (see e.g. Ma et al., 1996). The radius of curvature of the arc menisci (in the pore throat corners) R_{ij}^{MSP} is obtained based on the pore throat that was found during triangulation. The particle locations of the three spheres that form a pore throat determine the shape of that pore throat and thus determine the value of R_{ij}^{MSP} (see Appendix E). Note that radius R_{ij}^{MSP} is supposed to be smaller than the radius of the inscribed circle of a pore throat R_{ij}^{in} (Yuan et al., 2015), see Figure 5.2b. This, however, may not occur when particles do not touch, as illustrated in Figure 2b. In the MS-P approach it is assumed that the pore throat is elongated such that one principal radius in equation 5.1 goes to infinity. Thus, equation 5.1 can be approximated by:

$$P_{ij}^e = \frac{\gamma_{aw}}{R_{ij}^{MSP}} \quad (5.2)$$

For more details on the implementation of this method into DEM, the reader is referred to Yuan et al. (2016).

The second method to compute the entry pressure of a pore throat is to assume that the air-water interface has the shape of a hemisphere, with a contact angle of zero (see Figure 2c). We refer to this method as *PUA-hemisphere*. The radius of the

hemisphere corresponds to the inscribed circle in a pore throat R_{ij}^{in} . Then, the principal radii in equation 5.1 are assumed to be both equal to R_{ij}^{in} such that equation 5.1 can be recast into:

$$P_{ij}^e = \frac{2\gamma_{aw}}{R_{ij}^{ins}} \quad (5.3)$$

For both MS-P approximation and hemisphere approximation, the model presented in Chapter 4 was employed to obtain the capillary pressure-saturation curve for drainage. In that model, the saturation was assumed to be binary; i.e. a pore unit is assumed to be saturated either with water or air. Thus, pendular rings and water films are neglected. The simulation procedure to obtain capillary pressure-saturation curves was as follows. Initially, all pore units were saturated with water, except for the pore units along the air reservoir which were saturated with air. Next, a capillary pressure was imposed on the packing. This was done by setting the pressure difference between the air and water reservoirs ($P_{air} - P_w$) equal to the value of that capillary pressure. Then, for each pore throat in between an air saturated pore unit i and a water saturated pore unit j , the following criterion was evaluated: if the imposed capillary pressure was larger than the entry pressure (P_{ij}^e), air would invade pore unit j . If invasion occurred, then the criterion was checked again for all pore throats connecting to pore unit j . This was continued until no air invasion would occur. The saturation corresponding to that imposed capillary pressure was measured. Then, a new capillary pressure was imposed, the model checked again for invasions, and the new saturation was measured. This resulted in a capillary pressure-saturation curve. The algorithm does not allow for displacement of disconnected water-filled pore units, resulting in a residual water saturation after drainage.

5.2.2 Pore morphology method

The third method that we use to calculate capillary pressure-saturation curves is the Pore Morphology Method to which we refer to as *PMM*. For this we used GeoDict software (Math2Market, 2016). The pore morphology method determines the stationary air and water distribution in a porous material for a given capillary pressure. In static conditions, the capillary pressure is the same as the pressure difference between the air reservoir and the water reservoir, which are at a pressure P_{air} and P_w , respectively. To determine the pore space that is accessible to air (during drainage) the Young-Laplace equation is employed, where the air-water interfacial area is assumed to be a hemisphere with radius R_c :

$$R_c = \frac{2\gamma_{aw}}{P_{air} - P_w} \quad (5.4)$$

To identify the locations in the pore space where a hemisphere with radius R_c would fit, an erosion algorithm is employed, which is normally used in image analysis procedures. Considering the connectivity of air to the air-reservoir, the capillary pressure-saturation curves were constructed. For more information, the reader is referred to Hilpert and Miller (2001).

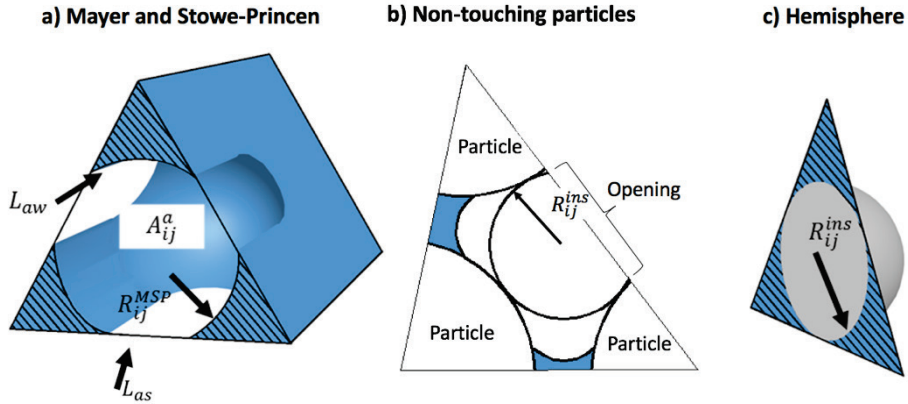


Figure 5.2: Schematic representation of air-water menisci in two different approximations for the estimation of the entry pressure of a pore throat; a) the Mayer and Stowe-Princen approximation, where the air-water interface has a complex shape in an elongated pore throat, b) an example of a pore throat with non-touching particles, and c) the hemisphere approach where the air-water interface is assumed to be spherical.

5.3 Simulation methods

In this research, we study granular materials that are reported in the literature, for which capillary pressure-saturation curves have been measured. For each granular material, we generated a packing of spheres that matched its porosity value and its particle size distribution. For each packing, capillary pressure-saturation curves were produced using the three different methods as described in section 5.2.

5.3.1 Materials

The particle size distributions of the 12 materials are listed in Table 5.1. We have chosen to simulate 4 glass bead samples and 8 sand samples. Out of 8 sands, four were Ottawa sands (samples OS12/20, OS20/30, OS30/40 and OS40/50). They had different particle size distributions, at a constant porosity value of 0.34 (Schroth et al., 1996), which enabled us to only study the effect of the particle size distribution. In addition, two sands that are reported in Oostrom et al. (1999) were studied, as they also had the same porosity value of 0.34 and originated from the same sand type but had different filter sizes (12S and 14S). The two remaining sands (F75, RS) had higher porosity values and different particle size distributions. They were used to study the applicability of the models on different types of sands. Two samples of glass-beads were chosen because they have been used in previous studies (GB1 and GB2), which enabled us to cross-verify our results. The other two glass bead samples (GB3 and GB4) were chosen because they had varying particle sizes and varying porosity values. Most granular materials had a porosity value between 0.34 and 0.36, but 4 granular materials had a porosity value higher than 0.38. All experimental capillary pressure-saturation curves were scaled to air-water systems using a surface tension of 0.072 Nm^{-1} and a contact angle of zero degrees.

Finally, we generated a packing of spheres that corresponds to the coating layer of paper, which is reported in Aslannejad et al. (2017). They extracted the pore geometry using FIB-SEM imaging and they subsequently constructed the capillary pressure-saturation curve using PMM directly on the extracted pore geometry. We use their reported values of Van Genuchten parameters to evaluate the approach.

5.3.2 Generation of a pack of spheres

In our DEM simulations, we have used the linear contact mechanics, as introduced by Cundall and Strack (1979). The mechanical parameters were adopted from Belheine et al. (2009), who have fitted DEM simulation of various triaxial tests to experimental

results. The particle stiffness was set to $9.8 \times 10^8 \text{ Nm}^{-1}$, the ratio between the normal and tangential force to 0.04, and the density was set to 2600 kg m^{-3} .

First, a cloud of 4000 spheres was generated in a modelling domain ($0.02 \times 0.02 \times 0.02 \text{ m}^3$) that was larger than the final packing dimensions, which was typically in the order of 1 mm^3 to 1 cm^3 . The particle sizes were chosen from the particle size distribution of the granular material of interest. Then, an arbitrary large friction angle (50°) was assigned to the particles. Next, a confining pressure was applied to all 6 boundaries of the box such that the cloud of particles got compacted to a stable configuration, which had a porosity value of approximately 0.43. Then, the friction angle was decreased in small steps such that the particles were gradually rearranged into a tighter packing until the desired porosity was achieved.

5.3.3 Capillary pressure-saturation relationship

The packing of spheres was imported in PMM whereas PUA was directly employed within Yade-DEM. During capillary pressure-saturation calculations in all methods, one boundary of the modelling domain of DEM was assumed to be an air reservoir at an air pressure P_{air} , and the opposite boundary was assumed to be a water reservoir at a water pressure of P_w . The air pressure was increased such that air could invade increasingly smaller pores. All capillary pressure-saturation curves were fitted with the Van Genuchten equations, see for more details Appendix A.

5.4 Results and Discussion

5.4.1 Verifying the packing procedure

To verify our approach of constructing capillary pressure-saturation curves of packings of spheres, we have reproduced a capillary pressure-saturation curve for the packing of spheres that corresponds to the glass beads used in Hilpert and Miller (2001), namely sample GB1. They measured the primary drainage curve and simulated it using PMM. Both their experimental and simulated curves (for 800^3 voxels), as well as our PMM simulated curve are shown in Figure 5.3. The capillary pressure-saturation curves that were constructed using PMM in Hilpert and Miller (2001) and in our simulations are similar, indicating that the packings of spheres are similar. Albeit we used DEM to make a packing of spheres while they used a random insertion algorithm that was developed by Yang et al. (1996). However, none of the simulated curves can match the experimentally measured curve. Both PMM curves have a smooth transition at the entry pressure, while experiments show a discontinuity of the curve at the entry pressure. In other words, the simulated curves can be fitted well with the Van Genuchten formula, because of the continuous behaviour of the curve around the entry pressure, whereas the experimental behaviour can be fitted best by the Brooks and Corey formula (1964), because of its discontinuity around the entry pressure. In the saturation range of 0.2 to 0.8 the capillary pressure of the simulated curves corresponds reasonably well to the experimental data. However, at low saturations (<0.20), the capillary pressure is overestimated by the PMM, because the hemisphere approximation does not hold for pendular rings (Hilpert and Miller, 2001). For pendular rings, the two principal radii r' and r'' in equation 5.1 are not equal; in fact, one of them is even negative (Scholtès et al., 2011).

Figure 5.4 shows the capillary pressure-saturation curves by PMM, PUA-MS-P and PUA-hemisphere, for the same packing as in Figure 5.3. PUA-hemisphere results in a curve that fits the experimental data better than the curve by PMM, especially for saturations larger than 0.8. Nonetheless, the PMM curve is still relatively close to that of PUA-hemisphere, because both methods assume the air-water interface to have a spherical shape.

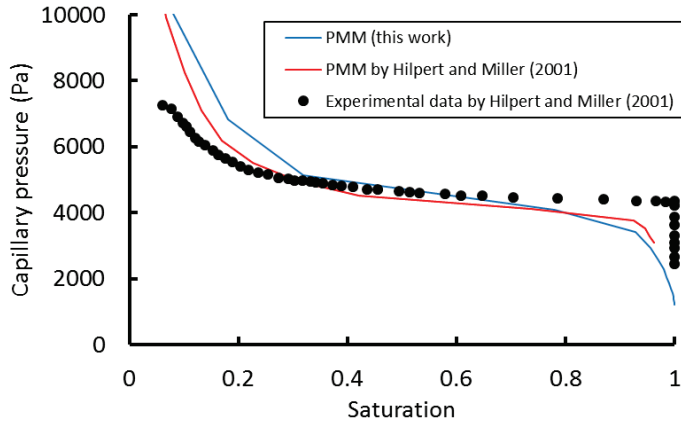


Figure 5.3: Capillary pressure-saturation data for a glass-bead packing (GB1) together with curves constructed using the pore morphology method (PMM). Simulated curves by Hilpert and Miller (2001) were for 800^3 voxels.

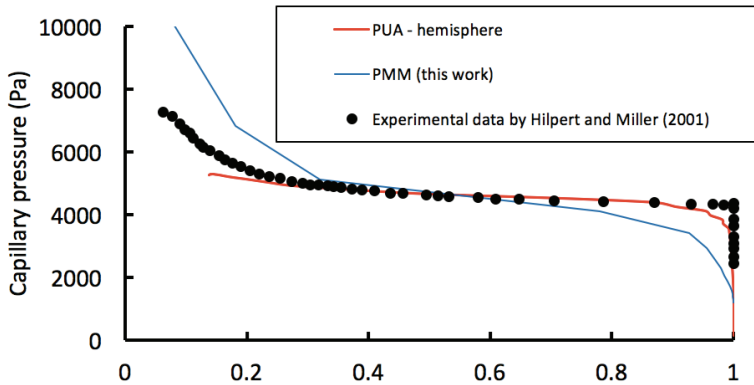


Figure 5.4: Capillary pressure – saturation data for a glass-bead packing (GB1) together with simulated curves, constructed by PUA in combination with the hemisphere approximation (PUA – hemisphere) as well as the pore morphology method (PMM).

Table 5.1: Particle size distribution and porosity values of the 12 granular materials and the coating layer.

Type	Name	D50 (mm)	Average diameter (mm) ^{*1}	St.dev (mm)	Porosity	Reference
Glass-Beads	GB1	0.13	0.12	0.012	0.356	Hilpert and Miller (2001)
Glass-Beads	GB2	0.87	0.74	0.2	0.34	Culligan et al. (2012)
Ottawa sand 12/20	OS12/20	1.11	1.02	0.14 ¹	0.34	Schroth et al. (1996)
Ottawa sand 20/30	OS20/30	0.71	0.69	0.08 ¹	0.34	Schroth et al. (1996)
Ottawa sand 30/40	OS30/40	0.53	0.50	0.05 ¹	0.34	Schroth et al. (1996)
Ottawa sand 40/50	OS40/50	0.36	0.35	0.04 ¹	0.34	Schroth et al. (1996)
Small glass beads	GB3	0.087 ^{*2}	0.085	0.0087 ¹	0.42	Likos and Jaafar (2013)
Large glass beads	GB4	0.30 ^{*2}	0.29	0.027	0.38	Likos and Jaafar (2013)
Ottawa sand F75	F75I	0.21 ^{*2}	0.17	0.051 ¹	0.39	Likos and Jaafar (2013)
River sand	RS	0.58 ^{*2}	0.48	0.13 ¹	0.38	Likos and Jaafar (2013)
#12 Sand	12S	0.70 ^{*2}	0.37	0.22 ¹	0.34	Oostrom et al. (1999)
#14 Sand	14S	0.46 ^{*2}	0.35	0.11 ¹	0.35	Oostrom et al. (1999)
Coating layer	CL	4.3x10 ⁻⁴	2.2x10 ⁻⁴	1.0x10 ⁻⁴	0.34	Aslannejad et al. (2017)

*1) Estimated values from the population of particle sizes that were generated in Yade-DEM. *2) Estimated values from reported particle size distributions in the original article.

Table 5.2: Van Genuchten parameters for all 12 granular materials and the coating layer (Van Genuchten parameters for experiments have been extracted from the literature, they are compared to values fitted to capillary pressure-saturation curves obtained from simulations using three different methods).

Type	Experiments		PMM-Hemisphere		PUA – Hemisphere		PUA – MS-P	
	α (Pa ⁻¹)	n	α (Pa ⁻¹)	n	α (Pa ⁻¹)	n	α (Pa ⁻¹)	n
Glass-Beads	2.17x10 ^{-4*}	24.6*	2.20x10 ⁻⁴	8.8	2.15x10 ⁻⁴	26.1	3.73x10 ⁻⁴	9.6
Glass-Beads	1.56x10 ⁻³	11.8	9.72x10 ⁻⁴	4.3	7.88x10 ⁻⁴	16.4	1.37x10 ⁻³	10.7
Ottawa sand 12/20	9.99x10 ⁻⁴	6.7	1.00x10 ⁻³	9.2	1.05x10 ⁻³	19.5	1.89x10 ⁻³	13.0
Ottawa sand 20/30	7.33x10 ⁻⁴	8.9	6.67x10 ⁻⁴	9.3	7.04x10 ⁻⁴	17.8	1.27x10 ⁻³	11.2
Ottawa sand 30/40	5.52x10 ⁻⁴	10.6	4.85x10 ⁻⁴	9.2	5.06x10 ⁻⁴	18.2	9.14x10 ⁻⁴	12.4
Ottawa sand 40/50	3.97x10 ⁻⁴	11.8	3.35x10 ⁻⁴	9.2	3.60x10 ⁻⁴	17.1	6.35x10 ⁻⁴	12.0
Small glass beads	1.12x10 ⁻⁴	7.4	9.50x10 ⁻⁵	16.3	1.02x10 ⁻⁴	20.2	1.81x10 ⁻⁴	18.5
Large glass beads	4.49x10 ⁻⁴	11.5	2.64x10 ⁻⁴	16.1	2.90x10 ⁻⁴	27.3	5.05x10 ⁻⁴	18.2
Ottawa sand F75	2.72x10 ⁻⁴	5.4	2.35x10 ⁻⁴	6.4	2.11x10 ⁻⁴	42.4	3.73x10 ⁻⁴	26.7
River sand	3.61x10 ⁻⁴	10.8	5.45x10 ⁻⁴	10.6	5.46x10 ⁻⁴	28.7	9.67x10 ⁻⁴	18.8
#12 Sand	1.78x10 ^{-3**}	8.3**	5.62x10 ⁻⁴	8.9	5.91x10 ⁻⁴	17.4	1.07x10 ⁻³	12.9
#14 Sand	1.07x10 ^{-3**}	9.9**	4.27x10 ⁻⁴	16.6	4.59x10 ⁻⁴	12.2	8.05x10 ⁻⁴	12.6
Coating layer of paper	5.16x10 ^{-7***}	5.0***	4.28x10 ⁻⁷	4.23	3.31x10 ⁻⁷	26.9	6.07x10 ⁻⁷	14.1

* Van Genuchten formula gave a poor fit to experimental data. The equation by Brooks and Corey (1964), $S_e = \left(\frac{P_c}{P_c}\right)^\lambda$, gave a better fit with best-fit values being: $P_c = 4312Pa$ and $\lambda = 10.7$. **In the original work by Oostrom et al. (1999) the Brooks and Corey parameters were reported for trichloroethylene and water, which was converted to air and water by correcting for interfacial tensions (0.035 Nm⁻¹ to 0.072 Nm⁻¹, respectively). The scaled-version of the Brooks and Corey parameters were then converted to Van Genuchten parameters. ***Van Genuchten parameters values were obtained using Pore Morphology Method and based on directly measured pore geometry and we corrected the reported values for a contact angle of 45°.

5.4.2 Pore morphology method vs. Pore unit assembly model

As we discussed in section 5.4.1, the capillary pressure-saturation curves are close to each other for PMM and PUA-hemisphere simulations on glass bead packing GB1. To confirm this for all packings, we have plotted the values of Van Genuchten parameter α for all 12 granular materials obtained with PMM against values obtained with PUA-hemisphere (see Figure 5.5a). In addition, the Van Genuchten parameters are reported in Table 5.2. Indeed, both models give approximately the same value of α and thus give approximately the same value of entry pressure. However, the values of Van Genuchten parameter n obtained from the two models are not the same, as can be seen from Figure 5.5b. The PUA-hemisphere method gives flatter capillary pressure-saturation curves, and thus larger values of n , than the PPM.

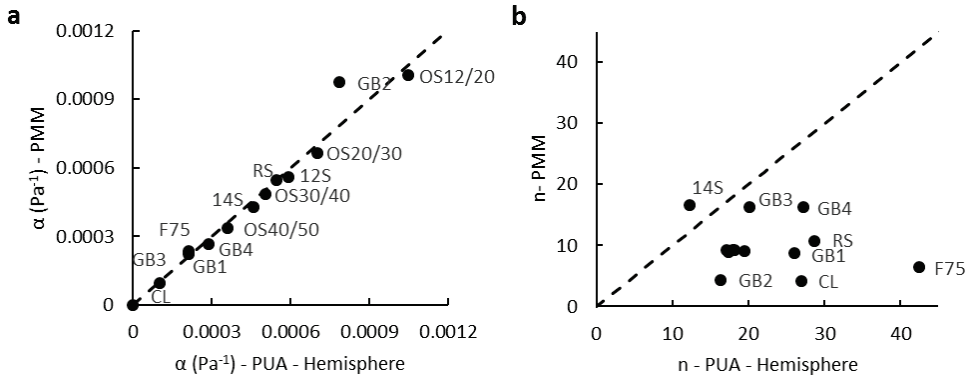


Figure 5.5: Van Genuchten parameter for capillary pressure-saturation curves that were computed using the pore morphology approximation (PMM) and the pore unit assembly method in combination with the hemisphere approximation (PUA-hemisphere). Data is reported for all 12 granular materials. a) α values and b) values of n . The dashed line indicates 1-to-1 ratio.

5.4.3 Hemisphere vs. Mayer and Stowe-Princen approximation

To study the capillary pressure-saturation curves obtained from PUA-hemisphere and PUA-MS-P approximations, we show in Figure 5.6 both curves for 8 granular materials having porosity values between 0.34 and 0.36. The results show that the hemisphere approximation gives an entry pressure that is twice as large as that of the MS-P approximation. To identify the underlying cause of this difference, we study the distributions in R_{ij}^{ins} and R_{ij}^{MS-P} for sand OS12/20, see Figure 5.7. Typically, the radii of curvature for arc menisci, R_{ij}^{MS-P} , are smaller than that of R_{ij}^{ins} (Bico and Quéré, 2002), which is also the case for throats with a triangular cross-section (Mason and Morrow, 1991). This is reflected in Figure 5.7, where MS-P results in an abundance of small values of R_{ij}^{MS-P} ($\pm 44 \mu\text{m}$) that is smaller than the smallest value of R_{ij}^{ins} , where R_{ij}^{ins} has an abundance at $79 \mu\text{m}$. However, both methods have a similar distribution for larger pore throats ($>200 \mu\text{m}$), which is related to the triangulation of packings of spheres. One throat is enclosed by three spheres that do not need to touch necessarily, depending on the force consideration in DEM. Therefore, some pore throats are not perfectly enclosed by solid and thus finding the value of R_{ij}^{MS-P} is not possible as the distance between two spheres may be too large to have R_{ij}^{MS-P} smaller than R_{ij}^{ins} . This occurs in 8.5% of the pore throats, which are typically relatively larger pore throats ($>150 \mu\text{m}$). Therefore, when the difference between air pressure and water pressure just exceeds the entry pressure of a sample, air will invade larger pore throats that have values of R_{ij}^{MS-P} , which are close to that of R_{ij}^{ins} . Therefore, the only difference between the MS-P and hemisphere approximation is the evaluation of entry pressure (using either equation 5.2 or 5.3, respectively), which indeed is a factor of two; this of course is an artefact of simulations rather than a physical phenomenon. Thus, we may conclude that MS-P cannot always be applied for simulations in the Pore Unit Assembly.

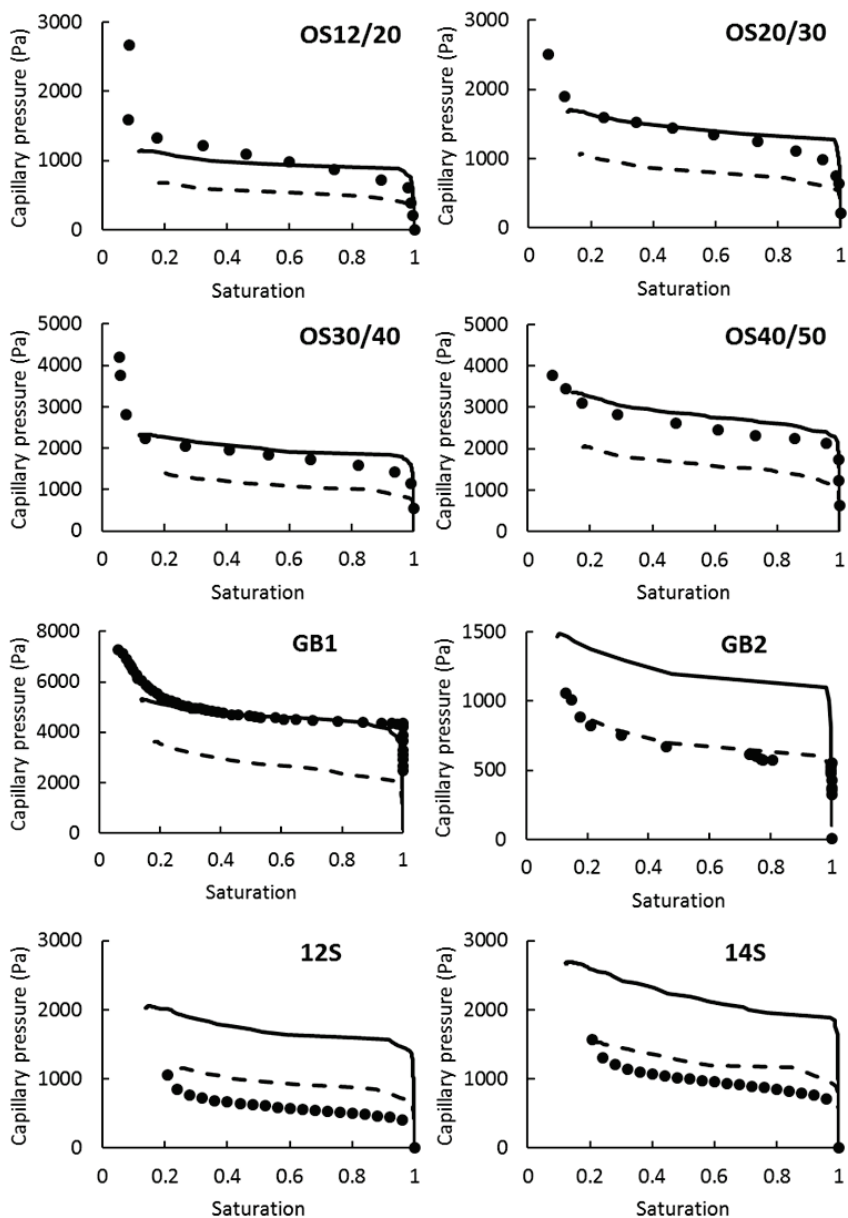


Figure 5.6: Capillary pressure-saturation curves for the granular materials that have a porosity value around 0.35. The dots represent experimental data; the lines represent simulations with PUA-hemisphere method (solid line) and PUA-MS-P method (dashed line). Note that for sands 12S and 14S, dots represent the fitting of Van Genuchten formula from data reported in Table 5.2 and Oostrom et al. (1999).

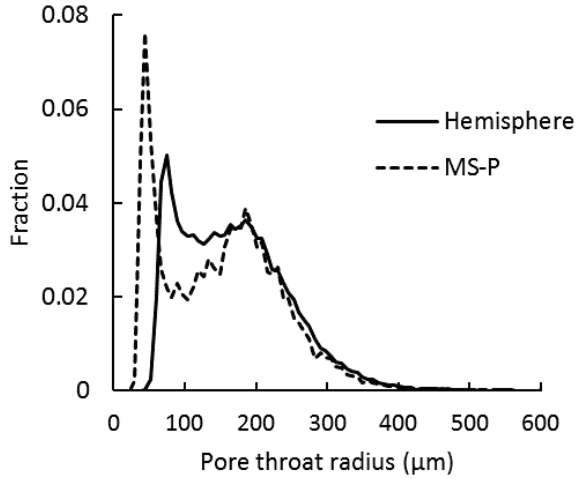


Figure 5.7: Pore throat radii for OS12/20 sand extracted from simulations with PUA-hemisphere (R_{ij}^{ins}) and PUA – MS-P (R_{ij}^{MS-P}) methods.

5.4.4 Comparison of simulated curves and experimental data

Figure 5.6 also shows that the drainage curves of PUA simulations, both the hemisphere approximation and the MS-P approximation, lack the steepening of the curve near residual water saturation, which are present in experimentally measured curves. This is mainly related to model simplifications; the particles are spherical and flow of water along corners is not simulated. Indeed, the pore throat size distribution of packings used in experiments may differ from that in simulations because particles will have a different shape than spheres. Also, corner flow is responsible for additional drainage which is not considered in the simulations and, therefore, the residual water saturation is slightly overestimated by the model.

Results shown in Figure 5.6 indicate that PUA-hemisphere method approximates well the entry pressure of five granular materials (OS12/20; OS20/30; OS30/40; OS40/50; GB1), but gives poor approximations for samples 12S, 14S, and GB2. However, the MS-P approximation reproduces the capillary pressure-saturation curve for glass-bead sample GB2 satisfactory. Glass bead sample GB2 has been previously investigated by Yuan et al. (2016), who have constructed its capillary pressure-saturation curve using PUA-MS-P simulations. Indeed, they also found a good match between experiments and simulations, similar to our results. Moreover, Joekar-Niasar et al. (2010) have also successfully reconstructed the capillary pressure-

saturation curve of GB2 using a pore-network model, based on a pore network that was obtained from X-ray tomography. They also used the MS-P approximation.

Furthermore, Figure 5.8 shows α values of experiments plotted against those obtained from the PUA-hemisphere method, for samples having a porosity value of 0.34 to 0.36. Similar to data in Figure 6, the α values of Ottawa sand samples and the glass bead sample GB1 correspond well to the experimental values. However, there are deviations for three samples, namely: 12S, 14S and GB2. To investigate whether experimental data exhibit the same difference in behaviour for the three samples 12S, 14S and GB2, we have plotted the values of α from experiments against the D50 values from experiments, for all samples with a porosity value between 0.34-0.35 (see Figure 5.9). One would expect a linear correlation between α and D50 (Benson et al., 2014). Indeed, Figure 5.9 shows that all data points fall on a straight line except for the three samples. We believe that the deviation of these samples from the line is not an experimental error.

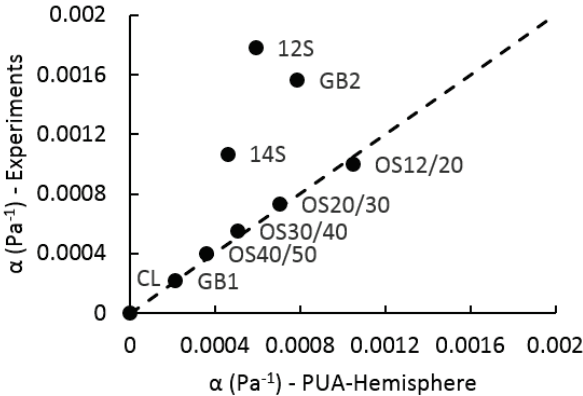


Figure 5.8: Values for Van Genuchten parameter α from experimental data reported in the literature compared to values obtained from simulations using PUA-hemisphere. The dashed line indicates 1-to-1 ratio.

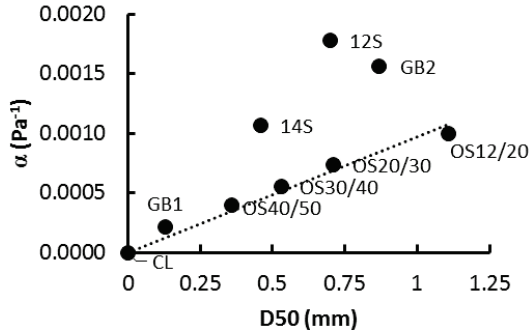


Figure 5.9: The experimentally determined values of α plotted against the D50 values of various particle packings. The dotted line indicates a linear fit ($\alpha = 0.97 \times D50$, with α in Pa and D50 in mm) for all granular materials except for 12S, 14S, and GB2.

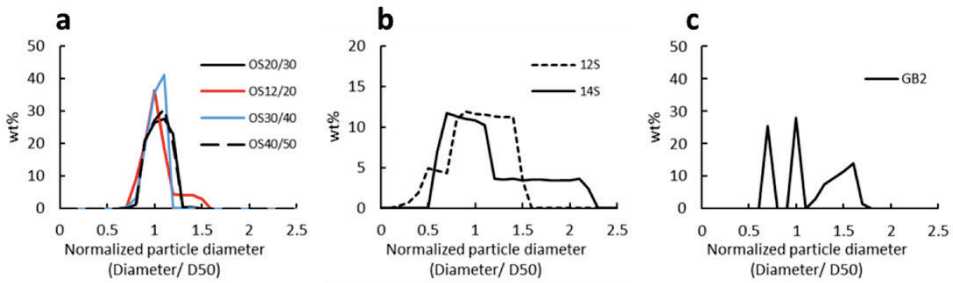


Figure 5.10: The particle size distributions of (a) Ottawa sand samples, (b) sand samples 12S and 14S and (c) glass bead GB2. The particle diameters are normalized to the corresponding D50 values.

The fact that the three samples behave differently in experiments implies that the nature of the granular material could affect the relation between α and D50; of course, the type of particle size distribution is another factor. Figure 5.10a shows the particle size distributions of all Ottawa sands for which the hemisphere approximation works well. These Ottawa sands have a relatively narrow and normal distribution of particle sizes. However, Figure 5.10b shows the wider distributions of samples 12S and 14S for which the MS-P approximation yields better results than the hemisphere approximation. Finally, Figure 5.10c shows the very irregular particle size distributions of sample GB2 for which the MS-P approximation works well. We may postulate that the particle size distribution may affect the shape of pore throats and thus the shape of air-water

interfaces. For example, elongated pore throats may exist in packings that have a wider particle size distributions. In elongated pore throats, the shape of the air-water interface may substantially deviate from that of a hemisphere, such that the MS-P approximation may be more applicable. But, for narrow distributions where the pore throats are thin, the hemisphere approximation seems to be more appropriate.

However, another explanation for the different behaviour of the three samples in our modelling efforts is that the packing of spheres does not represent the real granular material well, leading to a wrongly estimated capillary pressure-saturation curve. But, our results on glass-beads GB1 and GB2, which are best reproduced by the hemisphere approximation and the MS-P approximation, respectively, have been cross-referenced with other simulations and experiments, implying that our simulations are in accordance with other studies. Another explanation is that we have chosen samples that, in hindsight, tend to be better represented by the hemisphere approximation. While, for another set of samples, the hemisphere approximation may not work well; it remains a process of sampling from a large population of granular materials. Therefore, in the scope of this work, it is not possible to identify with certainty why the three samples behave differently from the others.

5.4.5 Application to coating layer of paper

To exemplify the concept of generating a capillary pressure-saturation curve prior to experiments, we evaluate the coating layer of paper, which is a typical example of cases where direct measurements of the capillary pressure-saturation curves are not feasible. Moreover, grains in the coating layer are irregularly shaped (Aslannejad et al., 2017) and thus the representation of the packing by spheres is a strong simplification. The value of α for the coating layer that is reported under experiments in Table 5.2 (last entry) was actually obtained by Aslannejad et al. (2017) from PMM simulations on the real pore geometry of the coating layer, obtained from FIB-SEM measurements. We also determined the value of α , for a packing of spheres with the same particle size distribution, using PMM, PUA-MS-P, PUA-hemisphere methods. We found that the α value was underestimated by the hemisphere approximation while overestimated by PUA-MSP method. The fact that PMM was not capable to reproduce the α value from Aslannejad et al. (2017) is caused by the simple pore geometry used in our results; i.e. that of a packing of spheres. Nevertheless, the value of α from the direct pore geometry is in between the α value by PUA-MS-P and PUA-hemisphere. Of course, the prediction of α values is better for granular materials with more spherical particles (i.e. glass-beads and filter sands) than for irregularly shaped particles.

5.5. Conclusion

In this Chapter, we have constructed capillary pressure-saturation curves for drainage of spherical particle packings using three different models with varying assumptions on the shape of the air-water interface, namely: (i) the Pore Unit Assembly method (PUA) in combination with the Mayer and Stowe – Princen method, (ii) PUA in combination with the hemisphere approximation or (iii) the Pore Morphology Method (PMM) in combination with the hemisphere approximation. We have generated equivalent spherical particle packings for 12 granular materials from the literature and the coating layer of a paper. From each packing, the capillary pressure-saturation curve was constructed using the three methods and the results were compared to experimental data from the literature. Results show that PMM and PUA-hemisphere give similar capillary pressure-saturation curves, albeit that PUA gives flatter curves than PMM. In these simulations, the hemisphere approximation results in an entry pressure value twice that of MS-P. Comparison with experimental data from the literature reveals that for five out of eight samples the hemisphere approximation reproduces capillary pressures well. The five samples have a narrow particle size distribution and show a different relation of experimentally determined α with D50 than the other three samples, which have a relative wide particle size distribution. Therefore, we suggest that the type of particle size distribution affects the type of invasion criterion that should be employed in capillary pressure-saturation computations, in the pore unit assembly method.

The effect of particle shape on porosity values of swelling granular materials: Discrete element method and the multi-sphere approximation

Abstract

In swelling materials, the degree of swelling affects hydraulic parameters, such as porosity, permeability, and retention properties. An example of swelling granular materials is Super Absorbent Polymer (SAP) particles, which can absorb 30 to 40 times their initial weight of saline fluids within a few minutes. Due to their fast swelling rate, measurements of the hydraulic parameters of a bed of SAP particles is complex or not feasible unless a quasi-static approach is employed. An alternative is to artificially construct packings of particles from which hydraulic properties can be derived. To do this, the Discrete Element Method (DEM) is employed in which SAP particle packings are constructed. DEM models are commonly based on packings of spheres. But, SAP particles have very irregular shapes and this affect their hydraulic properties significantly. Therefore, the shapes of particles were represented by sets of overlapping spheres also known as clumps. An algorithm was developed to make realistic clumps that are representative of real SAP particles. An inventory of real shapes was obtained using micro-CT scans of individual SAP particles, which were all converted to clumps. In DEM, particles were randomly generated based on 20 clumps and the particle size distribution of real SAP particles. The particles were then compacted to obtain a packing, from which the porosity values were obtained. These porosity values were close to experimental values and thus we concluded that our simulations of particle shape in DEM does improve the quality of simulations in case of granular materials.

6.1 Introduction

The geometry of pore space inside granular materials is formed by the arrangement of particles, particle sizes, and particle shapes. Consequently, both the properties of particles and the packing of particles determine the hydraulic parameters. For example, the permeability of a packing of particles decreases with decreasing particle size and decreasing porosity value, which indeed is the basis of the Kozeny-Carman equation that relates particle size and porosity to permeability (e.g. Bear, 1972). On top of that the permeability is lower when particles are irregularly shaped than when particles are spherical (Torskaya et al., 2014; Garcia et al., 2009). Moreover, the entry pressure of air to invade a saturated granular material increases with decreasing porosity values or decreasing particle sizes (e.g. Oh and Lu, 2014; Sweijen et al., 2016).

Regarding non-deforming granular materials, the pore geometry and the corresponding hydraulic parameters can be obtained experimentally. Column experiments can be conducted to measure various hydraulic properties while the pore space can be visualized using for example X-ray tomography or micro-CT. However, measuring those properties is difficult or impossible for granular materials that are being deformed over time, unless a quasi-static approach is employed, where deformation is applied in small discrete steps while measuring various properties.

An example of a fast deforming granular material is the swelling of Super Absorbent Polymer (SAP) particles, caused by fluid absorption (Buchholz and Graham, 1998). Fluid absorption occurs typically within a time frame less than 5 minutes (e.g. Kabiri et al., 2003; Esteves, 2011). During this process, SAP particles soften and increase in size (Knaebel et al., 1997). The characterization of a bed of swelling SAP particles is required to enable continuum-scale modelling, as described in Diersch et al. (2010). For example, the following three parameters all change with swelling and thus with time: porosity, permeability, and the capillary pressure-saturation curve. Therefore, experimental characterization may be complex. An alternative is to employ a grain-scale model that can obtain dependencies of hydraulic parameters on the swelling degree, but also on the state-of-stress.

A suitable grain-scale model is the Discrete Element Method (DEM), which can simulate the movement of individual particles in a packing during deformation (Sweijen et al. 2017b). DEM can be used to construct packings of spheres that represent specific granular materials (e.g. Belheine et al., 2009; Chareyre et al., 2012), by matching the particle size distribution and either the porosity or the state-of-stress of that material. The hydraulic properties can be measured independently from DEM simulations, by employing a variety of techniques. For example, the capillary pressure-saturation relationship can be constructed using the Pore Unit Assembly (PUA) method (Mason

and Mellor, 1995; Gladkikh and Bryant, 2005; Yuan et al., 2015; Sweijen et al., 2016; Mahmoodlu et al 2016) or by using the pore morphology method (Hilpert and Miller, 2005; Vogel et al., 2005). The permeability can be found by solving for water pressure using the pore finite volume method (Chareyre et al., 2012) or using direct simulations by solving Stokes equation (e.g. Garcia et al., 2009; Chareyre et al., 2012); the permeability can be computed afterwards using Darcy's law.

For swelling SAP particles, Sweijen et al. (2016) have constructed capillary pressure-saturation curves for various porosity values and degrees of swelling, using packings of spheres generated in DEM. The largest porosity value obtained was approximately 0.43, which corresponds to a loose packing of spheres. However, Mirnyy et al. (2012) found a maximum porosity value for dry SAP particles of 0.90 and Diersch et al. (2011) reported a porosity value of 0.70. These large porosity values are most likely a result of the irregularity in particle shapes.

Therefore, in this research we study whether the inclusion of particle shape in DEM would improve the estimation of porosity of generated packings. Particle shapes are included in DEM using sets of overlapping spheres that act as one particle, which are referred to as clumps (Favier et al., 1999). Other methods exist in DEM to account for particle shape, in context of particle mechanics. For example, Höhner et al. (2014, 2015) employed polyhedra as particles to account for the angularity of particles, in case of rotating drum. Pasha et al. (2016) studied the effect of particle shape on particle flow in a rotary batch seed coater, they found that using spherical particles that have a rolling friction yields similar results to as using clumps. However, the shape of particles is important for determining hydraulic parameters (Torskaya et al., 2014).

Therefore, we generated various packings of clumps that represent packings of real SAP particles. Ideally, the shape of each SAP particle in a packing should be considered, which is not feasible for packings that typically have more than 1000 particles of usually slightly different shapes. Therefore, we constructed a set of 20 clumps in a random fashion, based on shapes of real SAP particles. From 20 SAP particles, a 3-dimensional reconstruction was made using micro-CT, to which clumps were fitted using a newly developed algorithm based on that by Price et al. (2007). The set of clumps was used to construct various packings in DEM for different friction angles and confining stresses and for each packing the porosity was determined. In future work, the hydraulic properties of the packings can be determined, such as permeability, relative permeability and capillary pressure-saturation curves.

The aims of this research are as follows: i) to construct packings of SAP particles in DEM, using clumps; ii) to obtain the relation of porosity as function of the degree of swelling, iii) to study the effect of confining stress and how this can be

parameterized in terms of fitting equations and iv) to compare porosity values of simulations with those of experiments.

6.2 Realization of clumps

Each particle has its own unique shape and surface irregularities. Including all unique particle shapes is not feasible during simulations. Therefore, we have generated a library of 20 particles, in a random fashion, whose shapes are representative for most of the particles. For each particle, a set of overlapping spheres is constructed, to which we refer to as a clump. A clump represents the main shape and features of a class of particles (see Figure 6.1); e.g. cubical, elongated, or plate-like particles. When constructing a packing of SAP particles, shapes are chosen randomly from the library (following a probability distribution if known) and are given a size following the particle size distributions (usually known). In what follows, the methodology of generating a clump library is explained.

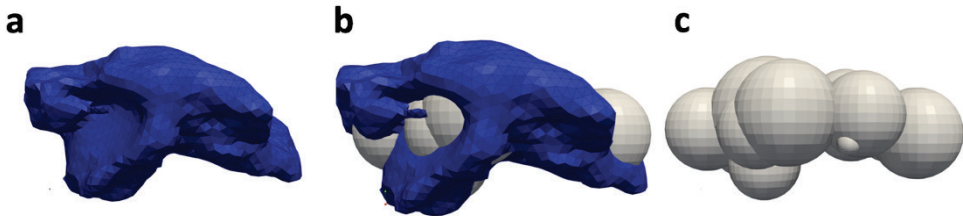


Figure 6.1: Illustration of: a) one SAP particle, b) one SAP particle and its corresponding clump realization, and c) the clump realization

6.2.1 Imaging of individual SAP particles

Individual SAP particles were scanned using a Micro-CT setup. First, SAP particles were put into a small petri-disk in one single layer such that no SAP particle touched another particle. Then, a stack of 2-dimensional images was taken with a $6\ \mu\text{m}$ resolution. The images were post-processed using image analysing software Aviso (FEI, 2016). The images were converted to a 3-dimensional image of the layer of SAP particles from which 20 individual SAP particles were randomly chosen and their shapes were extracted into surface plot files. The surface plots were subsequently used in the algorithm to construct multi-sphere approximations, as described in the following section.

6.2.2 Creating a library of clump shapes

A fitting algorithm was developed based on the work by Price et al. (2007). The aim was to find a set of overlapping spheres whose outer surface would lie as closely as possible on the surface of the particle. For example, an elongated particle should be represented by an elongated set of spheres. However, the details of particle shapes and their small irregularities were not fully reproduced, as this would have required too many spheres per clump; resulting in unfeasibly large computational times for DEM simulations.

The first step of the fitting algorithm was to import the surface mesh of a SAP particle, which was formed by a web of triangles. Next, four vertices on the surface of that particle were selected randomly and a sphere was fitted to pass through those four points. Then, a selection procedure was employed to check whether the fitted sphere was admissible or not.

For the sake of simplicity, we explain the selection procedure in two dimensions, where the shape of a particle is shown as a closed curve (see Figure 6.2), which is a string of points instead of a web of vertices (in three dimensions), and we use circles (instead of spheres) to represent a clump. Thus, circles will be chosen to fill out the particle shape such that their outer edges coincide with the particle boundary as much as possible. From the string of points, we randomly select three points, fit a circle to them, and check whether the circle is admissible.

If the selected points are on an almost straight line, the resulting circle will be much larger than the particle (circle I in Figure 6.2a). To avoid this scenario, we require the radius of a fitted circle to be smaller than the smallest principle axis of the particle. A fitted circle can stick too far out of the particle (circle II in Figure 6.2a); this is quantified in terms of *bulginess*. The bulginess is defined as the distance between a point on the perimeter of a particle, which falls inside a fitted circle, and the nearest point on the boundary of that circle. The maximum allowable bulginess for a fitted circle is defined to be a fraction (α) of the radius of that circle. Obviously, the bulginess can be bigger for larger spheres, which results in a tendency to generate large spheres rather than many small spheres. A circle can also be dismissed if its centre falls outside the particle (circle III in Figure 6.2a). To identify whether a centre of a circle k with coordinates X_k is located inside a particle, the following statement was employed which has to be true for all points on the boundary of a particle:

$$(X_k - X_i) \cdot \hat{\mathbf{n}} < 0 \quad (6.1)$$

with $\hat{\mathbf{n}}$ being the outward pointing normal vector of a surface element and X_i being a point on the boundary. However, to reduce the number of circles (in fact spheres) of a clump for irregular particles, a small fraction (φ) of them are allowed to have their

centres outside of the particle, provided they comply with the maximum allowable bulginess.

Once an admissible circle had been found (similar to circle IV in Figure 6.2a), the points on the surface of the particle that fall within that circle were blocked for further usage. Then, other circles were fitted to the remaining points. Obviously, it is not possible to have all points on the surface of a particle to fall within admissible spheres; many points may still fall outside the spheres (see e.g. Figure 6.2b). We required a pre-specified fraction ϑ of the total number of points to fall within admissible spheres. This completed the generation of a clump of spheres.

However, it is still possible to have the clump to fit the particle more closely. This was done by adjusting the radii of all spheres to have their outer surface as close as possible to the surface of the particle. Thus, we minimized the distance between the surface of the particle and the outer surface of the set of overlapping spheres. The centres of spheres were considered fixed, to avoid areas with a large vertex density (number of vertices per surface area) to have more weight during fitting of a sphere than areas with a low density, for example, to avoid that highly irregular areas have more weight than smooth areas. Vertices i on the surface of the particle that fall within a sphere k were assigned to that sphere. Vertices i on the surface of the particle that did not fall within any sphere, were assigned to the nearest sphere k (see Figure 6.2b). The total number of vertices that were assigned to sphere k was denoted as N_{ik} . The shortest distance between a vertex and its corresponding sphere was defined as d_{ik} . The following sum of residuals (Θ_k) was calculated for each sphere:

$$\Theta_k = \sum_{i=1}^{N_{ik}} d_{ik}^2 \quad (6.2)$$

The optimization algorithm was as follows: 1) for each vertex, the closest sphere was identified; 2) for each sphere, the radius was incrementally increased from 0 to a maximum value while calculating Θ_k ; 3) for each sphere, the lowest value of Θ_k gave the new radius of the sphere; 4) after updating all radii, step 1, 2, and 3 were repeated until $\sum_k \Theta_k$ converged to a minimum value.

One set of values for φ , α , and ϑ was used to generate all clumps. We used the values: $\varphi = 0.025$, $\alpha = 0.05$, and $\vartheta = 0.85$ as those gave the best fit of the volume-to-area ratio of clumps to that of particles, which is evaluated in Appendix F.

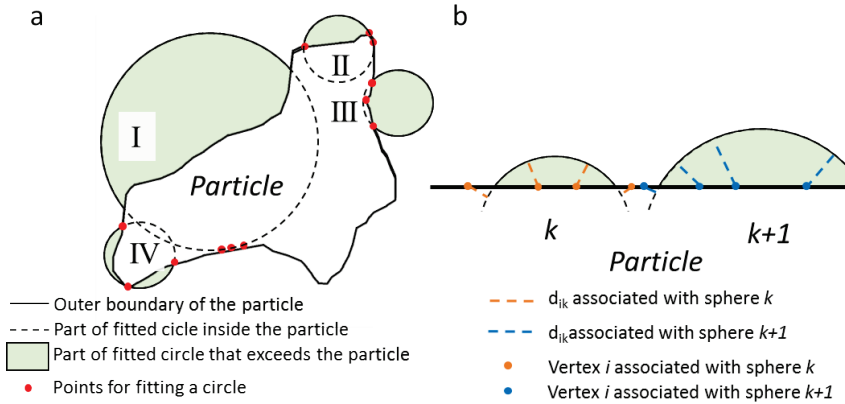


Figure 6.2: Two-dimensional schematic overview of the fitting procedure: a) possible scenarios that may occur during the fitting of a sphere in a particle; I) a circle that is too large, II) a circle with too much bulginess, III) a circle that has its centre outside of the particle, and IV) a circle that is considered a good fit and b) overview of the optimization procedure.

6.3 Numerical methods and experiments

6.3.1 Multi-sphere approximation in the Discrete Element Method

Here, we use open-source software Yade-DEM (Šmilauer et al., 2016) which is a 3-dimensional model based on the discrete element method (DEM), for more information see section 2.2. Here, we use Hertz-Mindlin contact mechanics, which has previously been implemented in Yade-DEM by Modenese et al. (2012).

To include the shape of real SAP particles, we employed the multi-sphere approximation. The advantage of using the multi-sphere approximation is that the sphere-to-sphere contact detection is the same as for spherical particles, which is faster than that of irregularly shaped particles (Favier et al., 1999; Kruggel-Emden et al., 2008). In the multi-sphere approximation, the sub spheres of a clump can have contacts with other clumps giving rise to contact forces acting on the sub spheres. The contact forces and torques are then projected to the centre of mass of the clump. For the centre of mass, the force balance is summed and integrated to find its acceleration. The acceleration is subsequently projected back to the sub spheres of the clump in order to have the relative positions of the sub spheres constant during the movements of the clump. The reader is referred to Šmilauer et al. (2015) for more information on the implementation of clumps in DEM.

6.3.2 Swelling of clumps

Swelling was included by increasing the particle sizes and by softening the particles. In this study, we assume that the shape of particles remains constant while they grow in size due to swelling. This assumption holds for relatively small stresses at the particle contact points, but for non-linear deformation, this assumption will not hold.

First, the degree of swelling is defined in terms of the absorption ratio, Q_i^{abs} (Buchholz and Graham, 1998):

$$Q_i^{abs} = \frac{M_i^w + M_i^s}{M_i^s} \quad (6.3)$$

in which M_i^w is the mass of water inside particle i and M_i^s is the mass of dry SAP in particle i . Based on equation 6.3, we define a volumetric grow factor f_v as:

$$f_v = \frac{V_i^w}{V_i^s} = \frac{\rho_s}{\rho_w} (Q_i^{abs} - 1) \quad (6.4)$$

in which V_i^w and V_i^s are the water and dry SAP volume, respectively, and ρ_w and ρ_s are the water and dry SAP density, respectively. The initial location of spheres in a clump, denoted as a position vector Y_k^0 , was changed according to f_v such that the location of a sphere after swelling (Y_k) is given by:

$$Y_k = (Y_k^0 - Y^0) f_v^{\frac{1}{3}} + Y^0 \quad (6.5)$$

in which Y^0 is the position of the centre of mass of the clump. The radii of all sub spheres were updated by simply applying: $r_k = r_k^0 f_v^{1/3}$, where r_k^0 is the initial radius of a sub sphere. Finally, to include the softening of the SAP particle during water absorption, the following equation was employed (Buchholtz ,1998; Knaebel et al., 1997; Sweijen et al., 2017b):

$$G_i = \frac{\beta}{\sqrt[3]{Q_i^{abs}}} \quad (6.6)$$

in which G_i is the shear modulus of particle i and β is a constant.

6.3.3 Clump insertion into the modelling domain

To generate a dense packing of clumps, first a loose packing was generated by randomly inserting clumps into a large cubic modelling domain of $5 \times 5 \times 5 \text{ cm}^3$. Clumps were inserted into the model domain as follows: i) a clump was randomly chosen from the shape library, ii) it was resized to match a randomly chosen size from the particle size distribution, where the smallest transect of a clump was used as particle size, iii) the

clump was resized and its shear modulus adjusted according to a predefined absorption ratio as described in section 6.3.2, and iv) the clump was randomly rotated and randomly placed in the modelling domain, such that it did not touch any boundary or other clump. The porosity of the cloud of clumps was typically larger than 0.90. For small particle sizes, defined as particle sizes smaller than half of the D50 of the particle size distribution, a sphere was inserted rather than a clump. This was done because small irregularities of small particles were assumed to have no effect on the mechanics of the packings.

To compact the cloud of particles, we applied a confining pressure of 0.3 Psi (2068 Pa) to all boundaries of the modelling domain. All boundaries were periodic. The model was run until force equilibrium was achieved inside the packing.

6.3.4 Parameterization

The mechanical parameters were chosen to resemble those of SAP particles. The shear modulus was set to 7100 Pa at $Q_i^{abs} = 30g/g$; i.e. β was 22.1 kPa, following Knaebel et al. (1997) and in Sweijen et al. (2017b). The Poisson ratio was chosen to be that of incompressible water, namely 0.5. The friction angle was set to that of acrylic acid, namely, 5.5° following Lorenz et al. (1997), but the friction angle was also varied from 0° to that of Labenne sand, namely 35° (Belheine et al., 2009). The particle size distribution was set to that of SAP particles, which were the same batch as measured using the micro-CT setup in section 6.2.1; D50 was set to $460\mu\text{m}$ and a standard deviation to $69\mu\text{m}$.

6.3.5 Experiments on a bed of particles

Experiments were performed on a bed of SAP particles to obtain the porosity as function of the absorption ratio, for a constant confining stress. Two pressures were used, namely: 0.3Psi (2068 Pa) and 0.015Psi (104 Pa). First, a predefined mass of dry SAP particles was put in a column having a diameter of 6 cm. At the bottom of the column, a filter was located that kept the particles in place while allowing water to pass through. At the top of the column, an impermeable weight was placed that corresponds to the predefined confining stress. The weight was able to move up or down freely. Then, the column was put in a container with water, such that water could flow into the particle bed. Then, after 4 hours, the column was taken out of the water and the total mass of the swollen particles and the interstitial water was measured. Then, the excess water was removed gently using a paper towel. This removed all interstitial water and only left swollen SAP particles. The mass was then measured again, which allowed for the determination of the porosity.

6.4 Results and Discussion

6.4.1 Minimum number of particles and shapes

Prior to any other simulations, the minimum number of both clumps and shapes should be determined to have the resulting porosity value independent of both the number of clumps and shapes. Therefore, we generated packings of 4000 dry SAP particles ($Q^{abs} = 1 \text{ g/g}$) for various numbers of shapes, ranging from 1 to 25 (note that 5 extra clump realizations were made based on 5 particles from the measured 20). Once a packing was generated, various porosity values were measured for varying subdomains in a packing. The subdomain was gradually increased from 10% of the dimensions of the modelling domain to 90% of the dimension. The porosity value of the subdomain was plotted as function of the number of particles in that subdomain (see Figure 6.3).

Figure 6.3 shows that increasing the number of particles resulted in the porosity value converging to a constant value, which was typically obtained after 1500 particles. To ensure that the reported porosity values are independent of the number of particles in a simulation, we used approximately 3000 particles to determine the porosity value. By increasing the number of shapes per simulation, the porosity value also converged to a single value for more than 10 shapes. Thus, in all subsequent simulations, 4000 particles and 20 shapes were used.

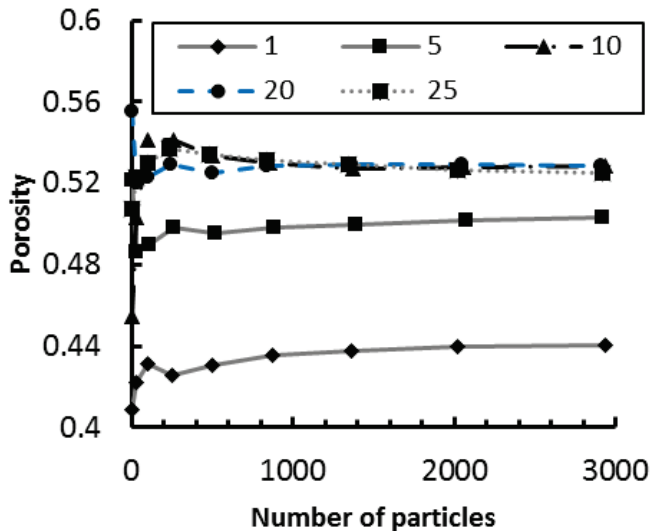


Figure 6.3: Porosity as function of the number of particles for which the porosity is determined. Varying lines correspond to different numbers of shapes used in the simulations. The simulations were conducted for dry SAP particles, having a friction angle of 35° .

6.4.2 The effect of absorption ratio on the porosity value

Using a confining stress of 0.3Psi (2068 Pa), different packings were constructed for various absorption ratios [1-40 g/g]. The conceptual experiment for these simulations was as follows: 1) SAP particles were swollen to a given absorption ratio; 2) the SAP particles were put into a triaxial cell; 3) the particles were compacted using an isotropic compaction; 4) the porosity of the packing was calculated. Using a triaxial compaction on already swollen particles, a simple packing was generated that had no particular loading history (i.e. the degree of anisotropy is minimalized).

Figure 6.4 shows that the porosity value monotonically decreases with increasing absorption ratio, which is caused by a decrease in shear modulus with increasing absorption ratio. This phenomenon was also reported by Mirnyy et al. (2012) and Diersch et al. (2011), who studied the swelling under a constant confining pressure. Figure 6.4 also shows the effect of the friction angle on the porosity - absorption ratio curve. The porosity value decreases with decreasing friction angle, which is a well-known phenomenon in the DEM literature (e.g. Schöpfer et al., 2009). Friction angles smaller than or equal to 5.5° gave results that correspond well with experimental data. In particular, a friction angle of 1° gave a good match. However, porosity values are overestimated when using the friction angle of sand (35°). We therefore conclude that the friction angle for SAP particles should be relatively low ($\leq 5.5^\circ$), which is in the order of magnitude of the friction angle of acrylic acid, 5.5° (Lorenz et al., 1997).

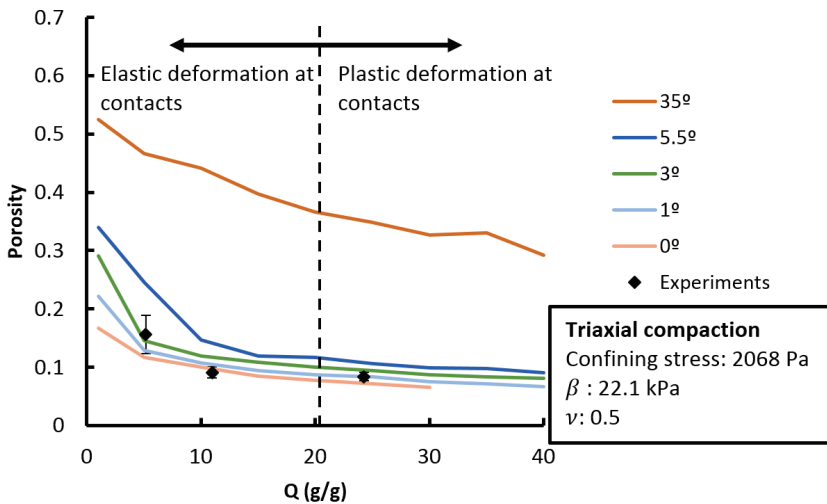


Figure 6.4: Porosity as function of absorption ratio using a 2068 Pa confining pressure, for a variety friction angles. The dashed line indicates the value of Q^{linear} .

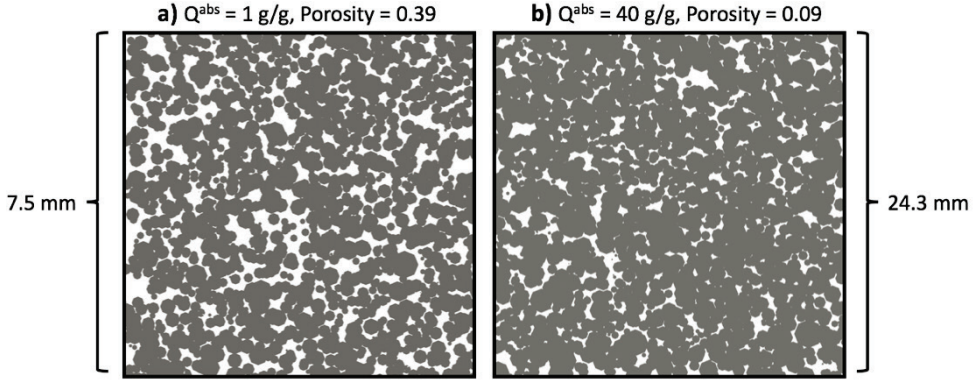


Figure 6.5: Two cross-sections of the clump packings for a) dry SAP particles and b) for swollen SAP particles. Grey denotes the solid phase, while white denotes the pore space.

6.4.3 Mechanical considerations

Swelling and deformation affects the structure of the particle packing, as shown in Figure 6.5. Dry SAP particles, under a loading stress of 0.3Psi, form a relatively loose packing of particles with a porosity of 0.39. In Figure 6.5a, it is clearly visible that high porosity zones exist and that the pores form an open and easily accessible network for water to flow. However, high particle density zones exist for swollen particles (see Figure 6.5b). Pores in Figure 6.5b show less connectivity than the open pore geometry of dry SAP particles, which is a result of more particle-particle connections and larger contact areas in packings of swollen particles. This is required to support the applied load for relatively soft swollen particles.

SAP particles are relatively soft compared to the confining pressure; i.e. the shear moduli of SAP vary between 22kPa to 6.5kPa during swelling, while the confining stress is 2068 Pa. In other words, the shear moduli are 10.6 times and 3.3 times higher than the confining stress, respectively, thus the particles are relatively soft. Therefore, contact mechanics may become non-linear during swelling. Therefore, we compute a threshold value for the absorption ratio (Q^{linear}) above which the contact mechanics is expected to become non-linear. Following Hertzian contact mechanics, the stress-strain ($\sigma - \varepsilon$) relationship at a contact point is given by (Popov, 2014; Johnson, 1987):

$$\sigma = \left(\frac{2}{\pi}\right) \left(\frac{E}{1 - \nu^2}\right) \varepsilon^{\frac{1}{2}} \quad (6.7)$$

where σ is the confining stress, ν the Poisson ratio and E is the Young's modulus, which is related to the shear modulus G by $E = 2G(1 + \nu)$. Using equation 6.6, we can rewrite equation 6.7 to:

$$Q^{linear} = \left(\left(\frac{2}{\pi} \right) \left(\frac{2(1 + \nu)}{1 - \nu^2} \right) \beta \frac{\varepsilon^{\frac{1}{2}}}{\sigma} \right)^3 \quad (6.8)$$

Typically, linear deformation is assumed when the strain is smaller than 1% (i.e. $\varepsilon < 0.01$). Therefore, we evaluate equation 6.8 at $\varepsilon = 0.01$, $\beta = 22.1$ kPa, $\sigma = 2068$ Pa, which results in $Q^{linear} = 20.2$ g/g. For Q^{abs} lower than Q^{linear} the deformation at the contact points is linear (see dashed line in Figure 6.4), where we assume that the stress at contact points does not exceed the mean stress in a packing too much. Thus, for values of Q^{abs} below 20.2 g/g the porosity predictions are reliable whereas for larger values of Q^{abs} the porosity prediction may not be reliable.

6.4.4 Gravity effect in case of small confining pressures

Figure 6.6 shows the porosity as function of absorption ratio for a confining stress σ_0 of 104 Pa (0.015 Psi). In that Figure two types of simulations are presented, namely one where we only use σ_0 and one where we use σ_0 and a correction term for the overburden stress inside a particle bed (σ_c), which is the weight of the overlying particles. For a relatively low confining pressure, the effect of overburden stress should be considered as it becomes a significant contribution to the compaction. The overburden stress is evaluated for a point in the middle of the SAP particle bed such that the final confining stress (σ) becomes:

$$\sigma = \sigma_0 + \frac{1}{2} \rho g h \quad (6.9)$$

Where ρ is the density of swollen SAP particles, which is that of water, and h is the height of the particle bed in experiments which is given by $h(Q_i^{abs}) = 7.1 \times 10^{-4} Q^{abs} [L]$, which is valid for $3 < Q^{abs} < 28$ [$\text{g} \cdot \text{g}^{-1}$]. Figure 6.6 shows that without using the correction term, the model overestimates porosity values from experiments. However, using the correction term results in a closer match in porosity values between simulations and experiments. Albeit that the experimental data point at $Q_i^{abs} = 5$ g/g shows a different behaviour than expected from modelling results and experimental results for 0.3 Psi (Figure 6.4). To understand the meaning of this data point, further investigation is required that goes beyond the scope of this work.

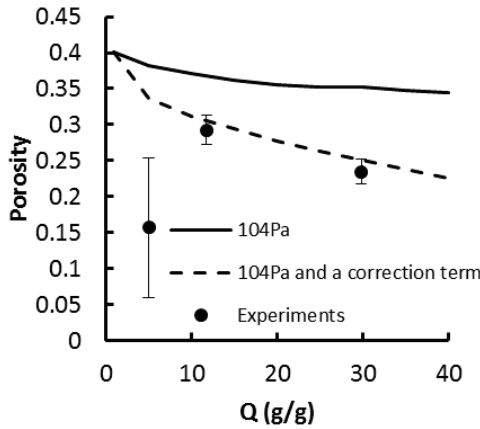


Figure 6.6: Porosity as function of absorption ratio using a 104 Pa, or 0.015 Psi, confining pressure (solid line) and a confining pressure with a correction term for gravity as in equation (dashed line), using a friction angle of 5.5° and $\beta = 22.1\text{kPa}$. Symbols represent experimental data.

6.4.5 Spheres versus Clumps

To test the effect of shape, we have simulated SAP particle packings for varying absorption ratios (1 to 40 g/g) for both clumps and spherical particles, using a friction angle of 5.5° and a confining stress of 0.3 Psi. Figure 6.7 shows the difference in porosity values between spheres and clumps for a confining pressure of 0.3 Psi. The porosity value of clumps, ranging from 0.10 to 0.34, is lower than that of spheres, ranging from 0.21 to 0.34. Thus, usage of clumps can result in lower porosity values than for spheres, which is a result of interlocking of irregularly shaped particles.

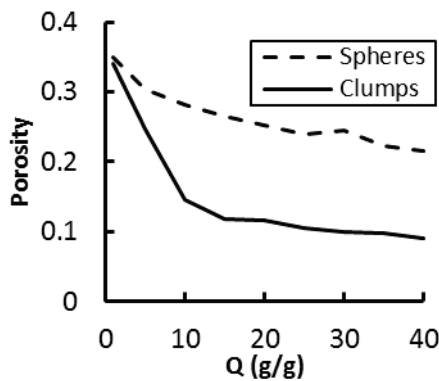


Figure 6.7: The porosity as function of absorption ratio for clumps and spheres, using a friction angle of 5.5° and $\beta = 22.1\text{kPa}$.

6.4.6 Initial porosity

SAP particles in a dry-state, where Q_i^{abs} equals unity, have a much larger shear modulus than particles that are slightly swollen (Anseth et al., 1996). Therefore, the shear modulus predicted by equation 6.6, which is valid for swollen particles, is an underestimation of the shear modulus of dry particles. To investigate the porosity value of particles in a dry-state, we have constructed packings with a shear modulus of 1 MPa and 100 MPa for a variety of friction angles. Figure 6.8 shows the porosity value as function of friction angle, for a 2kPa confining pressure. A shear modulus of 22.1kPa, which is predicted by equation 6.6 and using β of 22.1kPa, results in lower porosity values than when using a shear modulus of 1MPa or higher. A shear modulus of 100MPa results in a porosity value of 0.68 that is almost independent of the friction angle. This is close to the porosity value found in experiments, namely 0.69, which is for dry SAP particles without using a confining stress. The insensitivity of the porosity value on friction angle is caused by the extremely stiff particles, compared to a confining pressure of 2kPa, as well as the presence of particle shape. Thus, these packings have already the loosest arrangement resulting in a maximum value of porosity. For shear moduli 1MPa and 22.1kPa, the porosity value increases with increasing friction angle.

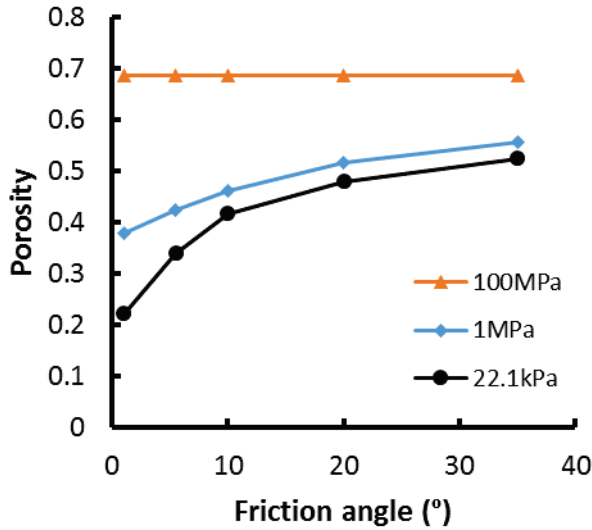


Figure 6.8: Porosity values of SAP particle beds in a dry-state, for three different shear moduli, using a confining stress of 2kPa. The shear moduli of 22.1 kPa is in accordance with equation 6.6 while the shear moduli 1MPa and 100MPa are estimated values for real SAP particles in dry-state.

6.4.7 Relationship of porosity, absorption ratio, and confining stress

To identify the dependency of porosity on both the absorption ratio and confining stress, we have conducted a series of simulations with varying values of Q^{abs} [1-40g/g] and σ [10 – 4000Pa], using a friction angle of 5.5° and equation 6.6 to describe the shear modulus in combination with a value for β of 22.1kPa. Figure 6.9 shows that the porosity decreases as function of absorption ratio, but this decrease becomes more pronounced with increasing confining stress. In the work by Diersch et al. (2010), the following fitting equation was employed to describe the porosity (ϕ) as function of absorption ratio for a constant confining stress:

$$\phi = \frac{2\phi_{max}}{1 + [(Q^{abs} - 1)\phi_{scale} + 1]^{\phi_{exp}}} \quad (6.10)$$

in which ϕ_{scale} and ϕ_{exp} are fitting parameters and ϕ_{max} is the maximum porosity value, which is that of dry SAP particles. Our model results are fitted by equation 6.10 using the following fitting equations:

$$\begin{aligned} \phi_{scale} &= 1 \\ \phi_{max} &= 0.32 \left(\frac{\sigma}{\beta} \right)^{-0.039} \\ \phi_{exp} &= 0.696 \left(1 - e^{-15.28 \frac{\sigma}{\beta}} \right) \end{aligned} \quad (6.11)$$

The fits are shown in Figure 6.9a as solid lines. The quality of fitting was described by a R^2 value of 0.98. However, as discussed in section 6.3.4, SAP have a different modulus when in a dry-state than predicted by equation 6.6. Let us assume that the transition from dry-state to slightly swollen occurs between Q^{abs} of 1 g/g and 5 g/g. If we replace the initial porosity in Figure 6.9a by that of dry SAP particles, namely 0.68, we can obtain fitting parameters for more realistic porosity and absorption ratio curves (see Figure 6.9b):

$$\begin{aligned} \phi_{scale} &= 6.45e^{-6.68 \frac{\sigma}{\beta}} \\ \phi_{max} &= 0.68 \\ \phi_{exp} &= 1.05 \left(\frac{\sigma}{\beta} \right)^{0.27} \end{aligned} \quad (6.12)$$

Using equations 6.12 to fit equation 6.10 to simulated data resulted in a reasonable fit although the fitted curves deviate significantly from their corresponding data. Fitting equations 6.11 and 6.12 can be employed for continuum-scale simulations where the confining stress can vary during simulations. Note, that the parameterization of equations 6.11 and 6.12 may change for various types of SAP particles.

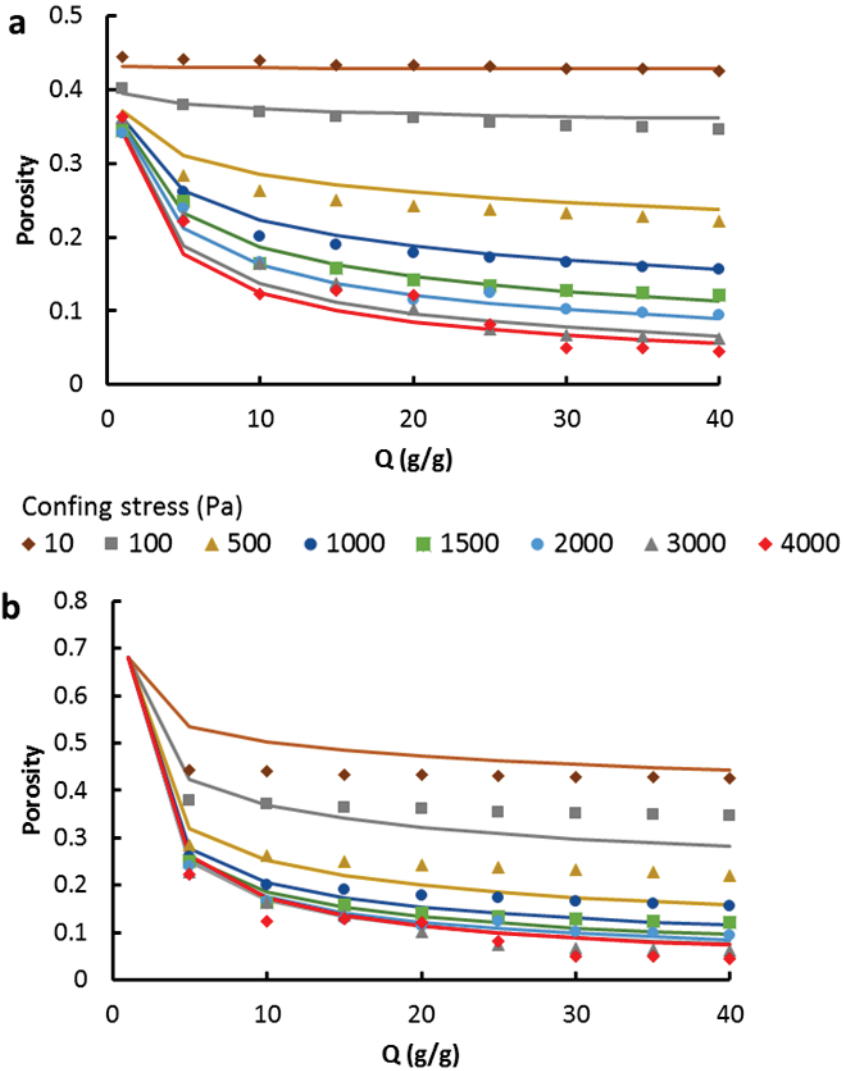


Figure 6.9: Porosity as function of absorption ratio for different confining stresses. Symbols represent data from clump simulations, the solid lines represent the fitting of equation 6.10 and the colours indicate the confining stress, using a) the shear modulus given by equation 6.6 and b) the shear modulus given by equation 6.6 but the initial porosity is set to 0.68. Note that for confining pressures 3000 and 4000 Pa, the porosity values should be considered as a indicative value as contact mechanics are showing non-linear deformation (following equation 6.8) as well as absorption ratio's higher than 20 g/g for confining stress 2068 Pa.

6.5 Conclusions

In this research, the effect of particle shape is investigated on hydraulic properties of packings of Super Absorbent Polymer (SAP). The discrete element method (DEM) is employed as grain-scale model in which particle shape is represented by sets of overlapping spheres, so called clumps or multi sphere approximations. Clumps were constructed based on 3-dimensional reconstructions of real SAP particles that were obtained from micro-CT imaging. Using clumps, particle packings were confined using 0.3Psi (2068 Pa) confining pressure. A variety of packings were generated for varying degree of swelling, friction angle, and confining stresses. The minimum number of particles required for porosity values to be independent on the number of particles was found to be 3000 particles. The minimum number of shapes (i.e. clump realizations) was found to be 10 to 15. This indicates that the variation in particle shapes is a statistical problem, which allows to simplify simulations because only a small number of particles shapes are needed. The porosity versus absorption ratio plots were generated for SAP particles for which we have experimental data. We found a good agreement with experiments if a relatively low friction angle was used ($<5.5^\circ$). A 3-dimensional surface of porosity, absorption ratio, and confining pressure was generated that can be employed as a closure equation in continuum-scale simulations.

Part III

Dynamics of swelling under unsaturated conditions

Dynamic pore-scale modelling of drainage in granular porous media: the pore-unit assembly method

Abstract

In this study, a dynamic pore-scale model was developed to simulate water flow in packings of spheres during dynamic drainage. The packings were generated using the Discrete Element Method (DEM). The pore space inside a packing of spheres was extracted using regular triangulation, resulting in an assembly of grain-based tetrahedra. Then, pore units were constructed by identifying and merging tetrahedra that belong to the same pores, resulting in an assembly of pore units. Each pore unit was approximated by a volume-equivalent regular shape (e.g. cube, octahedron), for which a local capillary pressure-saturation relationship was obtained. We assigned a single value for water pressure and a single value for saturation to each pore unit. To simulate unsaturated flow, a pore-scale version of IMPES (implicit pressure solver and explicit saturation update) was employed that uses the assembly of pore units. To test the model, the quasi-static capillary pressure-saturation curve was reproduced using the dynamic code, which yielded good results. Simulations of dynamic drainage revealed that drainage in packings of spheres occurred by means of finger-like infiltration, caused by heterogeneities in the pore structure. Consequently, dynamic effects occurred at high saturation values and then disappeared once the air reached the water reservoir, which occurred at saturation values of 0.76. Furthermore, we tested the effect of the number of particles and boundary conditions on the dynamic flow behaviour. Finally, a dynamic coefficient was determined and compared to that of experimental data.

Nomenclature

$a_{i,edge}^w$	Area of water in the cross-section of an edge in a regular shape [L ²]
a_i^{aw}	Air-water interfacial area in a pore unit [L ²]
a_{ij}^w	Surface area of water in the cross-section of pore throat ij [L ²]
a_{ij}	Cross-section area pore throat ij [L ²]
k_{ij}^w	Water conductivity of pore throat ij [TL ⁴ M ⁻¹]
K	Macro-scale permeability [L ²]
l	Length [L]
l_{edge}	Length of an edge of a regular shape [L]
l_{ij}	Distance between the centres of pore units i and j [L]
N_{edges}	Number of edges in a regular shape [-]
N_i	Number of pore units connecting to pore unit i [-]
N_i^w	Number of saturated pore units adjacent to pore unit i [-]
N_p	Total number of pore units [-]
q_{ij}^w	Volumetric water flux through pore throat ij [L ³ T ⁻¹]
r_i^c	Radius of curvature of the air-water interface in a pore unit [L]
r_{ij}^h	Hydraulic radius of pore throat ij [L]
r_i^{ins}	Radius of the inscribed sphere of pore unit i [L]
r_{ij}	Pore throat radius [L]
s_i^w	Water saturation in pore unit i [-]
s_i^{air}	Air saturation in pore unit i [-]
$s_i^{w,thr}$	Saturation corresponding to the inscribe sphere of a pore unit [-]
S^w	Macro-scale water saturation [-]
p^{air}	Air pressure [MT ⁻² L ⁻¹]
p_i^w	Water pressure in pore unit i [MT ⁻² L ⁻¹]
p_i^c	Capillary pressure in pore unit i [MT ⁻² L ⁻¹]
p_{ij}^e	Entry pressure of pore throat ij [MT ⁻² L ⁻¹]
P_{global}^c	Pressure difference between air and water reservoir [MT ⁻² L ⁻¹]
$\langle P^w \rangle$	Macro-scale water pressure, volumetric averaged [MT ⁻² L ⁻¹]
$\langle P^c \rangle$	Macro-scale capillary pressure, interfacial area averaged [MT ⁻² L ⁻¹]
V_i	Volume of pore unit i [L ³]
V_i^w	Water volume in pore unit i [L ³]

$V_{i, \text{corners}}^w$	Water volume in corners of a pore unit [L ³]
$V_{i, \text{edges}}^w$	Water volume in edges of a pore unit [L ³]
z	Centroid of averaging domain [L]
γ	Surface tension of water [MT ⁻²]
θ	Dihedral angle of an edge [Rad]
κ	Geometrical parameter of a regular shape [-]
λ	Geometrical parameter of a regular shape [-]
μ	Water viscosity [MT ⁻¹ L ⁻¹]
φ	Maximum ratio of pore throat radius to pore unit radius [-]
χ	Geometrical parameter that relates V_i with r_i^{ins} [-]
τ	Dynamic coefficient [MT ⁻¹ L ⁻¹]
Δt	Time step [T]
Ω_{ij}	Void volume associated with pore throat ij [L ³]
Φ_{ij}	Solid surface area in pore throat ij [L ²]

7.1 Introduction

Capillarity is fundamental to the flow of fluids in porous materials. For example, the rise of water into a hydrophilic porous material is due to capillary action. Capillarity is a key process relevant for many natural and industrial processes, for example: in unsaturated soils (Oh et al., 2014; Nuth et al., 2008; Nikoee et al., 2013; Likos et al., 2013; Hassanizadeh et al., 2002), carbon sequestration, oil & reservoir engineering, but also in water transport in thin porous media such as tissues (e.g. Sun et al., 2015), fuel cells (e.g. Qin et al., 2015), and hygienic products (Diersch et al., 2010).

Capillarity is often described as the relation between capillary pressure and saturation under equilibrium conditions. The capillary pressure-saturation relationship of air and water is often experimentally characterized where experiments may take hours to weeks. However, in many applications, flow of water may occur in much shorter time scales. For example, during dynamic drainage experiments by Camps-Roach et al. (2010) on a 20-cm long column, it took just 30 minutes for the majority of drainage to occur. Moreover, imbibition of ink in paper occurs even faster, within a second (Kettle et al., 2010). Such fast drainage and imbibition processes give rise to the concept of dynamic capillarity effect. Under fast transient drainage or imbibition, the difference in fluid pressures is not equal to the capillary pressure anymore. Many examples exist in the soil sciences and two-phase flow literature that describe the dynamic capillarity effect (see e.g. Topp et al. 1967; Bottero et al., 2011; DiCarlo et al., 2005). For comprehensive reviews of dynamic capillarity effects, see Hassanizadeh et al. (2002) and Diamantopoulos and Durner (2012).

Here, we would like to highlight a theory based on thermodynamic considerations, by Hassanizadeh and Gray (1993), who have derived the following dynamic capillarity relationship:

$$P^{air} - P^w = P^c(S) - \tau \frac{\partial S}{\partial t} \quad (7.1)$$

where P^{air} and P^w denote the macroscopic pressure of air and water, respectively, $P^c(S)$ denotes the capillary pressure, τ is a positive dynamic coefficient, and $\frac{\partial S}{\partial t}$ is the rate of change of saturation with time. Experiments have been conducted to explore equation 7.1 and to determine the value of τ (e.g. Zhuang et al., 2017; Bottero et al., 2011; Camps-Roach et al., 2010). It has been shown that for transient drainage, at any given saturation, $P^{air} - P^w$ is larger than P^c ; the larger the imposed pressure difference, the more negative $\frac{\partial S}{\partial t}$ and thus the larger the dynamic effect (e.g. Camps-Roach et al., 2010; Bottero et al., 2011). During dynamic imbibition, $P^{air} - P^w$ is smaller than P^c (see e.g. Bottero et al., 2006). O'Carroll et al. (2005) conducted Multi-

Step-Outflow (MSO) experiments on PCE and water, to investigate the effect of dynamic capillarity. In MSO, parameters are estimated by inverse modelling of experimental data. They found that the goodness of the fit of inverse modelling of the experiments improved significantly when the dynamic effect was included.

The dynamic capillarity effect has also been studied using pore-scale models. Pore-scale models can be divided in to two types, namely: i) models that discretize the pore space into pore bodies and pore throats, such as pore-network models (Thompson, 2010; Joekar-Niasar et al. 2010; Qin, 2015) and pore-unit assembly models (Mellor and Mason, 1995) and ii) models that employ direct simulations of flow within the pore geometry, such as Lattice-Boltzman (Vogel et al., 2005), smooth particle hydrodynamics (e.g. Kunz et al., 2016), and volume of fluid models. Direct simulations of two-phase flow are typically applied to a small number of pores, while pore-network and pore-unit assembly models can handle a very large number of pores. On the other hand, pore-network and pore-unit assembly models employ very simplified pore geometries and flow equations. Pore-network models have been mainly employed to study the effect of various parameters on two-phase flow. For example, Mogensen and Stenby (1998) developed a single-pressure algorithm to simulate dynamic imbibition. They studied the effects of contact angle and capillary number on the residual oil saturation after a water flooding event. Thompson (2002) developed a pore-network model for dynamic imbibition, to study water movement in fibrous porous materials. Joekar-Niasar et al. (2010) developed a complex pore-network model of two-phase flow based on a two-pressure algorithm. They included corner flow, capillary pressure in a pore body, snap-off, and flow dynamics of two viscous fluids. To evaluate their model, they conducted simulations on a 3-dimensional lattice of cubic pore bodies, with a coordination number of six (i.e. each pore body was connected to six other pore bodies). For such a cubic pore body, the local capillary pressure – saturation curve was analytically derived. The model has been used to study the effect of various parameters, such as viscosity ratio and capillary number, on the dynamic capillarity effect (Joekar-Niasar and Hassanizadeh, 2011).

Dynamics of flow often concurs with deformations of the solid phase, for example: deformation of soils due to a change in water saturation (Kharaghani et al., 2011; Lins and Schanz, 2005), ink penetration in paper, drying of foods, and swelling of materials, such as fluid absorption in super absorbent polymer particle beds in hygienic products (Diersch et al., 2010). However, in common pore network models, the pore geometry is assumed to be rigid.

An appropriate pore-scale model that can include deformation and flow is the coupling of pore-unit assembly method (PUA) with the Discrete Element Method (DEM). DEM is a particle-based model that is capable of simulating particle-particle

interactions during deformation of a granular material (Cundall and Strack, 1979). In the PUA method, the pore geometry of spherical particle packings can be extracted using a regular triangulation; four neighbouring particles form the vertices of a tetrahedron, which encloses a so-called pore unit. PUA has been applied on Finney packings to construct imbibition curves for varying contact angles (Gladkikh and Bryant, 2005).

More recently, PUA has been coupled to the Discrete Element Method (DEM) to enable simulation of hydro-mechanical coupling in saturated granular materials (Chareyre et al., 2012; Catalano et al., 2014). PUA in combination with DEM has also been used to construct equilibrium capillary pressure-saturation curves for packing of spheres. The size distribution of spheres and the porosity of the packing were matched to those of a granular material and subsequently the equilibrium capillary pressure-saturation curve was constructed; see for example Yuan et al. (2015), Sweijen et al. (2016), Sweijen et al. (2017a), Mahmoodlu et al. (2016).

Based on the coupling of PUA with DEM, we introduce in this work a pore-scale model for unsaturated flow to simulate dynamic drainage in a non-deforming packing of spheres. An algorithm was developed to simplify the complex pore geometry of pore units by fitting regular shapes into pore units. Dynamic drainage is simulated in packings of spheres by employing a single pressure algorithm to solve for water pressure, based on a finite difference scheme. Air is assumed to be at a constant and uniform pressure. We refer to this algorithm as a pore-scale version of IMPES (implicit pressure solver and explicit saturation update).

The aim of this research is to: i) develop a pore-scale model that captures the main geometrical information from packings of spheres; ii) to develop a dynamic pore-scale model to simulate unsaturated flow during dynamic drainage; iii) to test and verify the model by reproducing the quasi-static capillary pressure-saturation curve using the pore-scale version of IMPES and iv) to investigate dynamic effects in packings of spheres, by means of studying the effect of boundary conditions on dynamic drainage and by comparing the dynamic coefficient τ in simulations to that of experiments.

The outline of this study is as follows. First, we explain the algorithm to fit regular shapes into pore units. Then, we present the single pressure solver and the local rules for unsaturated flow. Finally, the model is tested by simulating dynamic drainage experiments.

7.2 Numerical model

Packings of spheres are generated for specific porosity values and particle sizes using the Discrete Element Method (DEM), see for more information Chapter 4 (section 4.3.2). Then, the pore structure is extracted using triangulation, resulting in an assembly of tetrahedra. Afterwards, the pore space is simplified by replacing the pore geometry inside each tetrahedron by that of a regular shape, which is often referred to as a platonic solid (e.g. tetrahedron, cube, octahedron). Finally, we obtain a pore-unit assembly. In the following sections, we explain the methodology of generating an assembly of regular shapes.

7.2.1 Representing pore units by regular shapes

The pore-unit assembly (PUA) method is employed to extract the pore space from the spherical particle packing. The extraction of the pore-unit assembly relies on regular triangulation of the packing of spheres to subdivide the pore space into *grain-based tetrahedra* (see Figure 7.1a). Each grain-based tetrahedron is enclosed by four spheres, where the vertices of the tetrahedron are located at the centres of spheres. One tetrahedron is connected to four other tetrahedra such that the pore space of the packing is subdivided into an *assembly of grain-based tetrahedra*. The facet of a grain-based tetrahedron is located at the narrowest opening between two neighbouring tetrahedra, and therefore represents a zero-volume pore throat that offers resistance to flow (see Figure 7.1a). In this research, we employ the implementation of triangulation in DEM by Chareyre et al. (2012).

The pore space inside a grain-based tetrahedron has a complex shape that is different for each grain-based tetrahedron. To enable unsaturated flow simulations, the pore space inside each grain-based tetrahedron is simplified by representing it by a *pore-based tetrahedron*, which is placed with its vertices into the pore throats and which has a volume equal to the pore volume of a grain-based tetrahedron (see Figure 7.1b). The size of a pore throat is characterized by radius r_{ij} of the inscribed circle between three particles that make-up a facet of a grain-based tetrahedron. While, the size of the pore space is described by radius r_i of the inscribed sphere inside the pore-based tetrahedron (see Figure 7.1b).

In some cases, the pore throat radius r_{ij} of pore throat ij can be larger than the radius r_i and/or r_j of the inscribed sphere of pore-based tetrahedra i and j (following Sweijen et al., 2016). Per definition, the pore throat size should be smaller than the pore size. However, this is not the case for larger pores that contain two or more grain-based tetrahedra. This happens in the case of pore units that are surrounded by more than 4

spheres. To alleviate this issue, we apply a merging algorithm with the aim of identifying grain-based tetrahedra that belong to the same pore unit.

When two grain-based tetrahedra are merged, another regular shape is chosen to represent the pore space inside the merged tetrahedra such that the vertices of a regular shape are fitted into the pore throats, see for example Figure 7.1c. Each regular shape represents a pore unit and has a void volume V_i and N_i adjacent pore throats. For example, a set of merged grain-based tetrahedra that has 6 adjacent pore throats is represented by an octahedron, which has 6 vertices. Here, we do not consider the exact relative location of those pore throats within the pore unit, but we merely assume them to match the location of pore throats (i.e. vertices) of a regular shape.

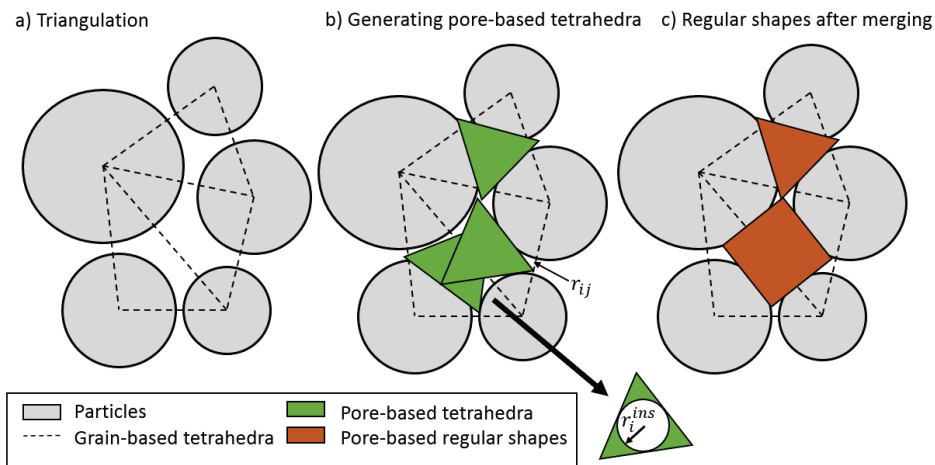


Figure 7.1: Two-dimensional illustration of the algorithm to find regular shapes to represent pore units: a) grain-based tetrahedra from triangulation, b) pore-based tetrahedra having the same volume as the void space inside the grain-based tetrahedra, note the indication of r_i^{ins} and r_{ij} and c) regular shapes that were found after merging of pore-based tetrahedra.

7.2.2 Merging algorithm

The aim of the merging algorithm is to identify grain-based tetrahedra that belong to the same pore unit, while considering the regular shape that is chosen to represent the merged grain-based tetrahedra. Initially, we replace the pore space of each grain-based tetrahedron by a pore-based tetrahedron, having 4 vertices (Figure 7.1b). To check whether the pore throats are smaller than the radius of pore-based tetrahedra, we

compute the radius of inscribed sphere of each pore-based tetrahedron. The radius of the inscribed sphere (r_i^{ins}) of a pore-based tetrahedron (in fact any regular shape) is given by:

$$r_i^{ins} = \chi \cdot \sqrt[3]{V_i} \quad (7.2)$$

in which χ is a dimensionless shape factor, whose value is different for different regular shapes, and V_i is the volume of the regular shape (and thus of the pore unit). Values of χ are given in Table 7.1. When the following criteria are not satisfied, we merge pore units i and j :

$$\begin{cases} \frac{r_{ij}}{r_i^{ins}} < \varphi \\ \frac{r_{ij}}{r_j^{ins}} < \varphi \end{cases} \quad (7.3)$$

where φ is a user-defined parameter less than unity, which determines the strictness of merging. In this research φ was set to 0.90. The method of merging grain-based tetrahedra is similar to the work by Bakke and Øren (1997), who used an imaging method (i.e. thinning) to draw Voronoi polyhedra around grains, from which the vertices were combined until the inscribed sphere with its centre on a vertex was always bigger than a pore throat.

The merging procedure starts with a pore-based tetrahedron that has the largest value of $\frac{r_{ij}}{r_i^{ins}}$; it will be merged to its neighbouring pore-based tetrahedron. After merging, a new regular shape is fitted into the merged tetrahedra, V_i and r_i^{ins} are subsequently updated. Then, a pore unit with the next largest value of $\frac{r_{ij}}{r_i^{ins}}$ is merged to its neighbour; this is repeated until conditions in equation 7.3 are satisfied for all pore units and throats. To avoid long chains of merged pore units, the maximum coordination number is set to 20, as otherwise pore units with very large coordination numbers may arise. Finally, a small number of unresolved pore throats remain (typically <1% of the pore throats). For those, we change their r_{ij} to $\varphi \min(r_i^{ins}, r_j^{ins})$. Finally, we ensure that only one pore throat exists between two pore units, as it may occur that more throats exist. If more throats exist, the throats are combined to one throat by taking an arithmetic average of pore throat properties (e.g. pore throat radii). The final set of merged tetrahedra is referred to as an *assembly of pore units*.

Benchmark testing revealed that our merging algorithm works well. For example, we generated different packings for which we knew in advance how the pore structure should be. First, a packing of spheres was generated having tetrahedral pore units (i.e. pore units have a coordination number of four). Secondly, a packing of

particles was generated having octahedral pore units (i.e. pore units have a coordination number of eight), see Figure 7.2a. Finally, spheres were put in a triangular prism (i.e. pore units have a coordination number of 5), see Figure 7.2b. In Appendix G, we compared the pore structure of a packing of spheres that was extracted by our merging algorithm to those obtained by other techniques.

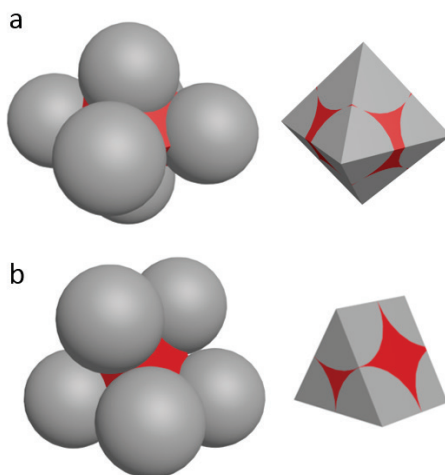


Figure 7.2: Three dimensional illustrations of packings of spheres from which the pore space is represented by a regular shape that is known prior to applying our merging algorithm: a) octahedral assembly of spheres that has a coordination number of 8, hence it will be fitted with a hexahedron and b) a triangular prism assembly of spheres, whose pore unit has a coordination number of 5.

Table 7.1: Geometrical constants for various regular shapes

		Tetrahedron	Octahedron	Cube	Octahedron + Cube	Icosahedron	Dodecahedron
N_i	Eq.	4	6	8	10	12	20
χ	7.2	$(8\sqrt{3})^{-1/3}$	$(4\sqrt{3})^{-1/3}$	$\frac{1}{2}$	$(8\left[1+\frac{\sqrt{2}}{3}\right])^{-1/3}$	$\frac{\sqrt{3}(3+\sqrt{5})}{12\left[\frac{5}{12}(3+\sqrt{5})\right]^{1/3}}$	$\left(\frac{4}{15+7\sqrt{5}}\right)^{1/3}\frac{\sqrt{250+110\sqrt{5}}}{20}$
$S_i^{w,thr}$	7.12	$1-\frac{\pi}{6\sqrt{3}}$	$1-\frac{\pi}{3\sqrt{3}}$	$1-\frac{\pi}{6}$	$1-\frac{\pi}{6\left(1+\frac{\sqrt{2}}{3}\right)}$	$1-\frac{\pi\sqrt{3}}{180}(3+\sqrt{5})^2$	$1-\frac{\pi(250+110\sqrt{5})^{\frac{3}{2}}}{1500(15+7\sqrt{5})}$
λ	7.16	$\sqrt[3]{6\sqrt{2}}$	$\sqrt[3]{\frac{6}{\sqrt{2}}}$	1	$\left(\frac{\sqrt{2}}{3}+\frac{1}{6\sqrt{2}}\right)^{-1/3}$	$\sqrt[3]{\frac{12}{5(3+\sqrt{5})}}$	$\sqrt[3]{\frac{4}{15+7\sqrt{5}}}$
θ	-	$\tan^{-1}(2\sqrt{2})$	$\cos^{-1}\left(-\frac{1}{3}\right)$	$\frac{1}{2}\pi$	$\frac{1}{2}\pi$ and $\cos^{-1}\left(-\frac{1}{3}\right)^{+1}$	$\cos^{-1}\left(-\frac{1}{3}\sqrt{5}\right)$	$\cos^{-1}\left(-\frac{1}{5}\sqrt{5}\right)$
N_{edges}	-	6	12	12	20	30	30
c_1	7.19	8.29	2.52	2.52	6.53	6.09	0.394
c_2	7.19	1.41	0.353	0.644	0.462	0.0989	0.245
κ	7.20	3.87	8.71	6.83	5.15	24.11	22.87

7.2.3 Pore-scale version of IMPES

To simulate flow of water in a pore-unit assembly, we employ a pore-scale algorithm of a finite difference scheme to solve implicitly for pressure and explicitly for saturation, which is often referred to as IMPES (see e.g. Chen et al., 2004; Huber and Helmig, 1999). Pressure is only solved for water, because air is assumed to be infinitely mobile compared to water and thus its pressure is assumed to be constant at p^{air} . Let us consider a pore unit i having a water saturation s_i^w , water pressure p_i^w and air saturation s_i^{air} . Per definition, we have:

$$s_i^{air} + s_i^w = 1 \quad (7.4)$$

In pore unit i , a local capillary pressure p_i^c is defined as follows:

$$p_i^c = p^{air} - p_i^w \quad (7.5)$$

The volumetric flux of water through pore throat ij (q_{ij}^w) is assumed to be linearly proportional to the pressure gradient, following e.g. Joekar-Niasar et al. (2010):

$$q_{ij}^w = k_{ij}^w (p_i^w - p_j^w) \quad (7.6)$$

in which k_{ij}^w is a pore throat conductivity. For saturated pore units, a volume balance is written as follows:

$$\sum_{j=1}^{N_i} q_{ij}^w = 0 \quad (7.7)$$

which yields the following equation, using equation 7.6:

$$\sum_{j=1}^{N_i} k_{ij}^w (p_i^w - p_j^w) = 0 \quad (7.8)$$

For partially saturated pore units, a different set of equations is employed for computing the water pressure. In what follows, we consider the air pressure p^{air} as reference pressure and sets its value to zero such that equation 7.5 reduces to $p_i^c = -p_i^w$. For partially-saturated pore units, the volume balance is given by:

$$\sum_{j=1}^{N_i} k_{ij}^w (p_i^w - p_j^w) = -V_i \frac{ds_i^w}{dt} \quad (7.9)$$

Equations 7.8 and 7.9 are can be written into a discretized form (see Appendix H) as:

$$a(p_i^w)^{t+\Delta t} - \sum_{j=0}^{N_i} b(p_j^w)^{t+\Delta t} = c \quad (7.10)$$

where coefficients a , b and c are defined in Table 7.2. Equation 7.10 form a linear set of equations that is solved for water pressure, using implicit solver Sparse supernodal LU factorization in Eigen libraries (Eigen, 2017). Once the water pressure is solved, the saturation is updated explicitly following:

$$(s_i^w)^{t+\Delta t} = (s_i^w)^t - \frac{\Delta t}{V_i} \sum_{j=1}^{N_i} k_{ij}^w \left((p_i^w)^{t+\Delta t} - (p_j^w)^{t+\Delta t} \right) \quad (7.11)$$

Table 7.2: Parameters to solve the linear system in equation 7.10.

	Name	a	b	c
$s_i^w = 1$	Saturated	$\sum_{j=1}^{N_i} k_{ij}^w$	k_{ij}^w	0
$0 < s_i^w < 1$	Partially saturated	$\left(\sum_{j=0}^{N_i} k_{ij}^w + \frac{V_i}{\Delta t} \frac{\partial s_i^w}{\partial p_i^w} \right)$	k_{ij}^w	$\frac{V_i}{\Delta t} \frac{\partial s_i^w}{\partial p_i^w} p_i^t$

7.2.4 Local capillary pressure saturation curve

A set of equations is derived to describe the local capillary pressure-saturation relationship for partially saturated pore units. See Appendix I for detailed and illustrated information. We define a threshold saturation, $s_i^{w,thr}$, for pore unit i that corresponds to a saturation at which air fills the inscribed sphere of the pore unit (Thompson, 2002; Joekar-Niasar et al., 2010):

$$s_i^{w,thr} = 1 - \frac{4}{3} \pi \chi^3 \quad (7.12)$$

When the saturation in a pore unit is smaller than $s_i^{w,thr}$, water resides in corners and edges of a pore unit. Thus, following the work by Joekar-Niasar et al. (2010), we can write:

$$V_i^w = V_{i,cornerRadius}^w + V_{i,edges}^w \quad (7.13)$$

where $V_{i,cornerRadius}^w$ and $V_{i,edges}^w$ is the volume of water residing in corners and edges, respectively. The volume of water in the corners can be computed, using equation 7.2:

$$V_{i, \text{corners}}^w = (r_i^c)^3 \left(\frac{1}{\chi^3} - \frac{4}{3} \pi \right) \quad (7.14)$$

where r_i^c is the radius of curvature of the air-water interface, which is given by Young's Laplace equation $r_i^c = \frac{2\gamma}{p_i^c}$, with γ being the interfacial tension of air-water ($0.072 \text{ N}\cdot\text{m}^{-1}$).

The volume of water along the edges is determined as follows. Consider an edge that has a dihedral angle θ . In the plane that is perpendicular to the length of an edge, the area occupied by water is given by, following Joekar-Niasar et al. (2010):

$$a_{i, \text{edge}}^w = \frac{1}{4} (r_i^c)^2 \left(\frac{1}{\tan\left(\frac{1}{2}\theta\right)} - \frac{\pi - \theta}{2} \right) \quad (7.15)$$

Note that the radius of curvature in an edge is given by $\frac{\gamma}{p_i^c} = \frac{1}{2} r_i^c$, because the second principal curvature is assumed to be flat. The length of the edges inside a regular shape is given by:

$$l_{\text{edge}} = \lambda \cdot \sqrt[3]{V_i} - 2r_i^c \quad (7.16)$$

where λ is a geometrical parameter that determines the length of one edge as a function of the volume of a regular shape (see Table 7.1 for its values). We substitute equations 7.15 and 7.16 into $V_{i, \text{edges}}^w = N_{\text{edges}} \cdot a_{i, \text{edge}}^w \cdot l_{\text{edge}}$, where N_{edges} is the number of edges in the regular shape. The total water volume in a pore unit, V_i^w , is given by:

$$V_i^w = (r_i^c)^3 \left(\frac{1}{\chi^3} - \frac{4}{3} \pi \right) + \frac{1}{4} (r_i^c)^2 N_{\text{edges}} (\lambda \cdot \sqrt[3]{V_i} - 2r_i^c) \left(\frac{1}{\tan\left(\frac{1}{2}\theta\right)} - \frac{\pi - \theta}{2} \right) \quad (7.17)$$

Thus, water saturation inside pore unit i can be written as:

$$s_i^w = \frac{V_i^w}{V_i} = \frac{c_1 \left(\frac{2\gamma}{p_i^c} \right)^3 + c_2 \sqrt[3]{V_i} \left(\frac{2\gamma}{p_i^c} \right)^2}{V_i} \quad (7.18)$$

where c_1 and c_2 are geometrical parameters defined by:

$$c_1 = \left[\left(\frac{1}{\chi^3} - \frac{4\pi}{3} \right) - \frac{N_{\text{edges}}}{2} \left(\frac{1}{\tan\frac{\theta}{2}} - \frac{\pi - \theta}{2} \right) \right] \quad (7.19)$$

$$c_2 = \lambda \frac{N_{\text{edges}}}{4} \left(\frac{1}{\tan\frac{\theta}{2}} - \frac{\pi - \theta}{2} \right)$$

Equations 7.18 and 7.19 are fitted by the following equation, following Joekar-Niasar et al. (2010):

$$p_i^c = \frac{2\gamma}{\chi^3 \sqrt{V_i} (1 - e^{-\kappa \delta_i^w})} \quad (7.20)$$

where κ is a geometrical constant; for more information about the fitting of equation 7.20, see Appendix J.

7.2.5 Geometrical parameters for a range of coordination numbers

The pore space does not only contain pore units that can be fitted with regular shapes, but also with irregular shapes that have other coordination numbers than regular shapes. To overcome this problem, we fit an equation to relevant geometrical properties, namely: κ , χ , and λ , as a function of N_i ; see Figure 7.3. When we can replace a pore unit by a regular shape, we will use the values of κ , χ and λ that are derived directly for that regular shape, otherwise we will use fitting equations to find values for those parameters. The fitted equations should yield values that correspond to a sphere for N_i converging to infinity. This was checked and all equations given in Table 7.3 satisfy this test.

Table 7.3: Fitted equations for geometrical parameters of regular shapes, which are used to estimate geometrical parameters of irregular shapes. The value of N_i should satisfy $3 \leq N_i < \infty$.

Parameter	Fitting equation
κ	$1.32N_i$
λ	$7.12(N_i)^{-0.89}$
χ	$\sqrt[3]{\frac{3}{4\pi}} (1 - e^{-0.170N_i})$

7.2.6 Local drainage

The entry pressure of pore throat ij , p_{ij}^e , defines the air-water pressure difference at which air can invade a water-saturated pore unit. To estimate the entry pressure, we assume that the air-water interface has the shape of a hemisphere. This method estimates the entry pressure values reasonably well for capillary pressure-saturation curves of filter sands using DEM and PUA (Sweijen et al., 2017a). The entry pressure is given by the Young's Laplace equation, assuming a perfectly water wet solid-phase:

$$p_{ij}^e = \frac{2\gamma}{r_{ij}} \quad (7.21)$$

During drainage, air can only invade from pore unit i to its neighboring pore unit j if:

$$p^{air} - p_j^w > p_{ij}^e \quad (7.22)$$

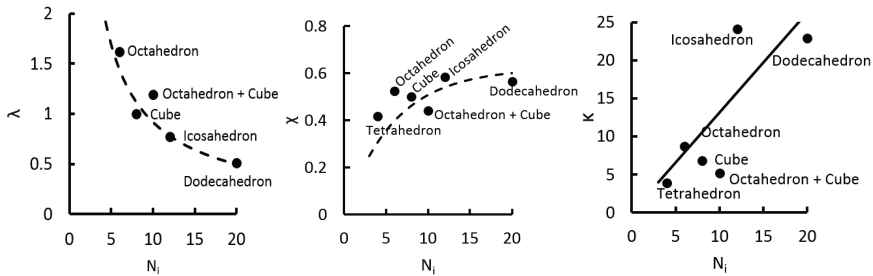


Figure 7.3: Pore-scale parameters needed for the local capillary pressure-saturation relationship for partially saturated pore units. Symbols indicate the values for various regular shapes, given in Table 7.1, and the dashed lines indicate the fitting by equations given in Table 7.3.

7.2.7 Air-water interfacial area

The air-water interfacial area within a pore unit (a_i^{aw}) is determined as follows. For pore units with $1 > s_i^w \geq s_i^{w,thr}$, the shape of the air-water interface is unknown. Therefore, we assume it to be equal to that of a sphere having the same volume as air, following Joekar-Niasar et al. (2010). For stable partially saturated pore units ($s_i^w < s_i^{w,thr}$), the water is residing in the edges and in the corners. We approximate the air-water interface as follows:

$$a_i^{aw} = \begin{cases} 4\pi \left(\chi^3 \sqrt{V_i(1-s_i^w)} \right)^2, & 1 > s_i^w \geq s_i^{w,thr} \\ (\pi - \theta) \frac{2\gamma}{p_i^c} N_{edges} \left(l_{edge} - \frac{4\gamma}{p_i^c} \right) + 4\pi \left(\frac{2\gamma}{p_i^c} \right)^2 \left(\frac{N_i^w}{N_i} \right), & s_i^w < s_i^{w,thr} \end{cases} \quad (7.23)$$

where N_i^w is the number of pore throats that are not invaded by air, yet. See Appendix I for more detail on the derivation of equation 7.23.

7.2.8 Hydraulic conductivity

The conductivity k_{ij}^w is assumed to depend on the local capillary pressure in pore units i and j and thus on the water saturation. Following Chareyre et al. (2012), we assume that k_{ij}^w can be approximated by:

$$k_{ij}^w = \frac{a_{ij}^w (r_{ij}^h)^2}{\mu l_{ij}} \quad (7.24)$$

in which a_{ij}^w is the surface area of water that resides inside the pore throat, μ is the viscosity of water, l_{ij} is the distance between centres of pore units i and j , and r_{ij}^h is a representative radius that is assumed to depend on the local capillary pressure. We define r_{ij}^h as follows:

$$r_{ij}^h = \begin{cases} r_{ij}^s & s_i^w > s_i^{w,thr} \text{ and } s_j^w > s_j^{w,thr} \\ \frac{4\gamma}{p_i^c + p_j^c} & s_i^w \leq s_i^{w,thr} \text{ or } s_j^w \leq s_j^{w,thr} \end{cases} \quad (7.25)$$

in which r_{ij}^s is the hydraulic radius of pore throat ij that is computed for a fully saturated pore throat, see Chareyre et al. (2010) for its definition. Moreover, a_{ij}^w depends on the local capillary pressure in pore units i and j such that a_{ij}^w is given by:

$$a_{ij}^w = \begin{cases} (a_{ij}^{w,sat} - \pi(r_{ij}^c)^2), & 0 < s_i^w \leq s_i^{w,thr} \\ a_{ij}^{w,sat}, & s_i^{w,thr} > s_i^w \geq 1 \end{cases} \quad (7.26)$$

in which $a_{ij}^{w,sat}$ is the area of pore throat ij . Note that in cases where $a_{ij}^{w,sat} - \pi(r_{ij}^c)^2 < 0$, we set a_{ij}^w equal to 0. Finally, we define r_{ij}^c is an effective curvature in pore throat ij , which is defined as:

$$r_{ij}^c = \begin{cases} \frac{2\gamma}{p_i^c} & s_i^w < 1, s_j^w = 1 \\ \frac{2\gamma}{p_j^c} & s_i^w = 1, s_j^w < 1 \\ \frac{4\gamma}{(p_i^c + p_j^c)} & s_i^w < 1, s_j^w < 1 \end{cases} \quad (7.27)$$

7.2.9 Time step & stability

Controlling the time step is essential for the numerical model to be accurate and stable. For each unsaturated pore unit, a time step Δt_i is computed, which is an estimation of the time needed for the next event to occur in that pore unit. Following Joekar-Niasar et al. (2010), we compute Δt_i that is required to fully empty or fill a pore unit during local drainage or imbibition, respectively. In addition, we have added a time step that is needed to reach a saturation of $s_i^{w,thr}$ to ensure that the local capillary pressure-saturation behaviour was reproduced. We define Δt_i as follows:

$$\Delta t_i = \begin{cases} \left. \begin{array}{l} \frac{V_i(s_i^w - s_i^{w,thr})}{\sum_{j=1}^{N_i^{ij}} q_{ij}^w} \quad \text{for } \sum_{j=1}^{N_i^{ij}} q_{ij}^w > 0 \quad \text{and} \quad 1 > s_i^w > s_i^{w,thr} \\ \frac{V_i s_i^w}{\sum_{j=1}^{N_i^{ij}} q_{ij}^w} \quad \text{for } \sum_{j=1}^{N_i^{ij}} q_{ij}^w > 0 \quad \text{and} \quad 0 < s_i^w \leq s_i^{w,thr} \end{array} \right\} \text{Drainage} \\ \left. \begin{array}{l} \frac{V_i(s_i^w - s_i^{w,thr})}{\sum_{j=1}^{N_i^{ij}} q_{ij}^w} \quad \text{for } \sum_{j=1}^{N_i^{ij}} q_{ij}^w < 0 \quad \text{and} \quad 0 < s_i^w < s_i^{w,thr} \\ \frac{V_i(s_i^w - 1)}{\sum_{j=1}^{N_i^{ij}} q_{ij}^w} \quad \text{for } \sum_{j=1}^{N_i^{ij}} q_{ij}^w < 0 \quad \text{and} \quad 1 > s_i^w \geq s_i^{w,thr} \end{array} \right\} \text{Imbibition} \end{cases} \quad (7.28)$$

Note, that in determining Δt_i the absolute value of saturation differences, e.g. $(s_i^w - s_i^{w,thr})$, should be larger than a truncation value of 10^{-6} in order to avoid Δt_i converging to zero. The minimum saturation that a pore unit can have is set to 10^{-6} , at that saturation, the pore unit was considered to be empty. Then, the smallest value of Δt_i of all pore units is used and multiplied by a safety factor of 0.2.

The numerical scheme presented above is a pore-scale version of IMPES, which is a highly non-linear system of equations that is known to have stability problems for capillary dominated flow (Thompson, 2002; Chen et al., 2004). To stabilize the solution,

we evaluate $\frac{\partial s_i^v}{\partial p_i^v}$ and k_{ij}^w backwards in time. Thus, we linearly extrapolate $\frac{\partial s_i^w}{\partial p_i^w}$ to the next time step. A similar approach was employed by Joekar-Niasar et al. (2010), who linearly extrapolated the gradient of capillary pressure over a pore throat, namely $\frac{\partial p_{ij}^c}{\partial s_{ij}^w} = \frac{p_i^c - p_j^c}{s_i^w - s_j^w}$, over time.

7.3. Simulation setup

7.3.1 Particle packing and its properties

To test our model, we simulated the fast drainage experiments by Zhuang et al. (2016). For this purpose, a packing of spheres was generated with properties similar to the sand that was used in that article. First, 4000 spheres were placed randomly into a large box ($5 \times 5 \times 5 \text{ cm}^3$) such that the initial porosity was larger than 0.90. Then, the packing was compacted, assuming an artificially large friction angle. After compaction, the porosity was approximately 0.43, which was further reduced by decreasing the friction angle, following the approach of Chareyre et al. (2002).

In making the particle packing, we matched the porosity value of 0.39 and the particle size distribution of the sand in Zhuang et al. (2016), which varied from 0.0 to 0.50 mm in diameter with an average diameter of 0.20 mm. The radii were multiplied by a factor of 1.28 to have the quasi-static capillary pressure-saturation curve from simulations match that of experiments (see Figure 7.4). This was required because the pore structure in the simulated particle packing was different than in experiments because of difference in particle shape and in the degree of compaction.

The permeability of the final packing of spheres ($2.11 \times 10^{-10} \text{ m}^2$) was 12.4 times larger than that of experiments ($1.7 \times 10^{-11} \text{ m}^2$), which is a consequence of using spherical particles rather than the actual particle shape (Torskaya et al., 2014). The viscosity of water was set to $10^{-3} \text{ Pa}\cdot\text{s}$, the surface tension of air-water to $0.072 \text{ N}\cdot\text{m}^{-1}$ and the contact angle to zero.

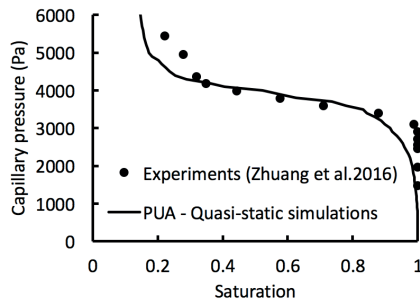


Figure 7.4: Quasi-static capillary pressure-saturation curve from experiments (symbols) and PUA simulations (solid line). For simulations, the particle radii had to be increased by a factor of 1.28.

7.3.2 Initial and boundary conditions

The top boundary of the packing was assumed to be an air reservoir at pressure p^{air} and the bottom boundary was assumed to be a water reservoir at a constant pressure P^{water} . All other boundaries were considered impermeable. Initially, the domain was assumed

to be fully water saturated, except for a row of pore units along the air reservoir that all had a value for p_i^c of 3000 Pa, which was just below the entry pressure of the granular material. Thus, along the air boundary, pore units were partially saturated at a saturation value of:

$$s_i^w = s_i^w(P_0^c) \quad \text{for } P_0^c \geq \frac{2\gamma}{r_i^{ins}} \quad (7.29)$$

Then, the pressure difference between the air and water reservoir was increased to P_{global}^c to initiate dynamic drainage.

7.3.3 Averaging procedure

The following three variables have been considered for each pore unit: water pressure, saturation, and air-water interfacial area. Macro-scale equivalents for those three variables were defined as their averages over all pore units. First, the macro-scale water saturation S is given by:

$$S = \frac{1}{\sum_{i=1}^{N_p} V_i} \sum_{i=1}^{N_p} s_i^w V_i \quad (7.30)$$

where N_p is the total number of pore units in the packing. The volume-averaged water pressure, $\langle P^W \rangle$, was computed by:

$$\langle P^W \rangle = \frac{1}{\sum_{i=1}^{N_p} s_i^w V_i} \sum_{i=1}^{N_p} p_i^w s_i^w V_i \quad (7.31)$$

The macro-scale capillary pressure, $\langle P^c \rangle$, was obtained by averaging the capillary pressure in pore units over their respective air-water interfacial area (Joekar Niasar et al., 2010):

$$\langle P^c \rangle = \frac{1}{\sum_{i=1}^{N_p} a_i^{aw}} \sum_{i=1}^{N_p} a_i^{aw} (p^{air} - p_i^w) \quad (7.32)$$

Hereafter, we define $\langle P^c \rangle$ as the capillary pressure, while $p^{air} - \langle P^W \rangle$ is referred to as the pressure difference between air and water, which under equilibrium conditions is the same as $\langle P^c \rangle$, but not under dynamic conditions. Under dynamic conditions, the relationship between capillary pressure and the air-water pressure difference is given by equation 7.1.

7.4 Results

7.4.1 Minimum number of particles and the effect of initial conditions

We first determined the minimum number of particles needed to have results of dynamic drainage independent of the number of particles. Figure 7.5 shows results of dynamic drainage simulations, using P_{global}^c of 7kPa. The relation between volume-averaged pressure difference and saturation was dependent on the number of particles for 3000 or less particles. But, it converged for simulations of 4000 particles or more. Therefore, the number of particles was set to 4000 particles for all simulations, which was similar to the number of particles employed in constructing quasi-static capillary pressure-saturation curves in Sweijen et al. (2016). A packing of 4000 particles contained approximately 18.500 grain-based tetrahedra, excluding tetrahedra along the boundary of DEM. This resulted in approximately 4000 pore units ($\approx 16 \times 16 \times 16$ pore units), which is in line with other pore-scale model studies of two-phase flow, for example: Qin (2015) used 960 pore units, Joekar-Niasar et al. (2010) used 42.875 pore units ($35 \times 35 \times 35$ pore units), Thompson (2005) employed 1728 pore units, and Sheng and Thompson (2016) used 1600 pore units.

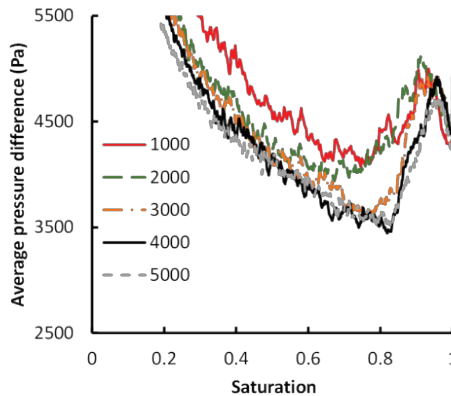


Figure 7.5: The effect of the number of particles on the average pressure difference, $p^{air} - \langle P^W \rangle$, as a function of saturation.

7.4.2 Verification of dynamic drainage showing viscous fingering

Simulations of unsaturated flow that are dominated by capillarity (i.e. low flow rates) are often unstable. For example, Thompson (2002) employed a single-pressure algorithm to simulate flow of water into a dry network of pores, solving pressure implicitly and saturation explicitly (IMPES). Their model did not have good mass-conservation for low flow rates. They employed a backward update of local capillary pressure and hydraulic conductivity and they did not account for the slope of the local capillary pressure-saturation curve ($\frac{\partial s_i^w}{\partial p_i^w}$) when solving for water pressure. To improve dynamic simulations, Joekar-Niasar et al. (2010) developed a numerical scheme where the saturation was solved semi-implicitly. This resulted in an accurate description of flow at low capillary numbers. They tested their model by reproducing a quasi-static capillary pressure-saturation curve using their dynamic code, following the work by Dahle et al. (2005).

To test our model for low flow rates, we employed the same procedure as Dahle et al. (2005). The modelling procedure was as follows: a global pressure difference, P_{global}^c , was applied that was slightly lower than the entry pressure. Subsequently, the dynamic code was allowed to reach equilibrium, then an incremental step in P_{global}^c was imposed before the model was run to equilibrium again. This sequence was repeated until the capillary pressure-saturation curve was reproduced. Thus, if a dynamic model can handle flow at low capillary numbers, the quasi-static capillary pressure-saturation curve can be accurately reproduced using the dynamic code.

The value of P_{global}^c was increased from 1500 Pa to 5500 Pa over 50 incremental steps of 80 Pa. Figure 7.6 shows the results of these simulation as well as the corresponding quasi-static capillary pressure-saturation curve. We can see that the step-wise curve obtained by the dynamic code matched the quasi-static curve satisfactorily. During a step in P_{global}^c , the dynamic code gave fluctuating values of both average pressure difference and average capillary pressure, which were always lower than P_{global}^c , but both pressure values converged to P_{global}^c at equilibrium. Such fluctuations were also observed in pore-scale simulations by Joekar-Niasar et al. (2010).

In our simulations, the dynamic and quasi-static curves deviated from each other around the entry pressure of the sample, where air in quasi-static simulations infiltrated the sample at lower capillary values than the dynamic curve. This is because in dynamic simulations, local imbibition caused some of the initially unsaturated pore units to become fully saturated again, while at other locations air infiltrated new pore units. Thus, by redistributing water, the pressure difference increased while the saturation remained constant. Local imbibition did not occur in quasi-static simulations.

Therefore, it seemed that air infiltrated at a higher capillary pressure than in quasi-static simulation. The numerical scheme was considered mass conservative, with a loss of water volume of only 10^{-5} of the initial water volume.

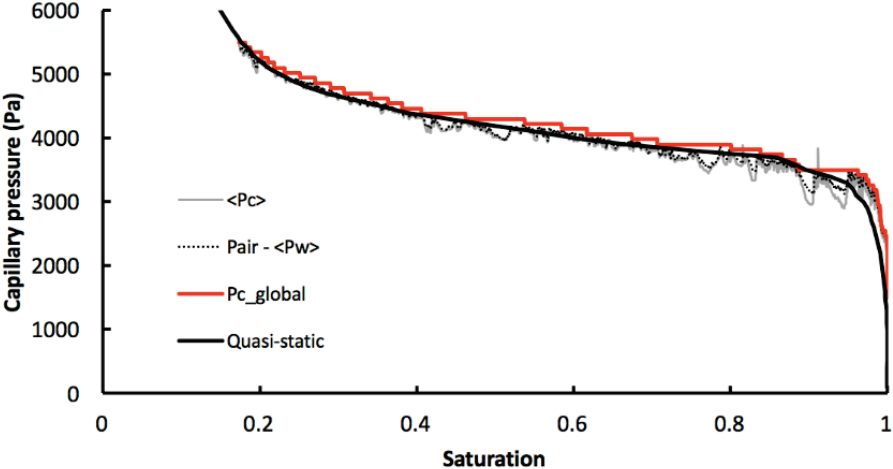


Figure 7.6: Reconstruction of the quasi-static capillary pressure-saturation curve (black solid line) using dynamic flow simulations.

7.4.3 Dynamic drainage: formation of air fingers

Simulations of dynamic drainage showed the formation of air fingers in an initially water saturated domain. The volume-averaged pressure difference between air and water, $p^{air} - \langle P^W \rangle$, and capillary pressure, $\langle P^c \rangle$, as function of saturation are presented in Figure 7.7. Furthermore, to illustrate the migration of air, 2-dimensional cross-sections are shown in Figure 7.8 that depict water pressure and water saturation distributions. For these simulations, the value of P_{global}^c was set to 7kPa.

Initially, the modelling domain was saturated with water, except for a row of pore units at the air boundary. Consequently, the water pressure was linearly distributed with relatively high values of water pressure at the air boundary (-3 kPa) and low values at the water boundary (-7 kPa); see Figure 7.8a. The pressure values along the air boundary corresponded to capillary pressure values that were initially imposed (i.e. P_0^c of 3 kPa). Then, air infiltrated the modelling domain by means of channels (so called air fingers). Figure 7.8b shows an air finger that has extended from the air boundary to the water reservoir. Consequently, the water pressure of pore units increased significantly. The water pressure in many pore units was in the range of -3 to -4 kPa, except for pore units near the water boundary, which had lower values of water pressure (-4 to -7 kPa). Afterwards, drainage of all pore units occurred and the water pressure gradually decreased to -7kPa.

The flow behaviour illustrated in Figure 7.8 resulted in a peculiar behaviour of $p^{air} - \langle P^W \rangle$ when plotted against saturation (see Figure 7.7). Initially, the value of $p^{air} - \langle P^W \rangle$ was higher than the value of $\langle P^c \rangle$. Then, the value of $p^{air} - \langle P^W \rangle$ decreased until it reached the value of $\langle P^c \rangle$ at saturation 0.82, which corresponded to the moment that air fingers reached the water reservoir. Drainage for saturations lower than 0.82 occurred with values of $p^{air} - \langle P^W \rangle$ close to the quasi-static capillary pressure-saturation curve. The value of $\langle P^c \rangle$ deviated from the quasi-static capillary pressure, which can be related to the approximation of surface area in pore units that is presented in eq. 7.23.

To investigate the effect of boundary conditions, dynamic drainage was also simulated for the case that all sides were open to water, having the same pressure as the water reservoir. Thus, Dirichlet boundary conditions were imposed for the side walls, using a water pressure of $-P_{global}^c$. Figure 7.9 shows 2-dimensional distributions of the saturation and water pressure at three different saturation values. Similar to results in Figure 7.8, air fingers are formed in the granular material. However, the air fingers did not infiltrate much further than the centre of the packing, whereas for closed side walls, the air fingers migrated down to the water reservoir. Consequently, the water pressure at saturation 0.85 is much lower (i.e. higher pressure differences) for simulations with

open side walls compared to simulations with closed side walls (compare Figures 7.8b and Figure 7.9b). The difference in $p^{air} - \langle P^W \rangle$ between the two simulations is shown in Figure 7.7, where simulations with open side boundaries show higher values of $p^{air} - \langle P^W \rangle$ and a smaller effect of air finger formation.

Air fingers were a consequence of preferential pathways in the pore structure due to small-scale heterogeneities, having a size of one or a few pore units. Reconstruction of quasi-static capillary pressure-saturation curves showed the same preferential pathways that were present in dynamic flow. The formation of air fingers during primary drainage is a common phenomenon, as for example shown in the modelling efforts by Aker et al. (1998). They studied the infiltration patterns during primary drainage for different viscosity ratios (i.e. the ratio of non-wetting phase viscosity over the wetting phase viscosity). Their drainage simulation, using a low viscosity ratio, clearly showed finger formations. Their results are compatible with our results, as air and water have a low viscosity ratio. Similarly, Joekar-Niasar et al. (2010) showed with their dynamic pore-network model that the pattern of the non-wetting fluid is much more irregular under low values of viscosity ratio.

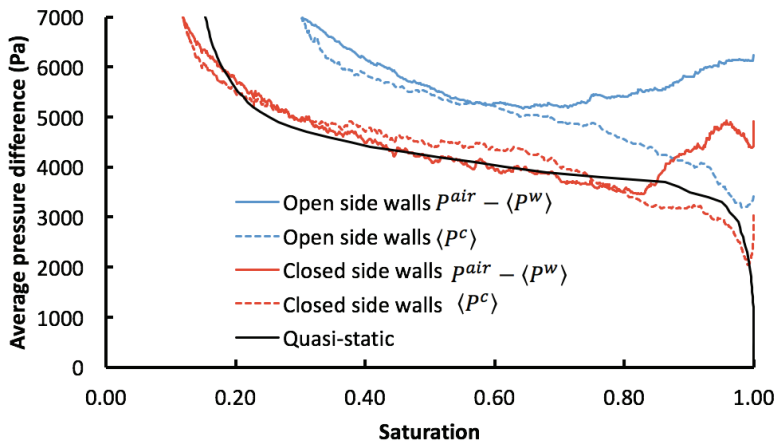


Figure 7.7: Averaged pressure difference as a function of saturation for dynamic drainage simulations with all sides open to water (denoted by blue lines) and with closed sides (denoted by red lines).

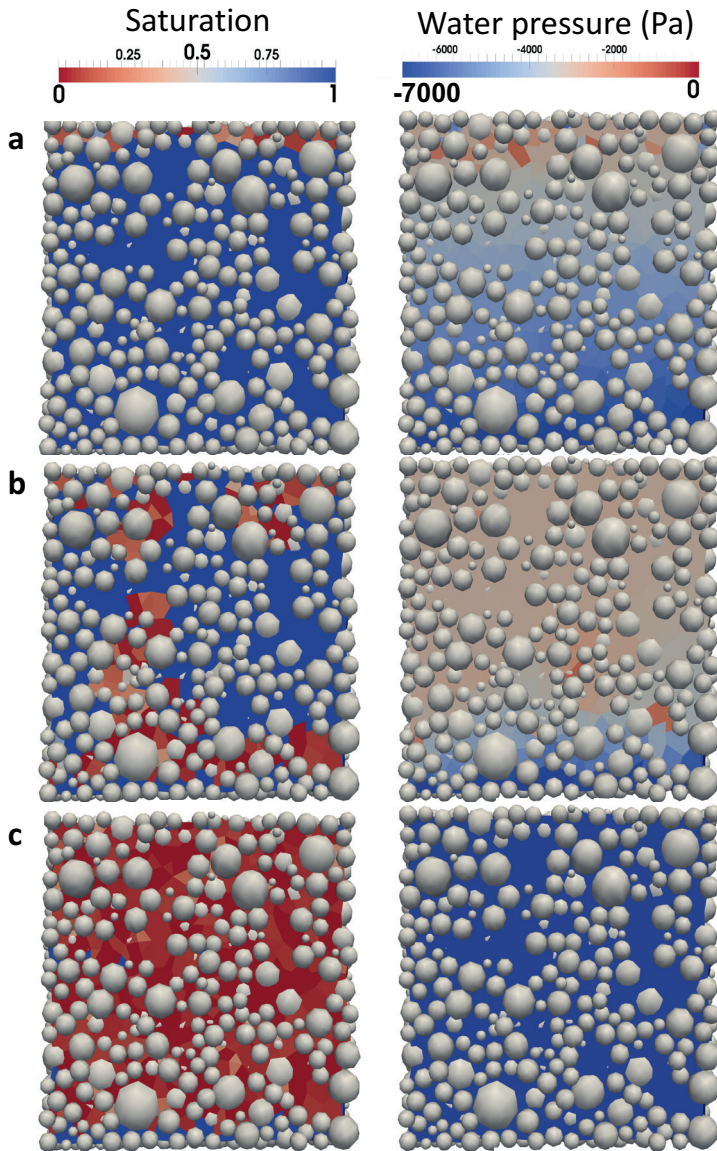


Figure 7.8: Distribution of water pressure and water saturation obtained using dynamic drainage simulations, where P_{global}^c was set to 7kPa. The sides are closed and the bottom represents a water reservoir while the top represents an air reservoir. Results for three different times, at which the average saturation values are: a) 1.0, b) 0.80, and c) 0.11. Cross-sections are taken in the middle of the sample.

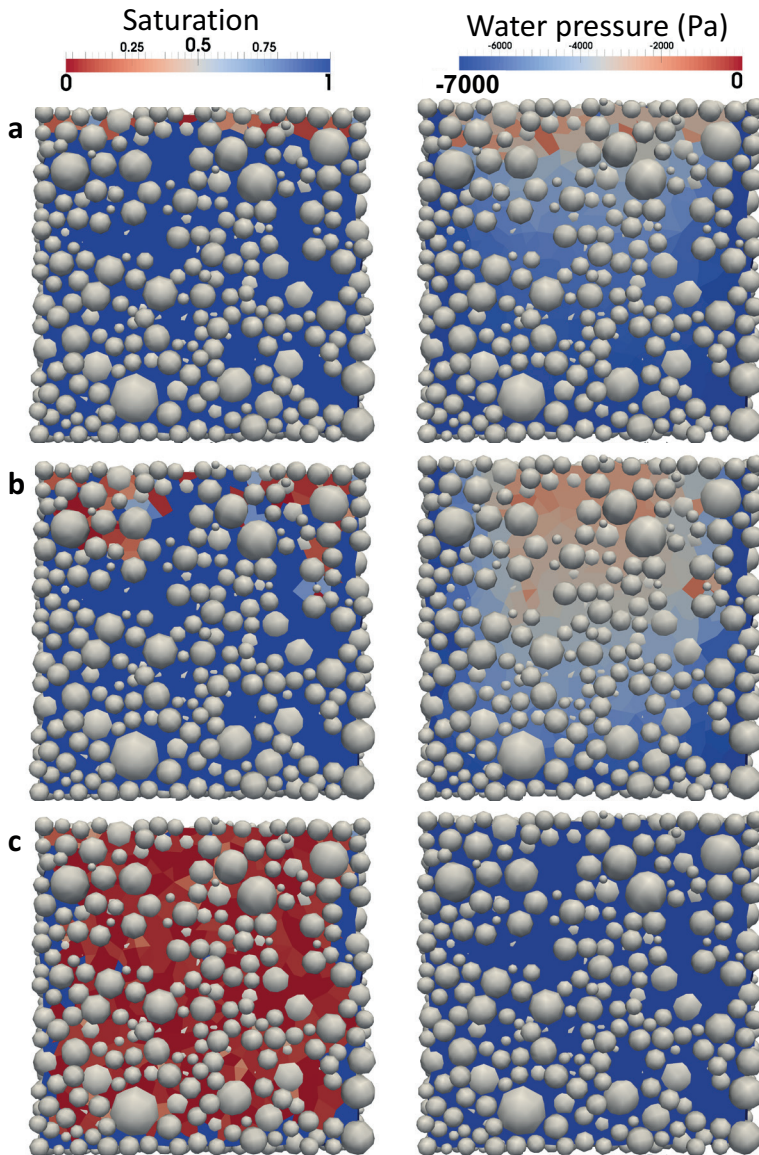


Figure 7.9: Cross-sections of dynamic drainage simulations for water pressure and water saturation, where P_{global}^c is 7kPa. The sides and bottom represent a water reservoir while the top boundary represents an air reservoir. Results for three different times, at which the average saturation values are: a) 1.0, b) 0.80 and c) 0.32. Cross-sections are taken in the middle of the sample.

7.4.4 The dynamic coefficient τ : simulations vs. experiments

To quantify the dynamic coefficient, we use equation 7.1 that was introduced by Hassanizadeh and Grey (1993). That equation was applied to results of three simulations, using three different values of P_{global}^c , namely: 7, 10, 14 kPa. To allow for comparison of the dynamic coefficients τ between simulations and experiments, we resize the modelling domain to have it closer to the size of the sample in experiments. The sample size in Zhuang et al. (2016) was 30 x 30 x 20 mm³, while that of our modelling domain was 3.2 x 3.2 x 3.2 mm³. Therefore, the modelling domain was resized to 7.9 x 2.0 x 2.0 mm³ such that the length of the flow direction was increased. Thus, the pore units in the flow direction were increased from 15 pore units to 40 pore units.

In general, a higher value of P_{global}^c resulted in a higher value of average pressure difference, for saturation values from 0.76 to 1.0 (see Figure 7.10a). However, for saturation values lower than 0.76, the average pressure difference curves converged to the quasi-static capillary pressure-saturation curve. During the saturation interval of 0.76 to 1.0, the rate of saturation change is relatively large (see Figure 7.10b). Figure 7.10c shows the value of τ as function of saturation, which quantifies the dynamic effect. Indeed, for saturations of 0.76 or higher, τ was relatively large but it decreased during drainage to almost zero (i.e. ~ 1 Pa·s), at a saturation value of 0.76 – 0.8. Note that the point at which τ reached almost zero shifted from 0.76 to 0.83 for P_{global}^c values of 7 kPa to 14 kPa, respectively. The decrease in τ was a result of the average pressure difference that converged to the capillary pressure (see Figure 7.10a). The value of τ increased again after a saturation of 0.5. This was related to an increase in the deviation of the pressure difference of air and water and the capillary pressure (see Figure 7.10a) as well as the low value of $\frac{\partial S}{\partial t}$, which converged to zero when the saturation reached the residual saturation.

The value of τ in our simulations was relatively small (less than 100 Pa·s) compared to other experimental studies, such as the work by Zhuang et al. (2016). They reported a value of τ in the range of 5×10^4 to 3×10^6 Pa·s for a sample size of 30 x 30 x 20 mm³. The low value of τ was caused by a relatively high rate of saturation change ($\frac{\partial S}{\partial t}$) that occurred in our simulations. The large value of $\frac{\partial S}{\partial t}$ was caused by a relatively large gradient in pressure between the air and water reservoir, which was much larger in simulations than experiments, because of the small modelling domain compared to the sample size of experiments.

To compare values of τ of simulations with experiments, we corrected the τ from simulations (τ_{sim}) to the size and permeability of experiments. The value of τ is

thought to be inversely proportional to the permeability (Stauffer, 1987) and linearly proportional to square of the length of the domain (Dahle et al., 2005), such that we can write:

$$\tau_{scaled} = \tau_{sim} \frac{K_{sim}}{K_{exp}} \left(\frac{l_{exp}}{l_{sim}} \right)^2 \quad (7.33)$$

where τ_{scaled} is the scaled value of τ_{sim} , K_{sim} and K_{exp} are the permeability values of simulations and experiments, respectively, and l denotes the length of the domain in flow direction. The value of τ in simulations (less than 100 Pa·s) was scaled to τ_{scaled} (less than 17.880 Pa·s), which is much closer to experimental data ($\sim 5 \times 10^4$ Pa·s to 3×10^6 Pa·s), but still slightly lower than in experiments. The τ value in Zhuang et al. (2016) was in accordance with the work by Hou et al. (2012), who reported values for τ of approximately 2×10^4 Pa·s for a sample of 1.27 cm in height and 2.54 cm in diameter (using Ottawa F95 sand having a particle diameter of 0.14mm). However, other pore-scale simulations reported lower values of τ that were close to the τ value of our simulations. For example, Joekar-Niasar et al. (2010) found a value for τ of approximately 100 Pa·s to 300 Pa·s, based on their dynamic pore-network simulations for a viscosity ratio of 0.1. Dahle et al. (2005) reported a value for τ of 274 Pa·s based on simulations of a bundle of tubes that had a characteristic length scale of 10^{-3} m.

Thus, in comparing pore-scale studies with experimental studies, one should consider the difference in domain size. Simulations were conducted on a relatively small sample ($7.9 \times 2.0 \times 2.0$ mm³), which is much smaller than samples employed in typical experiments. Our simulations were conducted on a sufficiently large number of particles to have an REV, but the modelling domain was still small. Of course, more particles can be used to form a larger domain, with much larger computational time, but upscaling length scales with multiple orders of magnitudes remains an issue for pore-scale simulations using the pore-assembly method.

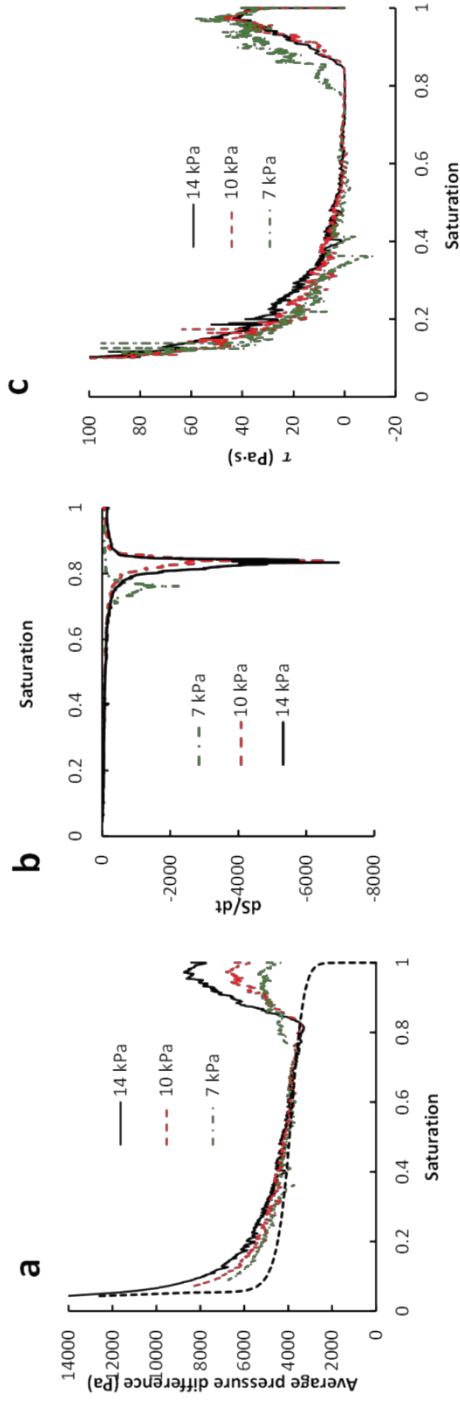


Figure 7.10: Investigation of dynamic effect for three dynamic drainage simulations using P_{global}^C of: 14 kPa (black solid line), 10 kPa (red dashed line) and 7 kPa (green dashed line). Results are reported as: a) average pressure difference vs. saturation, b) rate of saturation change vs. saturation, and c) the dynamic coefficient τ as a function of saturation.

7.5 Conclusions

This work presents a modelling technique for dynamic drainage in packings of spheres, using the pore-unit assembly approach. The pore space inside packings of spheres was extracted by a sequence of meshing techniques: first, a triangulation was applied to extract grain-based tetrahedra, then the grain-based tetrahedra were merged to find pore units. Subsequently, the pore space of each pore unit was replaced by a regular shape, for which the capillary pressure-saturation curves were determined. Using the assembly of pore units, a pore-scale version of IMPES (implicit pressure and explicit saturation scheme) was employed to solve for water pressure during dynamic drainage. The model was then verified by simulating the quasi-static capillary pressure-saturation curve using our model, which yielded a good reproduction of the quasi-static curve.

Dynamic drainage simulations revealed that air infiltrated via preferential pathways in the pore structure, resulting in air fingers. The pressure difference between air and water showed a non-monotonic functionality with saturation. During finger infiltration, dynamic effects occurred; the pressure difference between air and water was much larger than the capillary pressure. However, the air reached the water reservoir at relatively high values of saturation (0.82), after which further drainage occurred with the pressure difference between air and water being close to the capillary pressure value. The dynamic coefficient τ confirmed this non-monotonic behaviour with saturation. The value of τ was relatively low (<100 Pa·s) due to a high rate of saturation change, because of the small modelling domain. To compare τ values of simulations to experiments, the value of τ was corrected for the different sample size and permeability in simulations and experiments. This resulted in a larger τ value, namely 1.8×10^4 Pa·s, which is closer to the range of values in experimental data of Zhuang et al. (2016), namely 5×10^4 to 3×10^6 Pa·s. Thus, in comparing pore-scale simulations of dynamic drainage to experimental data, scaling by size is an import issue to be considered.

A grain-scale model for unsaturated flow in deforming packings of swelling particles: a study on small-scale swelling events

Abstract

In this Chapter, unsaturated flow in a deforming packing of swelling particles is investigated using a coupling of the discrete element method (DEM) with the pore-unit assembly method (PUA). In DEM, the movement of individual particles is computed for deforming packings of swelling spheres. Then, PUA discretizes the pore-space of packings of spheres into an assembly of pore units, which is used to compute unsaturated flow. A finite difference scheme is employed for unsaturated flow in deforming packings of spheres, based on the pore-scale version of IMPES (implicit pressure and explicit saturation scheme), which was introduced in Chapter 7. The aim of this research is to study transient drainage in packings of spheres as a result of water absorption by particles, their swelling, and the subsequent movement of particles. Two simulation scenarios are considered for swelling of particles, namely: i) using a confined box that remains constant in volume and ii) using a box with confined and impermeable sides and a moving top boundary that permeable to air but not to water. Simulation results reveal how swelling affect the pore geometry, water pressure, water saturation, and wetted solid surface area. Finally, the dependency of the wetted solid surface area on the saturation is investigated and compared to a semi-empirical relation from literature.

8.1 Introduction

Unsaturated flow of water in a porous medium often coincides with deformation of the solid phase. For example, ink injection in paper causes swelling of the paper (Rosenholm, 2015); fluid absorption of absorbent polymers in hygienic products causes swelling and deformation of the solid phase as well as drying of the pores (e.g. Diersch et al., 2010). The coupled behaviour of water flow in a porous medium and subsequent deformation of the porous media is referred to as hydro-mechanical coupling (e.g. Nikooee et al., 2013; Yuan and Chareyre, 2017). Effects of hydro-mechanical coupling are measurable in experiments. For example, Lins and Schanz (2005) studied how the capillary pressure-saturation curve of a sand changes when changing the confining pressure, thus changing the pore structure of sand.

Hydro-mechanical effects are typically quantified in terms of macro-scale quantities (e.g. saturation, pressure, porosity). However, understanding of underlying processes (at the pore-scale) is often desirable to explain macro-scale effects. Pore-scale quantities in hydro-mechanical studies are difficult to measure as the sample changes over time. For quasi-static experiments, imaging of the pore-space might be possible, but for fast dynamic experiments this is not feasible.

An alternative to experiments would be to conduct pore-scale modelling which is based on pore-scale physics and rules. In Chapter 7, we introduced a model for unsaturated flow in packings of spheres. However, that model did not include deformation of the packing of spheres. Therefore, we present here a numerical scheme where the pore-scale version of IMPES (implicit pressure solver and an explicit saturation update) that is presented in Chapter 7 is coupled to DEM. The aim is to simulate drying of a bed of super absorbent polymer (SAP) particles. SAP is a hydrophilic polymer that is often used as absorbent in hygienic products (e.g. Diersch et al. 2010). In this work, an initially dry bed of SAP particles is simulated that is assumed to become saturated instantaneously. Then, the absorption of pore water by SAP particles, their swelling, and drying of the bed are simulated.

In what follows, the coupling of DEM, pore-unit assembly method, and the pore-scale version of IMPES is presented. The aims are to conceptualize the coupling, to give details on the numerical scheme, and to test the numerical model for swelling.

8.2 Numerical methods

In this work, a coupling is described of the algorithm for unsaturated flow, which was presented in Chapter 7, to the Discrete Element Method (DEM). The resulting code is

able to simulate unsaturated flow in deformable and swelling granular materials. For simplification, we assume a one-way coupling where deformation affects the flow of water, but flow does not affect the state of stress of the granular material. The physical meaning of this assumption is that capillary and viscous forces, which act on particles, do not affect the movement of particles. However, in future work, this assumption can be relaxed by adding forces that arise from the occupancy of pore units by water, following the work by Yuan and Chareyre (2017).

8.2.1 Compatibility of DEM with the pore-unit assembly method

The coupling of DEM with the pore-unit assembly method relies on three levels of meshing, which are all interconnected (see section 7.2.1 for more details). The lowest level is that of the particle locations, which is dependent on the state of stress inside the packing, following DEM computations. The intermediate level is that of grain-based tetrahedra, where particle centres are at the vertices of the tetrahedra. The upper level is the pore-unit assembly, which are merged grain-based tetrahedra. Based on the assembly of pore units, unsaturated flow is computed. To achieve hydro-mechanical coupling, changes in particle locations are directly projected to the grain-based tetrahedra and subsequently to the pore-unit assembly.

The numerical procedure contains the following three computational steps for every time step, see Figure 8.1: i) update of particle locations, based on DEM, ii) update of relevant geometrical properties of the pore-unit assembly; iii) computation of water flow using the pore-scale version of IMPES. Thus, first a time step is made by DEM to go from time t to time $t + \Delta t$, then flow computations are conducted to compute the water pressure and saturation at time $t + \Delta t$. In what follows, additions to the IMPES scheme are evaluated for including deformation of pore units.

8.2.2 Change of pore-unit volume due to particle movement

To introduce deformation into the IMPES scheme that was introduced in Chapter 7, an extension is required to include the volume change of pore units. Consider a pore unit i that has a volume V_i . The change in pore unit volume is given by $\frac{dV_i}{dt}$, which is the sum of volume change due to the swelling of the surrounding particles $\left. \frac{dV_i}{dt} \right|_{abs}$ and volume change due to the relative movement of particles $\left. \frac{dV_i}{dt} \right|_{relmov}$ (see Figure 8.2). Thus, we have (Sweijen et al., 2017b):

$$\frac{dV_i}{dt} = \left. \frac{dV_i}{dt} \right|_{relmov} + \left. \frac{dV_i}{dt} \right|_{abs} \quad (8.1)$$

In this study, the volume of absorbed water is assumed to be equal to the change of particle volume. Thus, the change in pore-unit volume due to water absorption by SAP particles does not directly cause flow of water, since water is simply changed from being in a liquid state inside pore units to a solid state inside the SAP particles. But, a subsequent movement of particles will cause a change in void volume, which can cause suction of water. Therefore, the flux $\left. \frac{dV_i}{dt} \right|_{relmov}$ should be considered when solving for pressure, while $\left. \frac{dV_i}{dt} \right|_{abs}$ should only be considered when updating the water saturation.

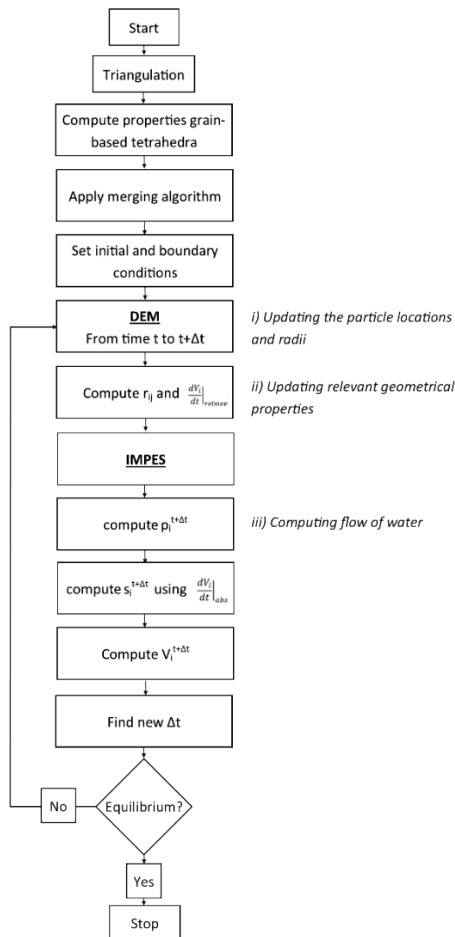


Figure 8.1: Flowchart of the numerical scheme for coupling of the discrete element method with the pore-unit assembly method in order to simulate dynamic drainage in a deforming and swelling granular material.

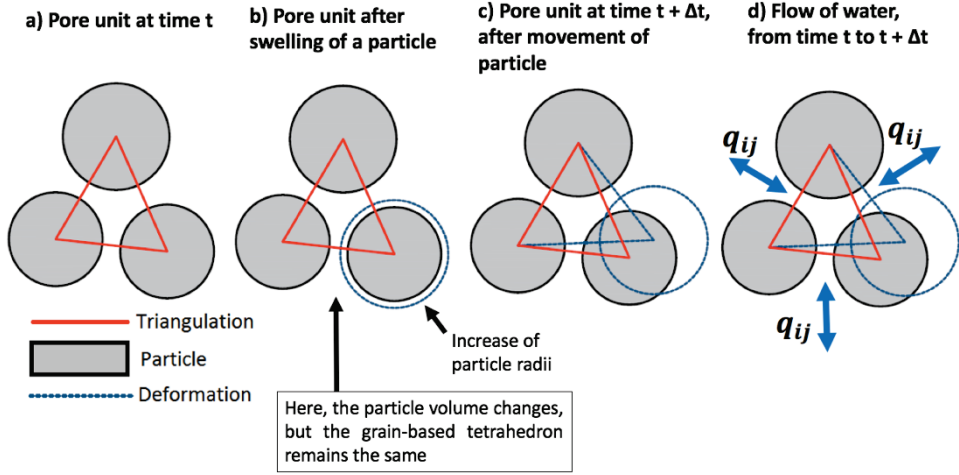


Figure 8.2: 2-dimensional illustration of a deforming pore unit: a) the initial configuration, b) configuration after swelling of a particle, c) movement of particles due to deformation and d) flow of water as a result of particle motion, with q_{ij} being the volumetric flux in pore throat ij .

8.2.3 Computation of unsaturated flow

In this section, a derivation is given for the governing equations of deforming pore units. Consider pore unit i that has a water pressure p_i , a water saturation s_i , and it is connected to neighbouring pore unit j via pore throat ij that has a conductivity k_{ij} . The volume balance of saturated pore units reads:

$$\sum_{j=1}^{N_i} k_{ij} (p_i - p_j) = - \left. \frac{dV_i}{dt} \right|_{relmov} \quad (8.2)$$

Equation 8.1 has been previously implemented to solve for water pressure in saturated pore units in a deforming non-swelling granular material, by Chareyre et al. (2012). For partially saturated pore units, we may write the following discretized volume balance:

$$\sum_{j=1}^{N_i} k_{ij} (p_i^{t+\Delta t} - p_j^{t+\Delta t}) = - \left(\left. \frac{dV_i s_i^w}{dt} \right|_{relmov} \right)^{t+\Delta t} \quad (8.3)$$

Equation 8.3 requires simplifications before we can solve it for water pressure. The right-hand term of equation 8.3 can be discretised into:

$$\left(\left. \frac{dV_i s_i^w}{dt} \right|_{relmov} \right)^{t+\Delta t} = \frac{s_i^{t+\Delta t} V_i^{t+\Delta t} - s_i^t V_i^t}{\Delta t} \quad (8.4)$$

The values of $\left.\frac{dV_i}{dt}\right|_{relmov}$ and $\left.\frac{dV_i}{dt}\right|_{abs}$ are known at time step $t + \Delta t$, since a time step Δt is already made in DEM before conducting a time-step in IMPES. When solving for water pressure, we only consider $\left.\frac{dV_i}{dt}\right|_{relmov}$, thus the apparent value of $V_i^{t+\Delta t}$ is given by:

$$V_i^{t+\Delta t} = V_i^t + \left(\left.\frac{dV_i}{dt}\right|_{relmov}\right)^{t+\Delta t} \Delta t \quad (8.5)$$

The value of $V_i^{t+\Delta t}$ will be updated after IMPES computations to include $\left.\frac{dV_i}{dt}\right|_{abs}$. We introduce the following approximation:

$$s_i^{t+\Delta t} = s_i^t + \left(\frac{ds_i}{dp_i}\right)^t \left(\frac{dp_i}{dt}\right)^{t+\Delta t} \Delta t \quad (8.6)$$

where $\frac{ds_i}{dp_i}$ is evaluated at time step t . Combining equations 8.4 to 8.6, results in:

$$\left(\left.\frac{dV_i s_i^w}{dt}\right|_{relmov}\right)^{t+\Delta t} = s_i^t \left(\left.\frac{dV_i}{dt}\right|_{relmov}\right)^{t+\Delta t} + \left(V_i^t + \left(\left.\frac{dV_i}{dt}\right|_{relmov}\right)^{t+\Delta t} \Delta t\right) \left(\frac{ds_i}{dp_i}\right)^t \left(\frac{dp_i}{dt}\right)^{t+\Delta t} \quad (8.7)$$

In equation 8.7, $\left(\frac{dp_i}{dt}\right)^{t+\Delta t}$ can be rewritten to $\frac{p_i^{t+\Delta t} - p_i^t}{\Delta t}$. Combining equations 8.3 and 8.7 and rearranging various terms yields:

$$\begin{aligned} p_i^{t+\Delta t} \left(\sum_{j=1}^{N_i} k_{ij}^t + \left[\frac{V_i^t}{\Delta t} + \left(\left.\frac{dV_i}{dt}\right|_{relmov}\right)^{t+\Delta t} \right] \left(\frac{ds_i}{dp_i}\right)^t \right) - \sum_{j=1}^{N_i} k_{ij}^t p_j^{t+\Delta t} \\ = -s_i^t \left(\left.\frac{dV_i}{dt}\right|_{relmov}\right)^{t+\Delta t} + \left[\frac{V_i^t}{\Delta t} + \left(\left.\frac{dV_i}{dt}\right|_{relmov}\right)^{t+\Delta t} \right] \left(\frac{ds_i}{dp_i}\right)^t p_i^t \end{aligned} \quad (8.8)$$

Equations 8.2 and 8.8 constitute a set of linear equations in the generalized form:

$$a p_i^{t+\Delta t} - \sum_{j=0}^{N_i} b p_j^{t+\Delta t} = c \quad (8.9)$$

where a , b and c are coefficients independent of $p_i^{t+\Delta t}$. Equation 8.9 can be solved for water pressure, similar to equation 7.10 in Chapter 7. Note that the change of pore-unit volume due to particle movement, $\left.\frac{dV_i}{dt}\right|_{relmov}$, is obtained from DEM simulations and that the definition of k_{ij} and $\frac{ds_i}{dp_i}$ can be found in Chapter 7, section 7.2.8 and section 7.2.4, respectively. The saturation is updated explicitly, while accounting for the water absorption by the swelling particles:

$$s_i^{t+\Delta t} = s_i^t + \frac{ds_i}{dp_i} [(p_i^w)^{t+\Delta t} - (p_i^w)^t] + \frac{\Delta t}{V_i^{t+\Delta t}} \left. \frac{dV_i}{dt} \right|_{abs} \quad (8.10)$$

By introducing terms for volume change in equations 8.8 and 8.10, two characteristic time steps are added to those for unsaturated flow, which should be considered when finding the minimum time step. The characteristic time step of a pore unit Δt_i is:

$$\Delta t_i = \min \left\{ \begin{array}{l} - \left(\frac{V_i s_i}{\left. \frac{dV_i}{dt} \right|_{abs}} \right) \quad \text{for} \quad \left. \frac{dV_i}{dt} \right|_{abs} < 0 \\ \left(\frac{V_i (1 - s_i)}{\left. \frac{dV_i}{dt} \right|_{abs}} \right) \quad \text{for} \quad \left. \frac{dV_i}{dt} \right|_{abs} > 0 \\ - \left(\frac{V_i s_i}{\left. \frac{dV_i}{dt} \right|_{relmov}} \right) \quad \text{for} \quad \left. \frac{dV_i}{dt} \right|_{relmov} < 0 \\ \left(\frac{V_i (1 - s_i)}{\left. \frac{dV_i}{dt} \right|_{relmov}} \right) \quad \text{for} \quad \left. \frac{dV_i}{dt} \right|_{relmov} > 0 \end{array} \right. \quad (8.11)$$

Equation 8.11 is applied in conjunction with equation 7.28, which accounts for the minimum time step during two-phase flow. To avoid Δt_i converging to zero, the minimum saturation and the minimum change in saturation ($1 - s_i$) is set to 10^{-6} . The absolute minimum value of Δt_i gives the overall time step.

8.3 Model setup

8.3.1 Discrete Element Method setup

In this work, the discrete element method was employed to simulate particle motion during swelling of particles. We used open source software Yade-DEM (Šmilauer et al., 2015). To simulate swelling, a simplified version of the swelling model was employed that was presented in Chapter 2. We employed Hertz-Mindlin contact mechanics in DEM; see Modenese et al. (2012) for more details. All particles were assumed to have a constant Young's modulus of 10 kPa. The particle-particle friction angle was set to 5.5° (Lorenz et al., 1997; Sweijen et al., 2017b) and the density was set to $1000 \text{ kg}\cdot\text{m}^{-3}$ (Mirnyy et al., 2012). All particles had an initial diameter of $460 \mu\text{m}$, which is typical of super absorbent polymer (SAP) particles (see Chapter 6).

A packing of particles was generated by inserting 2000 particles into a relatively large cubic modelling domain (10^3 mm^3). Then the particles were compacted by applying a 10 Pa confining stress to all boundaries of the modelling domain. This resulted in a porosity value of 0.38 and a domain size of 5.4^3 mm^3 . The permeability was determined using a virtual permeability test in Yade-DEM; the permeability was found to be $4.8 \times 10^{-10} \text{ m}^2$. Once, a packing of dry SAP particles was generated, the boundary conditions were set to the conditions described in the following section.

Swelling was applied by increasing all particle sizes using a growth factor that was introduced in Sweijen et al. (2017b). A simple kinetic law was used to describe the change of radius as function of time, although more complex and comprehensive models exist for swelling of spherical particles. Sweijen et al. (2017c) showed that a relatively simple kinetic law results in a similar variation of radius (R) vs. time dependency as various complex models (for free swelling), albeit that the kinetic coefficients have different values. Here, we employed the kinetic law proposed by Omidian et al. (1998) with an additional factor to account for partial wetting of the particle surface under unsaturated conditions:

$$\frac{dR_i}{dt} = \frac{A_i^w}{A_i} k^0 (R_{max} - R_i) \quad (8.12)$$

where k^0 is a kinetic coefficient, A_i^w is the surface area of particle i that is covered with water, A_i is the total surface area of particle i , R_i is the radius, R_{max} is the maximum radius. The maximum radius was set to $3.6R_0$, where R_0 was the initial radius; this corresponded to an absorption ratio of 30 g/g. However, only one pore volume of water was allowed to be absorbed by the particles, thus the maximum absorption ratio that was achieved was very small ($<1.5 \text{ g/g}$), therefore we assumed the Young's modulus to remain constant. For sake of simplicity, we also assumed that the transition of dry SAP to slightly swollen SAP obeys equation 8.12.

8.3.2 Initial and boundary conditions

Two scenarios were considered to test the numerical code, namely: i) swelling in a confined box, see Figure 8.3a and ii) swelling in a box having a moving top boundary, see Figure 8.3b. In the first scenario, the particles were confined in the modelling domain, but air could enter via all boundaries. Initially, the SAP particle bed was saturated with water, except for a row of pore units along the boundaries, which were partially saturated at a capillary pressure of 1kPa. During simulations, particles could swell until all water had been absorbed, then the swelling would cease.

In the second scenario, all side boundaries were assumed to be rigid and impermeable. The top boundary was assumed to be open to air (at zero pressure) and to

move freely. Initially, the particle bed was saturated with water, except for the row of pore units along the top boundary, which were partially saturated at a capillary pressure of 1kPa. The row of partially saturated pore units was needed for the initial conditions to have a solution when using IMPES. Particles were allowed to swell until fully swollen or until all pores became dry.

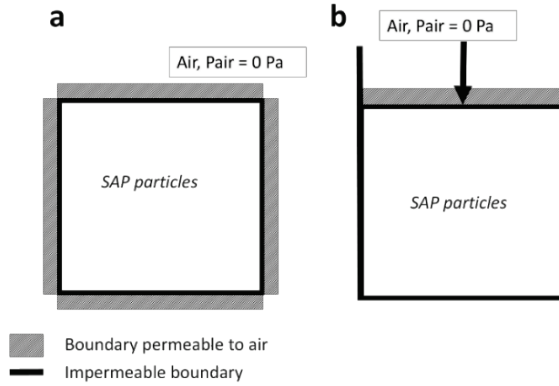


Figure 8.3: 2-dimensional illustration of the two scenarios that were used in this research: a) confined box, where all boundaries were fixed but permeable to air and b) a box with impermeable side boundaries, a moving top boundary that was permeable to air.

8.3.3 Conceptual coupling of unsaturated flow and swelling

The coupling of unsaturated flow with swelling has three different characteristic regimes, which can be identified using characteristic time scales. Each regime inherently requires a different modelling approach. First, we identify two characteristic time scales, namely that of swelling ($\tau_{swelling}$) and that of water flow (τ_{flow}). Following equation 8.12, swelling has the following characteristic time step:

$$\tau_{swelling} = \frac{1}{k_0} \quad (8.13)$$

The characteristic time scale of flow is defined the same way as for saturated flow, namely:

$$\tau_{flow} = \frac{l\mu}{\rho_w g K} \quad (8.14)$$

where μ is the viscosity of water, l is the length of the modelling domain, ρ_w is the density of water, g is the gravitational constant, and K is the intrinsic permeability of the modelling domain.

When flow of water is much faster than swelling of particles ($\tau_{swelling} \gg \tau_{flow}$), transient effects of water flow will be short lived. Thus theoretically, one could

employ a quasi-static algorithm for unsaturated flow where at each time step, water redistribution occurs instantaneously. In that case, only the swelling process is a kinetic process. However, when swelling of particles is much faster than flow of water ($\tau_{swelling} \ll \tau_{flow}$), flow of water occurs in a coupled fashion with swelling. In this work, we consider the case that $\tau_{swelling} \ll \tau_{flow}$ to test our one-way coupled algorithm.

However, transient effects of flow can dissipate relatively quickly in a small domain (see Chapter 7 for more details). The modelling domain in this study is 5.4^3 mm^3 , which is close to the thickness of the layer containing SAP particles in hygienic applications, which vary from several mm's to cm's (Buchholz and Graham, 1998). To have $\tau_{swelling} \ll \tau_{flow}$, a large swelling rate is required. We define a dimensionless number τ as follows:

$$\tau = \frac{\tau_{swelling}}{\tau_{flow}} = \frac{\rho_w g K}{k^0 l \mu} \quad (8.15)$$

To have $\tau_{swelling} \ll \tau_{flow}$, τ should be much smaller than unity. This is achieved by using simulations for k^0 values of 10^4 s^{-1} , which is not a physical value but considered permissible for the sake of testing our model. Note that in evaluating τ , the intrinsic permeability in simulations is typically much larger than that of experiments, because of using spherical particles in simulations (see e.g. the discussion in section 7.3). Thus, to have τ smaller than unity in experiments, the value of k would not need to be as small as in our simulations, because the permeability is typically lower in experiments. An additional advantage of a high value of k^0 is that the computational time is reduced as the physical time of the process is also relatively small.

Of course, a third characteristic time-scale exists, namely that of relaxation of particle contact stresses (τ_{def}). If it takes a long time for particle contacts to dissipate their potential energy (i.e. overlap) that was gained due to swelling, particles will swell but not move within the time frame of swelling ($\tau_{def} \gg \tau_{swelling}$). This would cause the porosity value to converge to zero during swelling, because the solid volume increases, but the particle bed does not expand. If $\tau_{def} \ll \tau_{swelling}$, then the overlap can dissipate and the particle bed will expand. We approximate τ_{def} as follows:

$$\tau_{def} = \sqrt{\frac{\rho}{E}} \quad (8.16)$$

in which E is the Young's modulus of the particles and ρ is the particle density (assumed to be 1 g cm^{-3}). Throughout our simulations, we assume $\tau_{swelling} \ll \tau_{flow}$ and $\tau_{def} \gg \tau_{swelling}$, thus the porosity will always converge to zero. However, in future work, the case of $\tau_{def} \ll \tau_{swelling}$ can be tested to study significant particle movements because of swelling particles.

8.4 Results and discussion

8.4.1 Swelling of particles in a rigid box

In this section, results are reported for simulations of swelling particles in a confined box. In what follows, swelling is expressed in terms of absorption ratio Q , which is defined as:

$$Q = \frac{\sum_{i=0}^{N_p} M_i^w + \sum_{i=0}^{N_p} M_i^s}{\sum_{i=0}^{N_p} M_i^s} \quad (8.17)$$

in which M_i^w is the mass of absorbed water in particle i , M_i^s is the initial mass and N_p the number of particles. Figure 8.4 shows the water volume, solid volume and the volume of the pore space as a function of the absorption ratio. The results show that the solid volume increased almost linearly with the absorption ratio, because a small-scale swelling event was simulated with an absorption ratio up to 1.48 g/g. Consequently, the solid volume appeared as a linear function of Q , while for larger absorption ratio's, the functionality would be a non-linear type. Figure 8.4 also shows the decrease in pore volume with absorption ratio, which was a direct consequence of increasing solid volume in a confined box. Hence, the porosity decreased with absorption ratio; see Figure 8.5.

Water saturation decreased during swelling, which was a consequence of water absorption by the particles. The dependency of saturation on absorption ratio revealed two stages of swelling, see Figure 8.4: i) water absorption that caused a decrease in porosity, while the saturation remained constant, and ii) water absorption that caused a decrease in porosity, while saturation decreased rapidly as air infiltrated into the particle packing. The transition between the two stages occurred at an absorption ratio of 1.32 g/g, which is slightly after absorption ratio of 1.28 g/g after which the average pressure difference between air and water exceeded the average entry pressure of the material. Due to air invasion, the wetted solid area decreased and, consequently, the absorption rate decreased and thus the absorption ratio as a function of time converged to a constant value of 1.48 g/g, for this particular simulation setup.

Figure 8.6 shows the evolution of absorption ratio and average radius with time as well as the analytical solution for radius over time following equation 8.12 for fully saturated pore units; i.e. $\frac{A_i^w}{A_i}$ equals unity. Initially, the increase in average radii followed the solution for the saturated case, but the average radii deviated from the saturated solution after an absorption ratio of 1.36 g/g. This corresponded to invasion of air into the pore space, which reduced the wetted solid area and thus the swelling rate (i.e. the wetted solid area decreased).

The simulations were not perfectly mass conservative, because the solid surface areas were computed not for grains but for grain-based tetrahedra; this became significant at lower porosity values, where particles showed a significant amount of overlap. With swelling, the amount of overlap increased from 3.1% to 10.1% and thus the solid surface area could not be computed accurately anymore, resulting in a mismatch of water uptake by the particles and the increase in particle size. In total 2% of the initial water volume was not accounted for.

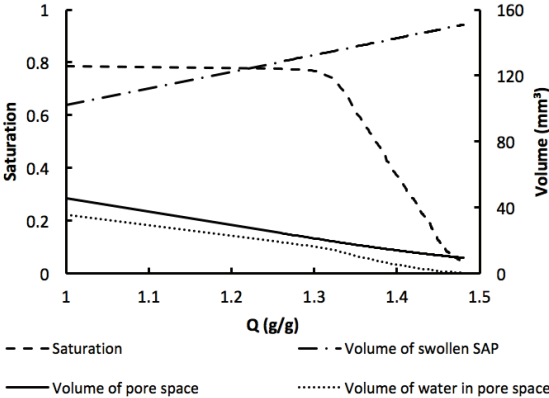


Figure 8.4: Results for swelling of particles in a confined box: volume and saturation as a function of absorption ratio.

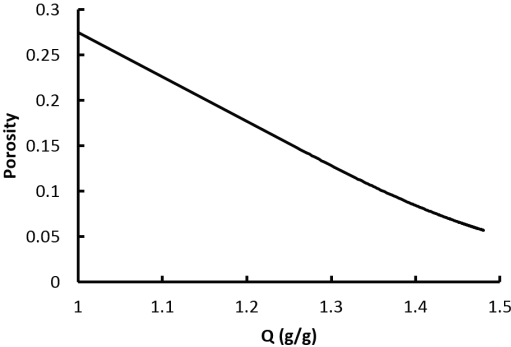


Figure 8.5: Porosity as a function of absorption ratio for swelling of particles in a confined box.

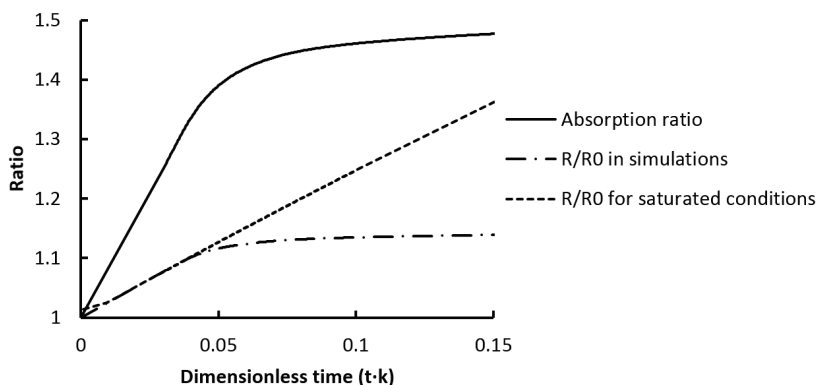


Figure 8.6: Absorption ratio and normalized average radii as a function of time for swelling of particles in a confined box. Note that the radius is the average particle radius.

8.4.2 Swelling of particles in a box with a moving top boundary

In this section, we evaluate simulations of swelling particles in a box that has a moving top boundary. We tested two scenarios, namely particles having a Young's modulus of 10kPa or 1.0 MPa. As a result, the initial porosity value was also different for both simulations, namely: 0.27 (for 10kPa) and 0.30 (for 1.0 MPa). The initial saturation for both samples was 0.81. Thus, more water was present in the packing using a Young's modulus of 1.0 MPa; resulting in more water absorption in that packing (see Figure 8.7). In both simulations, $\tau_{swelling}$ was smaller than τ_{def} and thus the porosity converged to zero (i.e. clogging of the packings occurred).

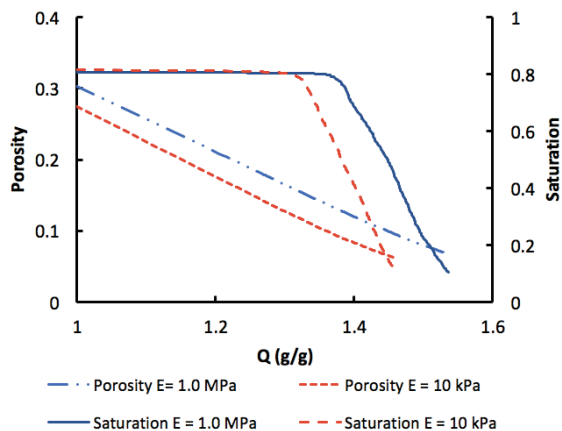


Figure 8.7: Porosity and saturation as a function of water absorption by the SAP particles. The blue lines indicate results for simulations using a Young's modulus of 1.0 MPa, while the red lines indicate results for 10 kPa.

Figure 8.7 shows the two stages of swelling that were identified in previous section, but then for particles having a Young’s modulus of 10 kPa and 1.0 MPa. That Figure shows that the fraction of wetted solid surface area remained roughly constant to its initial value until the saturation rapidly decreased; consequently, the fraction of wetted solid surface decreased as well. During invasion of air, the volumetric-averaged pressure difference between air and water increased (see Figure 8.8), which is a result of the effect of lower water saturations, thus higher values for capillary pressure, despite the opposing effect of decreasing pore unit radii and pore throat radii (see Figure 8.9).

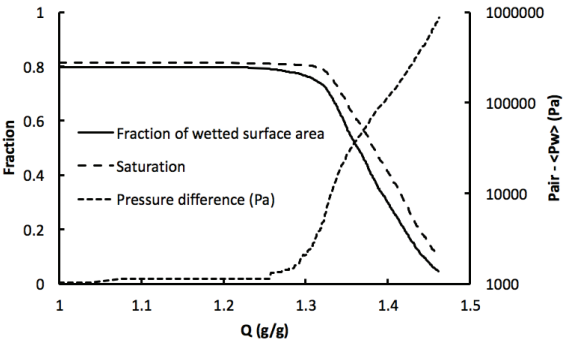


Figure 8.8: The dependency of saturation, pressure difference between air and water, as wetted solid surface area on absorption ratio for simulations using a Young’s modulus of 10 kPa. Note that the wetted solid surface area is normalized to total solid surface area.

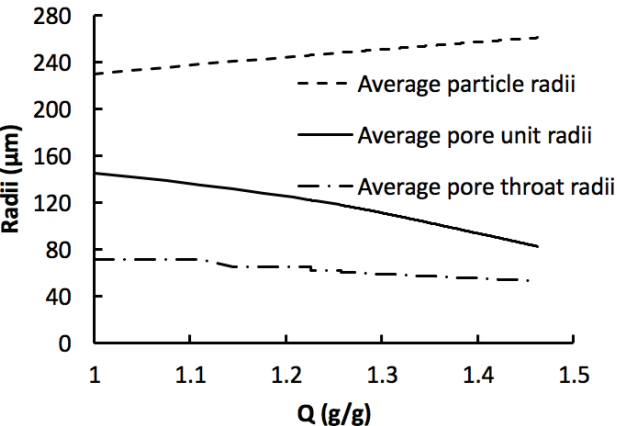


Figure 8.9: Arithmetic-averaged values of particle radii, pore unit radii and pore throat radii as a function of absorption ratio using a Young’s modulus of 10 kPa.

For packings with a higher initial porosity (using a Young’s modulus equal to 1.0 MPa), the moment of air invasion is later than that for a lower initial porosity value; see Figure 8.7. This was because of larger porosity values that allowed the particles to swell more before the water suction was sufficiently low to force air to infiltrate.

The two stages of swelling were also clearly visible in the plots of absorption ratio as function of time, see Figure 8.10. Initially, the absorption ratio increased linearly with time. However, when air invaded the sample, the swelling rate decreased because of a decrease in the fraction of wetted solid surface, see Figure 8.10.

The height of the particle bed did not change significantly because of the short time that it took for swelling to occur. In that case, the particles did not have enough time to dissipate energy at their contact points. The volume of the modelling domain increased by 0.3% for both 10 kPa and 1.0 MPa.

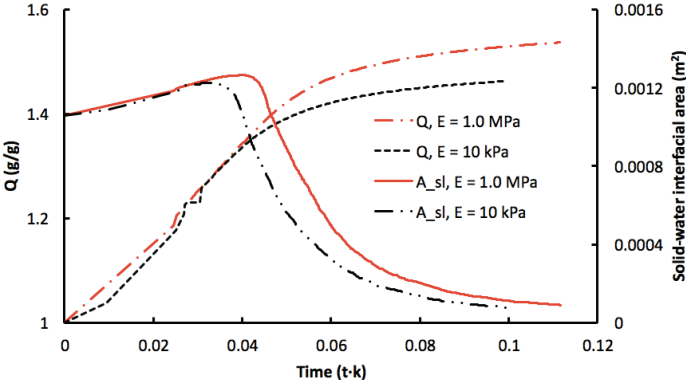


Figure 8.10: The absorption ratio and solid-water interfacial area as a function of normalized time for particles having a Young’s modulus of 1.0 MPa (red lines) and 10 kPa (black lines).

8.4.3 Solid-water interfacial area as function of swelling and saturation

In the continuum-scale model developed by Diersch et al. (2010), the following equation was employed to approximate the fraction of solid area covered by water as a function of saturation (S):

$$a_{sl} = \frac{1 - e^{-S\alpha_{exp}}}{1 - e^{-\alpha_{exp}}} \quad (8.18)$$

where α_{exp} is a fitting parameter that is also present in the functionality of Van Genuchten parameter α as a function of absorption ratio and porosity value (Diersch et al., 2010).

In Figure 8.11, we have plotted the fraction of wetted solid area that was found in our simulations as a function of saturation, using an effective saturation which was normalized to the initial water saturation. Equation 8.18 was also plotted in that Figure, using two values of α_{exp} , namely -1.04 and 10^{-3} , where any value in the positive limit of α_{exp} to zero (but not equal to zero) yielded similar results to that of 10^{-3} . A positive value of α_{exp} was used, because Mirnyy et al. (2012) reported a positive value of 0.4 for α_{exp} , based on experimental observations. However, a much better fit was achieved when using a negative value for α_{exp} , see Figure 8.11. The wetted surface area for a negative α_{exp} value is lower than for a positive value of α_{exp} . A reason for the underestimation of wetted solid area compared to experimental observations by Mirnyy et al. (2012) could be the presence of more heterogeneities within the pore structure. For example, a wider pore size distribution can be present in experiments due to the non-spherical particle shapes and higher porosity values. In that case, domains of smaller pore sizes could remain longer fully saturated, causing the wetted surface area to remain relatively high (i.e. a positive value of α_{exp}).

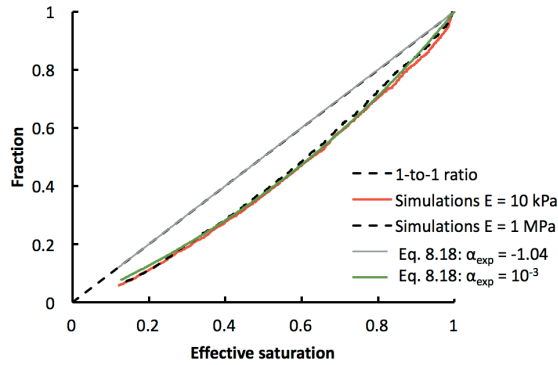


Figure 8.11: Wetted solid area normalized to the solid surface area as a function of effective saturation. The dashed line indicates the 1-to-1 ratio, which overlays light grey lines which are obtained using equation 8.17. The red and black lines are simulation results using two different Young’s moduli (10 kPa and 1 MPa, respectively).

8.5 Conclusions

A pore-scale modelling technique was presented for simulation of unsaturated flow in deforming and swelling granular materials. The discrete element method was used for calculations of swelling and subsequent deformation packings of spherical particles. Unsaturated flow was solved using a pore-scale version of IMPES (implicit pressure and explicit saturation scheme) that was tailored for pore units in a deforming packing of spheres. Deformation was included by changing the volume of pore units, pore unit radii, pore throat radii, and hydraulic conductivity during swelling. Two modelling scenarios were considered, namely: swelling of particles in a confined box and swelling in a box that had a moving top boundary. In the second scenario, swelling was assumed to be fast compared to particle motions. Consequently, the particles moved very little during swelling and thus the porosity decreased to a low value. Results revealed a two-stage swelling event. Initially, only the porosity of the particle packing decreased while the saturation remained constant, but after a threshold absorption ratio, the saturation started to decrease as well, because of air infiltration into the modelling domain. The relation between wetted solid surface area and saturation was satisfactorily described by a semi-empirical equation by Diersch et al. (2010). Albeit that the fraction was slightly overestimated by the semi-empirical equation, which was tailored for swelling particle packings having a larger porosity value than in our simulations.

Chapter 9

Summary and Perspectives

9.1 Summary

This thesis presents a grain-scale modelling technique for the study of swelling granular materials. An existing grain-scale model, namely the Discrete Element Method, has been extended with three functionalities that were presented in three sub parts of this thesis, namely: i) large swelling of individual particles; ii) a capillarity module based on the pore-unit assembly method and iii) a module for dynamic unsaturated flow during drainage of a deforming bed of particles. This work shows the applicability and versatility of the grain-scale model to describe swelling of a bed of particles under saturated and unsaturated conditions as well as dynamic and quasi-static conditions. The aim throughout this work is to study processes that occur in a bed of swelling particles, to answer research questions that cannot be answered with macro-scale investigations and to develop an appropriate tool based on grain-scale modelling.

In Chapter 2, we study a bed of swelling particles made from super absorbent polymers (SAP) under fully saturated conditions. In that work, the mechanical framework of DEM was tailored for swelling particles, where spherical particles could grow and soften during swelling. Values of particle-scale mechanical parameters were found in the literature and the swelling rate of individual particles was measured in experiments. We assumed particles to be spherical having a particle size distribution of real SAP particles. Although simplifications were employed, results of simulations corresponded reasonably well to experimental measurements in terms of the height of a free particle bed evolving over time. This was considered as an indication that DEM could be an appropriate tool to study the swelling of SAP particles.

In Chapter 2, we developed a new equation for the swelling rate, which we employed to translate the swelling rate in experiments to that in the numerical model. It was based on diffusion of water inside a swelling spherical particle. However, the solution was based on an approximation of the gradient in water content. Therefore, in Chapter 3, we developed a comprehensive model for water diffusion into a swelling spherical particle that had a free and moving boundary. In that model, not only water diffusion was considered as a time-dependent process, but also water uptake across the particle surface. A dimensionless variable was found that determined the contribution of

both diffusion and water uptake to the overall swelling rate of the particle. Analysis showed that the swelling rate of a particle can decrease when the water uptake at the surface is slower than the diffusion of water inside the particle. Thus, applying a coating layer to a swelling particle can initially slow down the overall swelling rate. The swelling rate of individual particles that was found using the model was compared to results from the swelling-rate equation of Chapter 2. The initial swelling rate was similar for both models, but small deviations occurred at later stages of swelling.

Swelling not only occurs under saturated conditions, but also under unsaturated conditions. Therefore, the pore-unit assembly method was employed in Chapter 4, coupled to DEM, to simulate capillarity phenomena. Using this coupled model, capillary pressure-saturation relationships were constructed for packings of SAP particles, with varying absorption ratios and porosity values. The capillary pressure-saturation curves were fitted with the Van Genuchten equation, which resulted into separate parameters for drainage and imbibition as function of absorption ratio and porosity. Then, the capillary pressures of all drainage and imbibition curves were scaled to the Van Genuchten parameter α for drainage and imbibition, respectively. The saturation was plotted as effective saturation. Consequently, all curves for drainage collapsed into one single scaled curve for drainage and all curves for imbibition collapsed into one single scaled curve for imbibition, indicating that the slope for all drainage curves were constant and the slopes for all imbibition curves were constant. Fitting equations for residual saturation, irreducible water saturation and Van Genuchten parameter α were determined. The fitting equations were considered to depend on porosity and absorption ratio, which were assumed to be independent variables for swelling materials. Porosity was considered as a proxy for the state-of-stress in a particle packing and the absorption ratio represented the degree of swelling.

Chapter 5 further elaborates on the coupling of the pore-unit assembly method with DEM by comparing simulated capillary pressure-saturation curves to those from the well-known pore morphology method and to those from experiments, based on literature data. In general, the capillary pressure-saturation curves constructed by the pore-unit assembly method correspond reasonably well to experimental data. This is especially true when considering that particles were assumed to be spherical and that only the particle size distribution and the porosity value were used as input parameters for the model. Of course, the ability of the model to accurately reproduce experimental data relies on the ability of spherical particles to represent real granular materials and on the pore-scale definition of entry pressure; i.e. should one use the Mayer-Stowe and Princen method or the hemisphere approximation to determine the entry pressure of a

pore throat. Nonetheless, the coupling of the pore-unit assembly method with DEM is versatile for studying effects of properties of particle packings on capillary pressure-saturation curves (see for example Mahmoodlu et al., 2016; Nikooee et al., 2016).

In Chapters 2 to 5, grain-scale simulations were conducted using spherical particles. This is a good assumption for either predictive simulations of granulates that have a near-to-spherical shape (e.g. glass-beads and filter sands) or qualitative simulations, where one is interested in various effects and processes. However, for predictive simulations of particles that are irregular in shape, non-sphericity becomes important because it affects hydraulic parameters. Since SAP particles are irregular in shape, the particle shape should be accounted for in predictive simulations. The effect of particle shape becomes apparent when studying porosity values of beds of SAP particles. Measurements have shown that porosity may vary from 0.70 to 0.10 during swelling. But, the range of porosity values in simulations of spherical particles are only within 0.45 to 0.20. Thus, SAP particles exhibit a much larger variation in porosity values than simulations of spherical particles can reproduce. Therefore, we employed in Chapter 6 an extended version of DEM for particles with non-spherical shapes. Sets of overlapping spheres were used to represent real SAP particles (often referred to as clumps). A clump generation algorithm was newly developed to construct 20 clumps representing 20 SAP particle shapes which were measured experimentally, using micro-CT. Results showed that simulations of those clumps yielded porosity values that were close to experimentally determined values. The packings of clumps can and will be utilized in future studies to investigate the effect of particle shape on hydraulic parameters, such as the permeability (using direct simulations) and the capillary pressure-saturation relationships (using the pore morphology method).

In Chapters 7 and 8, a tool was developed for investigating dynamics of flow during drainage of swelling and deformable granular materials. In Chapter 7, the pore-unit assembly method was extended to include dynamics of unsaturated flow in rigid packings of spheres, while in Chapter 8 the pore-unit assembly method was coupled with DEM to simulate deforming packings of swelling spheres. Chapter 7 focusses on dynamic drainage in packings of spheres. A merging algorithm was introduced to extract the assembly of pore units, based on triangulation of the pore space. A pore-scale version of IMPES (IMPLICIT Pressure solver and EXPLICIT Saturation update) was employed to solve the set of equations of unsaturated flow. Using the model, dynamic drainage was simulated for a particle packing, having a normal particle size distribution. Dynamic drainage occurred through infiltration of air via preferential pathways that were present in the pore structure, causing an irregular infiltration front. The finger-like infiltration

caused a non-monotonic relationship between pressure difference between air and water with saturation. In Chapter 8, the dynamic code was extended to include deformation of pore units and subsequently coupled to DEM. A one-way coupling was chosen, where deformation affected water flow, but water flow did not affect the mechanical aspects of the particle packing. The code was employed to simulate the swelling of a bed of particles in a confined box and in a box with a moving top boundary. The developed model can be used to simulate couplings of unsaturated flow, swelling and deformation for realistic time scales and scenarios for swelling of real SAP particles. Furthermore, the current form of the numerical scheme in Chapters 8 is tailored for swelling particles, but of course, deformation in any dense granular material can be simulated, such as dynamic drainage during triaxial tests of soils.

9.2 Perspectives

Grain-scale models offer useful insights into processes that occur in beds of swelling particles. In this work, various aspects were considered, but there are many remaining research questions regarding both grain-scale modelling and processes in swelling materials.

For example, properties of individual SAP particles were assumed to be independent of processes that occur inside particle beds. Thus, the swelling behaviour, shape, and other mechanical properties were imposed to individual particles. However, properties of individual particles can be affected by processes that occur in a bed of particles. For example, during swelling under a confining stress, SAP particles may swell towards domains of local stress minima (into pores), causing the particle shape to deviate from its initial shape. This would for example happen during swelling of a bed of particles in a confined box, which was studied in Chapter 8 (sections 8.4.1 and 8.4.2). To describe the response of particles to various processes that occur in their vicinity, comprehensive numerical models can be employed. Of course, adding such a complex coupling would be at the expense of both computational time and simplicity of the presented model.

Moreover, dynamic drainage was simulated in packings of spherical particles (see Chapters 7 & 8), although SAP particles are not spherical, as discussed in Chapter 6. As an addition to this work, the flow algorithm presented in Chapter 7 could be extended to allow for flow computations in packings of clumps. However, meshing of pore space currently relies on triangulation, where it assumes that pore throats are surrounded by three spheres. Therefore, triangulation will not work for clumps that contain numerous spheres, as a pore throat will be enclosed by more than three spheres.

Thus, for clumps, a new algorithm should be developed for identification of pore units, which is remains efficient.

Regarding swelling materials, the macro-scale model of Diersch et al. (2010) for swelling of a bed of particles is tailored for a constant confining stress. This is particularly embedded in the constitutive equations. However, to develop a more realistic model with varying confining stresses, the constitutive equations should be made dependent on the state of stress inside particle packings. In section 4.5, a relationship between Van Genuchten parameter α , absorption ratio, and porosity was found using the grain-scale modelling technique. Similarly, a 3-dimensional surface was generated to describe the relation between porosity value, absorption ratio and confining stress for swelling SAP particles (see section 6.4.7). These types of constitutive equations can be utilized in macro-scale simulations. However, the mechanical aspects of hydro-mechanical coupling should still be investigated, e.g. how does the mechanical strength of a particle packing change with swelling and with the occupancy of pores by water.

Finally, the grain-scale modelling technique that was presented in this thesis should not be considered as a replacement of macro-scale simulations or experiments. The grain-scale modelling technique should rather be used in conjunction with experiments and macro-scale simulations. Consider the grain-scale modelling technique as a virtual experiment, where grain-scale physics is imposed and macro-scale quantities are obtained. Virtual experiments can be used to verify macro-scale models and to give detailed insight in pore-scale processes. This is particularly true for complex cases such as swelling of granular materials, under unsaturated conditions.

Appendices

Appendix A

Van Genuchten equation

Capillary pressure and saturation data points from experiments and simulations were fitted with the Van Genuchten formula (Van Genuchten 1980), which reads:

$$S_e = \frac{1}{(1 + |\alpha P_c|^n)^{1-1/n}} \quad (A.1)$$

where α [Pa^{-1}] and n are fitting parameters, representing the inverse of the entry pressure and the pore size distribution, respectively. The effective saturation S_e defined as:

$$S_e = \frac{S - S_r}{S_{max} - S_r} \quad (A.2)$$

Here, S is the saturation, S_r is the residual water saturation after drainage, and S_{max} is the maximum water saturation after imbibition. For results on primary imbibition S_r is set to 0.0. For results on primary drainage S_{max} is set to 1.0. Typically, drainage and imbibition curves are fitted separately with the Van Genuchten function, leading to separate Van Genuchten parameters for drainage and imbibition, namely: α_{dr} , α_{imb} , n_{dr} , n_{imb} , where subscript *dr* indicates drainage, and *imb* indicates imbibition. All results were fitted using SWRC fitting program (Seki 2007).

Appendix B

An equation for the swelling rate of an individual particle

The swelling of a particle is assumed to be governed by the diffusion of water molecules into the particle. Consider a spherical particle with initial radius r_i^0 and radius $r_i(t)$ at later times. We introduce a local concentration of water $c_i^w(r, t)$ within the SAP particle, which is defined as the mass of water per unit volume. Similarly, $c_i^s(r, t)$ is the local solid mass concentration. Local volume fractions θ_w and θ_s are also defined as the volume of water and solid, respectively, per unit volume of space, such that:

$$\theta_w + \theta_s = 1 \quad (B.1)$$

If the mass density of pure water and solid are denoted by ρ_w and ρ_s , respectively, equation B.1 can be recast in the following form:

$$\frac{c_i^w}{\rho_w} + \frac{c_i^s}{\rho_s} = 1 \quad (B.2)$$

The particle has a volume $V_i(t)$, water mass $M_i^w(t) = \int_0^{r_i} 4\pi r^2 c_i^w(r, t) dr$, and solid mass $M_i^s = \int_0^{r_i} 4\pi r^2 c_i^s(r, t) dr$, which is a constant. They are related by:

$$V_i = V_i^w + V_i^s = \frac{M_i^w}{\rho_w} + \frac{M_i^s}{\rho_s} \quad (B.3)$$

Assuming radially symmetric diffusion of water into the particle, the local mass balance equation reads:

$$\frac{\partial c_i^w}{\partial t} = \frac{D}{r^2} \frac{\partial}{\partial r} \left(r^2 \frac{\partial c_i^w}{\partial r} \right), \quad 0 \leq r \leq r_i \quad (B.4)$$

where D [L^2T^{-1}] is the diffusion coefficient of water into the particle, which is assumed to be constant (i.e. linear diffusion). The initial condition is $c_i^w(0) = 0$, and boundary conditions are:

$$\begin{cases} \frac{\partial c_i^w}{\partial t} = 0 & \text{at } r = 0 \\ c_i^w = c_i^w|_{r_i} & \text{at } r = r_i \end{cases} \quad (B.5)$$

The second boundary condition assumes local equilibrium at the particle surface. We multiply equation B.4 by $4\pi r^2$ and subsequently integrate over r :

$$\int_0^{r_i} \frac{\partial c_i^w}{\partial t} 4\pi r^2 dr = \int_0^{r_i} \frac{D}{r^2} \frac{\partial}{\partial r} \left(r^2 \frac{\partial c_i^w}{\partial r} \right) 4\pi r^2 dr \quad (B.6)$$

We apply Leibniz integral rule to the left-hand side of equation B.6 and integrate the right-hand side and use boundary conditions B.5. We obtain:

$$\frac{d}{dt} \left\{ \int_0^{r_i} 4\pi r^2 c_i^w(r, t) dr \right\} - 4\pi r_i^2 c_i^w|_{r_i} \frac{dr_i}{dt} = 4\pi r_i^2 D \frac{\partial c_i^w}{\partial r} \Big|_{r_i} \quad (B.7)$$

The term inside the curly bracket is equal to the total mass of water in the grain, $M_i^w(t)$. The term $4\pi r_i^2 \frac{dr_i}{dt}$ can be replaced by $\frac{4\pi}{3} \frac{dr_i^3}{dt} = \frac{dV_i}{dt}$, which using equation B.3 can be written as $\frac{1}{\rho_w} \frac{dM_i^w}{dt}$. Therefore, B.7 is recast in the following form:

$$\left(1 - \frac{c_i^w|_{r_i}}{\rho_w} \right) \frac{dM_i^w}{dt} = 4\pi r_i^2 D \frac{\partial c_i^w}{\partial r} \Big|_{r_i} \quad (B.8)$$

We rewrite the term in brackets on the left-hand side of equation B.8 as $\frac{c_i^s|_{r_i}}{\rho_s}$, following equation B.2. Then, we assume that on the surface of the particle, the maximum water concentration is reached such that $\frac{c_i^s|_{r_i}}{\rho_s} = \frac{M_i^s}{\rho_s V_i^{max}} = \frac{4\pi}{3V_i^{max}} (r_i^0)^3$, with V_i^{max} being the maximum volume of the particle. Then, equation B.8 becomes:

$$\frac{4\pi (r_i^0)^3}{3V_i^{max}} \frac{dM_i^w}{dt} = 4\pi r_i^2 D \frac{\partial c_i^w}{\partial r} \Big|_{r_i} \quad (B.9)$$

We approximate $\frac{\partial c_i^w}{\partial r} \Big|_{r_i}$ by $\frac{c_i^w|_{r_i} - \bar{c}_i^w}{\alpha r_i}$ where αr_i is the distance from r_i to a location in the SAP particle at which c_i^w is equal to the average water concentration $\bar{c}_i^w(t)$. Finally, we note that $\frac{M_i^s}{\rho_s} = \frac{4\pi}{3} (r_i^0)^3$. With these considerations, equation B.9 becomes:

$$\frac{1}{V_i^{max}} \frac{dM_i^w}{dt} = \frac{3D}{\alpha} \frac{r_i}{(r_i^0)^3} \left(\frac{M_i^s (Q^{max} - 1)}{V_i^{max}} - \frac{M_i^w}{V_i} \right) \quad (B.10)$$

Equation B.10 is multiplied by V_i^{max} and divided by M_i^s , and the definition of Q_i^{abs} is used such that we obtain:

$$\frac{dQ_i^{abs}}{dt} = \frac{3D}{\alpha} \frac{r_i}{(r_i^0)^3} \left(Q^{max} - 1 - \frac{M_i^w V_i^{max}}{M_i^s V_i} \right) \quad (B.11)$$

We can show that $\frac{V_i^{max}}{V_i}$ is approximated by $\frac{Q^{max}}{Q_i^{abs}}$, such that equation B.11 is reduced to:

$$\begin{aligned} \frac{dQ_i^{abs}}{dt} &= K_i \left(\frac{Q^{max} - Q_i^{abs}}{Q_i^{abs}} \right) \\ K_i &= \frac{3D}{\alpha} \frac{r_i}{(r_i^0)^3} \end{aligned} \quad (B.12)$$

Equation B.12 bears similarities with an equation reported previously in the literature, namely: $\frac{dQ_i^{abs}}{dt} = K_i(Q^{max} - Q_i^{abs})$, which is a first-order kinetic rate for the increase of Q_i^{abs} (Buchholz, 1998b; Esteves, 2011). In equation B.12, $K_i \propto \frac{r_i}{(r_i^0)^3}$ reduces to $K_i \propto \frac{1}{(r_i^0)^2}$ for small-scale swelling, which is indeed reported in the literature as $K_i = \frac{\pi^2 D}{(r_i^0)^2}$ (Buchholz, 1998b; Esteves, 2011). We have calculated the difference between equation B.12 and $\frac{dQ_i^{abs}}{dt} = K_i(Q^{max} - Q_i^{abs})$ with $K_i = \frac{\pi^2 D}{(r_i^0)^2}$ as reported in (Buchholz, 1998b), which is shown in Figure B.1. That Figure shows that the swelling rate $\frac{dr_i}{dt}$ for both definitions of K_i exhibits the same monotonic decrease of $\frac{dr_i}{dt}$ with r_i , albeit that they differ from each other.

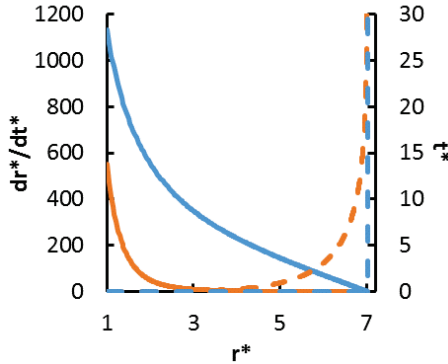


Figure B.1: Swelling rates for the swelling of individual particles, using dimensionless parameters: $t^* = \frac{tD}{(r_i^0)^2}$ and $r^* = \frac{r_i}{r_i^0}$. Solid lines indicate $\frac{dr^*}{dt^*}$ and dashed lines indicates t^* .

Orange represents results by equation B.12 whereas blue represents results with $\frac{dQ_i^{abs}}{dt} = \frac{\pi^2 D}{(r_i^0)^2} (Q^{max} - Q_i^{abs})$.

Free and moving boundary conditions of a swelling spherical particle

Here, a free-moving boundary condition is derived for a sphere based on the volume balance in that sphere. Let us start with a simple volumetric balance, the initial volume (V_0) and the volume of absorbed water (V_w) gives the total volume (V):

$$V = V_0 + V_w \quad (C.1)$$

We may rewrite equation C.1 as follows:

$$\frac{4}{3}\pi R_0^3 + \int_0^R \theta 4\pi r^2 dr = \frac{4}{3}\pi R^3 \quad (C.2)$$

where θ is the volumetric water content, R the particle radius and R_0 its initial value. Next, equation C.2 is differentiated with respect to time and combined with Leibniz integral rule, which yields:

$$\int_0^R \frac{\partial \theta}{\partial t} 4\pi r^2 dr = 4\pi R^2 \frac{dR}{dt} - \theta_b 4\pi R^2 \frac{dR}{dt} \quad (C.3)$$

We realize that $\frac{\partial \theta}{\partial t}$ can be replaced by $\frac{D}{r^2} \frac{\partial}{\partial r} \left(r^2 \frac{\partial \theta}{\partial r} \right)$ for spherical diffusion, which is then integrated to yield the final boundary condition:

$$D \frac{\partial \theta}{\partial r} \Big|_R = (1 - \theta(R, t)) \frac{dR}{dt} \quad (C.4)$$

Appendix D

Permeability as function of swelling and porosity change

For sake of completeness, we present in this section the dependency of permeability on porosity value and absorption ratio. The permeability is obtained using the Pore Finite Volume (PFV) method, which is based on the assembly of pore units (see section 2.4 for more details). At the top and bottom boundaries of the particle packing, water pressure was imposed with the top boundary having a larger water pressure. The side boundaries were considered impermeable. The water pressure was then solved using PFV and the permeability was subsequently obtained using Darcy's law. Figure D.1 shows the permeability as function of absorption ratio for varying porosity values. The permeability values (κ) were scaled to the particle radii. The particle radii were approximated by $(R_i^0)^2 Q^{\frac{2}{3}}$, following equation 4.4. This gives:

$$\bar{\kappa} = \frac{\kappa}{(R_i^0)^2 Q^{\frac{2}{3}}} \quad (D.1)$$

in which $\bar{\kappa}$ is the dimensionless permeability. What remains is that $\bar{\kappa}$ is constant over Q such that we can obtain $\bar{\kappa}$ as function of porosity (ϕ). For this we find, based on the Carman-Kozeny equation:

$$\bar{\kappa} = 0.077 \frac{\phi^3}{(1-\phi)^2} + 0.010 \quad (D.2)$$

Finally, the equation for $\kappa(Q, \phi)$ can be obtained by combining equations D.1 and D.2, which results in:

$$\kappa(Q, \phi) = \left[0.077 \frac{\phi^3}{(1-\phi)^2} + 0.010 \right] (R_i^0)^2 Q^{\frac{2}{3}} \quad (D.3)$$

Results in Appendix D are based on the work by J. Dekker (2016) and can be found in his B.S.c. thesis entitled: "Using a DEM-PFV coupled model to investigate the effect of porosity and swelling on the permeability of packings of AGM particles"

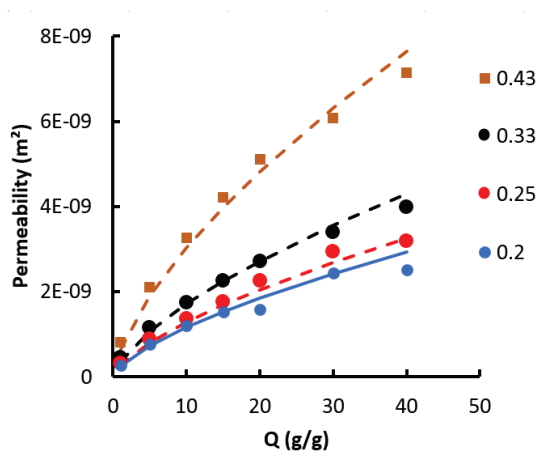


Figure D.1: Permeability values as function of absorption ratio for four different porosity values. The symbols indicate results from simulations with PFV, while the lines represent the fitting of equation D.3. Note that in total 6 porosity values were simulated, but only 4 are shown for visualization purposes.

Mayer and Stowe-Princen approximations

To compute the entry pressure of a pore throat, the Mayer and Stowe-Princen approximation can be employed to obtain the radius of curvature of arc menisci in a pore throat. Figure 5.2a shows a cross-section where a main terminal meniscus has just entered the pore throat and corners in the invaded part of the pore throat are still filled by water, forming arc menisci. The following quantities can be identified in Figure 5.2a: the length of air-water contact line (L_{aw}), the length of the air solid contact line (L_{as}), the cross-sectional area that is filled with air (A_{ij}^n) and the radii of the air-water interface in the plane of the pore throat (R_{ij}^{MSP}). The values of A_{ij}^n , L_{aw} and L_{as} are found on the pore geometry resulting from triangulation of the packing of spheres, for the computation of these values, see Yuan et al. (2016). For computing R_{ij}^{MSP} , we note that surface tensions should in balance with the pressure difference between pore unit i and j , such that:

$$(P_i - P_j)A_{ij}^n = L_{aw}\gamma_{aw} + L_{as}\gamma_{as} - L_{as}\gamma_{ws} \quad (E.1)$$

This equation can be rewritten using Young's equation, $\gamma_{as} - \gamma_{ws} = \gamma_{aw} \cos \theta$, to yield:

$$R_{ij}^{MSP} = \frac{A_{ij}^n}{L_{aw} + L_{as} \cos \theta} \quad (E.2)$$

where the smallest value of R_{ij}^{MSP} for which equation E.2 holds is chosen as radius for drainage.

Parameterization of the clump generation algorithm

F.1 Determination of φ , α , and ϑ

In this Appendix, the values of parameters φ , α , and ϑ are determined (see section 6.2.2 for their definition). Clump should represent SAP particles as good as possible, while not using too many spheres. To identify appropriate values of φ , α , and ϑ for SAP particles, we have chosen one SAP particle for which different clump realizations were generated by varying: i) φ values from 0.025 to 0.075, which defines the fraction of spheres having their centres outside the particle; ii) α values from 0.05 to 0.25, which defines the bulginess of the spheres, and iii) ϑ from 0.75 to 0.95, which defines the fraction of the surface of a particle that is overlaid by spheres. After all realizations were constructed, the quality of the clump was evaluated in terms of sphericity. Sphericity is computed for both the SAP particles and the clump realizations; it is defined as:

$$sphericity = \frac{\pi^{\frac{1}{3}}(6V)^{\frac{2}{3}}}{A} \quad (F.1)$$

in which V is the volume and A is the surface area of the particle or clump.

Figure F.1a shows the sphericity of all clump realizations of one SAP particle as function of the number of spheres. The sphericity decreases with increasing number of spheres per clump, which is related to the increase in surface area when using more spheres in a clump. The sphericity tends to go to unity when the number of spheres goes to unity, which is indeed the sphericity of a sphere. A broad range of clump realizations give a reasonable approximation of the sphericity of the SAP particle. In particular, using more than 9 particles per clump yields good results. The closest sphericity value was obtained using $\varphi = 0.025$, $\alpha = 0.05$, and $\vartheta = 0.85$, which gave a sphericity of 0.70 which is close to that of the SAP particle, which 0.72.

By matching the sphericity of a clump to that of a SAP particle, the ratio of volume to surface area is maintained. However, the magnitude of both the surface area and the volume of a clump can deviate from that of a particle. To investigate this phenomenon, we plot the normalized volume and normalized surface area in Figure F.1b, in respect to their corresponding values of the SAP particles. Thus, in that Figure, unity represents a perfect match (see dashed lines). Results show that the normalized

volume increases roughly linearly with the normalized surface area ratio. The best realization in terms of sphericity (deviation of sphericity within 5% deviation) yields a deviation in normalized volume and normalized surface area of 1.17 and 1.15, respectively. Even though, better approximations of both normalized values are found using different parameters ($\varphi = 0.025$, $\alpha = 0.05$, and $\vartheta = 0.75$), we use the value of φ , α , and ϑ that correspond to the best sphericity value. This is to preserve the volume-to-surface area ratio of a particle, which is deemed more important than to mimic the absolute values of surface area and volume.

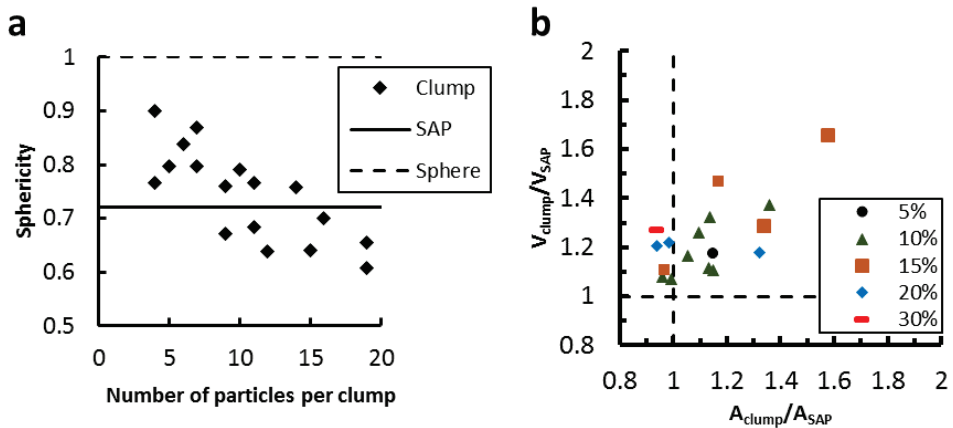


Figure F.1: Statistics of various clump realizations of one SAP particle using varying values of φ , α , and ϑ : a) the sphericity of clumps vs. the number of spheres per clump, where the solid line represents the sphericity of the SAP particle and the dashed line is the sphericity of a sphere. b) Normalized volume vs. normalized surface area ratio of various clump realizations. The colours and shapes indicate the deviation in sphericity of a clump in respect to the SAP particle.

F.2 Clump library

Figure F.2a shows the statistics of clump realizations for all SAP particles, using $\varphi = 0.025$, $\alpha = 0.05$, and $\vartheta = 0.85$. Clump realizations overestimate both the volume and surface area of the SAP particles for round-like SAP particles, by a factor up to 1.6. For plate-like particles, the clump realization overestimates the volume by a factor up to 2.8. This is an artefact of using spheres to represent a particle, because the likelihood of generating a sphere that sticks out of a thin particle is large and on top of that the fact that a sphere sticks out has a more pronounced effect for thin particles than for round-like particles. Subsequently, the volume gets overestimated. As a consequence, the sphericity of clumps that represent plate-like particles is larger than the particle, see Figure F.2b.

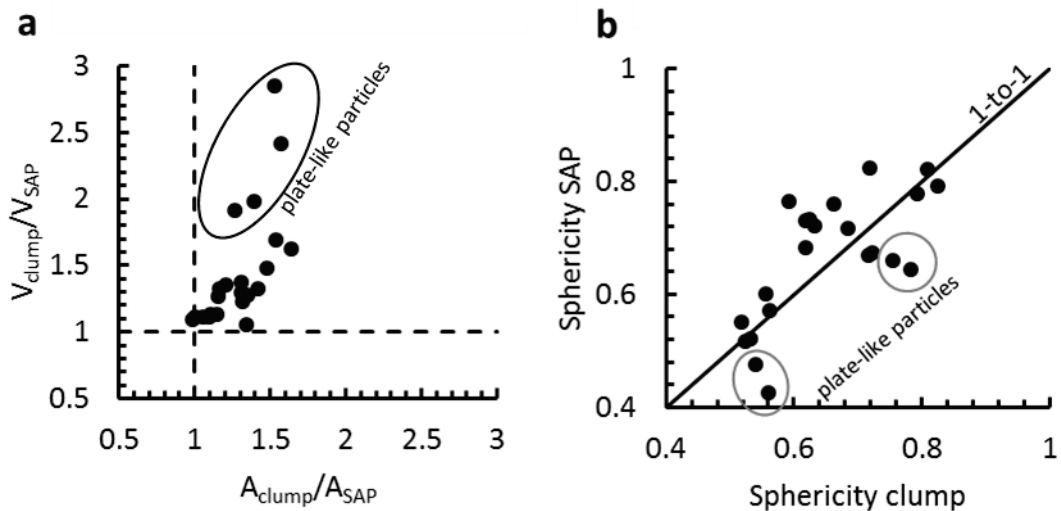


Figure F.2: Statistics of clump realizations of SAP particles. a) Ratio in volume versus the ratio in surface area of the clump and SAP particle. b) Sphericity of the SAP versus the sphericity of the clump.

Comparison of methods for extraction of pore unit properties

In this section, we compare extraction methods of pore structures by PUA in combination with the merging algorithm presented in Chapter 7, Avizo and Geodict. A packing of 1500 spheres was generated that represent Ottawa sand (F32/F50, 1:1 ratio, at a porosity of following Camps-Roach et al., 2010). The packing was exported and used in all three software's. Image analysing software Avizo (FEI, 2016) can extract the pore structure in terms of pore bodies (similar to pore units) and pore throats. Avizo sets the pore body radius equal to the radius of a sphere having the same volume as the pore body, whereas the pore throat radius is set equal to the radius of a circle having the same area as the pore throat. The packing was also imported into the pore morphology software GeoDict (Math2Market, 2016), in which the pore body and pore throat size distributions were computed based on inscribed spheres in the pore space.

Figure G.1a shows the distribution of pore body radius obtained by the three models. Results for PUA are very similar to that of GeoDict, because both models compute the radius based on inscribed spheres. Albeit in PUA, the inscribed sphere is that of a fitted regular shape and not the actual space in the packing of spheres. That is the reason for a small difference in mean pore body radius obtained from pore morphology and PUA, 70 μm and 88 μm , respectively. The distribution in pore body radius by Avizo software is very broad with a mean radius of 158 μm , because it calculates the radii from volume equivalent spheres rather than inscribed spheres.

The pore throat size distributions obtained from the three different methods are shown in Figure G.1b. The mean radii are 53 μm , 44 μm , and 66 μm for PUA, GeoDict, and Avizo, respectively. Thus, PUA gives higher values of pore throat radii than GeoDict. But, PUA gives lower values of pore throat radii than Avizo, because Avizo computes the radii of the area equivalent circle of a pore throat whereas PUA and GeoDict use an inscribed circle. Although the distribution in pore throat radii varies among the three methods, we believe that the -nit assembly yields reasonable results for pore throat radii.

The coordination numbers obtained from our model show a saw tooth distribution (see Figure G.1c). This is due to the merging algorithm that we have used. For example, one grain-based tetrahedron has a coordination number 4, while two

merged grain-based tetrahedra have a coordination number 6, and 3 merged tetrahedra have a coordination number of 8. Many pore units with those three coordination numbers are present in the reconstructed pore unit assembly. Nevertheless, the distribution in coordination number follows the trend of that by Avizo.

Based on the three distributions, we conclude that using triangulation and a subsequent merging algorithm captures the main features of the pore structure in packings of spheres, while being fast, typically less than a few seconds. Albeit various artefacts exist in the distributions that are related to the extraction algorithm.

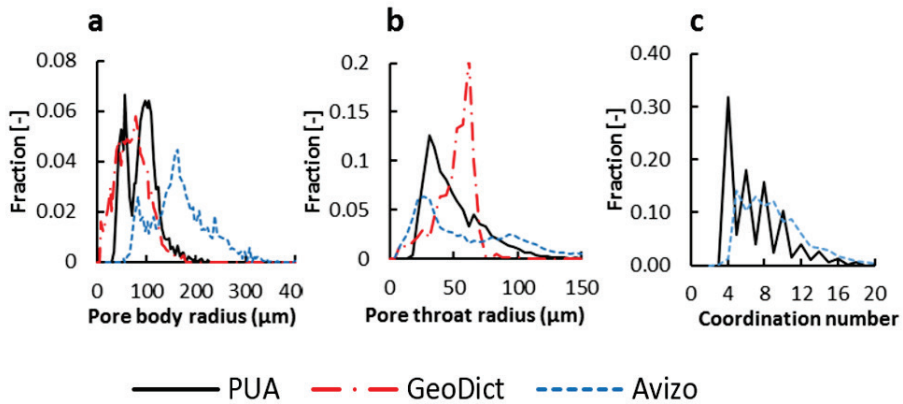


Figure G.1: Statistics of a packing of spheres that mimics Ottawa sand F32/F50 sand as obtained from three different methods for: a) pore unit radius, b) pore throat radius, and c) coordination number.

Discretization of volume-balance equations for unsaturated flow of water

The volume balance in equation 7.9 for unsaturated pore units is given by:

$$\sum_{j=1}^{N_i} k_{ij}^w (p_i^w - p_j^w) = -V_i \frac{ds_i^w}{dt} \quad (H.1)$$

Following the approach of Joekar-Niasar et al. (2010), $\frac{ds_i^w}{dt}$ is rewritten as $\frac{ds_i^w}{dp_i^w} \frac{dp_i^w}{dt}$ and a forward time difference scheme is employed to approximate equation H.1:

$$\sum_{j=1}^{N_i} k_{ij}^w \left((p_i^w)^{t+\Delta t} - (p_j^w)^{t+\Delta t} \right) = -V_i \frac{ds_i^w}{dp_i^w} \left(\frac{(p_i^w)^{t+\Delta t} - (p_i^w)^t}{\Delta t} \right) \quad (H.2)$$

where $\frac{\partial s_i^w}{\partial p_i^w}$ and k_{ij}^w are evaluated at time t and the term $\frac{dp_i^w}{dt}$ is evaluated for $t + \frac{\Delta t}{2}$.

Equation H.2 is rearranged such that we obtain:

$$(p_i^w)^{t+\Delta t} \left(\sum_{j=1}^{N_i} k_{ij}^w + \frac{V_i}{\Delta t} \frac{ds_i^w}{dp_i^w} \right) - \sum_{j=1}^{N_i} k_{ij}^w (p_j^w)^{t+\Delta t} = \frac{V_i}{\Delta t} \frac{ds_i^w}{dp_i^w} (p_i^w)^t \quad (H.3)$$

Appendix I

Local capillary pressure-saturation curve of a cube

I.1 Capillary pressure-saturation relationship

Here, a derivation is shown for the relation between capillary pressure and saturation of a pore unit, following the work by Joekar-Niasar et al. (2010). A derivation is shown for the case that the saturation is equal or smaller than the saturation corresponding to an inscribed sphere ($s_i^w \leq s_i^{w,thr}$). A cube is used as an example, because it is a platonic solid that is easy to visualize.

The size of one edge of a cube is related to the volume by: $\sqrt[3]{V_i}$, which in generalized form is $\lambda\sqrt[3]{V_i}$. The radius of the inscribed sphere (r_i^{ins}) of a cube is related to the volume by: $\frac{1}{2}\sqrt[3]{V_i}$, which in generalized form is: $\chi\sqrt[3]{V_i}$ (see equation 7.2). Consider a cube that has a saturation lower than $s_i^{w,thr}$, such that water is only present in corners and edges of a cube, see Figure I.1a. The water volume in all corners of the cube can be related to the radius of curvature r_i^c , where r_i^c is given by Young's Laplace equation such that $r_i^c = \frac{2\gamma}{p_i}$. Water in all the corners (see Figure I.1b) form a smaller cube that has an inscribed sphere with a radius r_i^c (see Figure I.1c). The total volume of that smaller cube is $\frac{(r_i^c)^3}{\chi^3}$, such that the water volume of all corners is given by:

$$V_{i, \text{corners}}^w = \frac{(r_i^c)^3}{\chi^3} - \frac{4}{3}\pi(r_i^c)^3 \quad (I.1)$$

where the value of χ is 0.5 for a cube. Next, the volume of water in edges is computed. The cross-sectional area of an edge is shown in Figure I.1d. The radius curvature of water in an edge is given by $\frac{1}{2}r_i^c = \frac{\gamma}{p_i}$, because the second curvature (tangential with the edge) is flat. The surface area of water that resides in that cross-section is thus given by:

$$a_{i, \text{edge}}^w = \frac{\left(\frac{1}{2}r_i^c\right)^2}{\tan\left(\frac{\theta}{2}\right)} - \left(\frac{1}{2}r_i^c\right)^2 \frac{(\pi - \theta)}{2} = \frac{1}{4}(r_i^c)^2 \left(\frac{1}{\tan\left(\frac{\theta}{2}\right)} - \frac{(\pi - \theta)}{2} \right) \quad (I.2)$$

where $\frac{(\frac{1}{2}r_i^c)^2}{\tan(\frac{\theta}{2})}$ is the generalized form of surface area of the square indicated by a dashed line in Figure I.1e and $(\frac{1}{2}r_i^c)^2 \frac{(\pi-\theta)}{2}$ is the surface area of the circle in that same square. The length of an edge is given by the total length minus twice the length of the corner segments shown in Figure I.1b. That length is thus given by:

$$l_{i,edge} = \lambda^3 \sqrt{V_i} - 2r_i^c \quad (I.3)$$

The number of edges in a cube is 12, denoted by N_{edges} . Thus, the volume of water that resides in all edges is:

$$V_{i,edges}^w = \frac{N_{edges}}{4} (r_i^c)^2 \left(\frac{1}{\tan(\frac{\theta}{2})} - \frac{(\pi-\theta)}{2} \right) (\lambda^3 \sqrt{V_i} - 2r_i^c) \quad (I.4)$$

Using equation I.1 and I.4, the local capillary-saturation curves can be obtained for all platonic solids, see section 7.2.4 and Table 7.2.

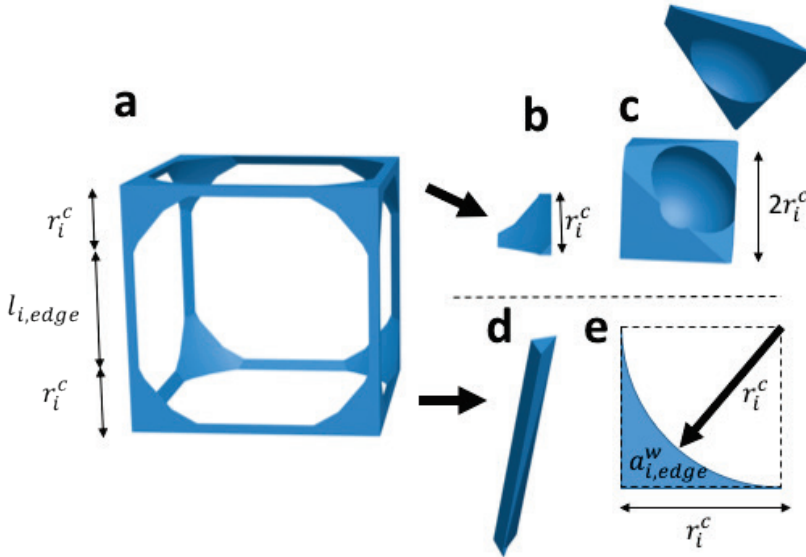


Figure I.1: Illustration of water in a cube for a water saturation lower than $s_i^{w,thr}$, a) illustration of the whole cube, b) illustration of water in a corner, c) smaller cube that contains the eight corners in (b), d) illustration of an edge of the cube and e) cross-sectional section of the edge shown in d.

I.2 Air-water interfacial area

The air-water interfacial area in a pore unit (a_i^{aw}) is determined for saturations lower than $s_i^{w,thr}$. Again, a distinction is made between water in corners and water in edges. The air-water interfacial area that is present in corners is simply given by the surface of a sphere with radius r_i^c , see Figure I.1c. However, the corners of the regular shapes are fitted in a pore throat, an interface does not exist once air breaks through a pore throat. To account for this phenomenon, a fraction is defined that describes the number of pore throats that are occupied with water ($N_i^{ij,w}$) over the total number of pore throats (N_i^{ij}). Thus, the air-water interfacial area inside the corners of a regular shape is given by:

$$a_{i,corner}^{aw} = 4\pi(r_i^c)^2 \left(\frac{N_i^{w}}{N_i} \right) \quad (I.5)$$

To determine the air-water interfacial area in an edge ($a_{i,edges}^{aw}$), we first determine the length of the air-water contact line in the cross-section of an edge (see Figure I.1e), which is: $r_i^c(\pi - \theta)$. Thus, $a_{i,edges}^{aw}$ is given by:

$$a_{i,edges}^{aw} = r_i^c(\pi - \theta)l_{i,edge}N_{edges} \quad (I.6)$$

Finally, we obtain the total air-water interfacial area:

$$a_i^{aw} = r_i^c(\pi - \theta) + 4\pi(r_i^c)^2 \left(\frac{N_i^{w}}{N_i} \right) \quad (I.7)$$

Appendix J

Local capillary pressure-saturation relationships for regular shapes

In the work by Joekar-Niasar et al. (2010), the local capillary pressure-saturation curve was employed for all saturation values smaller than unity, by extrapolating the value of p_i^c at $s_i^{w,thr}$, which is $\frac{2\gamma}{r_i^{ins}}$, to values of $s_i^w > s_i^{w,thr}$. We report the capillary pressure-saturation curves for all regular shapes that are employed in this study. The capillary pressure-saturation relationship in a pore unit for $s_i^w \leq s_i^{w,thr}$ reads (see equation 7.18):

$$s_i^w = \frac{V_i^w}{V_i} = \frac{c_1 \left(\frac{2\gamma}{p_i^c}\right)^3 + c_2 \sqrt[3]{V_i} \left(\frac{2\gamma}{p_i^c}\right)^2}{V_i} \quad (J.1)$$

where c_1 and c_2 are geometrical constants that are defined in equation 7.19. Following Joekar-Niasar et al. (2010), we can introduce a dimensionless parameter

$$R^* = \left(\frac{2\gamma}{p_i^c}\right) / \sqrt[3]{V_i} \rightarrow \left(\frac{2\gamma}{p_i^c}\right) = R^* \sqrt[3]{V_i} \quad (J.2)$$

Substituting equation J.2 into equation J.1 gives:

$$s_i^w = c_1 R^{*3} + c_2 R^{*2} \quad (J.3)$$

We can fit equation J.3 with $R^* = \chi[1 - e^{-\kappa s_i^w}]$, where κ is a shape constant that is independent of the size of the pore unit, but it does depend on the type of regular shape. The final relation between capillary pressure and saturation is given by:

$$p_i^c = \frac{2\gamma}{\chi \sqrt[3]{V_i} (1 - e^{-\kappa s_i^w})} \quad (J.4)$$

which indeed is the local capillary pressure-saturation curve introduced by Joekar-Niasar et al. (2010). In that work, the value of κ for a cube was found to be 6.83 in that work and we found the same value.

Finally, we determine the value of $\frac{\partial s_i^w}{\partial p_i^w}$ by determining $\left(\frac{\partial p_i^w}{\partial s_i^w}\right)^{-1}$. Note that $s_i^w = f(p_i^c)$ has no solution for $s_i^w \geq s_i^{w,thr}$ and thus we do not determine $\frac{\partial s_i^w}{\partial p_i^w}$ by first inverting equation J.4. In Chapter 7, we assume an air pressure of zero, such that $p_i^c = -p_i^w$, thus using equation J.4 yields:

$$\frac{\partial s_i^w}{\partial p_i^w} = -\left(\frac{\chi \sqrt[3]{V_i}}{2\gamma}\right) \frac{(1 - e^{-\kappa s_i^w})^2}{\kappa e^{-\kappa s_i^w}} \quad (J.5)$$

References

- Aker, E., Måløy, K. J., & Hansen, A. (1998). Simulating temporal evolution of pressure in two-phase flow in porous media. *Physical Review E*, 58(2), 2217.
- Anseth, K. S., Bowman, C. N., & Brannon-Peppas, L. (1996). Mechanical properties of hydrogels and their experimental determination. *Biomaterials*, 17(17), 1647-1657.
- Aslannejad, H., Hassanizadeh, S., Raoof, A., de Winter, D., Tomozeiu, N., & van Genuchten, M. T. (2017). Characterizing the hydraulic properties of paper coating layer using FIB-SEM tomography and 3D pore-scale modeling. *Chemical Engineering Science*, 160, 275-280.
- Bakke, S., & Øren, P. (1997). 3-D pore-scale modelling of sandstones and flow simulations in the pore networks. *Spe Journal*, 2(02), 136-149.
- Bear, J. (1972). *Dynamics of fluids in porous media* Courier Corporation.
- Behseresht, J., Prodanovic, M., Bryant, S. L., Jain, A. K., & Juanes, R. (2008). Mechanisms by which methane gas and methane hydrate coexist in ocean sediments. Paper presented at the *Offshore Technology Conference*.
- Belheine, N., Plassiard, J., Donzé, F., Darve, F., & Seridi, A. (2009). Numerical simulation of drained triaxial test using 3D discrete element modeling. *Computers and Geotechnics*, 36(1), 320-331.
- Bennethum, L. S., & Cushman, J. H. (1996). Multiscale, hybrid mixture theory for swelling systems—I: Balance laws. *International Journal of Engineering Science*, 34(2), 125-145.
- Benson, C. H., Chiang, I., Chalermyanont, T., & Sawangsuriya, A. (2014). Estimating van genuchten parameters α and n for clean sands from particle size distribution data. *From soil behavior fundamentals to innovations in geotechnical engineering: Honoring roy E. olson* (pp. 410-427)
- Bico, J., & Quéré, D. (2002). Rise of liquids and bubbles in angular capillary tubes. *Journal of Colloid and Interface Science*, 247(1), 162-166.
- Bottero, S., Hassanizadeh, S., Kleingeld, P., & Bezuijen, A. (2006). Experimental study of dynamic capillary pressure effect in two-phase flow in porous media. Paper presented at the *Proceedings of the XVI International Conference on Computational Methods in Water Resources (CMWR), Copenhagen, Denmark*, 18-22.
- Bottero, S., Hassanizadeh, S., Kleingeld, P., & Heimovaara, T. (2011). Nonequilibrium capillarity effects in two-phase flow through porous media at different scales. *Water Resources Research*, 47(10)
- Bouklas, N., & Huang, R. (2012). Swelling kinetics of polymer gels: Comparison of linear and nonlinear theories. *Soft Matter*, 8(31), 8194-8203.
- Boutt, D. F., Cook, B. K., McPherson, B. J., & Williams, J. (2007). Direct simulation of fluid-solid mechanics in porous media using the discrete element and lattice-Boltzmann methods. *Journal of Geophysical Research: Solid Earth*, 112(B10)
- Brandt, K. A., Goldman, S. A., & Inglin, T. A. (1987). *Hydrogel-Forming Polymer Compositions for use in Absorbent Structures*.
- Brooks, R. H., & Corey, A. T. (1964). Hydraulic properties of porous media and their relation to drainage design. *Transactions of the ASAE*, 7(1), 26-0028.
- Buchholz, F. L. (1998a). Absorbency and superabsorbency. In F. L. Buchholz, & A. T. Graham (Eds.), *Modern superabsorbent polymer technology* (pp. 1-17) John Wiley & Sons, Inc.

- Buchholz, F. L. (1998b). The structure and properties of superabsorbent polyacrylates. In F. L. Buchholz, & A. T. Graham (Eds.), *Modern superabsorbent polymer technology* (pp. 167-222) John Wiley & Sons, Inc.
- Buchholz, F. L., & Graham, A. T. (Eds.). (1998). *Modern superabsorbent polymer technology* John Wiley & Sons, Inc.
- Bultreys, T., De Boever, W., & Cnudde, V. (2016). Imaging and image-based fluid transport modeling at the pore scale in geological materials: A practical introduction to the current state-of-the-art. *Earth-Science Reviews*, 155, 93-128.
- Caldwell, J., & Kwan, Y. (2004). Numerical methods for one-dimensional stefan problems. *International Journal for Numerical Methods in Biomedical Engineering*, 20(7), 535-545.
- Camps-Roach, G., O'Carroll, D. M., Newson, T. A., Sakaki, T., & Illangasekare, T. H. (2010). Experimental investigation of dynamic effects in capillary pressure: Grain size dependency and upscaling. *Water Resources Research*, 46(8)
- Catalano, E., Chareyre, B., & Barthélémy, E. (2014). Pore-scale modeling of fluid-particles interaction and emerging poromechanical effects. *International Journal for Numerical and Analytical Methods in Geomechanics*, 38(1), 51-71.
- Cavarretta, I., Rocchi, I., & Coop, M. R. (2011). A new interparticle friction apparatus for granular materials. *Canadian Geotechnical Journal*, 48(12), 1829-1840.
- Chambers, D. R., Fowler Jr, H. H., Fujiura, Y., & Masuda, F. (1992). *Super-Absorbent Polymer having Improved Absorbency Properties*,
- Chareyre, B., Briançon, L., & Villard, P. (2002). Theoretical versus experimental modeling of the anchorage capacity of geotextiles in trenches. *Geosynthetics International*, 9(2), 97-123.
- Chareyre, B., Cortis, A., Catalano, E., & Barthélemy, E. (2012). Pore-scale modeling of viscous flow and induced forces in dense sphere packings. *Transport in Porous Media*, 94(2), 595-615.
- Chen, Z., Huan, G., & Li, B. (2004). An improved IMPES method for two-phase flow in porous media. *Transport in Porous Media*, 54(3), 361-376.
- Cho, G., Dodds, J., & Santamarina, J. C. (2006). Particle shape effects on packing density, stiffness, and strength: Natural and crushed sands. *Journal of Geotechnical and Geoenvironmental Engineering*, 132(5), 591-602.
- Choo, J., White, J. A., & Borja, R. I. (2015). Hydromechanical modeling of unsaturated flow in double porosity media. *International Journal of Geomechanics*, *Accepted*,
- Coetzee, C., & Els, D. (2009). Calibration of discrete element parameters and the modelling of silo discharge and bucket filling. *Computers and Electronics in Agriculture*, 65(2), 198-212.
- Crank, J. (1984). *Free and moving boundary problems* Clarendon press Oxford.
- Culligan, K. A., Wildenschild, D., Christensen, B. S., Gray, W. G., Rivers, M. L., & Tompson, A. F. (2004). Interfacial area measurements for unsaturated flow through a porous medium. *Water Resources Research*, 40(12)
- Cundall, P. A., & Strack, O. D. (1979). A discrete numerical model for granular assemblies. *Geotechnique*, 29(1), 47-65.
- Dahle, H. K., Celia, M. A., & Hassanizadeh, S. M. (2005). Bundle-of-tubes model for calculating dynamic effects in the capillary-pressure-saturation relationship. *Upscaling multiphase flow in porous media* (pp. 5-22) Springer.

- Diamantopoulos, E., & Durner, W. (2012). Dynamic nonequilibrium of water flow in porous media: A review. *Vadose Zone Journal*, 11(3)
- DiCarlo, D. A. (2005). Modeling observed saturation overshoot with continuum additions to standard unsaturated theory. *Advances in Water Resources*, 28(10), 1021-1027.
- Diersch, H. G., Clausnitzer, V., Myrnyy, V., Rosati, R., Schmidt, M., Beruda, H., . . . Virgilio, R. (2010). Modeling unsaturated flow in absorbent swelling porous media: Part 1. theory. *Transport in Porous Media*, 83(3), 437-464.
- Diersch, H. G., Clausnitzer, V., Myrnyy, V., Rosati, R., Schmidt, M., Beruda, H., . . . Virgilio, R. (2011). Modeling unsaturated flow in absorbent swelling porous media: Part 2. numerical simulation. *Transport in Porous Media*, 86(3), 753-776.
- Dullien, F. A., Zarcone, C., Macdonald, I. F., Collins, A., & Bochar, R. D. (1989). The effects of surface roughness on the capillary pressure curves and the heights of capillary rise in glass bead packs. *Journal of Colloid and Interface Science*, 127(2), 362-372.
- Eigen. (2017). Eigen: A C linear algebra library. [Http://eigen.Tuxfamily.Org](http://eigen.tuxfamily.org)
- Espinoza, D., Vandamme, M., Pereira, J., Dangla, P., & Vidal-Gilbert, S. (2014). Measurement and modeling of adsorptive–poromechanical properties of bituminous coal cores exposed to CO 2: Adsorption, swelling strains, swelling stresses and impact on fracture permeability. *International Journal of Coal Geology*, 134, 80-95.
- Esteves, L. P. (2011). Superabsorbent polymers: On their interaction with water and pore fluid. *Cement and Concrete Composites*, 33(7), 717-724.
- Fasano, A., & Mikelic, A. (2002). The 3D flow of a liquid through a porous medium with absorbing and swelling granules. *Interfaces and Free Boundaries*, 4(3), 239-261.
- Favier, J., Abbaspour-Fard, M., Kremmer, M., & Raji, A. (1999). Shape representation of axisymmetrical, non-spherical particles in discrete element simulation using multi-element model particles. *Engineering Computations*, 16(4), 467-480.
- Finney, J. (1970). Random packings and the structure of simple liquids. I. the geometry of random close packing. *Proceedings of the Royal Society of London.A.Mathematical and Physical Sciences*, 319(1539), 479-493.
- Frijns, A. J. H., Huyghe, J., & Janssen, J. D. (1997). A validation of the quadriphasic mixture theory for intervertebral disc tissue. *International Journal of Engineering Science*, 35(15), 1419-1429.
- Gallipoli, D., Wheeler, S., & Karstunen, M. (2003). Modelling the variation of degree of saturation in a deformable unsaturated soil. *Géotechnique.*, 53(1), 105-112.
- Garcia, X., Akanji, L. T., Blunt, M. J., Matthai, S. K., & Latham, J. P. (2009). Numerical study of the effects of particle shape and polydispersity on permeability. *Physical Review E*, 80(2), 021304.
- GeoDict, Math2Market, Kaiserslautern, Germany. (2017).
- Gladkikh, M., & Bryant, S. (2005). Prediction of imbibition in unconsolidated granular materials. *Journal of Colloid and Interface Science*, 288(2), 526-539.
- Graham, A. T., & Wilson, L. R. (1998). Commercial processes for the manufacture of superabsorbent polymers. In F. L. Buchholz, & A. T. Graham (Eds.), *Modern superabsorbent polymer technology* (pp. 69-118) John Wiley & Sons, Inc.
- Grosshans, D., Knaebel, A., & Lequeux, F. (1995). Plasticity of an amorphous assembly of elastic gel beads. *Journal De Physique II*, 5(1), 53-62.

- Hassanizadeh, S. M., Celia, M. A., & Dahle, H. K. (2002). Dynamic effect in the capillary pressure–saturation relationship and its impacts on unsaturated flow. *Vadose Zone Journal*, 1(1), 38-57.
- Hassanizadeh, S. M., & Gray, W. G. (1993). Thermodynamic basis of capillary pressure in porous media. *Water Resources Research*, 29(10), 3389-3407.
- Hilpert, M., & Miller, C. T. (2001). Pore-morphology-based simulation of drainage in totally wetting porous media. *Advances in Water Resources*, 24(3), 243-255.
- Höhner D., Wirtz S., Scherer V. (2014) A study on the influence of particle shape and shape approximation on particle mechanics in a rotating drum using the discrete element method. *Powder Technology*, 253 (2014), 256-265.
- Höhner D., Wirtz S., Scherer V. (2015) A study on the influence of particle shape on the mechanical interactions of granular media in a hopper using the Discrete Element Method. *Powder Technology*, 278 (2015), 286-305.
- Holtzman, R., & Juanes, R. (2010). Crossover from fingering to fracturing in deformable disordered media. *Physical Review E*, 82(4), 046305.
- Hou, L., Chen, L., & Kibbey, T. C. (2012). Dynamic capillary effects in a small-volume unsaturated porous medium: Implications of sensor response and gas pressure gradients for understanding system dependencies. *Water Resources Research*, 48(11)
- Huber, R., & Helmig, R. (1999). Multiphase flow in heterogeneous porous media: A classical finite element method versus an implicit pressure–explicit saturation-based mixed finite element–finite volume approach. *International Journal for Numerical Methods in Fluids*, 29(8), 899-920.
- Huyghe, J. M., & Janssen, J. (1997). Quadriphasic mechanics of swelling incompressible porous media. *International Journal of Engineering Science*, 35(8), 793-802.
- Jain, A., & Juanes, R. (2009). Preferential mode of gas invasion in sediments: Grain-scale mechanistic model of coupled multiphase fluid flow and sediment mechanics. *Journal of Geophysical Research: Solid Earth (1978–2012)*, 114(B8)
- Joekar-Niasar, V., Hassanizadeh, S. M., & Dahle, H. (2010). Non-equilibrium effects in capillarity and interfacial area in two-phase flow: Dynamic pore-network modelling. *Journal of Fluid Mechanics*, 655, 38-71.
- Joekar-Niasar, V., Prodanović, M., Wildenschild, D., & Hassanizadeh, S. (2010). Network model investigation of interfacial area, capillary pressure and saturation relationships in granular porous media. *Water Resources Research*, 46(6)
- Joekar-Niasar, V., & Hassanizadeh, S. M. (2011). Effect of fluids properties on non-equilibrium capillarity effects: Dynamic pore-network modeling. *International Journal of Multiphase Flow*, 37(2), 198-214.
- Johnson, K. L. (1987). *Contact mechanics*. Cambridge university press.
- Kabiri, K., Omidian, H., Hashemi, S., & Zohuriaan-Mehr, M. (2003). Synthesis of fast-swelling superabsorbent hydrogels: Effect of crosslinker type and concentration on porosity and absorption rate. *European Polymer Journal*, 39(7), 1341-1348.
- Kabiri, K., Omidian, H., Zohuriaan-Mehr, M., & Doroudiani, S. (2011). Superabsorbent hydrogel composites and nanocomposites: A review. *Polymer Composites*, 32(2), 277-289.
- Kainth, A. P. S., Richard, I., Dodge, N., Feldkamp, J. R., & Munschau, S. A. (2004). *Superabsorbent Materials having High, Controlled Gel-Bed Friction Angles and Composites made from the Same*,

- Karadimitriou, N., Hassanizadeh, S., Joekar-Niasar, V., & Kleingeld, P. (2014). Micromodel study of two-phase flow under transient conditions: Quantifying effects of specific interfacial area. *Water Resources Research*, *50*(10), 8125-8140.
- Karadimitriou, N., Musterd, M., Kleingeld, P., Kreutzer, M., Hassanizadeh, S., & Joekar-Niasar, V. (2013). On the fabrication of PDMS micromodels by rapid prototyping, and their use in two-phase flow studies. *Water Resources Research*, *49*(4), 2056-2067.
- Kettle, J., Lamminmäki, T., & Gane, P. (2010). A review of modified surfaces for high speed inkjet coating. *Surface and Coatings Technology*, *204*(12), 2103-2109.
- Kharaghani, A., Metzger, T., & Tsotsas, E. (2011). A proposal for discrete modeling of mechanical effects during drying, combining pore networks with DEM. *AIChE Journal*, *57*(4), 872-885.
- Knaebel, A., Rebre, S., & Lequeux, F. (1997). Determination of the elastic modulus of superabsorbent gel beads. *Polymer Gels and Networks*, *5*(2), 107-121.
- Krugger-Emden, H., Rickelt, S., Wirtz, S., & Scherer, V. (2008). A study on the validity of the multi-sphere discrete element method. *Powder Technology*, *188*(2), 153-165.
- Kunz, P., Zarihos, I., Karadimitriou, N., Huber, M., Nieken, U., & Hassanizadeh, S. (2016). Study of multi-phase flow in porous media: Comparison of sph simulations with micro-model experiments. *Transport in Porous Media*, *114*(2), 581-600.
- Kutluay, S., Bahadir, A., & Özdeş, A. (1997). The numerical solution of one-phase classical stefan problem. *Journal of Computational and Applied Mathematics*, *81*(1), 135-144.
- Lamminmäki, T., Kettle, J., Puukko, P., Ridgway, C., & Gane, P. (2012). Short timescale inkjet ink component diffusion: An active part of the absorption mechanism into inkjet coatings. *Journal of Colloid and Interface Science*, *365*(1), 222-235.
- Langston, P., Tüzün, U., & Heyes, D. (1995). Discrete element simulation of granular flow in 2D and 3D hoppers: Dependence of discharge rate and wall stress on particle interactions. *Chemical Engineering Science*, *50*(6), 967-987.
- Likos, W. J., & Jaafar, R. (2013). Pore-scale model for water retention and fluid partitioning of partially saturated granular soil. *Journal of Geotechnical and Geoenvironmental Engineering*, *139*(5), 724-737.
- Lindquist, W. B., Lee, S., Coker, D. A., Jones, K. W., & Spanne, P. (1996). Medial axis analysis of void structure in three-dimensional tomographic images of porous media. *Journal of Geophysical Research: Solid Earth*, *101*(B4), 8297-8310.
- Lindquist, W. B., Venkatarangan, A., Dunsmuir, J., & Wong, T. (2000). Pore and throat size distributions measured from synchrotron X-ray tomographic images of fontainebleau sandstones. *Journal of Geophysical Research: Solid Earth*, *105*(B9), 21509-21527.
- Lins, Y., & Schanz, T. (2005). Determination of hydro-mechanical properties of sand. *Unsaturated soils: Experimental studies* (pp. 15-32) Springer.
- Lorenz, A., Tuozzolo, C., & Louge, M. (1997). Measurements of impact properties of small, nearly spherical particles. *Experimental Mechanics*, *37*(3), 292-298.
- Lu, N., Wu, B., & Tan, C. P. (2007). Tensile strength characteristics of unsaturated sands. *Journal of Geotechnical and Geoenvironmental Engineering*, *133*(2), 144-154.
- MacKay, A. (1973). To find the largest sphere which can be inscribed between four others. *Acta Crystallographica Section A: Crystal Physics, Diffraction, Theoretical and General Crystallography*, *29*(3), 308-309.

- Mahmoodlu, M. G., Raoof, A., Sweijen, T., & van Genuchten, M. T. (2016). Effects of sand compaction and mixing on pore structure and the unsaturated soil hydraulic properties. *Vadose Zone Journal*, 15(8)
- Malakpoor, K., Kaasschieter, E. F., & Huyghe, J. M. (2007). Mathematical modelling and numerical solution of swelling of cartilaginous tissues. part I: Modelling of incompressible charged porous media. *ESAIM: Mathematical Modelling and Numerical Analysis*, 41(04), 661-678.
- Mašín, D. (2010). Predicting the dependency of a degree of saturation on void ratio and suction using effective stress principle for unsaturated soils. *International Journal for Numerical and Analytical Methods in Geomechanics*, 34(1), 73-90.
- Mason, G., & Mellor, D. W. (1995). Simulation of drainage and imbibition in a random packing of equal spheres. *Journal of Colloid and Interface Science*, 176(1), 214-225.
- Mason, G., & Morrow, N. R. (1991). Capillary behavior of a perfectly wetting liquid in irregular triangular tubes. *Journal of Colloid and Interface Science*, 141(1), 262-274.
- Mayer, R. P., & Stowe, R. A. (1965). Mercury porosimetry—breakthrough pressure for penetration between packed spheres. *Journal of Colloid Science*, 20(8), 893-911.
- Michelucci, D., & Fofou, S. (2004). Using cayley-menger determinants for geometric constraint solving. Paper presented at the *Proceedings of the Ninth ACM Symposium on Solid Modeling and Applications*, 285-290.
- Mirnyy, V., Clausnitzer, V., Diersch, H. G., Rosati, R., Schmidt, M., & Beruda, H. (2012). Wicking in absorbent swelling porous materials. *Wicking in Porous Materials: Traditional and Modern Modeling Approaches*, , 161-200.
- Modenese, C., Utili, S., & Houlsby, G. (2012). DEM modelling of elastic adhesive particles with application to lunar soil. *Earth and Space*, 1, 45-54.
- Mogensen, K., & Stenby, E. H. (1998). A dynamic two-phase pore-scale model of imbibition. *Transport in Porous Media*, 32(3), 299-327.
- Montellà, E., Toraldo, M., Chareyre, B., & Sibille, L. (2016). Localized fluidization in granular materials: Theoretical and numerical study. *Physical Review E*, 94(5), 052905.
- Mousavi, M. A., & Bryant, S. L. (2012). Connectivity of pore space as a control on two-phase flow properties of tight-gas sandstones. *Transport in Porous Media*, 94(2), 537-554.
- Murad, M. A., & Cushman, J. H. (1996). Multiscale flow and deformation in hydrophilic swelling porous media. *International Journal of Engineering Science*, 34(3), 313-338.
- Nikooee, E., Sweijen, T., & Hassanizadeh, S. M. (2016). Determination of the relationship among capillary pressure, saturation and interfacial area: A pore unit assembly approach. Paper presented at the *E3S Web of Conferences*, , 9 02002.
- Nikooee, E., Habibagahi, G., Hassanizadeh, S. M., & Ghahramani, A. (2013). Effective stress in unsaturated soils: A thermodynamic approach based on the interfacial energy and hydromechanical coupling. *Transport in Porous Media*, 96(2), 369-396.
- Nuth, M., & Laloui, L. (2008). Effective stress concept in unsaturated soils: Clarification and validation of a unified framework. *International Journal for Numerical and Analytical Methods in Geomechanics*, 32(7), 771-801.
- O'Carroll, D. M., Phelan, T. J., & Abriola, L. M. (2005). Exploring dynamic effects in capillary pressure in multistep outflow experiments. *Water Resources Research*, 41(11)

- Ogarko V., Rivas N., Luding S. (2014) Structure characterization of hard sphere packings in amorphous and crystalline states. *Journal of chemical physics*, 140(2014): 211102
- Oh, S., & Lu, N. (2014). Uniqueness of the suction stress characteristic curve under different confining stress conditions. *Vadose Zone Journal*, 13(5)
- Omidian, H., Hashemi, S., Sammes, P., & Meldrum, I. (1998). A model for the swelling of superabsorbent polymers. *Polymer*, 39(26), 6697-6704.
- Omidian, H., Hashemi, S., Sammes, P., & Meldrum, I. (1999). Modified acrylic-based superabsorbent polymers (dependence on particle size and salinity). *Polymer*, 40(7), 1753-1761.
- Oostrom, M., Hofstee, C., Walker, R., & Dane, J. (1999). Movement and remediation of trichloroethylene in a saturated heterogeneous porous medium: 1. spill behavior and initial dissolution. *Journal of Contaminant Hydrology*, 37(1), 159-178.
- Øren, P., & Bakke, S. (2003). Reconstruction of berea sandstone and pore-scale modelling of wettability effects. *Journal of Petroleum Science and Engineering*, 39(3), 177-199.
- Oren, P., Bakke, S., & Arntzen, O. J. (1998). Extending predictive capabilities to network models. *SPE Journal*, 3(04), 324-336.
- Pan, Z., & Connell, L. D. (2012). Modelling permeability for coal reservoirs: A review of analytical models and testing data. *International Journal of Coal Geology*, 92, 1-44.
- Pasha M., Hare C., Ghadiri M., Gunadi A., Piccione P. M. (2016). Effect of particle shape on flow in discrete element method simulation of a rotary batch seed coater. *Powder Technology 296 (2016) 29-36*.
- Plassiard, J., Belheine, N., & Donzé, F. (2009). A spherical discrete element model: Calibration procedure and incremental response. *Granular Matter*, 11(5), 293-306.
- Popov, V. (2010). *Contact mechanics and friction: Physical principles and applications* Springer Science & Business Media.
- Price, M., Murariu, V., & Morrison, G. (2007). Sphere clump generation and trajectory comparison for real particles. *Proceedings of Discrete Element Modelling 2007*,
- Princen, H. M. (1969). Capillary phenomena in assemblies of parallel cylinders. *Journal of Colloid and Interface Science*, 30(3), 359-371.
- Prodanović, M., & Bryant, S. L. (2006). A level set method for determining critical curvatures for drainage and imbibition. *Journal of Colloid and Interface Science*, 304(2), 442-458.
- Qin, C. (2015). Water transport in the gas diffusion layer of a polymer electrolyte fuel cell: Dynamic pore-network modeling. *Journal of the Electrochemical Society*, 162(9), F1036-F1046.
- Qin, C., & Hassanizadeh, S. (2014). Multiphase flow through multilayers of thin porous media: General balance equations and constitutive relationships for a solid-gas-liquid three-phase system. *International Journal of Heat and Mass Transfer*, 70, 693-708.
- Radu, F. A., Bause, M., Knabner, P., Lee, G. W., & Friess, W. C. (2002). Modeling of drug release from collagen matrices. *Journal of Pharmaceutical Sciences*, 91(4), 964-972.
- Raouf, A., & Hassanizadeh, S. (2012). A new formulation for pore-network modeling of two-phase flow. *Water Resources Research*, 48(1)
- Raouf, A., & Hassanizadeh, S. M. (2010). A new method for generating pore-network models of porous media. *Transport in Porous Media*, 81(3), 391-407.

- Romero, E., Della Vecchia, G., & Jommi, C. (2011). An insight into the water retention properties of compacted clayey soils. *Géotechnique*, 61(4), 313-328.
- Rosenholm, J. B. (2015). Liquid spreading on solid surfaces and penetration into porous matrices: Coated and uncoated papers. *Advances in Colloid and Interface Science*, 220, 8-53.
- Rostami, A., Habibagahi, G., Ajdari, M., & Nikooee, E. (2013). Pore network investigation on hysteresis phenomena and influence of stress state on the SWRC. *International Journal of Geomechanics*, , 04014072.
- Salager, S., El Youssoufi, M. S., & Saix, C. (2010). Definition and experimental determination of a soil-water retention surface. *Canadian Geotechnical Journal*, 47(6), 609-622.
- Scholtès, L., Chareyre, B., Nicot, F., & Darve, F. (2009). Micromechanics of granular materials with capillary effects. *International Journal of Engineering Science*, 47(1), 64-75.
- Schöpfer, M. P., Abe, S., Childs, C., & Walsh, J. J. (2009). The impact of porosity and crack density on the elasticity, strength and friction of cohesive granular materials: Insights from DEM modelling. *International Journal of Rock Mechanics and Mining Sciences*, 46(2), 250-261.
- Schroth, M., Istok, J., Ahearn, S., & Selker, J. (1996). Characterization of miller-similar silica sands for laboratory hydrologic studies. *Soil Science Society of America Journal*, 60(5), 1331-1339.
- Seki, K. (2007). SWRC fit? a nonlinear fitting program with a water retention curve for soils having unimodal and bimodal pore structure. *Hydrology and Earth System Sciences Discussions Discussions*, 4(1), 407-437.
- Sheng, Q., & Thompson, K. (2013). A unified pore-network algorithm for dynamic two-phase flow. *Advances in Water Resources*, 95, 92-108.
- Shmulevich, I. (2010). State of the art modeling of soil–tillage interaction using discrete element method. *Soil and Tillage Research*, 111(1), 41-53.
- Shmulevich, I., Asaf, Z., & Rubinstein, D. (2007). Interaction between soil and a wide cutting blade using the discrete element method. *Soil and Tillage Research*, 97(1), 37-50.
- Simms, P., & Yanful, E. (2005). A pore-network model for hydromechanical coupling in unsaturated compacted clayey soils. *Canadian Geotechnical Journal*, 42(2), 499-514.
- Singh, P. P., Cushman, J. H., & Maier, D. E. (2003). Multiscale fluid transport theory for swelling biopolymers. *Chemical Engineering Science*, 58(11), 2409-2419.
- Šmilauer, V., Catalano, E., Chareyre, B., Dorofeenko, S., Duriez, J., Gladky, A., . . . Sibille, L. (2015). Yade reference documentation. *Yade Documentation 2nd Ed.*, doi:10.5281/zenodo.34073
- Snoeck, D., Jensen, O. M., & De Belie, N. (2015). The influence of superabsorbent polymers on the autogenous shrinkage properties of cement pastes with supplementary cementitious materials. *Cement and Concrete Research*, 74, 59-67.
- Stauffer, F. (1978). Time dependence of the relations between capillary pressure, water content, and conductivity during drainage of porous media. IAHR symposium on scale effects in porous media, Thessaloniki, Greece. Vol. 29. 1978
- Sun, Y., Kharaghani, A., Metzger, T., Müller, J., & Tsotsas, E. (2015). Lotion distribution in wet wipes investigated by pore network simulation and X-ray micro tomography. *Transport in Porous Media*, 107(2), 449-468.

- Sweijen, T., Chareyre, B., Hassanizadeh, S., & Karadimitriou, N. (2017b). Grain-scale modelling of swelling granular materials; application to super absorbent polymers. *Powder Technology* 318 (2017):411-422.
- Sweijen, T., Hassanizadeh, S., Aslannejad, H., & Leszczynski, S. Grain-scale modelling of swelling granular materials using the discrete element method and the multi-sphere approximation. *Poromechanics VI* (pp. 329-336)
- Sweijen, T., van Duijn, C., & Hassanizadeh, S. (2017c). A model for diffusion of water into a swelling particle with a free boundary: Application to a super absorbent polymer particle. *Chemical Engineering Science*,
- Sweijen, T., Aslannejad, H., & Hassanizadeh, S. M. (2017a). Capillary pressure-saturation relationships for porous granular materials: Pore morphology method vs. pore unit assembly method. *Advances in Water Resources*,
- Sweijen, T., Nikoee, E., Hassanizadeh, S. M., & Chareyre, B. (2016). The effects of swelling and porosity change on capillarity: DEM coupled with a pore-unit assembly method. *Transport in Porous Media*, 113(1), 207-226.
- Takhar, P. S. (2014). Unsaturated fluid transport in swelling poroviscoelastic biopolymers. *Chemical Engineering Science*, 109, 98-110.
- Tanaka, T., & Fillmore, D. J. (1979). Kinetics of swelling of gels. *The Journal of Chemical Physics*, 70(3), 1214-1218.
- Tarantino, A. (2009). A water retention model for deformable soils. *Géotechnique*, 59(9), 751-762.
- Tarantino, A., & Tombolato, S. (2005). Coupling of hydraulic and mechanical behaviour in unsaturated compacted clay. *Géotechnique*, 55(4), 307-317.
- Terzaghi, K., & Peck, R. B. (1968). *Soil mechanics in engineering practice: 2d ed* J. Wiley.
- Tester, R. F., & Morrison, W. R. (1990). Swelling and gelatinization of cereal starches. II. waxy rice starches. *Cereal Chem*, 67(6), 558-563.
- Thompson, K. E. (2002). Pore-scale modeling of fluid transport in disordered fibrous materials. *AIChE Journal*, 48(7), 1369-1389.
- Thornton, C., Cummins, S. J., & Cleary, P. W. (2011). An investigation of the comparative behaviour of alternative contact force models during elastic collisions. *Powder Technology*, 210(3), 189-197.
- Tong, A., Catalano, E., & Chareyre, B. (2012). Pore-scale flow simulations: Model predictions compared with experiments on bi-dispersed granular assemblies. *Oil & Gas Science and Technology—Revue d'IFP Energies Nouvelles*, 67(5), 743-752.
- Topp, G., Klute, A., & Peters, D. (1967). Comparison of water content-pressure head data obtained by equilibrium, steady-state, and unsteady-state methods. *Soil Science Society of America Journal*, 31(3), 312-314.
- Torskaya, T., Shabro, V., Torres-Verdín, C., Salazar-Tio, R., & Revil, A. (2014). Grain shape effects on permeability, formation factor, and capillary pressure from pore-scale modeling. *Transport in Porous Media*, 102(1), 71-90.
- Tsuji, Y., Kawaguchi, T., & Tanaka, T. (1993). Discrete particle simulation of two-dimensional fluidized bed. *Powder Technology*, 77(1), 79-87.
- Van De Fliert, B., & Van Der Hout, R. (2000). A generalized stefan problem in a diffusion model with evaporation. *SIAM Journal on Applied Mathematics*, 60(4), 1128-1136.

- Van Genuchten, M. T. (1980). A closed-form equation for predicting the hydraulic conductivity of unsaturated soils. *Soil Science Society of America Journal*, 44(5), 892-898.
- Van Noorden, T., & Pop, I. (2008). A stefan problem modelling crystal dissolution and precipitation. *IMA Journal of Applied Mathematics*, 73(2), 393-411.
- Vanapalli, S., Fredlund, D., Pufahl, D., & Clifton, A. (1996). Model for the prediction of shear strength with respect to soil suction. *Canadian Geotechnical Journal*, 33(3), 379-392.
- Vidales, A., Riccardo, J., & Zgrablich, G. (1998). Pore-level modelling of wetting on correlated porous media. *Journal of Physics D: Applied Physics*, 31(20), 2861.
- Vogel, H., Tölke, J., Schulz, V., Krafczyk, M., & Roth, K. (2005). Comparison of a lattice-boltzmann model, a full-morphology model, and a pore network model for determining capillary pressure–saturation relationships. *Vadose Zone Journal*, 4(2), 380-388.
- Wang, L., Rezaei, E., & Hayashi, Y. (1998). *Absorbent Materials having Improved Absorbent Property and Methods for Making the Same*, Google Patents
- Wang, Y., & Tonon, F. (2010). Calibration of a discrete element model for intact rock up to its peak strength. *International Journal for Numerical and Analytical Methods in Geomechanics*, 34(5), 447-469.
- Weiqing, X. (1990). The stefan problem with a kinetic condition at the free boundary. *SIAM Journal on Mathematical Analysis*, 21(2), 362-373.
- Widuliński, Ł., Kozicki, J., & Tejchman, J. (2009). Numerical simulations of triaxial test with sand using DEM. *Archives of Hydro-Engineering and Environmental Mechanics*, 56(3-4), 149-172.
- Woodhouse, J., & Johnson, M. (1991). Effect of superabsorbent polymers on survival and growth of crop seedlings. *Agricultural Water Management*, 20(1), 63-70.
- Xie, X., Bahnemann, J., Wang, S., Yang, Y., & Hoffmann, M. R. (2016). "Nanofiltration" enabled by super-absorbent polymer beads for concentrating microorganisms in water samples. *Scientific Reports*, 6, 20516. doi:10.1038/srep20516 [doi]
- Yang, A., Miller, C. T., & Turcoliver, L. (1996). Simulation of correlated and uncorrelated packing of random size spheres. *Physical Review E*, 53(2), 1516.
- Yeh, A., & Li, J. (1996). A continuous measurement of swelling of rice starch during heating. *Journal of Cereal Science*, 23(3), 277-283.
- Yuan, C., & Chareyre, B. (2017). A pore-scale method for hydromechanical coupling in deformable granular media. *Computer Methods in Applied Mechanics and Engineering*, 318, 1066-1079.
- Yuan, C., Chareyre, B., & Darve, F. (2015). Pore-scale simulations of drainage in granular materials: Finite size effects and the representative elementary volume. *Advances in Water Resources*,
- Zhang, F., Damjanac, B., & Huang, H. (2013). Coupled discrete element modeling of fluid injection into dense granular media. *Journal of Geophysical Research: Solid Earth*, 118(6), 2703-2722.
- Zhuang, L. (2017). *Advanced Theories of Water Redistribution and Infiltration in Porous Media: Experimental Studies and Modeling*.
- Zohuriaan-Mehr, M. J., & Kabiri, K. (2008). Superabsorbent polymer materials: A review. *Iranian Polymer Journal*, 17(6), 451.

Samenvatting

Dit proefschrift presenteert een korrelschaal-modelleringsstechniek voor het bestuderen van zwellende en granulaire materialen. Een bestaand korrelschaalmodel, namelijk de *Discrete Element Method* (DEM), is uitgebreid met drie functionaliteiten die in drie delen van dit proefschrift worden gepresenteerd, namelijk: i) zwelling van individuele korrels; ii) een module voor waterverspreiding door capillaire werking in granulaire materialen, op basis van de *pore-unit assembly* methode; en iii) een module voor dynamische en onverzadigde stroming tijdens het drogen van deformerende granulaire materialen. In dit werk wordt de toepasbaarheid en veelzijdigheid van het korrelschaalmodel gedemonstreerd om zwelling van een laag van korrels te beschrijven, onder verzadigde en onverzadigde omstandigheden, evenals dynamische en quasi-statische omstandigheden. De onderzoeksdoelen zijn: i) het bestuderen van processen die zich voordoen in zwellende granulaire media, ii) om onderzoeksvragen te beantwoorden die niet met macroschaalonderzoeken kunnen worden beantwoord en iii) om geschikte numerieke modellen te ontwikkelen op basis van korrelschaal technieken.

In hoofdstuk 2 werd een laag van zwellende korrels bestudeerd, gemaakt van zogenaamde Super Absorberende Polymeren (SAP), die onder volledig verzadigde omstandigheden zwol. Het mechanische kader van DEM was aangepast om het zwellen van individuele korrels mogelijk te maken, waar bolvormige korrels groeiden en zachter werden gedurende het zwellen. Mechanische parameters voor de SAP-korrels werden gevonden in de literatuur, maar de snelheid van het zwellen werd gemeten in experimenten. We veronderstelden dat korrels bolvormig waren, met een korrelgrootteverdeling van echte SAP-korrels. Inachtnemend dat vereenvoudigingen werden toegepast, kwamen de resultaten van numerieke modelleringen redelijk goed overeen met experimentele data. Dit werd dan ook beschouwd als een aanwijzing dat DEM een geschikt hulpmiddel is om de zwelling van SAP-korrels te bestuderen.

In hoofdstuk 2 was een nieuwe vergelijking ontwikkelend voor de zwelsnelheid van individuele korrels, waarmee de zwelsnelheid in experimenten vertaald kon worden naar de zwelsnelheid in het numerieke model. De nieuwe vergelijking was gebaseerd op diffusie van water in een zwellende en bolvormige korrel. De oplossing was echter gebaseerd op een benadering van een gradiënt in watergehalte. Daarom hebben we in hoofdstuk 3 een uitgebreid model ontwikkeld voor waterdiffusie in een zwellende en bolvormige korrel, dat een vrij bewegend oppervlak heeft. In dat model werd niet alleen

waterdiffusie beschouwd als een tijdsafhankelijk proces, maar ook wateropname over het oppervlak van de korrel werd beschouwd als een tijdsafhankelijk proces. Er werd een dimensieloze variabele gevonden die de bijdrage van zowel diffusie als wateropname aan de totale zwelsnelheid van de korrel bepaald. Resultaten lieten zien dat het zwelsnelheid van een korrel kan dalen wanneer de wateropname aan het oppervlak langzamer is dan de diffusie van water in de korrel. Dus het aanbrengen van een coating op de korrel kan de totale zwelsnelheid vertragen.

Zwelling van granulaire materialen komt niet alleen voor in verzadigde omstandigheden, maar ook in onverzadigde omstandigheden. Daarom werd de *pore-unit assembly* methode gebruikt in hoofdstuk 4, gekoppeld aan DEM, om capillariteitsverschijnselen te bestuderen. Met behulp van dit gekoppelde model werden capillaire druk- en verzadigingsrelaties geconstrueerd voor lagen van SAP-korrels, met verschillende absorptiegehaltes en porositeitswaarden. De capillaire druk- en verzadigingskrommen werden gefit met de *Van Genuchten* vergelijking, waar de Van Genuchten parameters een functie waren van absorptiegehalte en porositeit. Vervolgens werden de capillaire drukken van alle capillaire druk- en verzadigingskrommen geschaald met de Van Genuchten parameter α . De verzadiging werd geschaald tot een effectieve verzadiging. Uiteindelijk vielen alle capillaire druk- en verzadigingskrommen in een enkele geschaalde kromme. Fittings vergelijkingen voor residuele verzadiging en Van Genuchten parameters werden bepaald. Deze vergelijkingen waren afhankelijk van porositeit en absorptiegehalte. Porositeit werd beschouwd als een maat voor het stressgehalte in een korrel laag en het absorptiegehalte vertegenwoordigd de mate van zwelling.

In hoofdstuk 5 werd de koppeling tussen de *pore-unit assembly* methode en DEM bestudeerd, door middel van capillaire druk- en verzadigingskrommen te vergelijken met die van de poriemorfologie methode en die van experimenten die gerapporteerd zijn in de literatuur. In het algemeen kwamen de capillaire druk- en verzadigingskrommen, die waren geconstrueerd met de *pore-unit assembly* methode, redelijk goed overeen met experimentele data. Natuurlijk was de kwaliteit van de numerieke modellen afhankelijk van de mate van vergelijkbaarheid tussen bollen in het model en de echte korrels in experimenten. Daarnaast was ook de methode waarmee de indringingswaarde van capillaire druk bepaald werd van belang, i.e. is de “Mayer-Stowe en Princen methode” of de “bolvormige benadering” beter om de vorm van de lucht-water oppervlak te bepalen.

In hoofdstuk 2 tot en met 5 werden korrel-schaal simulaties uitgevoerd met behulp van bolvormige deeltjes. Dit is een goede aanname voor kwantitatieve onderzoeken van granulaten die bijna bolvormig zijn of voor kwalitatieve onderzoeken, waar men geïnteresseerd is in verschillende processen. Voor kwantitatieve modellen van

onregelmatige korrels wordt de mate van niet-bolvormigheid belangrijk, omdat het sterk hydraulische parameters beïnvloedt. Aangezien SAP-korrels onregelmatig zijn, moet de vorm van de korrels mee worden genomen voor kwantitatieve simulaties. Het effect van de vorm wordt duidelijk bij het bestuderen van porositeitswaarden van SAP-korrel lagen. Metingen hebben aangetoond dat de porositeit kan variëren van 0,70 tot 0,10 gedurende zwelling. Maar het bereik van porositeitwaardes in simulaties van bolvormige deeltjes ligt slechts binnen 0,45 tot 0,20. Zo hebben SAP-korrels een veel grotere variatie in porositeitswaarden dan simulaties van bolvormige korels kunnen reproduceren. Daarom hadden we in Hoofdstuk 6 een uitgebreide versie van DEM gebruikt voor korrels met onregelmatige vormen. Hiervoor werden sets van overlappende bollen gebruikt, om zo echte SAP-korrels na te bootsen. Een algoritme voor het genereren van sets van bollen werd ontwikkeld om zo 20 sets te maken die 20 SAP-korrels vertegenwoordigen. De 20 SAP-korrels waren experimenteel gemeten met behulp van een micro-CT setup. Resultaten toonden aan dat simulaties met sets van overlappende bollen porositeitswaarden hebben die dicht bij experimenteel vastgestelde waarden liggen. De numeriek geproduceerde lagen van SAP-korrels kunnen en zullen in toekomstige onderzoeken gebruikt worden om het effect van vorm op hydraulische parameters te onderzoeken, zoals de permeabiliteit (met behulp van directe simulaties) en de capillaire druk- en verzadigingskrommen (met behulp van de poriemorfologie methode).

In hoofdstukken 7 en 8 werd een nieuwe module ontwikkeld voor het onderzoeken van dynamiek van onverzadigde stroming tijdens het drogen en de zwelling van korrelvormige materialen. In hoofdstuk 7 werd de *pore-unit assembly* methode uitgebreid met dynamiek van onverzadigde stroom in niet-deformerende lagen van bollen, terwijl in hoofdstuk 8 de *pore-unit assembly* methode werd gekoppeld met DEM om zo deformatie te modelleren. Hoofdstuk 7 richt zich op dynamische aspecten van drogen van poreuze materialen. Er werd een samenvoegingsalgoritme geïntroduceerd om de assemblage van porie-eenheden te extraheren. Een pore-scale versie van IMPES (IMplicit Pressure Solver en EXplicit Saturation Update) werd gebruikt om de reeks vergelijkingen van onverzadigde stroom op te lossen. Met behulp van het model werd het dynamische drogen gesimuleerd. Invasie van lucht vond plaats via vingerachtige stroming, dit veroorzaakte een niet-monotone relatie van drukverschil tussen lucht en water met verzadiging. In hoofdstuk 8 werd de dynamische code uitgebreid met deformatie van de poreuze media. Er werd gekozen voor een éénrichtingskoppeling, waarbij de deformatie de onverzadigde stroming beïnvloedde, maar de onverzadigde stroming had geen invloed op de mechanische aspecten van de laag korrels.

Ten slotte, moet de korrel-schaal-modellerings-techniek die in dit proefschrift is gepresenteerd niet worden beschouwd als een vervanging van macroschaal simulaties of experimenten. De korrel-schaal-modellerings-techniek moet eerder worden gebruikt in combinatie met experimenten en macroschaal simulaties. Beschouw de korrel-schaal-modellerings-techniek als een virtueel experiment, waar de fysica op schaal van korrels wordt opgelegd en waar eigenschappen op de macroschaal een resultaat zijn. Virtuele experimenten kunnen gebruikt worden om macroschaalmodellen te verifiëren en gedetailleerd inzicht te verkrijgen in korrel-schaalprocessen. Dit geldt in het bijzonder voor complexe gevallen zoals zwelling van korrelige materialen onder onverzadigde omstandigheden.